

An Exploration of Perovskite Materials for
Thermochemical Water Splitting

Thesis by
Chih-Kai Yang

In Partial Fulfillment of the Requirements for the degree
of
Doctor of Philosophy



CALIFORNIA INSTITUTE OF TECHNOLOGY

Pasadena, California

2015

(Defended August 15, 2014)

To my family

© 2014

Chih-Kai Yang

All Rights Reserved

ACKNOWLEDGEMENTS

I want to begin by thanking my parents and my family members for their endless support and love overseas. I am devoutly grateful to my girlfriend, Yi-Chun Chen, for sharing my joys and tears at every moment in my life at Caltech.

I also thank my research advisor, Prof. Sossina Haile, for her guidance and the chance of doing research in this lab. Her prudence and honest attitude to probing the problems of science educated me a lot.

To interact with many intelligent scientists and kind people in lab let me feel blessed. I appreciate the consultations, discussions, and encouragement from Prof. William Chueh. The members who are/were working in thermochemical project, Prof. Yong Yao, Dr. Tim Davenport, Dr. Hari Prasad Dasari, Mike Ignatowich, and Stephen Wilke, provided lots of help and discussions. When I was in charge of the X-ray powder diffractometer at Caltech, I was really grateful for the help from Dr. Ayako Ikeda, Dr. Jaemin Kim, and Dr. Chatr Panithipongwut for solving all hardware and software issues. Also, the help from Carolyn Richmonds and Chirranjeevi (BG) Balaji Gopal for my XPS measurements and ECR station modifications is very important to me. Although Dr. Mary Louie, Dr. Taesik Oh, and Dr. WooChul Jung were working on the different projects, their suggestions inspired and helped me a lot. Good friends in lab, Rob Usiskin, Vanessa Evoen, Dr. Sara Thoi, Dr. Aron Varga, Anupama Khan, and Chris Kucharczyk, enriched my lab life.

I am also indebted to my Taiwanese friends at Caltech: Yun-Hua Hong, Alice Ju, Wei-Guang Liu, Chun-Hui Lin, Shu-Hao Chang, Wei-Ting Lai, Chien-Yao Tseng, Yun Mou, His-Chun Liu, Hsin-Hua Lai, I-Ren Lee, Ruo-Gu Huang, Wei-Chen Chen, Ray Huang, Wei-Hsun Lin, Yi Chen, Hsieh-Chen Tsai, Ho-Cheng Tsai, Ho-Hsuan Wei, Min-feng Tu, Tiffany Wang. I thank them for sharing joys with me and offering help without hesitation.

I particularly acknowledge Prof. Chia-Hung Hsu and Prof. Jia-Hong Huang in Taiwan. Every time I am depressed and want to give up, I am greatly beholden to their comfort and encouragement.

The six five years I've spent at Caltech was a journey of self-discovery to me. Perseverance sometimes could not guarantee achievements. I learned how to accept the imperfection and let it be.

Last, I want to finish by thanking my family again; after I gave up my initial purpose, they are still my strongest support for my new dream-seeking journey.

ABSTRACT

Two-step thermochemical water splitting is a promising technology for the hydrogen production of solar energy. This process possesses the advantages of utilizing the full solar spectrum, producing flexible fuels, and requiring no precious metal catalysts. It furthermore temporally separates the oxygen release and hydrogen production steps, eliminating the possibility of O₂ and H₂ recombination. Ceria, which undergoes non-stoichiometric changes in oxygen content, has been demonstrated as an effective material for solar-driven thermochemical fuel production, but the process requires extremely high temperatures (~ 1600 °C), leading to efficiency penalties and challenges in reactor design and construction. Accordingly, the objective of this work is the development of new thermochemical reaction substrate materials which enable operation at lower temperatures and ideally increase fuel productivity and efficiency. Here we explore perovskite systems, specifically La_{1-x}Sr_xMnO_{3-δ}, La_{0.8}Sr_{0.2}Mn_{1-y}Fe_yO_{3-δ}, and La_{0.8}Sr_{0.2}Mn_{1-y}Al_yO_{3-δ}. The link between the solid-state chemistry, redox properties, hydrogen production, and reaction kinetic limitations will be discussed. This study aims to learn how to design and tailor the good catalytic oxides for solar-driven thermochemical water splitting application.

TABLE OF CONTENTS

Acknowledgements	iii
Abstract.....	iv
Table of Contents	v
List of Illustrations and/or Tables	vi
Chapter 1: INTRODUCTION.....	1
1.1 Energy Crisis	1
1.2 Solar Hydrogen.....	3
1.3 Two-Step Thermochemical Splitting of Water	5
1.4 Nonstoichiometric Two-Step Thermochemical Splitting of Water	8
1.5 Discovery of Perovskites materials for Thermochemical Water Splitting	12
1.6 Literature Review and Problems Statements	14
BIBLIOGRAPHY	17
Chapter 2: EXPERIMENTAL APPROACHES AND TECHNIQUES.....	20
2.1 Introduction	20
2.2 Materials Preparation	20
2.3 Powder X-ray Diffraction.....	21
2.4 Mercury Porosimetry.....	22
2.5 Scanning Electron Microscopy	24
2.6 Thermogravimetric Analysis (TGA)	24
2.7 Quadrupole Mass Spectrometry.....	28
2.8 Thermochemical Water Splitting Cycle	29
BIBLIOGRAPHY	31
Chapter 3: THERMOCHEMICAL WATER SPLITTING WITH LANTHANUM STRONTIUM MANGANITE.....	32
3.1 Solid Solution Oxide $\text{La}_{1-x}\text{Sr}_x\text{MO}_{3-\delta}$	32
3.2 Lanthanum Strontium Manganite ($\text{La}_{1-x}\text{Sr}_x\text{MnO}_{3-\delta}$).....	33
3.3 Sr Content Impacts on Redox Properties of $\text{La}_{1-x}\text{Sr}_x\text{MnO}_{3-\delta}$	36
3.4 Thermal Stability Characterization of $\text{La}_{1-x}\text{Sr}_x\text{MnO}_{3-\delta}$	41
3.5 Thermochemical Water Splitting Cycles of $\text{La}_{1-x}\text{Sr}_x\text{MnO}_{3-\delta}$	45
3.6 Reaction Kinetics Discussion.....	53
BIBLIOGRAPHY	60
Chapter 4: SOLAR TO FUEL PRODUCTIVITY AND EFFICIENCY	62
4.1 Introduction.....	62
4.2 Fuel Production Reaction Extent	62
4.3 Temperature Effect on Reaction Extent.....	68
4.4 Materials-Related Impacts on Reaction Extent	75
4.5 Approaches to Designing New Materials from Solar to Fuel Efficiency Aspects.....	86
BIBLIOGRAPHY	98
Chapter 5: B SITE DOPING EFFECTS ON THERMOCHEMICAL CYCLING	99
5.1 Introduction.....	99
5.2 New Oxides Structure Characterizations.....	99
5.3 Thermochemical Cycling of $\text{La}_{0.8}\text{Sr}_{0.2}\text{Mn}_{1-x}\text{Fe}_x\text{O}_{3-\delta}$	106
5.4 Fe Substitution Impacts on Redox Natures of $\text{La}_{0.8}\text{Sr}_{0.2}\text{Mn}_{1-x}\text{Fe}_x\text{O}_{3-\delta}$	109

5.5 Thermochemical Cycling of $\text{La}_{0.8}\text{Sr}_{0.2}\text{Mn}_{1-x}\text{Al}_x\text{O}_{3-\delta}$	115
BIBLIOGRAPHY	122
Chapter 6: REACTION KINETICIS ASPECTS STUDIES	123
6.1 Introduction.....	123
6.2 Thermodynamic Influences on Kinetics	123
6.3 Concrete Examples: Thermal Reduction Kinetics	129
6.4 Concrete Examples: on Water Splitting Kinetics	134
6.5 Enhancing Reaction Kinetics through Materials Modification.....	139
BIBLIOGRAPHY	149
Chapter 7: CONCLUSIONS AND FUTURE OUTLOOK.....	150
7.1 Conclusions	150
7.2 Future Work.....	151

List of Figures	Page
1-1	Current and projected world energy demand.....1
1-2	Projected temperature changes for various CO ₂ emission scenarios.....2
1-3	Role of renewable energy production in the United States, 2013.....3
1-4	Temperature variations of ΔH° , $T\Delta S^\circ$, and ΔG° of water and carbon dioxide.....4
1-5	Concept diagram of two-step thermochemical water splitting and fuel cell combined system.....6
1-6	Temperature variations of ΔG° under 1 bar for thermal reduction reaction and water dissociation reaction of three different metal oxides pairs.....7
1-7	Temperature variations of Gibbs free energy of the gas-phase water oxidation reaction and ceria oxidation with different nonstoichiometric values.....11
1-8	The perovskite-type structure.....13
2-1	Flow chart of the porous pellets preparations.....21
2-2	Scheme of mercury pushed into an open pore of sample.....23
2-3	Various useful signals generated when the focused electron beam strikes on a specimen.....24
2-4	Non-stoichiometry of La _{0.7} Sr _{0.3} MnO _{3±δ}25
2-5	Schemes of partial molar enthalpy and entropy extraction from the oxygen non-stoichiometry dependence of temperature and oxygen partial pressure.....26
2-6	Schemes of the analyzer of a quadrupole mass spectrometry27
2-7	Schemes of the thermochemical station setup and mass spectrometry results of one thermochemical water splitting cycle.....30
3-1	Hydrogen productions from two-step thermochemical water splitting of La _{0.8} Sr _{0.2} CrO _{3-δ} , La _{0.8} Sr _{0.2} MnO _{3-δ} , and La _{0.8} Sr _{0.2} FeO _{3-δ}32
3-2	Non-stoichiometry of La _{0.9} Sr _{0.1} MnO _{3±δ} and schematic profile of oxygen content vs log p(O ₂) for La _{1-x} Sr _x MnO _{3±δ}34
3-3	Reduction enthalpy and entropy of La _{0.9} Sr _{0.1} MnO _{3±δ} extracted from the oxygen non-stoichiometry dependence of temperature and oxygen partial pressure.....35
3-4	Thermogravimetric measurements for La _{1-x} Sr _x MnO _{3±δ} with various Sr content38
3-5	Extracted reduction enthalpy and entropy of for La _{1-x} Sr _x MnO _{3-δ} (x=0.1, 0.2, 0.3, and 0.4)....40
3-6	X-ray powder diffraction patterns of La _{1-x} Sr _x MnO _{3-δ} before and after thermochemical cycling between 800-1400 °C.....43
3-7	Microstructure of La _{1-x} Sr _x MnO _{3-δ} before thermochemical cycle between 800-1400 °C.....45
3-8	Thermochemical cycle of 1400 – 800 °C using La _{0.8} Sr _{0.2} MnO _{3-δ}46
3-9	Impact of strontium substitution in La _{1-x} Sr _x MnO _{3-δ} on thermochemical water splitting during 1400 – 800 °C cycle.....49

3-10	Characteristic hydrogen production and oxygen release times as functions of Sr content.....	51
3-11	Hydrogen and oxygen yield in $\text{La}_{1-x}\text{Sr}_x\text{MnO}_{3-\delta}$	52
3-12	λ plotted as function of oxygen partial pressure and Sr content in $\text{La}_{1-x}\text{Sr}_x\text{MnO}_{3-\delta}$	56
3-13	Scheme of simplified thermogravimetric measurements.....	58
3-14	Peak flux of hydrogen plotted against change in oxygen content and change in chemical potential.....	59
4-1	Thermogravimetric curves of $\text{La}_{0.9}\text{Sr}_{0.1}\text{MnO}_{3-\delta}$ and $\text{La}_{0.6}\text{Sr}_{0.4}\text{MnO}_{3-\delta}$	63
4-2	Scheme of moles of reactant species involved in water splitting reaction.....	64
4-3	Reaction extent of water splitting reaction.....	68
4-4	Fixed water splitting reaction temperature (T_{WS}) reaction extent computed with the redox properties of CeO_2	70
4-5	Fixed thermal reduction reaction temperature (T_{TR}) reaction extent computed with the redox properties of CeO_2	73
4-6	Water splitting reactions with $\text{La}_{0.8}\text{Sr}_{0.2}\text{MnO}_{3-\delta}$ conducted at different temperatures.....	75
4-7	Reaction extent of CeO_2 , $\text{La}_{0.7}\text{Sr}_{0.3}\text{Mn}_{3-\delta}$, and $\text{La}_{0.6}\text{Sr}_{0.4}\text{Mn}_{3-\delta}$	77
4-8	Comparisons of reaction extent change with oxygen non-stoichiometry and with $P_{\text{O}_2, \text{solid}}$	78
4-9	Moles of water vapor required to induce the indicated stoichiometry change per mole of oxide at 800 °C.....	82
4-10	Reduction enthalpy impacts on reaction extent.....	84
4-11	Reduction entropy impacts on reaction extent.....	85
4-12	Relation between calculated efficiency and $r_{\text{H}_2\text{O}}$ for $\text{CeO}_{2-\delta}$	88
4-13	Second level HHV efficiency optimization for $\text{CeO}_{2-\delta}$	90
4-14	Example of third level HHV efficiency optimization for $\text{CeO}_{2-\delta}$	93
4-15	Efficiency analysis of $\text{La}_{1-x}\text{Sr}_x\text{MnO}_{3-\delta}$ and equilibrium hydrogen productivity expressed as the function of T_{WS}	95
4-16	Required heat inputs for individual processes of maximum HHV efficiency.....	95
4-17	HHV efficiency improved by the injected steam heat recovery.....	97
5-1	X-ray powder diffraction patterns of $\text{La}_{0.8}\text{Sr}_{0.2}\text{Mn}_{1-x}\text{Fe}_x\text{O}_{3-\delta}$ as-synthesized samples.....	100
5-2	Microstructure of $\text{La}_{0.8}\text{Sr}_{0.2}\text{Mn}_{1-x}\text{Fe}_x\text{O}_{3-\delta}$ before and after thermochemical cycle between 800-1400 °C.....	103
5-3	X-ray powder diffraction patterns of $\text{La}_{0.8}\text{Sr}_{0.2}\text{Mn}_{1-x}\text{Al}_x\text{O}_{3-\delta}$ as-synthesized samples.....	104
5-4	Microstructure of $\text{La}_{0.8}\text{Sr}_{0.2}\text{Mn}_{1-x}\text{Al}_x\text{O}_{3-\delta}$ as-synthesized porous monoliths.....	105

5-5	Thermochemical cycles between 800-1400 °C performed with $\text{La}_{0.8}\text{Sr}_{0.2}\text{Mn}_{1-x}\text{Fe}_x\text{O}_{3-\delta}$ ($x=0, 0.3, 0.5, 0.75, 0.85, \text{ and } 1$) porous samples.....	107
5-6	5 th thermochemical cycle of $\text{La}_{0.8}\text{Sr}_{0.2}\text{Mn}_{1-x}\text{Fe}_x\text{O}_{3-\delta}$ ($x=0, 0.3, 0.5, 0.75, 0.85, \text{ and } 1$) porous samples.....	109
5-7	Oxygen non-stoichiometry changes within the thermochemical cycle of $\text{La}_{0.8}\text{Sr}_{0.2}\text{Mn}_{1-x}\text{Fe}_x\text{O}_{3-\delta}$ ($x=0, 0.3, 0.5, 0.75, 0.85, \text{ and } 1$).....	109
5-8	Oxygen non-stoichiometry of $\text{La}_{0.75}\text{Sr}_{0.25}\text{FeO}_{3-\delta}$, extracted partial molar enthalpy and entropy of $\text{La}_{0.75}\text{Sr}_{0.25}\text{FeO}_{3-\delta}$ and the comparison with $\text{La}_{0.8}\text{Sr}_{0.2}\text{MnO}_{3-\delta}$, and thermodynamic framework applied with the redox properties of $\text{La}_{0.75}\text{Sr}_{0.25}\text{FeO}_{3-\delta}$	111
5-9	Oxygen non-stoichiometry of $\text{La}_{0.8}\text{Sr}_{0.2}\text{Mn}_{1-x}\text{Fe}_x\text{O}_{3-\delta}$ ($x=0, 0.25, 0.5, \text{ and } 0.75$) measured by thermogravimetric analyzer.....	113
5-10	Extracted reduction enthalpy and entropy of $\text{La}_{0.8}\text{Sr}_{0.2}\text{Mn}_{1-x}\text{Fe}_x\text{O}_{3-\delta}$	115
5-11	5 th thermochemical cycle of $\text{La}_{0.8}\text{Sr}_{0.2}\text{Mn}_{1-x}\text{Al}_x\text{O}_{3-\delta}$ ($x=0, 0.25, 0.5, \text{ and } 0.75$) porous samples...	117
5-12	Oxygen non-stoichiometry changes within the thermochemical cycle of $\text{La}_{0.8}\text{Sr}_{0.2}\text{Mn}_{1-x}\text{Al}_x\text{O}_{3-\delta}$ ($x=0, 0.25, 0.5, \text{ and } 0.75$).....	118
5-13	Redrawing the thermochemical cycle of $\text{La}_{0.8}\text{Sr}_{0.2}\text{Mn}_{1-x}\text{Al}_x\text{O}_{3-\delta}$ ($x=0, 0.25, 0.5, \text{ and } 0.75$) as the flux of δ	121
6-1	Scheme of moles of reactant species involved in thermal reduction reaction.....	126
6-2	Simulation of oxygen non-stoichiometry (δ) evolution of $\text{La}_{0.6}\text{Sr}_{0.4}\text{MnO}_{3-\delta}$ during thermal reduction reaction.....	130
6-3	Simulation of oxygen release fluxes of $\text{La}_{1-x}\text{Sr}_x\text{MnO}_{3-\delta}$ ($x=0.1, 0.2, 0.3, \text{ and } 0.4$) during thermal reduction reaction.....	133
6-4	Gas carrier flow rate impacts on reduction reaction equilibrium kinetics.....	134
6-5	Simulation of hydrogen release fluxes of $\text{La}_{1-x}\text{Sr}_x\text{MnO}_{3-\delta}$ ($x=0.1, 0.2, 0.3, \text{ and } 0.4$) during water splitting reaction.....	138
6-6	Inject steam flow rate impacts on water splitting reaction.....	139
6-7	Thermochemical cycle of 1400 – 800 °C of $(\text{La}_{0.50}\text{Sr}_{0.50})_x\text{MnO}_{3-\delta}$ ($x=0.9, 0.94, 1, 1.04, 1.08, \text{ and } 1.16$).....	141
6-8	Gas evolution amounts of $(\text{La}_{0.50}\text{Sr}_{0.50})_x\text{MnO}_{3-\delta}$ generated from the thermochemical cycle of 1400 – 800 °C.....	143
6-9	Microstructure of as-synthesized porous $(\text{La}_{0.50}\text{Sr}_{0.50})_x\text{MnO}_{3-\delta}$ ($x=0.9, 0.94, 1, 1.04, 1.08, \text{ and } 1.16$) pellets.....	144
6-10	X-ray powder diffraction patterns of as-synthesized porous $(\text{La}_{0.50}\text{Sr}_{0.50})_x\text{MnO}_{3-\delta}$ ($x=0.9, 0.94, 1, 1.16, \text{ and } 1.24$) pellets.....	146

6-11	Crystal structure of $A_{n+1}B_nO_{3n+1}$ (n=1, 2, and 3) and it is also called Ruddlesden-Popper phase.147
7-1	HHV efficiency optimization for hypothetical materials.....154

List of Tables	Page
1-1 Properties and applications of compounds with perovskite and related structure.....	13
2-1 The diffractometer settings used.....	22
2-2 Thermodynamics data of $\text{CeO}_{2-\delta}$	36
3-1 Room-temperature structural parameters for $\text{La}_{1-x}\text{Sr}_x\text{MnO}_{3-\delta}$	44
3-2 Cycle-averaged fuel productivity of $\text{La}_{1-x}\text{Sr}_x\text{MnO}_{3-\delta}$	52
5-1 Refined room-temperature structural parameters for $\text{La}_{0.8}\text{Sr}_{0.2}\text{Mn}_{1-x}\text{Fe}_x\text{O}_{3-\delta}$ as-synthesized samples and the porosity of the porous monolith.....	101
5-2 Refined room-temperature structural parameters for $\text{La}_{0.8}\text{Sr}_{0.2}\text{Mn}_{1-x}\text{Al}_x\text{O}_{3-\delta}$ as-synthesized samples and the porosity of the porous monolith.....	104
5-3 Literature reported fuel productivities of $\text{La}_{1-y}\text{Sr}_y\text{Mn}_{1-x}\text{Al}_x\text{O}_{3-\delta}$	120
6-1 Room-temperature structural parameters for as-synthesized $(\text{La}_{0.50}\text{Sr}_{0.50})_x\text{MnO}_{3-\delta}$ ($x=0.9, 0.94, 1, 1.16,$ and 1.24) samples.....	146

Chapter 1

INTRODUCTION

1.1 Energy Crisis

World energy demand in the past two decades has increased at a rate of 1.9 percent per year^[1]. The U.S. Energy Information Administration projects that of world energy demand from 2010 to 2040 will grow at a total average growth rate of around 1.4 percent per year (Figure 1-1). Strong and fast economic growth and population expansion in the developing nations largely drive this increase in global energy demand. The peak oil prediction from Hubbert Peak Theory^[2] forecasts a potential shortage of oil. Although many factors make the model and therefore the time of which oil production will peak uncertain, it is clear that society is consuming the finite fossil fuel resource base at an alarming rate^[3], the general trend of the shortage of fossil fuels is still alarming. Therefore, the exploration of new energy resources is crucial.

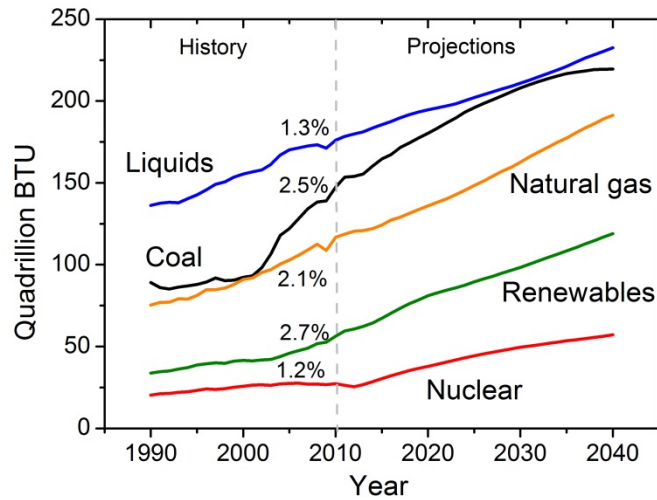


Figure 1-1 Current and projected world energy demand from 1990 to 2040 from ref. [1].

The percentage corresponds to the average annual growth rate.

Furthermore, the energy crisis people are facing is not only the quantity of energy but also its quality. From the world energy demand among various sources shown in Figure 1-1, liquids, coal, and natural gas supply around 80% of the total demand. These carbon based fuels generate a large amount of greenhouse gas such as CO₂ and CH₄. The most recent report from the IPCC (Intergovernmental Panel on Climate Change) ^[4] shows a high correlation between global warming and the rise in CO₂ emission. In this report, various emission scenarios and their corresponding temperature increase trends are proposed (Figure 1-2). Since we are currently on the high CO₂ emission path, the average predicted temperature increase would be around 0.3°C per decade. Global warming causes climate changes that have tremendous impacts on the environment. For example, melting of the ice caps and glaciers cause the rise of sea levels because of thermal expansion of water and this changes endanger the ecosystem. Furthermore, in the recent past few decades, global warming has been implicated in the dramatic weather changes such as strong storms, torrential floods, and droughts. Although these impacts from global warming have been foreseen for a long time, the speed and ubiquity of these consequences have been unprecedented. In the Third National Climate Assessment report released by the White House in 2014 ^[5], the scientists declared that “Climate change, once considered an issue for a distant future, has moved firmly into the present.” Therefore, the discovery of alternative, renewable, and clean energy resources is necessary right now in order to combat the energy crisis, palliate the dependence on carbon-based fuels, and slow down the global warming effects.

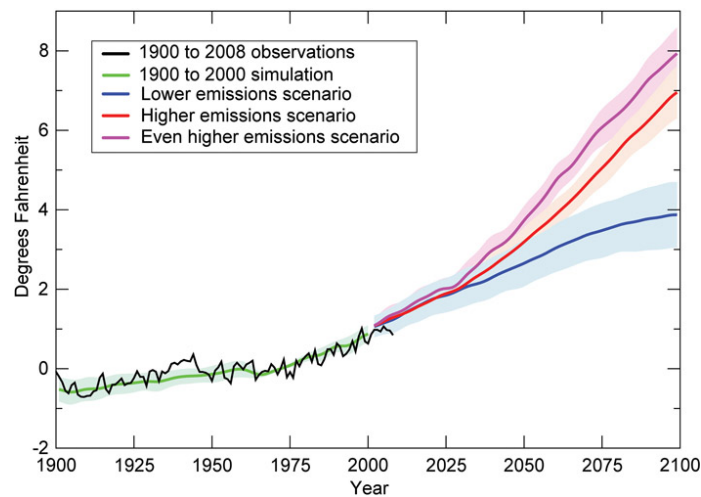


Figure 1-2 Projected temperature changes for various CO₂ emission scenarios^[4].

1.2 Solar Hydrogen

Fuel produced by renewable resources is one of the promising solutions for the energy and climate crises. Renewable energy production is around 11% of the total United States primary energy productions^[6], Figure1-3. Primary renewable resources include hydroelectric power, geothermal energy, solar/ photovoltaics (PV) energy, wind energy, and biomass energy. Solar energy is a particularly attractive resource due to the abundance of sunlight. A recent analysis shows that the energy from the Sun striking on the earth's surface in one and a half hours can provide more energy than worldwide energy consumption in a year (based on the all sources combined data of from 2001).^[7] However, solar accounts for only 0.33% of all primary energy sources utilized in the US. Thus huge gap between solar energy availability and solar energy utilization presents a tremendous opportunity to address world energy needs. Thus, this dissertation focuses on solar energy utilization, specifically, fuel production from water splitting driven by solar energy. Solar-driven water splitting utilizes the abundance of water and the unlimited solar resource for fuel production. Because the reactant, the product, and the whole reaction are carbon-lean, the climate and environment would not be sacrificed for fuel production and consumption.

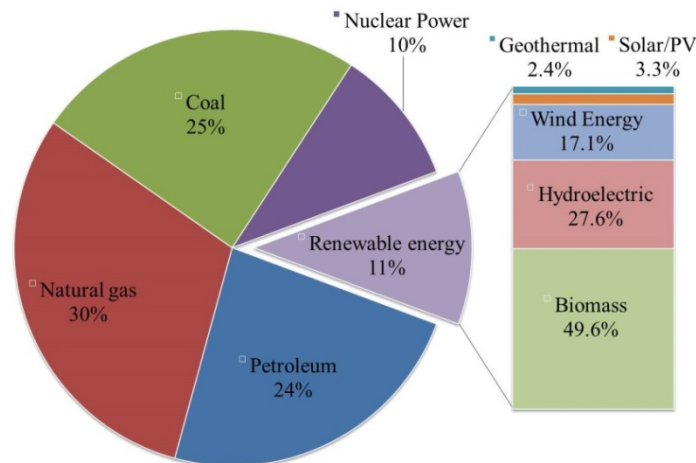


Figure 1-3 Role of renewable energy production in the United States, 2013. ^[6]

Various approaches to solar-driven water splitting have been widely studied, such as the combined operation of photovoltaics (PV) and electrolyzer^[8], and photocatalytic water splitting.^[9] Most recently, solar-driven thermochemical water splitting has attracted significant attention due to its potential for large scale hydrogen production.^[10-14]

At a first glance, the direct thermochemical hydrogen production from water is the simplest pathway to convert solar energy to fuel. However, from the thermodynamic properties of water, this single-step thermolysis reaction is not practical due to its extremely high operation temperature.^[12, 15] Water and carbon dioxide thermolysis reactions are shown in Figure 1-4. In order to get the reaction thermodynamically favorable, the operating temperature has to be higher than 4,330 °K and 3,330 °K for water and carbon dioxide splitting, respectively. Many problems can arise with such high operating temperatures, and the following factors must be addressed ^[16]:

1. A complicated reactor design or secondary solar concentrator is necessary for achieving such high temperatures.
2. High stability of reactor materials is critical.
3. Recombination of products (H_2 and O_2) or generation of intermediates (e.g., OH) can occur and need to be avoided.

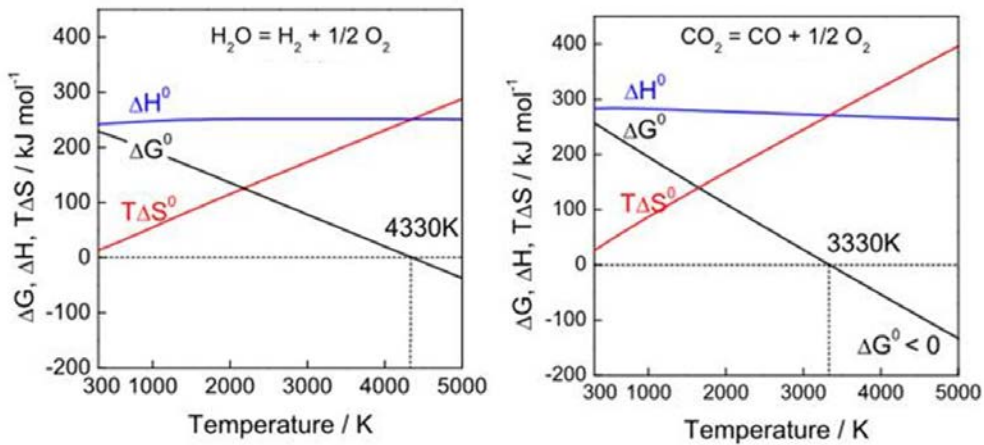


Figure 1-4 Temperature variations of ΔH° , $T\Delta S^\circ$, and ΔG° for water and carbon dioxide.^[12]
The partial pressure of each gas species is 1 bar.

1.3 Two-Step Thermochemical Splitting of Water

In order to lower the operating temperature of thermally-driven hydrogen production, multi-step reactions have been considered^[17]. In particular, the effectiveness of metal oxides for two-step thermochemical water splitting cycles has been examined for around four decades^[20-21]. The main concept is depicted by the following equations:



Here, M represents a metal and MO_n is its corresponding metal oxide. In a typical two-step thermochemical water splitting cycle, a metal oxide is reduced at very high temperature (~2000 K) by concentrated solar energy in the first step. During this reduction reaction, oxygen molecules will be released, as shown in Equation 1.1. In the second step, the reduced metal oxide (or metal, if it's fully reduced to the metal phase) is quenched to a lower temperature and H_2O steam is simultaneously injected into the reactor. The reduced metal oxide will be reoxidized by H_2O and release H_2 , Equation 1.2. The first step is called the thermal reduction (TR) step and the second step is called the water splitting (WS) step. After the reduced metal oxide is reoxidized (at the end of the WS step), solar energy is used to ramp the temperature back up to perform the reduction reaction again. Upon cycling the metal oxide between the thermal reduction (TR) step and the water splitting (WS) step, water can be dissociated and fuel (hydrogen) can be produced. Equation 1.3 is the sum of Equation 1.1 and 1.2 and describes the net reaction of a two-step thermochemical water splitting cycle. Figure 1-5 shows the concept of two-step thermochemical water splitting cycle and its combination with a fuel cell system. The mechanism of a two-step

thermochemical water splitting cycle can also be used for CO₂ splitting application, as shown in the Figure 1-5.

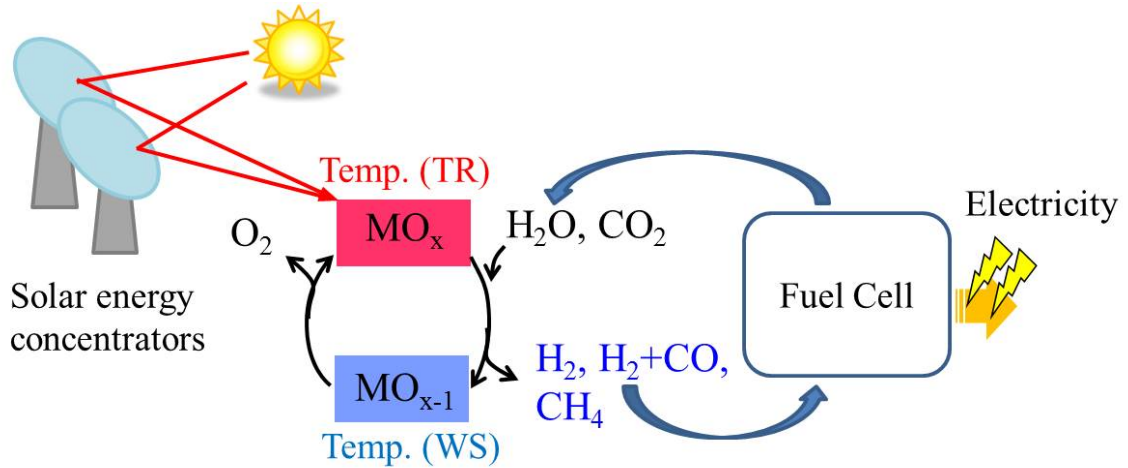


Figure 1-5 Concept diagram of two-step thermochemical water splitting and fuel cell combined system.

The very first demonstration of a two-step thermochemical water splitting cycle used a Fe₃O₄/ FeO redox pair^[22] and the cycle proceeded as follows:



Equation 1.4 represents the thermal reduction step. It is a highly endothermic reaction ($\Delta H^\circ=316.6$ kJ/mol). At 1 bar of oxygen partial pressure, the temperature to reduce the magnetite (Fe₃O₄) to wustite (FeO) is above 3,000 K (shown in Figure 1-6).^[12] For the second step of the cycle, the reaction shown in Equation 1.5 is exothermic ($\Delta H^\circ=-33.6$ kJ/mol) and can proceed below 1000 K, as shown in Figure 1-6(b). In comparison to Fe₃O₄/ FeO redox pair, Mn₃O₄/ MnO and Co₃O₄/ CoO show the lower temperatures when the reduction reaction free energy goes to zero at, suggesting it is easier to perform the thermal reduction step with these oxides (Figure 1-6(a)). However, for the water splitting step shown in Figure 1-6 (b), the temperature range needs to be widened in order to extrapolate their intersection with the zero free energy dashed line. At the given

temperature located in the negative free energy region, the distance between the curve to the zero free energy line can be considered as the thermodynamics driving force for the reaction. Therefore, Mn_3O_4/MnO and Co_3O_4/CoO pairs possess a larger driving force for the thermal reduction reaction as compared to the Fe_3O_4/FeO redox pair, but their driving forces for being re-oxidized by water are much less.

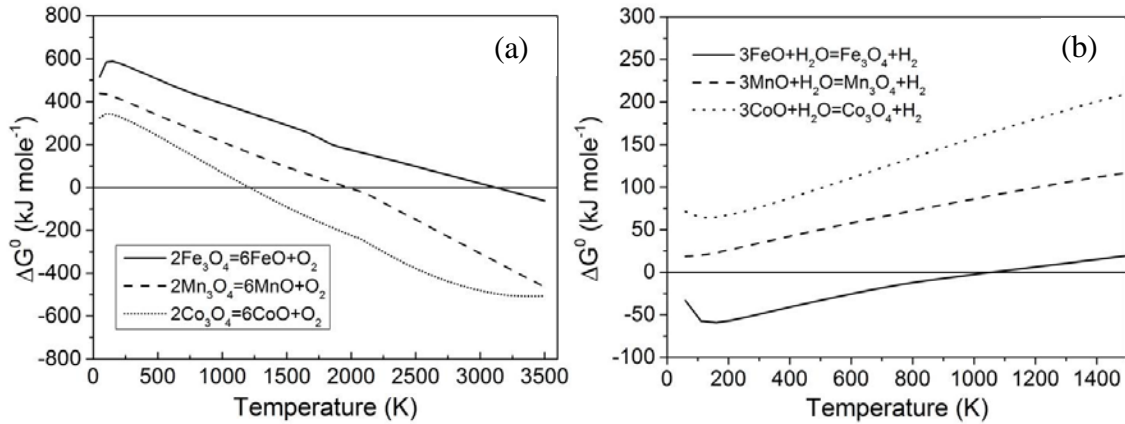


Figure 1-6 Temperature variations of ΔG° (with 1 bar of each gas species partial pressure) for thermal reduction reaction (a) and water dissociation reaction (b) of three different metal oxides pairs.^[12] Free energy curves are calculated with HSC database.^[15]

Another potential candidate is the ZnO/Zn redox pair for the two-step thermochemical water splitting cycle^[22], and the corresponding reactions for each step are described with Equation 1.6 and 1.7.



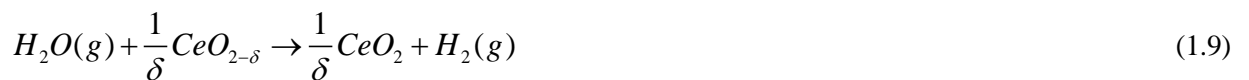
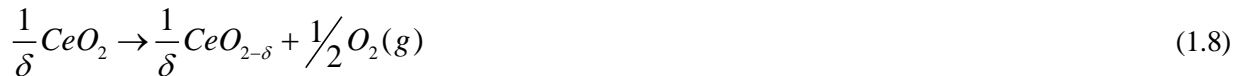
ΔH° for Equation (1.6) is 489 kJ and the temperature for which $\Delta G^\circ=0$ is around 2,235 °K. For the second step, the reaction proceeds thermodynamically below about 1,400 °K at 1 bar.^[23] In contrast to the hydrolysis reaction with FeO shown in Equation 1.5, the reactant here is metallic Zn. This re-oxidation reaction is a heterogeneous reaction and Zn (g) and

O₂ can coexist in a meta-stable state if the nucleation sites are insufficient ^[24]. In order to prevent reoxidation, the Zn has to be quenched from the gaseous state. Therefore, the kinetics of Zn conversion is mainly controlled by diffusion of Zn (g) and O₂ to the reactor walls ^[23, 25], and the Zn nanoparticle in the water splitting step is required in order to have sufficient kinetics. These constraints make the ZnO recovery and reactor design difficult.

From the cases mentioned above, we can see that the water dissociation temperature can be lowered by a two-step cycle as compared to direct water splitting. Since oxygen release and hydrogen production occur in separate steps, this two-step cycle eliminates O₂ and H₂ recombination and simplifies their isolation and purification. However, when utilizing these oxides for two-step cycle, phase transitions are involved and these cause the new challenges. For example, within the case of Zn/ZnO cycling, the recombination of Zn(g) and O₂(g) block the reaction shown in Equation 1.7. Also, with the phase transition involvement, bulk diffusion limits the reaction kinetics.

1.4 Nonstoichiometric Two-Step Thermochemical Splitting of Water

The operation temperature of the two-step thermochemical water splitting cycle is redox materials dependent. Although the reduction temperature of the Fe₃O₄/FeO and ZnO/Zn pairs is much lower than that of direct water thermolysis, it is still too high for practical and long-term operation. And, the bulk diffusion is the rate limiting step when phase transition is involved in the two-step cycling. Therefore, a potential mechanism that can lower the reduction temperature is desirable. Recently, a new approach called nonstoichiometric two-step thermochemical water splitting cycle was proposed and demonstrated by our group ^[14]. This strategy utilizes the ability of selected non-stoichiometric metal oxides to release and uptake oxygen in response to temperature changes. The redox material we used is cerium oxide (ceria) and its two-step thermochemical water splitting cycle is presented in the following:



The sum of the two equations above is the pure water dissociation reaction. In comparison to the metal oxide redox pairs mentioned before, this approach performs the reduction reaction partially at the thermal reduction step rather than a stoichiometric phase change. For cerium oxide reduced from 800 °C to 1600 °C under an atmosphere of 10 ppm oxygen balanced with inert gas, the oxygen release amount is around 5.9 mL (STP) per gram CeO₂, corresponding to the oxygen nonstoichiometric change (δ of CeO_{2- δ) of ~0.09. After quenching and steam injection, the water splitting step is conducted. When the reoxidization reaction temperature is 800 °C, meaning the cycling temperature window is 800 °C to 1600 °C, the hydrogen productivity is around 11.8 mL (STP) per gram CeO₂. The ratio of hydrogen produced to oxygen released was found to be around 2, as expected from the pure water dissociation reaction shown in Equation 1.3. Furthermore, since the oxygen nonstoichiometric changes between cycles matched the thermodynamic properties of cerium oxide (to be discussed later), this means both the thermal reduction and reoxidization reactions are produced to completion under the given experimental conditions. Even though the fuel productivity per cycle of this approach is less than the stoichiometric phase change method, the high diffusivity of oxygen through nonstoichiometric ceria leads to rapid fuel production kinetics.}

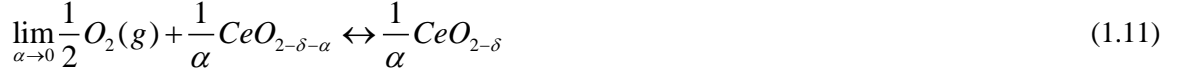
The redox (reduction and oxidization) properties of the metal oxide govern its behavior within the two-step thermochemical water splitting cycle. Taking CeO₂ as an example, the mechanism behind the thermal reduction reaction is the valence change of cerium cation, and the corresponding equation shown in Equation 1.8 can be rewritten as



The equation is written with Kröger–Vink notation ^[28], where Ce_{Ce}^{\times} , Ce'_{Ce} , and $V_O^{\bullet\bullet}$ represent the ions of Ce⁴⁺, Ce³⁺, and oxygen vacancy, respectively. Kröger–Vink notation is widely used in describing defect reactions. When a defect is notated as M_S^C , it represents the species M (atom, “V” for vacancy, “i” for interstitial (if it is not a regular site), “e” for electron, and “h” for electron hole) site on the host lattice site S, and possesses the effective charge C (“/” for single negative charge, “••” for double positive charge, and “X” for neutral charge). Therefore, Equation 1.10 describes the reduction reaction of CeO₂ where

Ce cations are reduced from Ce^{4+} to Ce^{3+} , the neutral oxygen molecular is released, and the double positive charged oxygen vacancies are created due to charge conservation.

For the second step, the reoxidation reaction can be obtained by reversing the Equation 1.10. In Equation 1.10, Ce'_{Ce} can be considered as a small polaron the equation can be expressed the reaction with infinitesimal change in non-stoichiometry.



Within the range where the oxygen nonstoichiometric change possesses ideal solution behavior, the equilibrium constant for this oxidization reaction is given by ^[14]

$$K_{oxd} = \exp\left(-\frac{\Delta G_{oxd}^0}{RT}\right) = \exp\left(-\frac{\Delta H_{oxd}^0 - T\Delta S_{oxd}^0}{RT}\right) \quad (1.12)$$

where ΔG_{oxd}^0 , ΔH_{oxd}^0 , and ΔS_{oxd}^0 are the standard Gibbs free energy, enthalpy, and entropy of oxidation reaction, respectively. In an ideal solution, the oxidation enthalpy is independent of defect concentration, and the configurational entropy is used to describe the solution with non-interacting defects that distribute randomly.

The equilibrium constant for this oxidization reaction can be linked to the defect species as follows:

$$K_{oxd} = \frac{[Ce_{Ce}^{\times}]^2 [O_o^{\times}]}{(p_{O_2}^*)^{1/2} [Ce'_{Ce}]^2 [V_o^{\bullet\bullet}]} = \frac{(1-2\delta)^2 (1-\delta/2)}{(p_{O_2}^*)^{1/2} 4\delta^2 (\delta/2)} \quad (1.13)$$

where $p_{O_2}^*$ represents the oxygen partial pressure relative to the standard state (1 atm), and $[\]$ stands for the concentration of defect species. The final expression is achieved by applying electroneutrality ($2\delta = [Ce'_{Ce}] = 4[V_o^{\bullet\bullet}]$) and conservation of crystal site ($1 = [Ce'_{Ce}] + [Ce_{Ce}^{\times}]$).

For understanding how to select the redox medium for thermochemical water splitting application on thermodynamics grounds, the comparison between the chemical potential of the nonstoichiometric oxide (ΔG_{oxd}^0) and $\Delta G_{\text{rxn_water}}^0$ of the water oxidation reaction under the same reoxidization conditions is the straightforward method. Figure 1-7 shows this comparison with ceria oxidation with different nonstoichiometric values. Since this describes the oxidation reaction, meaning the half-cycle operated at the relatively lower temperature (T_1) of water splitting, we assume the ceria possesses certain nonstoichiometric value after the thermal reduction reaction. For a given nonstoichiometric value at a specific reaction temperature, the reaction can proceed only if the free energy curve of the reduced oxide is lower than the curve of water oxidation reaction, meaning $\Delta G_{\text{oxd}}^0 < \Delta G_{\text{rxn_water}}^0$, as shown by the red line in the figure. Although actual operating conditions are not at standard state, this kind of comparison still provides the valuable insights for screening redox materials.

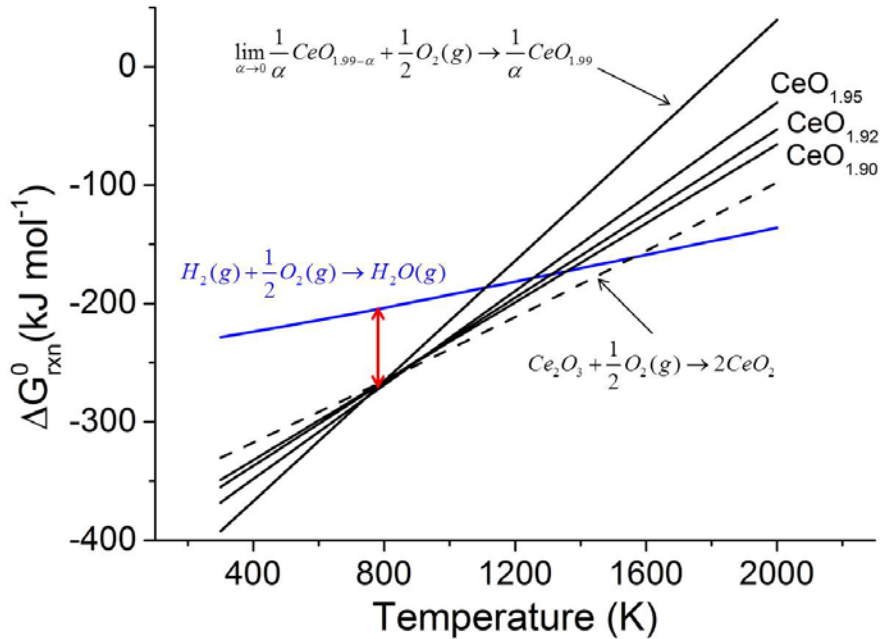


Figure 1-7 Temperature variations of Gibbs free energy of the gas-phase water oxidation reaction (with the gas species at 1 atm), ceria oxidation with different nonstoichiometric values (the oxygen partial pressure at 1 atm).^[14]

On Figure 1-7, the red virtual line in the figure represents the difference between two free energy curves of reduced oxide and water, and can be considered as the thermodynamics driving force of water splitting reaction. Therefore, if the red line is shifted left at lower water splitting reaction temperature, the thermodynamics driving force becomes larger. However, the low reaction temperature would also limit the reaction kinetics. In addition, with the fixed thermal reduction temperature, the lower water splitting reaction temperature means a larger temperature window and can potentially introduce thermal shock concerns. The change in ΔG_{oxd}^0 with different nonstoichiometric values results from the cerium–oxygen bond enthalpy change and the configurational entropy change from defect concentration variations. This dependence of ΔG_{oxd}^0 on nonstoichiometric values shows that the thermodynamics driving force for water splitting changes with the differing extent of the reoxidation reaction. In Figure 1-7, the slope of the curve is determined by ΔS_{oxd}^0 , the y-intercept on is ΔH_{oxd}^0 ($\Delta G_{oxd}^0 = \Delta H_{oxd}^0 - T\Delta S_{oxd}^0$). Therefore, from the thermodynamics properties ($\Delta H_{rxn_water}^0$ and $\Delta S_{rxn_water}^0$) of water thermolysis, the prerequisite for thermochemical water splitting on materials' redox properties can be set as

$$\begin{aligned} \Delta H_{oxd}^0 &< \Delta H_{rxn_water}^0 (= -241kJ / mol \cdot O) \\ \Delta S_{oxd}^0 &< \Delta S_{rxn_water}^0 (= -44.4J / k \cdot mol \cdot O) \end{aligned} \quad (1.14)$$

These conditions will ensure that the half cycle of thermochemical water splitting (Equation 1.11) is thermodynamically favorable and its corresponding reduction reaction temperature is lower than the temperature for direct water dissociation.

1.5 Discovery of Perovskites materials for Thermochemical Water Splitting

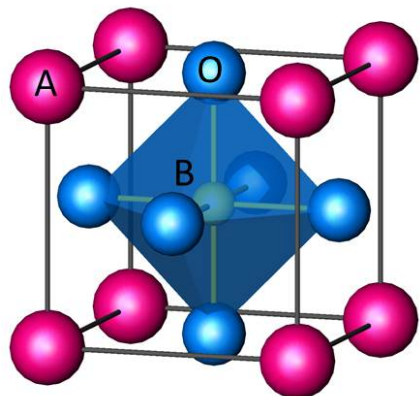


Figure 1-8 The perovskite-type structure. Red balls represent the A atoms of ABO_3 , blue balls represent the oxygen atoms, and yellow balls located inside the blue octahedral represent the B atoms.

The perovskite structure was first named by the mineralogist Lev Perovski after the ideal composition $CaTiO_3$ found by Gustav Rose (1839) ^[30]. Many mixed metal oxides with formula ABO_3 , for which A and B cations differ in their ionic radius or charge valence, are classified in the perovskite structure family ^[29]. Some non-oxide compounds with similar structure (ABX_3 , X is anion) are also classified as perovskites. The crystal structure is shown in Figure 1-8. For the perovskite oxides, A is coordinated by 12 other atoms. Site B is surrounded by oxygen atoms octahedrally and builds the corner-sharing BO_6 octahedra (blue).

Table 1-1 lists example compounds with perovskite and related structures used for different applications. The table shows that perovskite and its derivatives have been widely studied for different properties and applied in various science and engineering fields. For the two-step thermochemical water splitting cycle, the redox properties of metal oxide govern the feasibility and performance of the reactions. These properties are also studied for solid oxide fuel cell (SOFC) and in other solid state chemistry fields. Thus, the tunability of perovskites and the large body of literature in this area motivate further exploration of perovskites for thermochemical water splitting.

Table 1-1 Properties and applications of compounds with perovskite and related structure

Property	Compounds	Application	References
Super Conductivity	SrTiO_3 , $\text{Ba}_x\text{La}_{5-x}\text{Cu}_5\text{O}_5$	Super conductors	[33] [34]
Optical	YAlO_3	Laser	[35]
Proton conductivity	BaCeO_3 , BaZrO_3 , SrCeO_3	SOFC electrolyte / Hydrogen sensor	[36] [37] [38] [39]
Ironic conductivity	$(\text{La},\text{Sr})(\text{Ga},\text{Mg})\text{O}_3$	SOFC electrolyte	[40]
Mixed conductivity	$(\text{Ba},\text{Sr})(\text{Co},\text{Fe})\text{O}_3$ $\text{Sr}(\text{Ti},\text{Fe})\text{O}_3$	SOFC electrode	[41] [42]
Electrical/ Dielectric	BaTiO_3 , $\text{Ba}(\text{Zn},\text{Ta})\text{O}_3$	dielectric resonator, thin film resistor	[43] [44]
Ferroelectric/ Piezoelectric	$\text{Pb}(\text{Zn},\text{Nb})\text{O}_3$, $\text{Pb}(\text{Zr},\text{Ti})\text{O}_3$	ferroelectric tunable capacitance/ Piezoelectric transducer	[45] [46]

1.6 Literature Review and Problem Statement

After the concept of oxygen nonstoichiometric cycle is demonstrated ^[14, 27], the interest in two-step thermochemical water splitting cycles was renewed due to the lower operation temperature (as compared to direct water splitting), and ease of operation relative to cycles involving stoichiometric phase changes. Two classes of non-stoichiometric (variable valence) oxides have been studied: fluorites based on ceria ($\text{CeO}_{2-\delta}$) ^[14, 27, 47-48] and perovskites based on lanthanum manganite ($\text{LaMnO}_{3-\delta}$, in which δ may be < 0) ^[49, 50] or lanthanum aluminate ($\text{LaAlO}_{3-\delta}$) ^[51]. For the ceria-based class of compounds, extensive studies have revealed that this group of materials generally requires rather high temperatures (> 1500 °C) ^[14, 27] to reduce the oxide to an extent that the cycling yields non-

trivial amounts of fuel and appreciable oxygen nonstoichiometric change for the first step of the cycle. Although proof of principle has been successfully demonstrated with CeO_2 installed in a solar reactor ^[27], such high temperatures ($>1500^\circ\text{C}$) nevertheless create significant challenges for reactor design and operation.

In 2012, several systems of perovskites were demonstrated for two-step thermochemical water splitting cycles by our group ^[49]. Almost simultaneously, two other laboratories reported experimental results from lanthanum manganite based perovskites. Scheffe et al. ^[51] evaluated the potential of $\text{La}_{1-x}\text{Sr}_x\text{MnO}_{3-\delta}$ compounds ($x = 0.2, 0.3, 0.4$) for thermochemical fuel production on the basis of literature data for the bulk thermodynamic redox properties and supplemented the analysis with an experimental study of the reduction behavior of the composition with $x = 0.35$. Although the fuel production half-cycle was not directly probed, the authors were able to show greater oxygen release from the perovskite than from ceria at moderate temperatures, indicating the potential for greater fuel productivity under reduced temperature cycling conditions. McDaniel et al. ^[51] evaluated the $\text{La}_{0.6}\text{Sr}_{0.4}\text{Mn}_{1-x}\text{Al}_x\text{O}_{3-\delta}$ system and demonstrated high levels of fuel productivity for a high temperature reduction step of just 1350°C . These authors suggested, however, that obtaining high hydrogen yields would require large quantities of excess steam to drive the reaction to completion.

Prior to these studies of thermally driven CO_2 and H_2O dissociation with lanthanum manganite based perovskite, a handful of researchers have demonstrated CH_4 to syngas conversion over $\text{La}_{1-x}\text{Sr}_x\text{MnO}_{3-\delta}$ ^[52-54]. This process also relies on the oxygen uptake and release of the oxide, but the materials redox properties were not explicitly considered in these studies. In sum, this previous work indicates that perovskite-structured materials have significant promise as reactive media for solar-driven thermochemical fuel production, but direct evaluation of this class of materials for this application is extremely limited.

The main goals and the approaches of the present work are:

1. To provide a greater understanding of perovskite-structured oxides for solar fuels generation.
 - Among several perovskite-structured oxides found and demonstrated by our group ^[50], we examined the $\text{La}_{1-x}\text{Sr}_x\text{MnO}_{3-\delta}$ system in particular because

of the availability of thermogravimetric data. We complement an analytical evaluation of these materials with extensive thermochemical cycling experiments.

2. To tailor the redox properties of the $\text{La}_{1-x}\text{Sr}_x\text{MnO}_{3-\delta}$ system via B site cation doping.
 - We varied the chemical nature of the BO_6 polyhedral unit within the $\text{La}_{1-x}\text{Sr}_x\text{MnO}_{3-\delta}$ system and examined the fuel production capacity and kinetics. Although the thermogravimetric data and other redox properties of these new compositions are limited, the composition dependent features of oxygen release and fuel production provide insight into the role of materials chemistry.
3. To explore new approaches for improving the reaction kinetics.
 - In order to achieve maximum efficiency, it is essential to ensure rapid reaction kinetics and minimize reaction periods. We provide potential approaches for enhancing the reaction kinetics without introducing noble metal catalysts.
4. To evaluate the advantages and disadvantages of using perovskite-structured materials for solar-driven thermochemical water splitting.
 - Many perovskite-structured materials that provide very high fuel productivity are examined to demonstrate the advantages of perovskite-structured materials for solar-driven thermochemical water splitting. An efficiency analysis will also be conducted to examine the strengths and weaknesses.

BIBLIOGRAPHY

1. International Energy Outlook 2013, U.S. Energy Information Administration, 2011.
2. Hubbert Peak Theory, Wikipedia [Online], Available: http://en.wikipedia.org/wiki/Hubbert_peak_theory
3. “Why the Peak Oil Theory Falls Down: Myths, Legends, and the Future of Oil Resources”, IHS CERA, 2007.
4. Report from IPCC - Intergovernmental Panel on Climate Change, project 2007, http://www.ipcc.ch/publications_and_data/ar4/wg1/en/tssts-6-4-2.html
5. Third National Climate Assessment report, May 6, 2014., http://www.whitehouse.gov/climate-change?utm_source=email&utm_medium=email&utm_content=email329-text3&utm_campaign=climate
6. U.S. Energy information administration, Monthly Energy review 2014
7. Solar FAQs edited by Jeff Tsao, Nate Lewis, and George Crabtree, Available: <http://www.sandia.gov/~jytsao/Solar%20FAQs.pdf>
8. M. Carmo, D. L. Fritz, J. Mergela and D. Stolten, International Journal of Hydrogen Energy, 2013, vol. 38, 4901-4934
9. M. G. Walter , E. L. Warren , J. R. McKone , S. W. Boettcher, Q. Mi , E. A. Santori and N. S. Lewis , Chemical Reviews, 2010, 110(11), 6446-6473
10. A. Kudo and Y. Miseki, Chem. Chemical Society Reviews, 2009, 38, 253-278.
11. K. Maeda, Journal of Photochemistry and Photobiology C: Photochemistry Reviews, 2011, 12, 237-268.
12. T. Kodama and N. Gokon, Chemical Reviews, 2007, 107, 4048-4077.
13. A. Steinfeld, International Journal of Hydrogen Energy, 2002, 27, 611-619.
14. W. C. Chueh and S. M. Haile, Philosophical Transactions of the Royal Society A, 2010, 368, 3269-3294.
15. HSC Chemistry database 5.1.
16. A. Kogan, International Journal of Hydrogen Energy, 1998, 23, 89.
17. J. E. Funk, Industrial and Engineering Chemistry Process Design and Development, 1966, 5, 336-342.
18. J. E. Miller, A. H. McDanie and M. D. Allendorf, Advanced Energy Materials, 2013, 4, 1-19.
19. T. Nakamura, Energy, 1977, 19, 467-475.
20. S. Ihara, International Journal of Hydrogen Energy, 1980, 5, 527-534.
21. T. Nakamura, Solar Energy 1977, 19, 467.
22. A. Steinfeld, International Journal of Hydrogen Energy, 2002, 27, 611-619
23. K. Wegner, H. C. Ly, R. J. Weiss, S. E. Pratsinis and A. Steinfeld, International Journal of Hydrogen Energy, 2006, 31, 55-61.
24. A. Weidenkaff, A. Steinfeld, A. Wokaun, B. Eichler and A. Reller, Solar Energy, 1999, 65, 59-69

25. M. Keunecke, A. Meier and R. Palumbo, *Chemical Engineering Science*, 2004, 59, 2695–2704
26. T. Melchior, N. Piatkowski and A. Steinfeld, *Chemical Engineering Science*, 2009, 64, 1095–1101.
27. W. C. Chueh, C. Falter, M. Abbott, D. Scipio, P. Furler, S. M. Haile and A. Steinfeld, *Science*, 2010, 330, 1797–1801.
28. F. A. Kroger and H. J. Vink, 1956, *Solid State Physics* vol 3, ed F Seitz and D Turnbull (New York: Academic)
29. Y.-M. Chiang, D. Birnie III and W. D. Kingery, *Physical Ceramics*, 1997, Wiley, page 38.
30. A. Navrotsky, D. J. Weidner and A. G. Union, Washington, DC (1989) Vol. 45, p. xi.
31. S. Stølen, E. Bakken and C. E. Mohn, *Physical Chemistry Chemical Physics*, 2006, 8, 429–447
32. S. Stølen and T. Grande, *Chemical Thermodynamics of Materials: Macroscopic and Microscopic Aspects*, John Wiley & Sons, Chichester, 2003.
33. P. Chaudhari, R. H. Koch, R. B. Laibowitz, T. R. McGuire and R. J. Gambino, *Physical Review Letters*, 1987, 58, 2684.
34. J. G. Bednorz and K. A. Müller, *Condensed Matter*, 1986, 64, 189-193
35. D. J. Singh, *Physical Review B*, 2007, 76, 214115
36. K. H. Ry and S. M. Haile, *Solid State Ionics*, 1999, 125, 355-367
37. Y. Yamazaki, C. K. Yang and S. M. Haile, 2001, *Scripta Materialia*, 2011, 65, 102–107.
38. U. Röder-Roith, F. Rettig, K. Sahner, T. Röder, J. Janek and R. Moos, *Solid State Ionics*, 2011, 192, 101-104
39. K.D. Kreuer, *Annual Review of Materials Research*, 2003, 33, 333–59
40. T. Ishihara, H. Matsuda and Y. Takita, *Journal of the American Ceramic Society*, 1994, 116, 3801
41. Z. Shao and S. M. Haile, *Nature*, 2004, 431, 170-173
42. W. Jung and H. L. Tuller, *ECS Transactions*, 2011, 35, 2129-2136
43. R. F. Blunt, W. F. Love, *Physical Review*, 1949, 76, 1202
44. H. Tamura, T. Konoike, Y. Sakabe and K. Wakino, *Journal of the American Ceramic Society*, 1984, 67, 59-61
45. H. Fan, S.-H. Lee, C.-B. Yoon, G. T. Park, J. J. Choi and H. E. Kim, *Journal of the European Ceramic Society*, 2002, 22, 1699–1704
46. L. Bellaiche, *Current Opinion in Solid State and Materials Science*, 2002, 6, 19–25
47. M. Kang, X. M. Wu, J. Zhang, N. Zhao, W. Wei and Y. H. Sun, *Rsc Adv*, 2014, 4, 5583-5590.
48. J. R. Scheffe, R. Jacot, G. R. Patzke and A. Steinfeld, *Journal of Physical Chemistry C*, 2013, 117, 24104-24114.

49. Chih-Kai Yang, Yamazaki, Yoshihiro and Sossina M. Haile, U.S. Patent, Filed: August 31, 2012, "CATALYSTS FOR THERMOCHEMICAL FUEL PRODUCTION AND METHOD OF PRODUCING FUEL USING THERMOCHEMICAL FUEL PRODUCTION"
50. J. R. Scheffe, D. Weibel and A. Steinfeld, *Energy and Fuels*, 2013, 27, 4250-4257.
51. A. H. McDaniel, E. C. Miller, D. Arifin, A. Ambrosini, E. N. Coker, R. O'Hayre, W. C. Chueh and J. H. Tong, *Energy & Environmental Science*, 2013, 6, 2424-2428.
52. A. Evdou, L. Nalbandian and V. T. Zaspalis, *Journal of Membrane Science*, 2008, 325, 704-711.
53. A. Evdou, V. Zaspalis and L. Nalbandian, *International Journal of Hydrogen Energy*, 2008, 33, 5554-5562.
54. L. Nalbandian, A. Evdou and V. Zaspalis, *International Journal of Hydrogen Energy*, 2009, 34, 7162-7172.

Chapter 2

EXPERIMENTAL APPROACHES AND TECHNIQUES

2.1 Introduction

Methods of sample preparations and experimental techniques for materials characterization are described in this chapter. The method of screening the potential oxides from the thermodynamic perspective is also included. The related concepts will also be used for the solar to fuel efficiency calculations in a later chapter.

2.2 Materials Preparation

While there are many synthesis routes available for the preparation of ceramic oxides, the solid state reaction (SSR) method is used in this work. In comparison with chemical solution routes, such as the Pechini process ^[1], or sol-gel methods ^[2], solid state reaction is simple, fast, and low cost. In this method, oxide and carbonate starting materials are simply allowed to react at high temperature to yield the desired compound. However, accurate control of the composition and its uniformity are major challenges in SSR. Therefore, high purity starting materials and the meticulous prevention of contamination during the process are required for good desired composition control. And the sufficient mixing by long period ball milling for minimizing the inhomogeneity within the oxides is also important. For example, when we prepared the $\text{La}_{1-x}\text{Sr}_x\text{MnO}_{3-\delta}$ powders with the solid-state reaction, stoichiometric quantities of La_2O_3 (Alfa Aesar, REacton[®], 99.99%), SrCO_3 (Sigma-Aldrich[®], 99.9%), and MnCO_3 (Sigma-Aldrich[®], 99.9%) were mixed and attritor-milled in isopropanol for 6 hours at 500 rpm. After drying within the oven at 90 °C, the powder was calcined at 1000 °C for 3 hours under air. Before the powder mixing, the La_2O_3 powder was annealed at 1200°C for 10 hours in order to minimize its hydration with the moisture in air.

For the two-step thermochemical water splitting cycle, the gas access is crucial to the reaction kinetics. In order to maximize the sample surface area for reaction, the porous form of the sample is required. Porous monoliths were fabricated from calcined powders by mixing these powders with isopropanol (3 mL liquid per gram of powder) to obtain a thick paste. This paste was then placed (without application of pressure) into an alumina cylindrical mold with an inner diameter of 10 mm

and fired at 1500 °C for 6 hours under air. The result was a loosely sintered, but mechanically rigid, porous body. Figure 2-1 is the flow chart of the overall fabrication process. The example shown in the inserted picture in Figure 2-1 is $\text{La}_{0.8}\text{Sr}_{0.2}\text{MnO}_{3-\delta}$ with a diameter of 7 mm and a length of 4.5 mm. However, the size is composition dependent, the thermal stability and sinterability of the metal oxide will affect the monolith porosity and size.

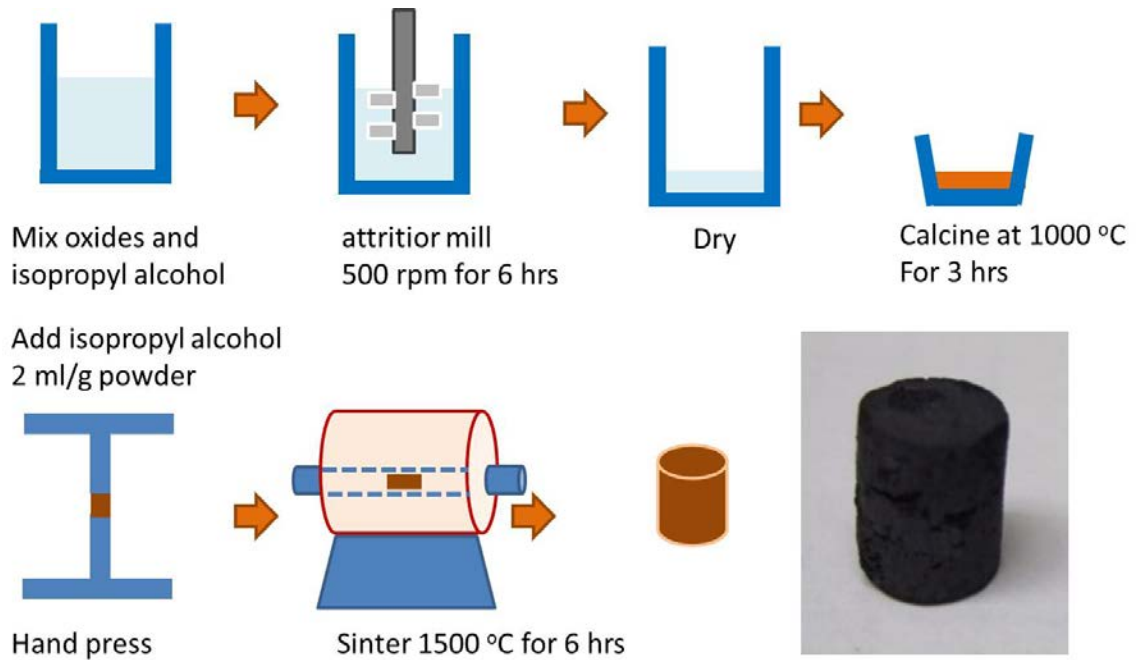


Figure 2-1 Flow chart of the porous pellets preparations. The inset presents the porous $\text{La}_{0.8}\text{Sr}_{0.2}\text{MnO}_{3-\delta}$ prepared with this flow chart.

2.3 Powder X-ray Diffraction

Since the thermochemical water splitting cycle is conducted at high temperature, the thermal stability of the test oxide is essential. In order to check that there is no crystal structure change or decomposition during the cycles, X-ray powder diffraction is used. The X-ray is generated from a high power applied X-ray tube and its wavelength depends on the anode material (copper, in this case) and the applied accelerating voltage. The incident X-ray will interact with the sample (interact with the electron clouds of the atoms in compound). When the Bragg's Law ($2d \sin \theta = n\lambda$) is

satisfied with the incident X-ray geometry, the sample produces constructive interference and the diffracted ray. The pattern from the collected diffracted ray reveals information on the interspacing between the atomic planes. The crystal structure can be determined by comparing the pattern with a pattern of the same material composition in the database or the refinement analysis.

All phase characterizations are performed by X-ray powder diffraction (Panalytical, PW3040-PRO, Cu K α radiation), for which the material was lightly hand-milled. The settings of the measurements are listed in Table 2-1. PANalytical X'Pert HighScore Plus (Panalytical[®]) is used for Rietveld refinement analysis in this work.

Table 2-1. The diffractometer settings used.

Diffractometer	Panalytical, PW3040-PRO
Setting	
Target	Cu Cu K α radiation: K α 1=1.5406 Å K α 2=1.5444 Å K β =1.3922 Å
Current	40 mA
Voltage	45kV
Step size	0.0334225 degree
Dwell time	0.69986 degree/sec
Scan range of 2 θ	20-90°

2.4 Mercury Porosimetry ^[3]

Mercury does not wet most substances and cannot penetrate pores by capillary action unless an external force applied. Due to this characteristic, mercury can be used for porosity measurements. When the surface of a material comes into contact with mercury, the surface tension acts tangentially to the solid-liquid interface. When performing the porosity measurement with Mercury porosimetry, an external pressure is applied to push mercury into the pores of the sample (as shown in Figure 2-2). For the pore with the diameter D , the relation between the pore diameter and the applied pressure can be derived as in Equation 2.1:

$$D = -4\gamma \cos \theta / P \quad (2.1)$$

where γ is the surface tension of mercury, θ is the contact angle (angle between the material surface and the tension force vector), and P is the applied pressure. For a given liquid-solid system, the term

of $-4\gamma \cos \theta$ is constant, and the size of the pore into which mercury will be intruded is inversely proportional to the applied pressure. The intrusion process involves moving a mass of mercury into a confined pore space, and Hagen–Poiseuille equation^[4] shown with Equation 2.2 shows the relation between the pore volume and the applied pressure.

$$\Phi = \frac{dV}{dt} = \frac{\pi \left(\frac{D}{2}\right)^4}{8\eta} \frac{|\Delta P|}{L} \quad (2.2)$$

where Φ is the volumetric flow rate, V represents the volume of fluid (mercury) intruded into the pore, L is the length of the pore space, and η is the viscosity of fluid (mercury). $\frac{|\Delta P|}{L}$ represents the pressure drop per unit length of the pore (deepness of mercury intrusion).

By measuring the volume of mercury that intrudes into the pores of sample with various applied pressures, the volume of pores (decided by D and L) in the corresponding size class can be obtained.

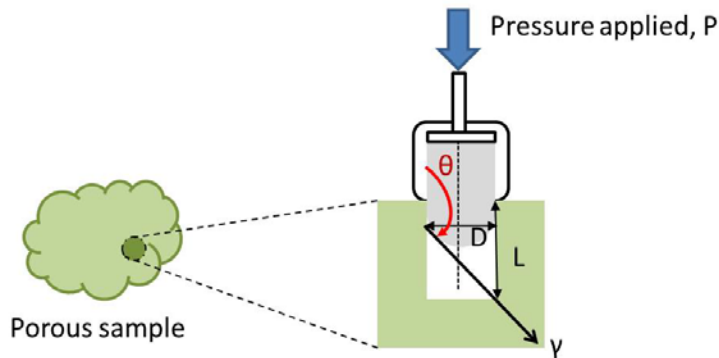


Figure 2-2. Scheme of mercury pushed into an open pore of sample.

AutoPore IV, micromeritics was used for Mercury porosimetry. Its resolution of the mercury volume change is around 0.1 μL . Closed pores cannot be detected with this method and will be one of the error sources. However, closed pore would not contribute heavily to water splitting due to the limited gas access. As compared to the conventional porosity measurement performed by measuring the sample dimensions and volume, Mercury porosimetry can minimize the measurement errors

from the irregular sample shape, also it provides the information of the average pores size distribution.

2.5 Scanning Electron Microscopy (SEM) ^[5]

Scanning Electron Microscopy (SEM) is a type of electron microscopy which allows imaging of morphology of a sample. Here a focused electron beam strikes a specimen, and the electrons interact with the atoms of specimen in various ways generating a variety of signals (shown in Figure 2-3). Backscattered electrons (BSEs) and secondary electrons (SEs) are primarily used for SEM image formation. The SEM images provide the specimen features such as grain size and pore size, which helps us understand the thermal stability properties of the specimen after the sintering process or after the thermochemical cycles. The morphology of the samples within this work was examined by ZEISS 1550VP Field Emission SEM with the applied voltage 10-15 kV and current 25 nA.

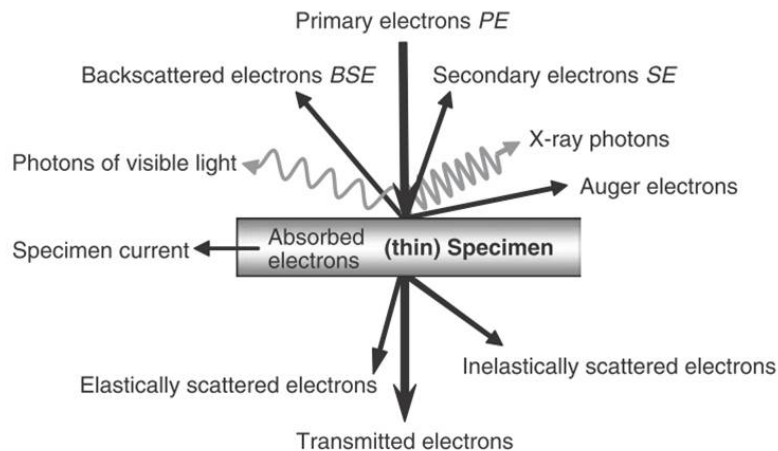


Figure 2-3. Various useful signals generated when the focused electron beam strikes on a specimen ^[4].

2.6 Thermogravimetric Analysis (TGA)

Thermogravimetric Analysis (TGA) is a technique used for monitoring the specimen mass change from the reduction and oxidization reactions under a controlled-temperature and gas atmosphere-controlled environment. Figure 2-4 shows one example of thermogravimetric measurement with

the sample $\text{La}_{0.7}\text{Sr}_{0.3}\text{MnO}_{3-\delta}$ [6]. By flowing different mixed gases through the thermogravimetric furnace, the oxygen partial pressure around the sample can be controlled. We assume that all the weight changes are only from the oxygen release and incorporation due to the thermal reduction and oxidation reactions. Under the given gas atmosphere and programed temperature, enough equilibration time is necessary. When mass stops changing with time, we can consider that the oxygen migration between the sample and the gas atmosphere around it have reached the equilibrium.

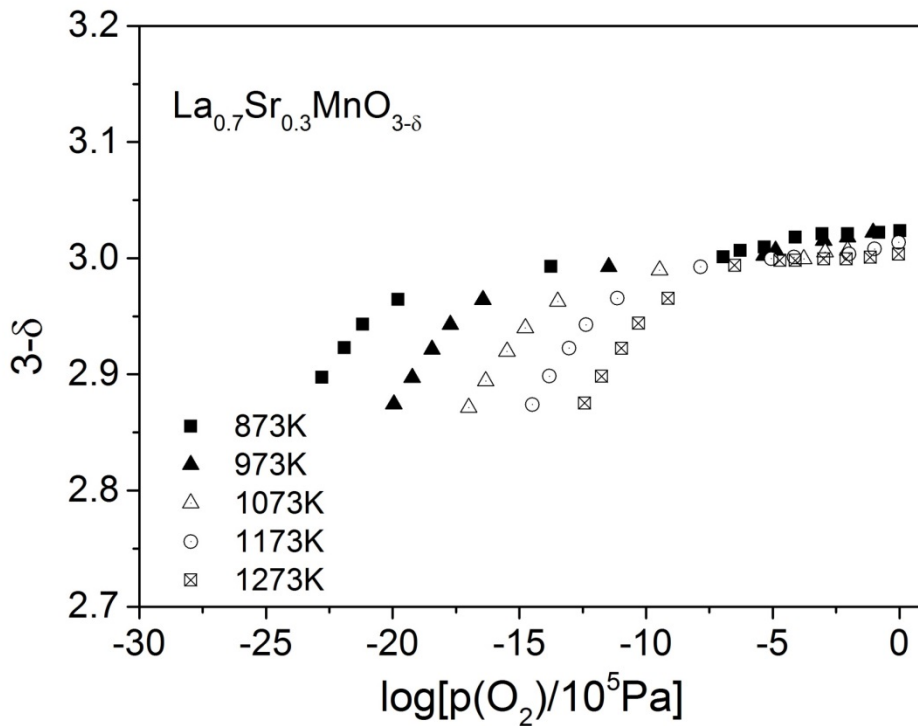


Figure 2-4. Nonstoichiometry of $\text{La}_{0.7}\text{Sr}_{0.3}\text{MnO}_{3-\delta}$. (Data are taken from ref. [6])

As it is mentioned in Chapter 1, the redox properties of metal oxide are important to the thermochemical water splitting reactions. These properties can be extracted from the oxygen nonstoichiometry, δ , dependence of $p(\text{O}_2)$ and temperatures [7].

Under equilibrium conditions, oxygen in the gas phase and in the metal oxides have the same chemical potential. This equilibrium can be expressed with Equation 2.2:

$$\mu_o^{(s)} = \mu_o^{(g)} \equiv \mu_o = \mu_o^0 + \left(\frac{RT}{2}\right) \ln p(O_2^*) \quad (2.3)$$

where μ_o^0 represents chemical potential of oxygen at standard state.

The quantity $\mu_o^{(s)}$ is equivalent to the partial molar gibbs energy of oxygen which can be decomposed into the partial molar enthalpy (h_o) and entropy (s_o) according to

$$\mu_o = h_o - Ts_o \quad (2.4)$$

With Equation 2.3, 2.4, and the Gibbs-Helmholtz relation $\left(\frac{\partial(G/T)}{\partial(1/T)}\right)_p \equiv H$, the new relations can

be generated:

$$\Delta h_o = h_o - h_o^0 = \left(\frac{R}{2}\right) \left[\frac{\partial \ln p(O_2)}{\partial(1/T)}\right] \quad (2.5)$$

$$\Delta s_o = s_o - s_o^0 = \left(-\frac{1}{2}\right) \left[\frac{\partial(RT \ln p(O_2))}{\partial T}\right] \quad (2.6)$$

where h_o^0 and s_o^0 are standard enthalpy and entropy of oxygen (which means at 1 atm). Δh_o and Δs_o here are oxidization enthalpy and entropy, respectively. For reduction reaction, the values are negative of the values extracted by the equations above.

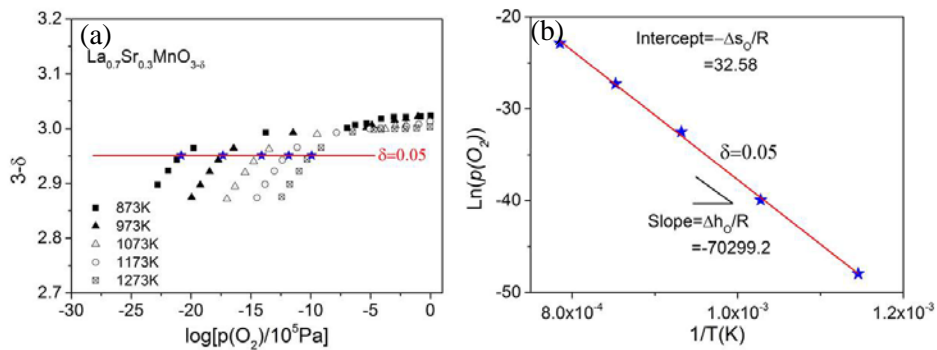


Figure 2-5. Schemes of Δh_o and Δs_o extraction from the oxygen non-stoichiometry dependence of temperature and oxygen partial pressure. (a) Nonstoichiometry of $\text{La}_{0.7}\text{Sr}_{0.3}\text{MnO}_{3-\delta}$.^[6] (b) Δh_o and Δs_o extraction with $\delta = 0.05$. The extracted values of Δh_o and Δs_o within this example are -584.4 kJ/mol- O_2 and -270.8 J/mol- O_2 -K, respectively.

Figure 2-5 shows how we can extract the Δh_o and Δs_o based on the oxygen nonstoichiometry, δ , dependence of $p(\text{O}_2)$ and temperatures measured by thermogravimetry. With the fixed δ value, the data points of different temperatures are taken and used for plotting $\ln p(\text{O}_2)$ vs. $1/T$ as shown in the left of the figure. From the relations described with Equation (2.2) to (2.5), the Δh_o and Δs_o can be extracted from the slope and intercept of the $\ln p(\text{O}_2)$ vs. $1/T$ plot, respectively. Repeating this procedure for a different δ value, we get the Δh_o and Δs_o values corresponding to different oxygen nonstoichiometry.

The straight line shown in the plot implies that Δh_o is essentially independent of temperature. If the oxide behaves as the ideal solution, its Δh_o should be without dependence of δ . The Δs_o with the nonstoichiometry values are due to the configurational entropy variance.

In this work, thermogravimetric analysis was performed for $\text{La}_{0.8}\text{Sr}_{0.2}\text{Mn}_{1-x}\text{Fe}_x\text{O}_{3-\delta}$ with the thermogravimetric analyzer (Netzsch STA 449C Jupiter). The measurements were conducted under controlled temperature and atmosphere, with temperature capability up to 1400 °C. Oxygen partial pressure in the system with values above 10^{-5} atm was controlled by using premixed ultra-high purity (UHP) O_2 in UHP argon. The gas carrier with lower oxygen partial pressures was generated by passing the premixed UHP H_2 in UHP argon through a room-temperature water bubbler. The measurement atmosphere spanned from 0.20 atm O_2 to 0.03 atm humidified H_2 . An online oxygen sensor (MicroPoas) was used for monitoring the actual $p(\text{O}_2)$ in the system.

For a given measurement program (the settings of the controlled temperatures, temperature ramp rates, gas atmospheres, and duration periods for the measurement), baseline measurements (system without sample) were performed for buoyancy effects correction before the measurements with sample put in system. The samples for TGA measurements were prepared with the same method used for the porous pellets for thermochemical cycling. The sample mass used for the measurement

was around 1.0 grams. Such large mass of sample benefits the precision in the measurement of relatively small mass changes from oxygen release and incorporation.

2.7 Quadrupole Mass Spectrometry^[8]

The mass spectrometry is an instrument which can be used to measure the mass to charge ratio, of ionized atoms or other electrically charged particles. Quadrupole Mass Spectrometry (QMS) is a type of mass spectrometry that uses a quadrupole as the mass analyzer. The scheme of the analyzer of a quadrupole mass spectrometry is illustrated in Figure 2-6. The actual analyzer is located in vacuum (with working pressure less than 10^{-5} torr). When detecting, the gas molecules to be analyzed enter the analyzer vacuum chamber via a capillary which ends with the leak valve. After passing the ionizer (hot filament), the natural gas molecules will be ionized. Then, the ionized molecules will be sorted in the quadrupole mass filter. The quadrupole is set by four cylindrical electrodes parallel to each other. Two opposite rods are applied a electric potential of $(U+V\cos(\omega t))$ and the other two rods have a potential of $-(U+V\cos(\omega t))$, where U is a dc voltage and $V\cos(\omega t)$ is an ac voltage. The applied potentials affect the trajectory of the ionized molecules traveling through the filter. With the given dc and ac voltages, only the ionized molecules with certain mass-to-charge ratio can pass through the quadrupole filter and other ions will be thrown out of their original path. After the sorted ionized molecules leave the mass filter, they will be collected by the detector (Faraday detector or a secondary electron multiplier (SEM)) and the ion currents will be generated. By oscillating the electric field (varying ω and holding V and U) applied to the quadrupole, it can monitor the ions passing through the quadrupole filter and generate the mass spectrum.

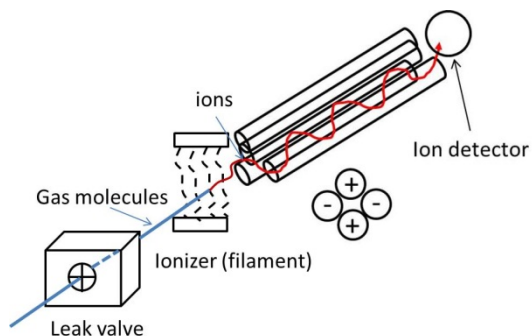
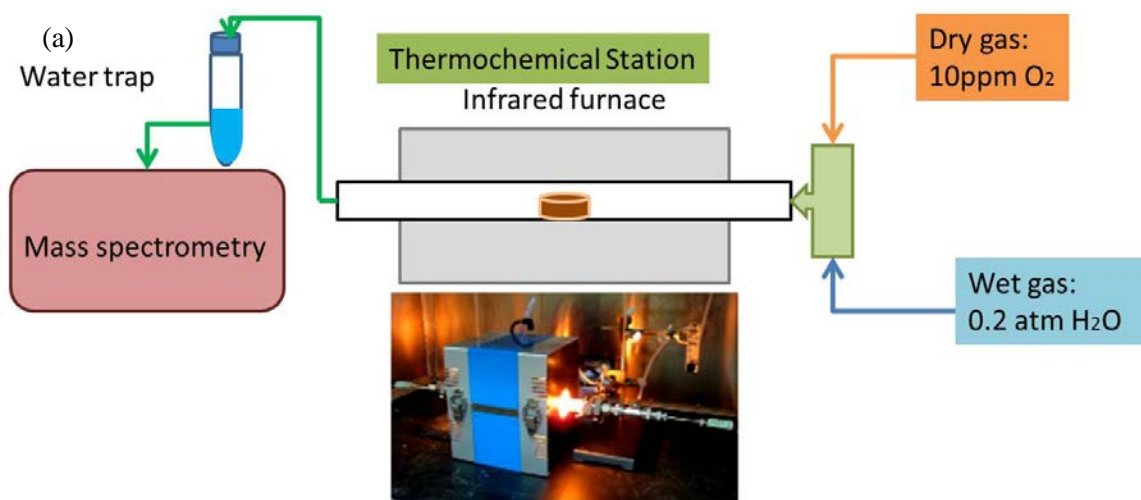


Figure 2-6 Schemes of the analyzer of a quadrupole mass spectrometry.

A quadrupole mass spectrometer (QMS, OMNI Star, Pfeiffer-vacuum) is connected to our thermochemical cycle station. The evolved gases (inert gas for thermal reduction step and steam for water splitting step) that exit the reactor are sampled by QMS. Therefore, the oxygen release and fuel (hydrogen or carbon monoxide) production will change their corresponding ion concentrations within the reaction gases and can be detected based on the ion current changes. Gas calibration measurement is required to convert the ion current to gas species concentrations. Then, the amount of fuel generated from the thermochemical cycles can be calculated from the mass spectrometry measurements.

2.8 Thermochemical Water Splitting Cycle

Thermochemical water splitting cycle was carried out with our in-house thermochemical fuel production test station shown in Figure 2-7. The station consists of a set of gas mass flow controllers (MFCs), an infrared furnace (Ulvac-Riko VHT-E44), a water trap, and a quadrupole mass spectrometer. The sample is loaded into a horizontal alumina tube reactor (9.5 mm diameter), which is placed in the infrared furnace, which has rapid heating and cooling capability (up to 1000 K min^{-1}). Temperature was measured with an S-type thermocouple placed in the axial center of the reactor and in contact with the porous pellet sample. Thermal reduction was carried out in all cases using 10 ppm oxygen balanced with argon (termed “dry gas”). The purpose of using a gas of known oxygen content rather than pure inert gas is that it provides a thermodynamically defined oxygen chemical potential, essential for analyzing and understanding material behavior.



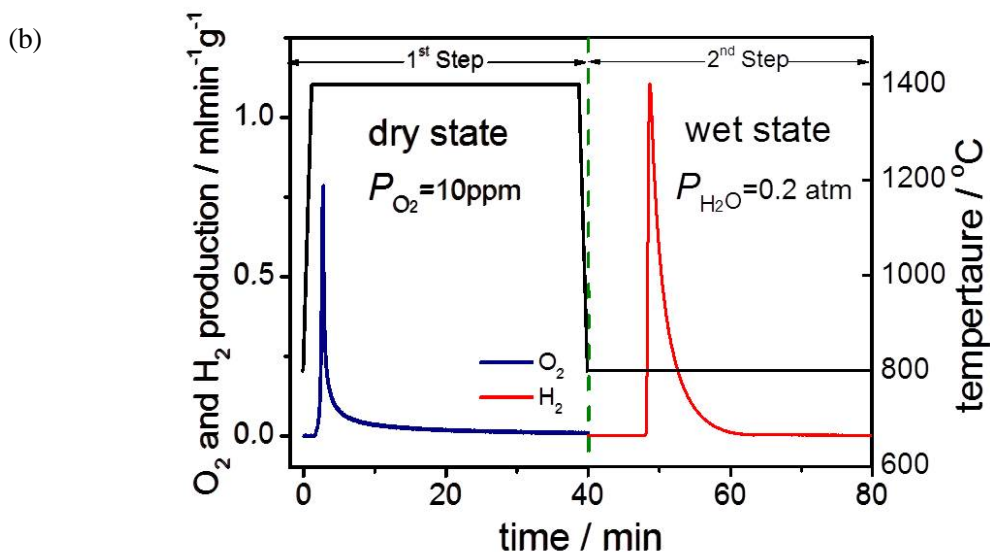


Figure 2-7. (a) Schemes of the thermochemical station setup. (b) Mass spectrometry results of one thermochemical water splitting cycle.

After the thermal reduction half-cycle is complete, the sample is rapidly quenched to water-splitting temperature. When the desired temperature is reached, the steam is introduced. The steam is generated by flowing ultrahigh purity (UHP) argon through a sealed water bottle set within a controlled temperature oven. With the oven temperature set at 60 °C, the UHP Ar gas which flows through it will be saturated with the purified water and acts as the reaction carrier gas with $p(H_2O) = 0.20$ atm, corresponding to $p(O_2) = 1.6 \times 10^{-7}$ atm. The water trapper is set at the downstream of the reactor for collecting the excess steam. Evolved oxygen and hydrogen gases were detected using mass spectroscopy (OMNI Star, Pfeiffer-vacuum). For a quantitative determination of gas content, the mass spectroscopy was calibrated daily using 6 different hydrogen partial pressures ranging from 0 to 5.05×10^{-3} atm, and seven different oxygen partial pressures ranging from 1×10^{-5} to 3.83×10^{-3} atm.

Figure 2-7 (b) shows the typical result of one thermochemical water splitting cycle which includes one thermal reduction and one water splitting reaction. The example was performed with the $La_{0.8}Sr_{0.2}MnO_{3\pm\delta}$ as the test sample and 1400 °C and 800 °C as the thermal reduction and water splitting reaction temperatures, respectively.

BIBLIOGRAPHY

1. J.D.G. Fernandes, D.M.A. Melo, L.B. Zinner, C.M. Salustiano, Z.R. Silva, A.E. Martinelli, M. Cerqueira, C. Alves Junior, E. Longo and M.I.B. Bernardi, *Materials Letters*, 2002, 53, 122–125.
2. A. Rostamnejadi, H. Salamati, P. Kameli and H. Ahmadvand, *Journal of Magnetism and Magnetic Materials*, 2009, 321, 3126-3131.
3. Mercury Intrusion Porosimetry Theory, presented by Micromeritics Instrument Corporation.
http://www.micromeritics.com/Repository/Files/Mercury_Porosimetry_Theory_poster.pdf
4. S. P. Sutera and R. Skalak, *Annual Review of Fluid Mechanics*, 1993, 25, 1-19.
5. D. Stokes, “Principles and Practice of Variable Pressure: Environmental Scanning Electron Microscopy (VP-ESEM),” Wiley, Hoboken, 2008.
6. J. Mizusaki, N. Mori, H. Takai, Y. Yonemura, H. Minamiue, H. Tagawa, M. Dokiya, H. Inaba, K. Naraya, T. Sasamoto and T. Hashimoto, *Solid State Ionics*, 2000, 129, 163-177.
7. J. Mizusaki, Y. Mima, S. Yamauchi and K. Fueki, *Journal Of Solid State Chemistry*, 1989, 80, 102-111.
8. E. Hoffmann, V. Stroobant, “Mass Spectrometry:Principles and Applications,” Wiley, Hoboken, 2007.

Chapter 3

THERMOCHEMICAL WATER SPLITTING WITH LANTHANUM STRONTIUM MANGANITE

3.1 Solid Solution Oxide $\text{La}_{1-x}\text{Sr}_x\text{MO}_{3-\delta}$

The compositional flexibility perovskites provides a high possibility of identifying a suitable material for efficient thermochemical fuel production. First, we need to decide the type of perovskites among the classes of $\text{A}^{(3+)}\text{B}^{(3+)}\text{O}_3$, $\text{A}^{(2+)}\text{B}^{(4+)}\text{O}_3$, and $\text{A}^{(1+)}\text{B}^{(5+)}\text{O}_3$. Then, the multi-valent element must be selected since this element plays a major role in the redox properties of the perovskite. In this study, the solid solution oxides $\text{La}_{1-x}\text{Sr}_x\text{MO}_{3-\delta}$ ($\text{M} = 3\text{d}$ transition metals such as Cr, Mn, Fe, Co, etc.) are considered first because their redox properties have been widely studied for various applications such as the electrode, electrolyte, and interconnect for SOFC [1-3].

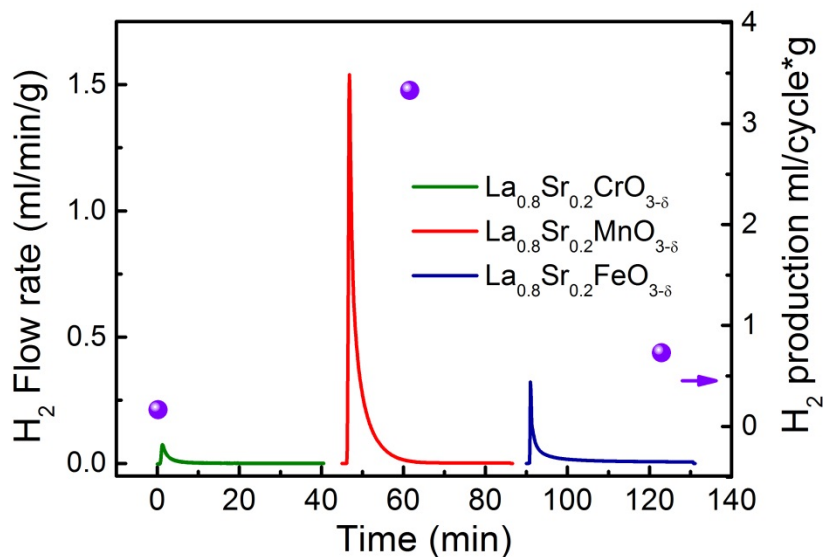
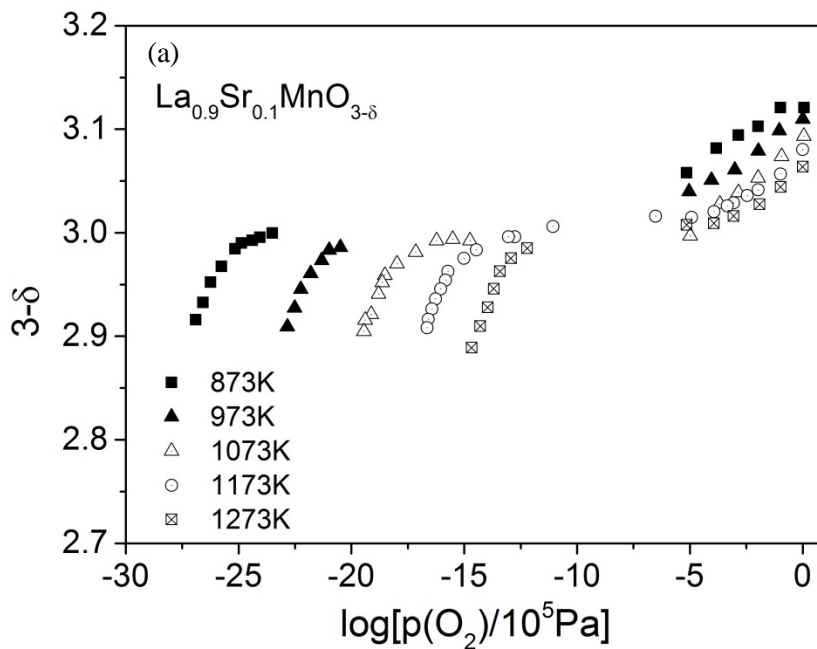


Figure 3-1. Hydrogen productions from two-step thermochemical water splitting of $\text{La}_{0.8}\text{Sr}_{0.2}\text{CrO}_{3-\delta}$, $\text{La}_{0.8}\text{Sr}_{0.2}\text{MnO}_{3-\delta}$, and $\text{La}_{0.8}\text{Sr}_{0.2}\text{FeO}_{3-\delta}$. (Oxides were thermally reduced at 1400°C under $p(\text{O}_2)=10^{-5}$ atm for 40 mins, and the water splitting reaction were performed at 800°C under the steam with $p(\text{H}_2\text{O})=0.2$ atm for 40 mins.)

At a first step, preliminary thermochemical water splitting measurements were conducted using $\text{La}_{0.8}\text{Sr}_{0.2}\text{MO}_{3-\delta}$ ($\text{M}=\text{Cr}, \text{Mn}, \text{Fe}, \text{Co}$); the cycling conditions were 1400 °C under 10 ppm oxygen ($p(\text{O}_2)=10^{-5}$ atm) balanced with Ar for the TR step, and 800 °C under the steam with $p(\text{H}_2\text{O})=0.2$ atm for the WS step. The reaction duration for both steps was 40 minutes. The cobaltite of this group melted during the thermal reduction reaction, and was not considered further. Figure 3-1 shows the preliminary results for hydrogen production of other three oxides. Of these three, $\text{La}_{0.8}\text{Sr}_{0.2}\text{MnO}_{3-\delta}$ produced the most hydrogen. Therefore, strontium-doped lanthanum manganite ($\text{La}_{1-x}\text{Sr}_x\text{MnO}_{3-\delta}$) was selected to be the candidate oxide for further investigation.

3.2 Lanthanum Strontium Manganite ($\text{La}_{1-x}\text{Sr}_x\text{MnO}_{3-\delta}$)

$\text{La}_{1-x}\text{Sr}_x\text{MnO}_{3\pm\delta}$ is one of the most common materials used in the cathode of solid oxide fuel cells (SOFC) cathodes for O_2 reduction reactions. It is a very good electronic conductor with a electronic conductivity of around 200–300 S/cm ($\text{La}_{0.8}\text{Sr}_{0.2}\text{MnO}_{3\pm\delta}$ at 900 °C) [4-5]. Since our purpose aims at thermochemical cycle applications, the properties of oxygen non-stoichiometry, defect equilibrium, surface activity, and diffusivity of $\text{La}_{1-x}\text{Sr}_x\text{MnO}_{3\pm\delta}$ are critical for this study.



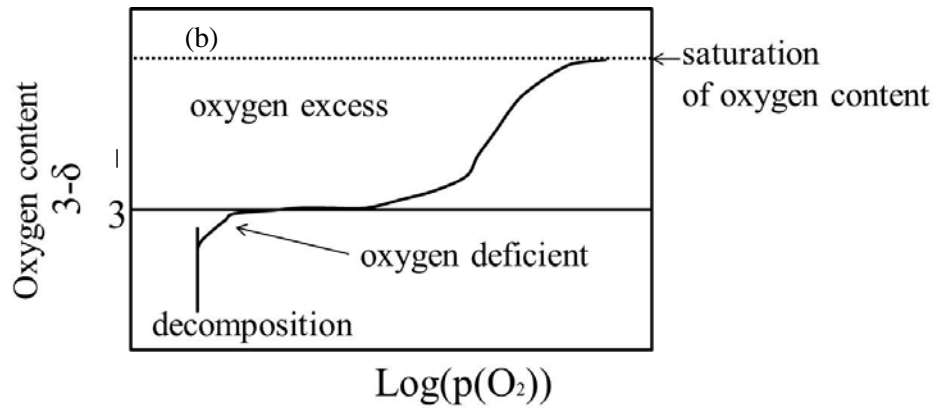


Figure 3-2. (a) Non-stoichiometry of $\text{La}_{0.9}\text{Sr}_{0.1}\text{MnO}_{3-\delta}$, (b) Schematic profile of oxygen content vs $\log p(\text{O}_2)$ for $\text{La}_{1-x}\text{Sr}_x\text{MnO}_{3-\delta}$. TGA data are obtained from ref. [3].

The relationship between oxygen content ($3-\delta$) change and oxygen partial pressure ($p(\text{O}_2)$) reflects the redox properties of $\text{La}_{1-x}\text{Sr}_x\text{MnO}_{3-\delta}$, as shown in Figure 3-2. It is interesting that both the oxygen deficient ($3-\delta < 3$) and the oxygen excess ($3-\delta > 3$) are found in a wide range of $p(\text{O}_2)$. The region of oxygen excess is attributed to the formation of metal vacancies, and this region is less apparent when the Sr content increases^[3]. At high $p(\text{O}_2)$, the oxygen excess reaches a saturation value which decreases with increasing the Sr content^[5]. The oxygen deficient region, occurs due to the charge compensation via oxygen vacancy creation for the transition metal ion valence change that results from the reduction reaction. When the reduction reaction is extreme, $\text{La}_{1-x}\text{Sr}_x\text{MnO}_{3-\delta}$ decomposes and produces the material $(\text{La}_{1-x}\text{Sr}_x)_2\text{MnO}_4$ ^[6].

Figure 3-3 shows the Δh_O and Δs_O of $\text{La}_{0.9}\text{Sr}_{0.1}\text{MnO}_{3-\delta}$ extracted from the thermogravimetric measurements shown in Figure 3-2 (a); the extraction method has been described in Chapter 2.6. From the extracted values, the difference between the values across the oxygen excess and deficient regions might be a result of the different governing defect reactions in each domain.

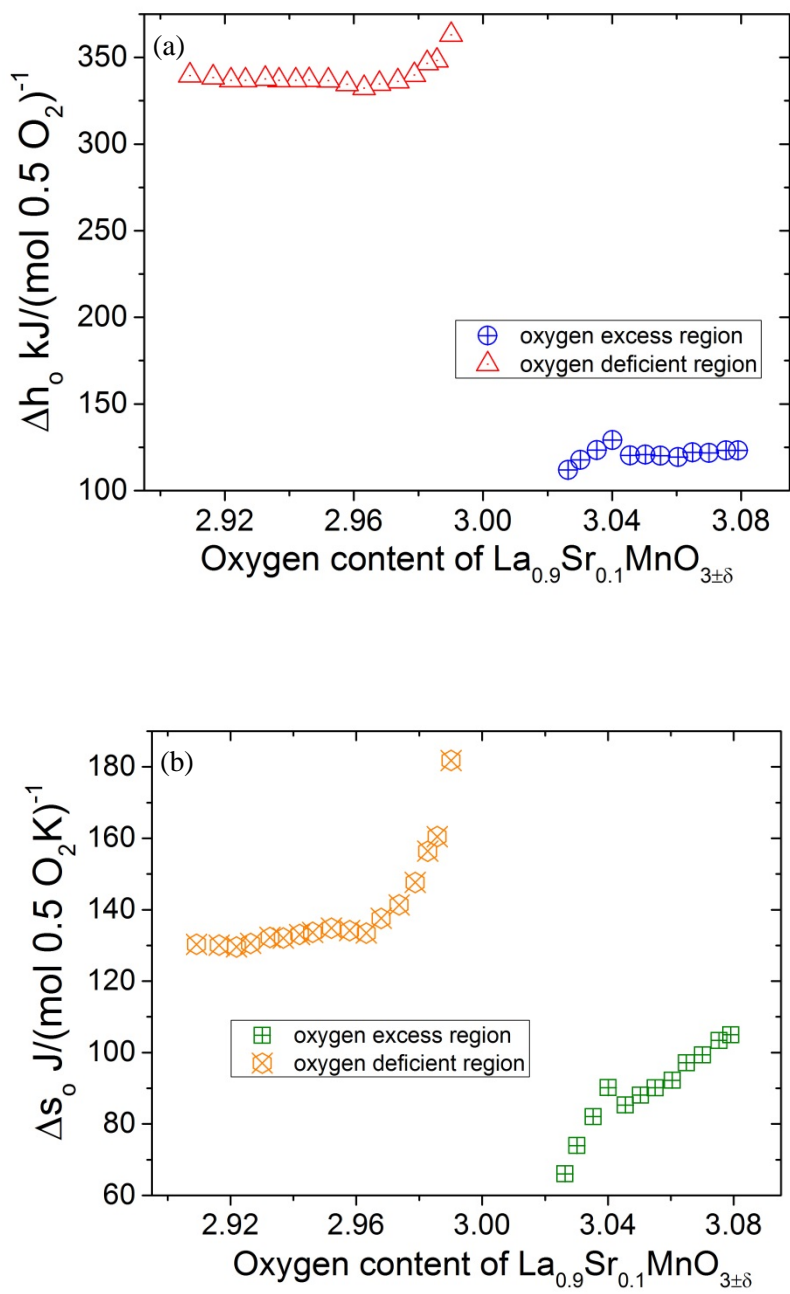


Figure 3-3. Thermodynamic characteristics of $\text{La}_{0.9}\text{Sr}_{0.1}\text{MnO}_{3\pm\delta}$ (a) enthalpy and (b) entropy of reduction as functions of oxygen non-stoichiometry. The TGA data of $\text{La}_{0.9}\text{Sr}_{0.1}\text{MnO}_{3\pm\delta}$ are taken from ref. [3].

At first impression, the oxygen excess region is attractive for the thermochemical cycles because it expands the range of oxygen non-stoichiometry change. Also, the smaller reduction enthalpy within the oxygen excess region implies the weaker bonding between oxygen and metal ions that may lead to a more facile oxygen release. Unfortunately, thermodynamic limitations prevent the realization of these advantages for thermochemical water splitting. The thermodynamic prerequisite for redox medium has been described with Equation (1.14) and it shows that the enthalpy of reduction (Δh_O) of $\text{La}_{0.9}\text{Sr}_{0.1}\text{MnO}_{3+\delta}$ within the oxygen excess region ($3+\delta>3$) is smaller than the values of water (241 kJ/mol-O).

Because the oxygen excess region of $\text{La}_{1-x}\text{Sr}_x\text{MnO}_{3\pm\delta}$ cannot contribute to the two-step thermochemical cycle and the oxygen excess region will disappear with increasing Sr content, the focus of our studies will mainly be on the oxygen deficient region of $\text{La}_{1-x}\text{Sr}_x\text{MnO}_{3\pm\delta}$. Also, the thermogravimetric measurements from the reference [3] (*vide infra*) show the different behaviors of the curves which reflect the distinctness of their redox properties. The impacts of Sr content substituted La on A site on the performance of the two-step thermochemical water splitting cycle will be targeted here.

3.3 Sr Content Impacts on Redox Properties of $\text{La}_{1-x}\text{Sr}_x\text{MnO}_{3-\delta}$

The multi-valent element within the active oxide is the expected element which governs the redox properties applied for thermochemical cycling. Since for $\text{La}_{1-x}\text{Sr}_x\text{MnO}_{3-\delta}$, the multi-valent element, Mn, is located on the B site, the impact from the A site composition on the redox properties of the material should be minimal. However, the thermogravimetric measurements in the literature^[3] show distinct behaviors of oxygen non-stoichiometry changed by varying $p(\text{O}_2)$ among $\text{La}_{1-x}\text{Sr}_x\text{MnO}_{3-\delta}$ with different Sr contents.

The thermogravimetric data reported by Misuzaki and coworkers^[3] were selected for analysis from the variety of datasets available in the literature because they span the widest range of temperatures (600-1000 °C) and widest number of compositions. However, the highest temperature of the datasets is still lower than the thermal reduction temperature we are applying (1400 °C). The oxygen content in $\text{La}_{1-x}\text{Sr}_x\text{MnO}_{3-\delta}$ for temperature out of the datasets measurement temperature range can be extrapolated with the analysis method for Δh_O and Δs_O extraction demonstrated and shown in Figure 2-5 (b). Take the example shown in Figure 2-5, to extend the red fitted line in (b),

the $\ln(p(O_2))$ values of $\text{La}_{0.7}\text{Sr}_{0.3}\text{MnO}_{3-\delta}$ with $\delta=0.05$ for any temperature of interest can be obtained. To repeat this extrapolation for different oxygen content (δ), the thermogravimetric data at temperature of interest can be interpolated/ extrapolated. Figure 3-5 shows oxygen content in $\text{La}_{1-x}\text{Sr}_x\text{MnO}_{3-\delta}$ for several different values of x . The high temperature thermogravimetric data (1000-1400 °C) shown in the figure were extrapolated. The same analysis method was also applied for computing the thermogravimetric data with the measurement temperatures in order to check the quality of analysis.

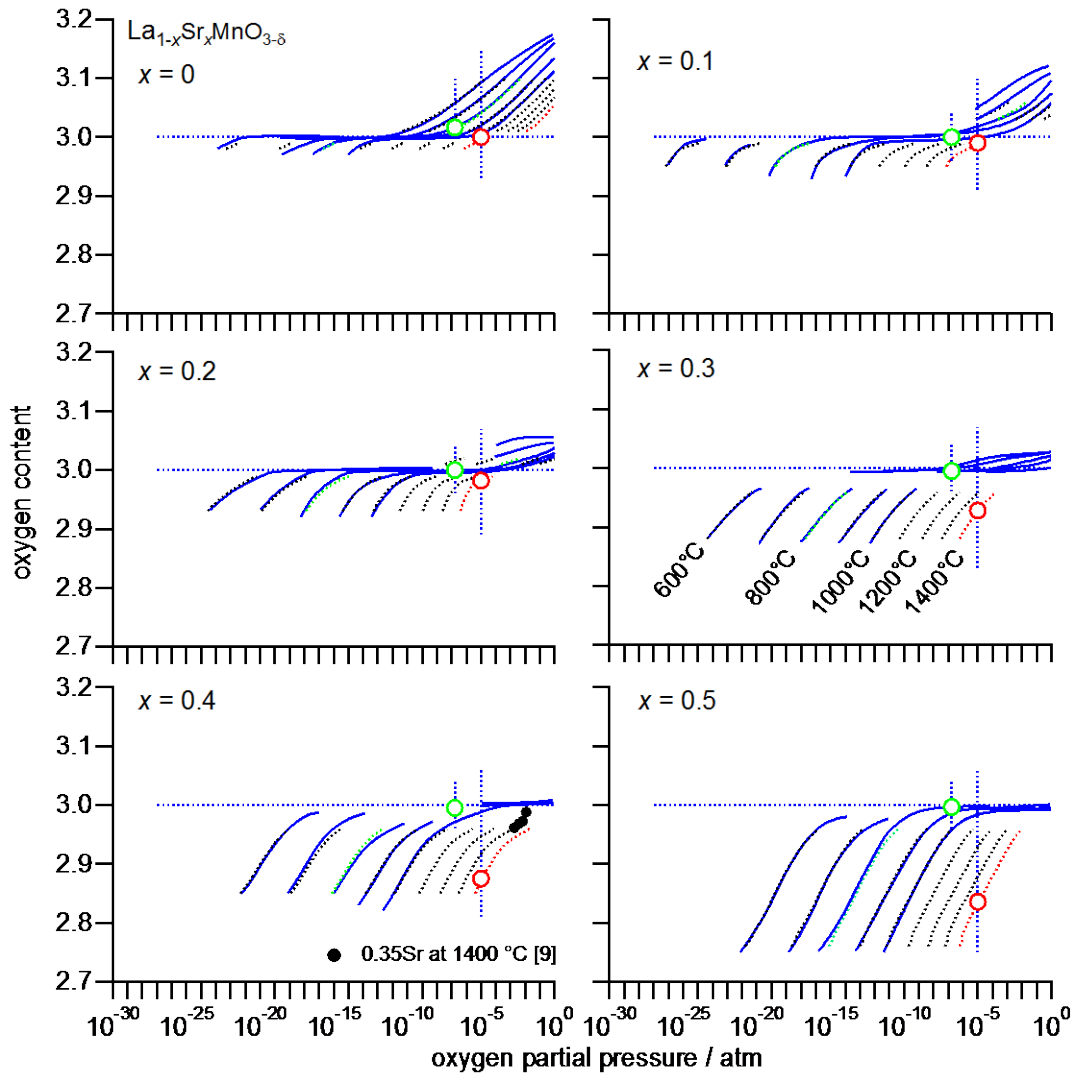


Figure 3-5. Oxygen content in $\text{La}_{1-x}\text{Sr}_x\text{MnO}_{3-\delta}$ for several different values of x , as indicated. Solid blue lines are the experimental data for Mizusaki and co-workers^[3] collected for the temperature range from 600 to 1000 °C. High temperature experimental data for the $x = 0.35$ composition^[7] are shown on the $x = 0.4$ plot as solid black dots. Dotted lines are fit and/or extrapolated values, derived as described in the text. Red dotted lines refer to extrapolated behavior at 1400°C, at which reduction was carried in the present thermochemical cycling experiments. Green dotted lines refer to fit data at 800°C, at which oxidation was performed. Open red and green circles indicate, respectively, expected values of oxygen content upon reduction under 10 ppm O_2 and oxidation under 20% H_2O . The difference in oxygen content between these open circles corresponds to the oxygen non-stoichiometry change within the thermochemical cycling, $\Delta\delta_{\text{max}}$.

From Figure 3-5, the oxygen stoichiometry in $\text{La}_{1-x}\text{Sr}_x\text{MnO}_{3-\delta}$ is highly dependent on Sr content. In the absence of Sr, the material has a high concentration of excess oxygen ($\delta < 0$), believed to be charge and site balanced by cation vacancies (on both the A and B sites).^[3] With increasing Sr content, this oxygen excess region diminishes and, simultaneously, the oxygen deficient region enlarges. In the presence of Sr, charge balance is achieved either by an enhanced Mn^{4+} concentration or the presence of oxygen vacancies, the balance of which depends on T and $p(\text{O}_2)$.^[3] Most significant for this discussion is the observation that the computed values of oxygen content (dotted lines) are in good agreement with the experimental values (solid lines). This agreement provides confidence in the extrapolation of the oxygen nonstoichiometry values to high temperature.

Overlain on the data plots in Figure 3-5 are vertical lines corresponding to the values of oxygen partial pressure for the reduction and oxidation half-cycles employed in this work, 10^{-5} and 1.6×10^{-7} atm, respectively. Oxidation (water splitting) was performed at 800 °C using a gas stream of 20% H_2O in Ar. The equivalent oxygen chemical potential is computed assuming equilibrium for the thermolysis reaction, $\text{H}_2\text{O}(g) \leftrightarrow \text{H}_2(g) + 1/2\text{O}_2(g)$, and mass balance in the product generation (moles of $\text{H}_2 =$ twice the moles of O_2). The equilibrium change in oxygen content, $\Delta\delta = \delta_i - \delta_r$, is indicated on these plots as the difference between oxygen content at the intersection of these respective vertical lines with the non-stoichiometry curves at 800 and 1400 °C. Excluding the undoped composition, it is evident that the greater the Sr content, the greater the expected change in

oxygen content and hence fuel production. In the case of $\text{LaMnO}_{3-\delta}$, a contribution to $\Delta\delta$ appears due to the possibility of entering the oxygen excess region. Because accessing this nonstoichiometry would require significant atomic level structural rearrangements (cyclic generation and annihilation of cation vacancies), the undoped composition is not evaluated in this study.

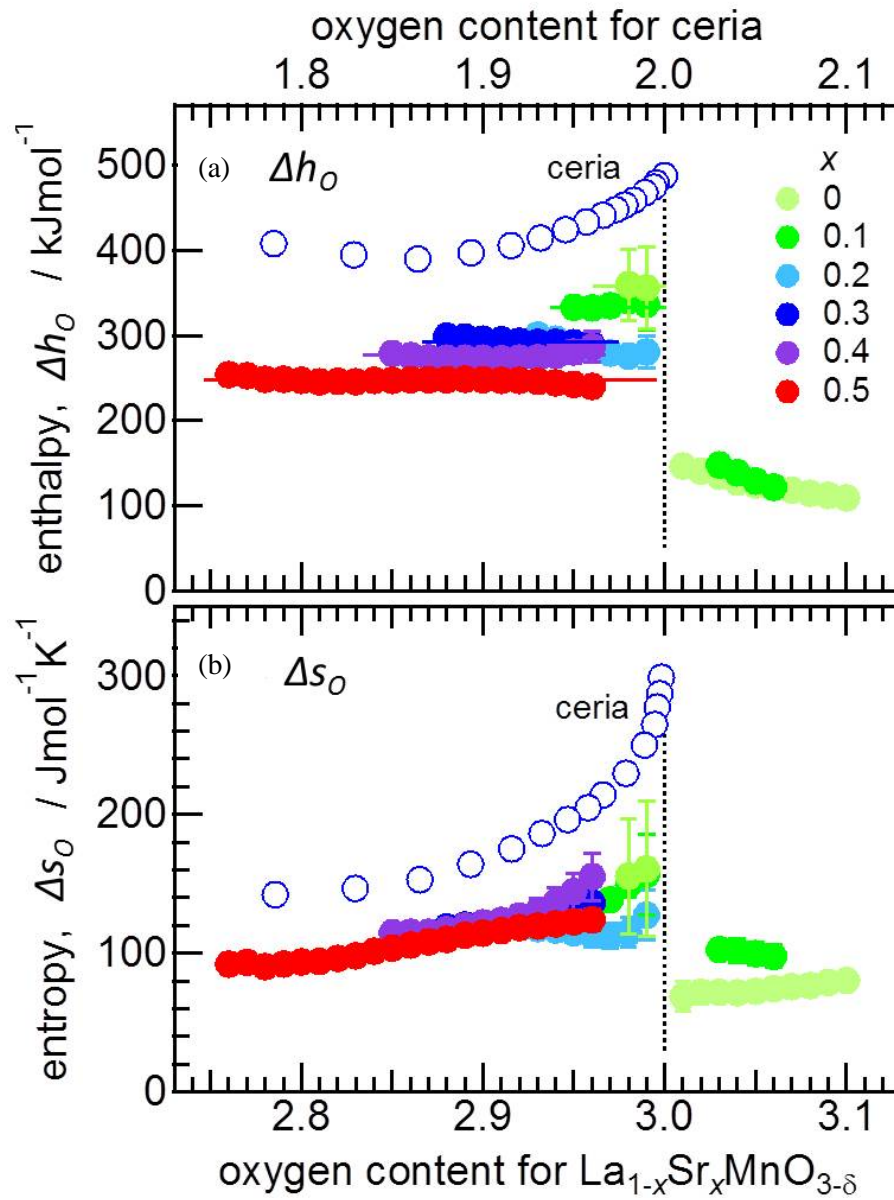


Figure 3-6. Thermodynamic characteristics of the reduction of $\text{La}_{1-x}\text{Sr}_x\text{MnO}_{3-\delta}$: a) enthalpy and b) entropy of reduction as functions of oxygen non-stoichiometry; data for undoped ceria^[17] shown for comparison.

The redox properties of $\text{La}_{1-x}\text{Sr}_x\text{MnO}_{3-\delta}$ (enthalpy (Δh_o) and entropy (Δs_o) of reduction) were extracted with the same method mentioned above (see in Figure 2-5) and illustrated in Figure 3-6. The extracted thermodynamic functions shown in Figure 3-6 reveal important trends. Ignoring for the moment the oxygen excess region, a monotonic decrease in the enthalpy of reduction is evident with increasing Sr content, falling from ~ 350 kJ/mol-O for the undoped composition to ~ 230 kJ/mol-O for $x = 0.5$. In contrast, the entropy is relatively constant. This behavior directly reflects the fact that the material attains a higher oxygen deficiency with increasing Sr content at any given experimental condition of temperature and oxygen partial pressure and further reveals that the greater reducibility is due to a decrease in the enthalpy penalty of reduction rather than due to an increase in the entropy gain. A rough metric of reducibility is given by $T_{\text{eq}} = \Delta h_o(\delta_0)/\Delta s_o(\delta_0)$, which specifies the temperature at which a nonstoichiometry value of δ_0 would occur under a standard oxygen pressure of 1 atm. Again, the monotonic decrease in Δh_o with minimal change in Δs_o implies the reduction temperature monotonically decreases with Sr content. A second important observation from the results in Figure 3-6 is the relative insensitivity, within the oxygen deficient region, of Δh_o to oxygen content. This is a feature of ideal solution behavior, in which the enthalpy of the reaction is independent of the number of defects. In such case, there is no apparent tendency towards either clustering or ordering of defects. Mizusaki et al. drew the same conclusion, that strontium-doped lanthanum manganite displays ideal solution behavior, from a more detailed analysis of the defect chemistry.^[3] Within the oxygen deficient region one also sees that the enthalpy and entropy values of the manganite are substantially smaller than those of ceria,^[17] considered a benchmark material for thermochemical fuel production. Because the enthalpy is particularly high for ceria, the temperatures required for reduction are higher than they are for strontium-doped lanthanum manganite. Indeed, the high enthalpy is the fundamental reason that thermochemical cycling with ceria must be carried out at extremely high temperatures.^[16]

Both the enthalpy and entropy of reduction of $\text{La}_{1-x}\text{Sr}_x\text{MnO}_{3-\delta}$ undergo abrupt changes at the boundary between the oxygen deficient and oxygen excess regions, where the latter region is

observed only in low Sr content compositions (undoped or 10 at% Sr). Given the substantially different means by which the structure accommodates excess oxygen from that in which it accommodates oxygen vacancies, such a result is not surprising. The enthalpy of reduction undergoes a particularly strong decrease in value, indicating that reduction occurs relatively easily for a material that has an excess of oxygen. Conversely, it implies that oxidizing the material with steam to utilize the oxygen excess capacity will be difficult. Anticipation of such behavior is another reason that the undoped material has not been experimentally evaluated in this study.

3.4 Thermal Stability Characterization of $\text{La}_{1-x}\text{Sr}_x\text{MnO}_{3-\delta}$

Thermal stability is an important feature of the active oxide for thermochemical water splitting cycles since the operation is under harsh reducing environments (very high reduction temperature and low oxygen partial pressure). There are many possible effects of the low thermal stability such as (1) evaporation of cations, (2) phase decomposition /transformation, and (3) pores shrinkage, etc. The above phenomenon can result in materials failure or reaction kinetics degradation. To evaluate the thermal stability of $\text{La}_{1-x}\text{Sr}_x\text{MnO}_{3-\delta}$, X-ray powder diffraction (XRD) and scanning electron microscopy (SEM) measurements are applied.

Several structural distortions of the parent cubic perovskite structure have been reported for $\text{La}_{1-x}\text{Sr}_x\text{MnO}_{3-\delta}$, based on the Sr concentration, oxygen partial pressure, and temperature, as determined most reliably by neutron powder diffraction^[11-12]. Near-stoichiometric ($\delta \approx 0$) $\text{LaMnO}_{3\pm 0}$, in which the Mn has an average 3+ oxidation state, displays a Jahn-Teller distortion, and adopts an orthorhombic structure. Under typical processing conditions, the undoped composition ($\text{LaMnO}_{3\pm 0}$) contains oxygen excess ($3-\delta > 3$) and the accompanying high concentration of Mn^{4+} eliminates the distortion, resulting in a rhombohedral structure with space group $R\bar{3}c$. Introduction of Sr similarly generates a high concentration of Mn^{4+} under ambient conditions (rather than oxygen vacancies), resulting in the same rhombohedral structure. Very high concentrations of Sr ($x \geq 0.47$) lead to a tetragonal structure ($I4/mcm$) and ultimately a cubic structure ($Pm\bar{3}m$) beyond 0.7 Sr^[11-12]. The Sr content of the materials examined in the present studies is limited at $x=0.4$, at which, under ambient conditions, the cubic phase is not expected. Extreme reduction and the concomitant generation of a high concentration of vacancies can lead to the vacancy ordered Brownmillerite phase. This ordered

phase readily occurs in cobaltite and ferrite perovskites, but for strontium-doped lanthanum manganite it has been observed only upon reduction with hydrides or upon exposure to 50% hydrogen gas ^[11-12]. Such extreme reducing conditions are not encountered under typical thermochemical cycling conditions, and accordingly the Brownmillerite phase is not anticipated to form as part of the fuel generation process.

Figure 3-7 shows the results of X-ray powder diffraction patterns taken under ambient conditions at room temperature of $\text{La}_{1-x}\text{Sr}_x\text{MnO}_{3-\delta}$ ($x = 0.1, 0.2, 0.3, \text{ and } 0.4$) before and after thermochemical cycling between 800-1400 °C. The synthesis culminated with a 6 hours sintering step at 1500 °C and the thermochemical cycling culminated with oxidization under 20% H_2O at 800 °C. The pellets before and after the thermochemical cycling were gently ground to powder for XRD measurements. Lattice parameters for $\text{La}_{1-x}\text{Sr}_x\text{MnO}_{3-\delta}$ determined by Rietveld analysis of these patterns are summarized in Table 3-1. All of the as-synthesized materials display a rhombohedral structure ($R\bar{3}c$), consistent with literature ^[9-10] reports. No structural changes were observed in cycling of the working oxides with Sr content of 20 at% ($x=0.2$ of $\text{La}_{1-x}\text{Sr}_x\text{MnO}_{3-\delta}$) or higher. A phase transformation from rhombohedral to orthorhombic was detected in the case of the 0.1 Sr sample, as revealed by the splitting of the peak at around 47° 2 θ . This behavior reflects the fact that the water splitting step under 20 % steam at 800 °C presents a less oxidizing atmosphere, $p(\text{O}_2)\approx 1.6\times 10^{-7}$ atm, than the original synthesis condition of laboratory air ($p(\text{O}_2)\approx 0.2$ atm). Slight reduction of $\text{La}_{0.9}\text{Sr}_{0.1}\text{MnO}_{3-\delta}$ has been shown by Mitchell et al ^[9] to induce transformation to the orthorhombic phase, as a result of the previously described Jahn-Teller distortion. The other compositions display slight increases in cell volume, also consistent with slight reduction relative to the as-synthesized condition.

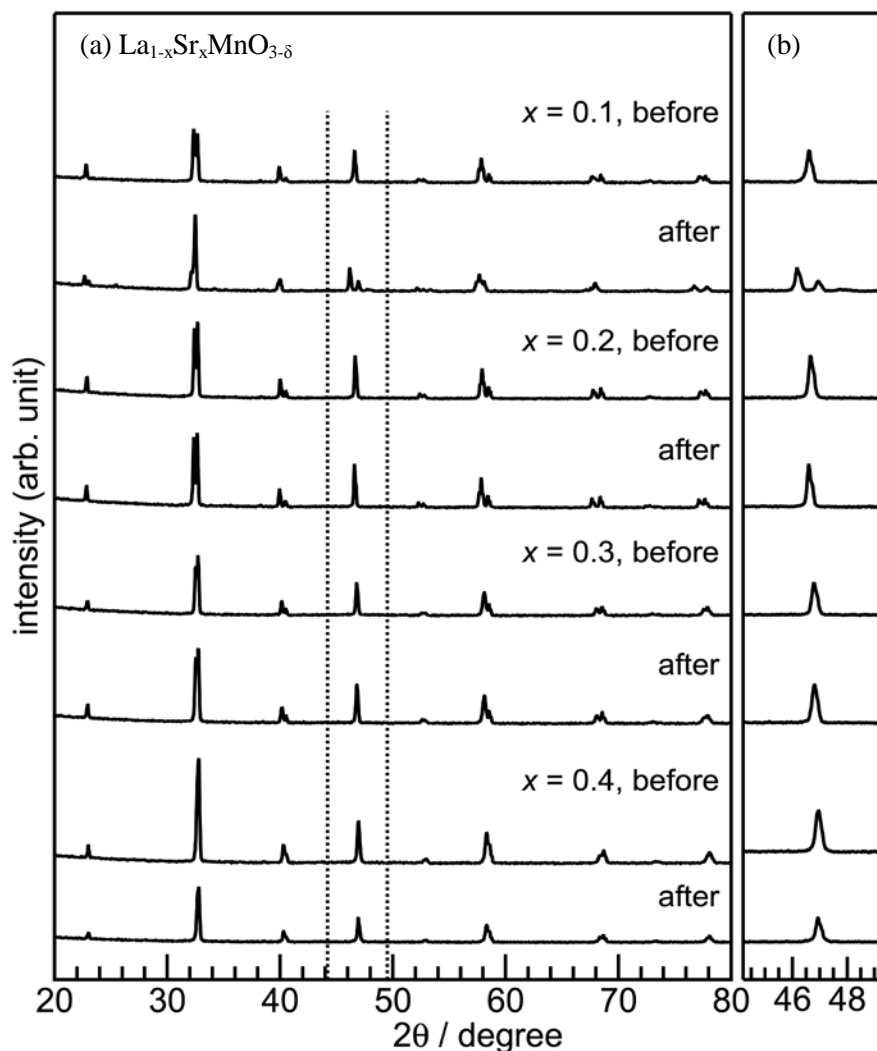


Figure 3-7. X-ray powder diffraction patterns of $\text{La}_{1-x}\text{Sr}_x\text{MnO}_{3-\delta}$ before and after thermochemical cycling between 800-1400 °C: (a) wider range and (b) narrower range showing phase change from rhombohedral ($R\bar{3}c$) to orthorhombic ($Pbnm$) in $\text{La}_{0.9}\text{Sr}_{0.1}\text{MnO}_{3-\delta}$ after cycling. Dashed lines in (a) indicate the region shown in (b).

The porosities were measured by two kinds of methods. One is the volumetric method, which is to compare the calculated/ theoretical density of samples (with the lattice parameters and molecular weight) and the apparent density of porous samples. So, the porosity is calculated by the relation $\text{Porosity} = \left(1 - \left(\frac{\text{Density of porous pellet}}{\text{Theoretical density}} \right) \right) \times 100\%$. With this method, the non-perfect

cylinder shape of the pellets would cause the error within the calculations. The other method is to use the mercury porosimetry, and the results are listed in Table 3-1 with the column title “Porosity^M.” For each composition, three porous pellets were put into the sealed sample cup of mercury porosimetry. As mentioned in Chapter 2, mercury is only able to be intruded into the open pores of the pellets, the porosity values listed (Porosity^M) are accounted for the open pore contribution. From the porosity values shown in Table 3-1, there is no systematic trend with composition shown in the table. Samples after cycling show a decrease in porosity. These average porosity decreases mainly resulted from the sintering effects (grain growth). Enhancing the refractory property of the materials by doping to slow diffusion of cations might mitigate this degradation.

Table 3-1. Room-temperature structural parameters for $\text{La}_{1-x}\text{Sr}_x\text{MnO}_{3-\delta}$: (I) as-synthesized and (II) after thermochemical cycling. Within the column title, x represents the Sr content of $\text{La}_{1-x}\text{Sr}_x\text{MnO}_{3-\delta}$. For the crystal structure, R and O are used as abbreviations for rhombohedral and orthorhombic structure, respectively. Porosity^M represents the open pore porosities measured by mercury porosimetry and “x” means the lost measurements. The Rietveld refinements are calculated by the software X'Pert Plus with $K_{\alpha 2}$ subtraction. For the samples with the space group of $R\bar{3}c$, the Rietveld refinements were carried out using the hexagonal setting of this space group.

(I)

x	a (Å)	b (Å)	c (Å)	Crystal structure (space group)	Molar volume Å ³	Porosity (%)	Porosity ^M (%)
0.1	5.5325(2)	5.5325(2)	13.3585(6)	R ($R\bar{3}c$)	354.1	54.6	52.0
0.2	5.5276(2)	5.5276(2)	13.3664(4)	R ($R\bar{3}c$)	353.7	58.8	63.8
0.3	5.5084(2)	5.5084(2)	13.3625(6)	R ($R\bar{3}c$)	351.1	49.7	56.4
0.4	5.4875(3)	5.4875(3)	13.3533(9)	R ($R\bar{3}c$)	348.2	56.6	56.6

(II)

x	a (Å)	b (Å)	c (Å)	Crystal structure (space group)	Molar volume Å ³	Porosity (%)	Porosity ^M (%)

0.1	5.5494(4)	7.7549(6)	5.5854(4)	O (<i>Pbnm</i>)	240.4	45.6	×
0.2	5.5357(1)	5.5357(1)	13.3737(3)	R (<i>R$\bar{3}c$</i>)	354.9	54.4	×
0.3	5.5090(2)	5.5090(2)	13.3635(4)	R (<i>R$\bar{3}c$</i>)	351.2	45.2	×
0.4	5.4890(2)	5.4890(2)	13.3612(6)	R (<i>R$\bar{3}c$</i>)	348.6	48.9	×

Secondary electron microscopy (SEM) images of $\text{La}_{1-x}\text{Sr}_x\text{MnO}_{3-\delta}$ are shown in Figure 3-9. The grain size decreases with increasing Sr content, from $\sim 5 \mu\text{m}$ for 0.1 and 0.2 Sr to $\sim 1 \mu\text{m}$ for 0.3 and 0.4 Sr. The finer structure of the high Sr content materials suggests enhanced kinetics may be observed for these materials due to the presumably higher specific surface area and the shorter solid-state diffusion length.

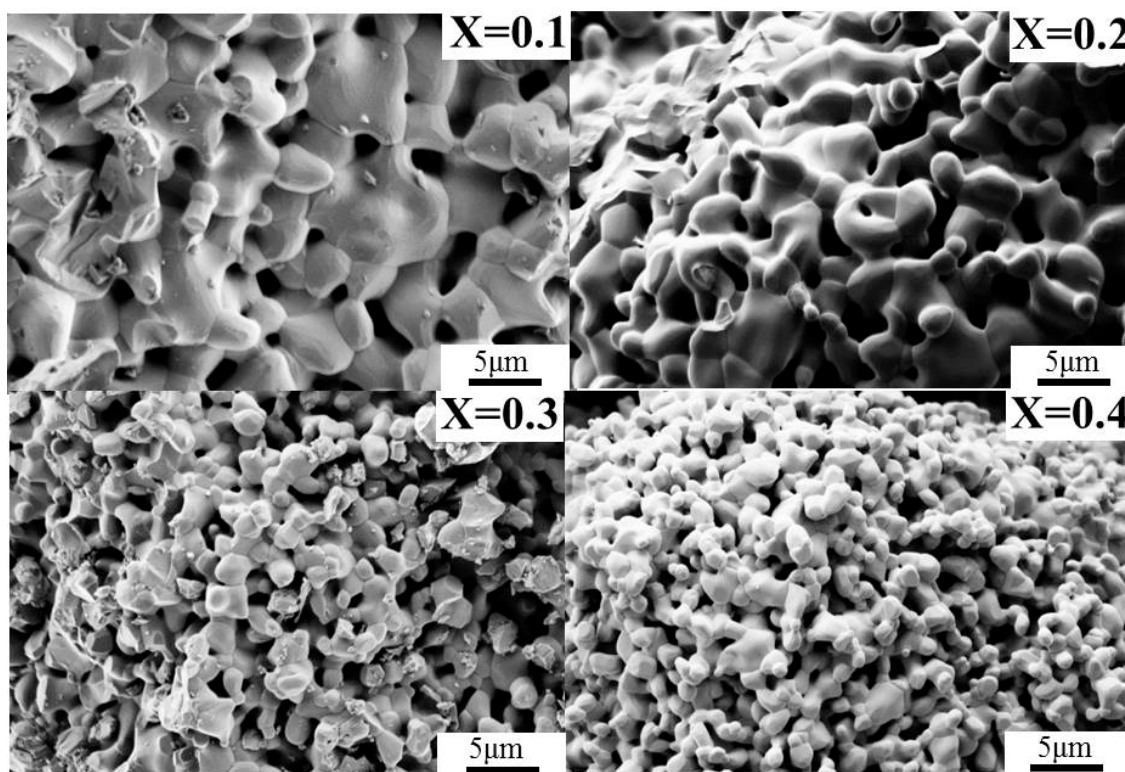


Figure 3-8. Microstructure of $\text{La}_{1-x}\text{Sr}_x\text{MnO}_{3-\delta}$ before thermochemical cycle between 800-1400 °C

3.5 Thermochemical Water Splitting Cycles of $\text{La}_{1-x}\text{Sr}_x\text{MnO}_{3-\delta}$

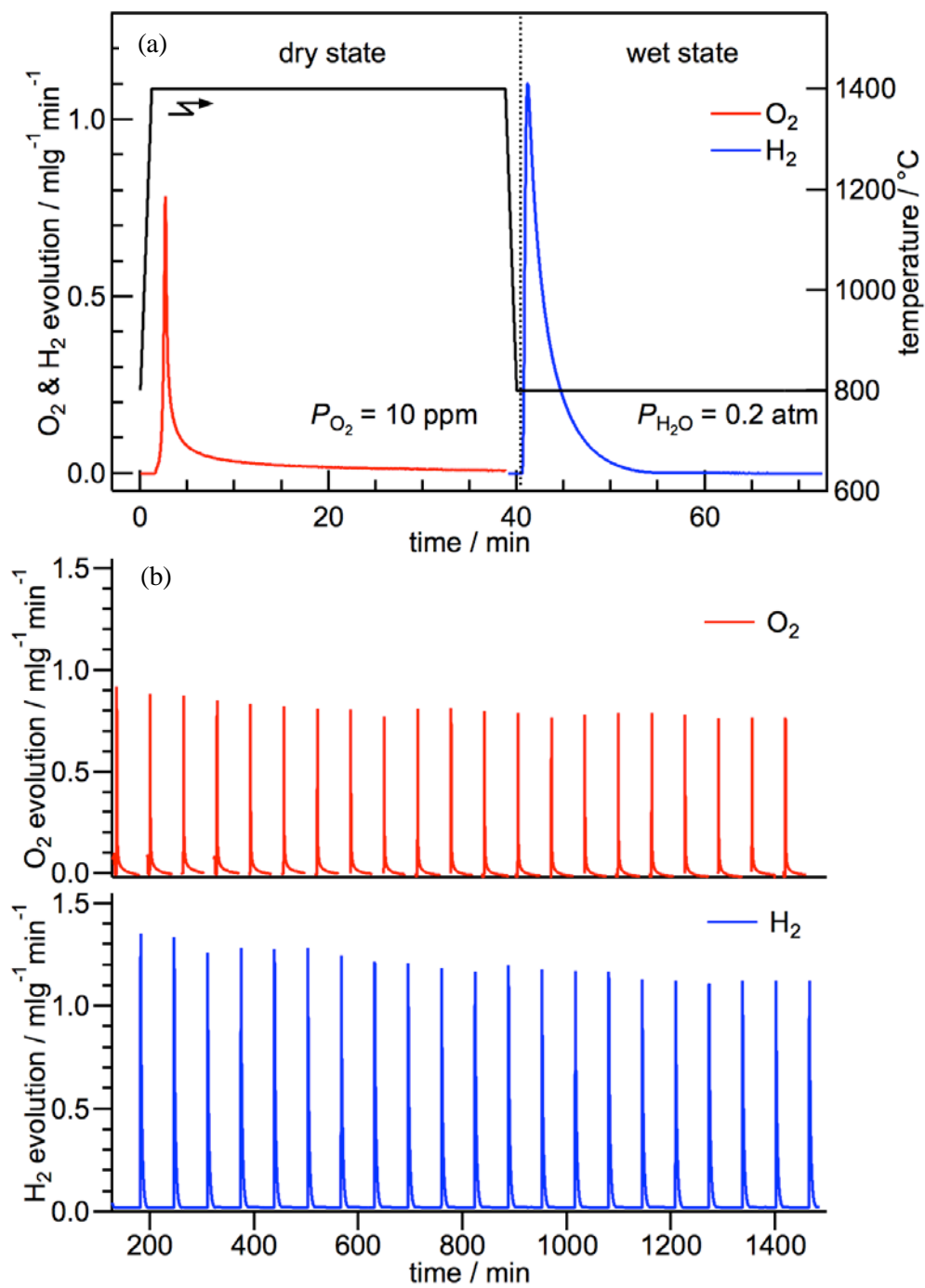


Figure 3-9. Thermochemical cycling behavior of 1400 – 800 °C using $\text{La}_{0.8}\text{Sr}_{0.2}\text{MnO}_{3-\delta}$ between $T_{\text{TR}}=1400 \text{ }^\circ\text{C}$ (under $p(\text{O}_2)=10^{-5} \text{ atm}$) and $T_{\text{WS}}=800 \text{ }^\circ\text{C}$ (under $p(\text{H}_2\text{O})=0.2 \text{ atm}$): a) Evolved gas profiles for a typical cycle using thermal reduction for 40 min and water splitting for 30 min. b)

Profiles for 21 continuous cycles for thermochemical water splitting. Red and blue colors correspond to oxygen and hydrogen evolution, respectively. The high-temperature reduction and low-temperature oxidation steps were held for 47 and 16 min, respectively.

Typical oxygen release and hydrogen production profiles for $\text{La}_{0.8}\text{Sr}_{0.2}\text{MnO}_{3-\delta}$ are presented in Figure 3-9 (a) ($T_{\text{H}} = 1400\text{ }^{\circ}\text{C}$, atmosphere = 10 ppm O_2 balanced with Ar; $T_{\text{L}} = 800\text{ }^{\circ}\text{C}$, atmosphere = 20% H_2O balanced with Ar). In this example, reduction and oxidation were carried out for 40 and 30 min, respectively. For the thermal reduction reaction, the working oxide was heated from $800\text{ }^{\circ}\text{C}$ to $1400\text{ }^{\circ}\text{C}$. Three minutes after the initiation of heating from $800\text{ }^{\circ}\text{C}$, the oxygen peak appears when the temperature reaches around $1300\text{ }^{\circ}\text{C}$. This kind of delay of oxygen release is because the thermal reduction reaction is not a isothermal process and its reaction driving force increases steadily as the target temperature is reached ($1400\text{ }^{\circ}\text{C}$). Since the driving force during the temperature ramp up is mainly changed by the term " $T\Delta S_0$ " in the Gibbs free energy equation, both the ramp rate and the reduction entropy of the working oxides would affect the initial peak rise behavior.

For the water splitting step (shown with a blue curve in Figure 3-9 (a)) hydrogen is immediately produced upon introduction of steam at the low temperature step. The observation that strontium-doped lanthanum manganite can dissociate H_2O through a thermochemical process is fully consistent with the thermodynamic expectations. The data further reveal that the reduction reaches 90% completion after 46 min, as determined from an evaluation of the peak decay behavior, whereas the oxidation reaches the same extent of completion after just 6.2 min. Based on these observations, cycling experiments were performed using reduction and oxidation periods of 45 and 16 min, respectively. The results, as shown in Figure 3-9 (b), show relatively stable yields of both oxygen and hydrogen over 21 cycles.

Figure 3-10, 3-11, and 3-12 show the influence of Sr content on the thermochemical cycling behavior. The raw oxygen and hydrogen evolution profiles, Figure 3-10, reveal that the oxygen release and hydrogen production per cycle increase, on a per gram basis, with increasing Sr content, which is also in general agreement with thermodynamic expectations (the extrapolated $\Delta\delta$ values shown in Figure 3-5). Furthermore, the oxygen release kinetics, as roughly characterized by how quickly the gas evolution decays from its peak value, are largely unaffected by Sr content. In

contrast, the fuel production kinetics, as measured by the same metric, are strongly affected by Sr doping level, and, even with a 65 min oxidation period, fuel production is clearly incomplete for the $x = 0.4$ composition. The difference in reduction and oxidation kinetics is further evident from an examination of the time required for the gas concentration to decrease to a value of 10% of the peak (Figure 3-11). In the case of oxygen release, the required time for the peak to decay from its apex to 10% of the apex is just 1-2 minutes, irrespective of oxide composition, whereas for hydrogen production it increases from about 1 min at $x = 0.1$ to almost an hour at $x = 0.4$. Possible origins of this kinetic behavior are considered below. The cycling profiles presented in Figure 3-10(b) reflect oxidation half-cycle times that correspond to approximately 90% of reaction completion for the 'slow' compositions, for 0.3 and 0.4 Sr, as determined from the evaluation of the profile decay behavior. While the reduction behavior appears, at first glance, to be rapid, particularly in comparison to these oxidation reactions, it is noteworthy that the oxygen release profiles are characterized by extremely long tails, not easily visible in Figure 3-10(a).

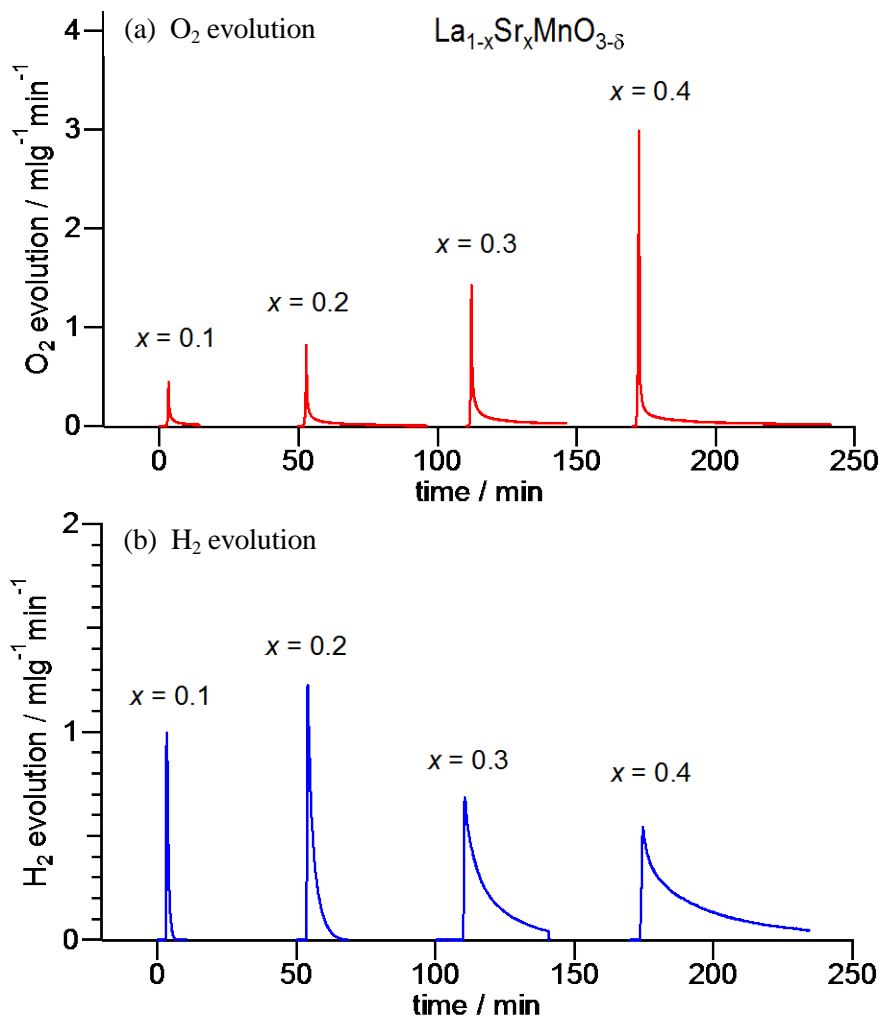


Figure 3-10. Impact of strontium substitution in $\text{La}_{1-x}\text{Sr}_x\text{MnO}_{3-\delta}$ on thermochemical water splitting during 1400 – 800 °C cycle: a) oxygen evolution at 1400 °C, b) hydrogen evolution at 800 °C. The reduction time for 0.1, 0.2, 0.3, and 0.4 Sr at 1400 °C were 12, 47, 60, and 70 min, respectively, while the oxidation time at 800 °C were 8, 16, 36, and 65 min, respectively.

The cycling conditions of Figure 3-10 were repeated over multiple cycles as a means of evaluating stability and of gaining statistically averaged fuel production data. The per cycle oxygen and hydrogen yields for the $x = 0.2$ and 0.4 compositions (obtained from an integration of the area of the

peak profiles) are presented in Figure 3-12. The error bars reflect the uncertainty in the integrated values due to background drift. Both materials show rather stable fuel productivity, indicating that, at least for thermal exposure periods of 22 and 15 hours, respectively, mass losses from the material are negligible. Although the porosity $\text{La}_{0.8}\text{Sr}_{0.2}\text{MnO}_{3-\delta}$ and $\text{La}_{0.6}\text{Sr}_{0.4}\text{MnO}_{3-\delta}$ decreased around 4% and 7% after the cycling, respectively, the impacts from these porosity loss on the stability of gas evolutions are not obvious. Direct measurement of the sample mass after the completion of the cycling experiments showed no more than 0.5% loss for all compositions. Accordingly, fuel productivity numbers quoted below are the averaged values over the multiple cycles. The cycling data further reveal that the $\text{H}_2:\text{O}_2$ molar ratio is within experimental error of the theoretical value of 2, for 0.2 Sr, indicating that all oxygen vacancies created during reduction are consumed for fuel production during oxidation. In contrast, for 0.4 Sr, the ratio is consistently slightly less than 2, a result also obtained for the remaining two compositions. Such behavior may reflect incomplete oxidation by steam at 800 °C, which is followed by oxidation by Ar/O_2 at 800 °C prior to high temperature reduction. In this way, the oxygen released on heating can exceed the corresponding production of hydrogen from reaction with steam. In addition, loss of hydrogen due to leaks is a ubiquitous challenge and can also account for some of the deviation. Loss of hydrogen relative to oxygen due to inherent material behavior, for example, inaccessibility of vacancies due to ordering, would be expected to be cumulative (with a declining per cycle hydrogen and oxygen productivity), and the stable behavior argues against any such interpretation.

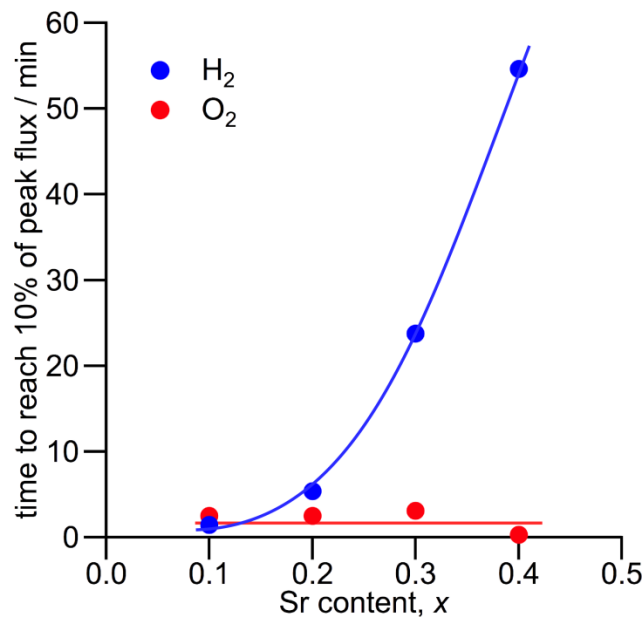


Figure 3-11. Characteristic hydrogen production and oxygen release times as functions of Sr content. Characteristic time is defined as that required for the off-gas detection to fall to 10% of the peak value.

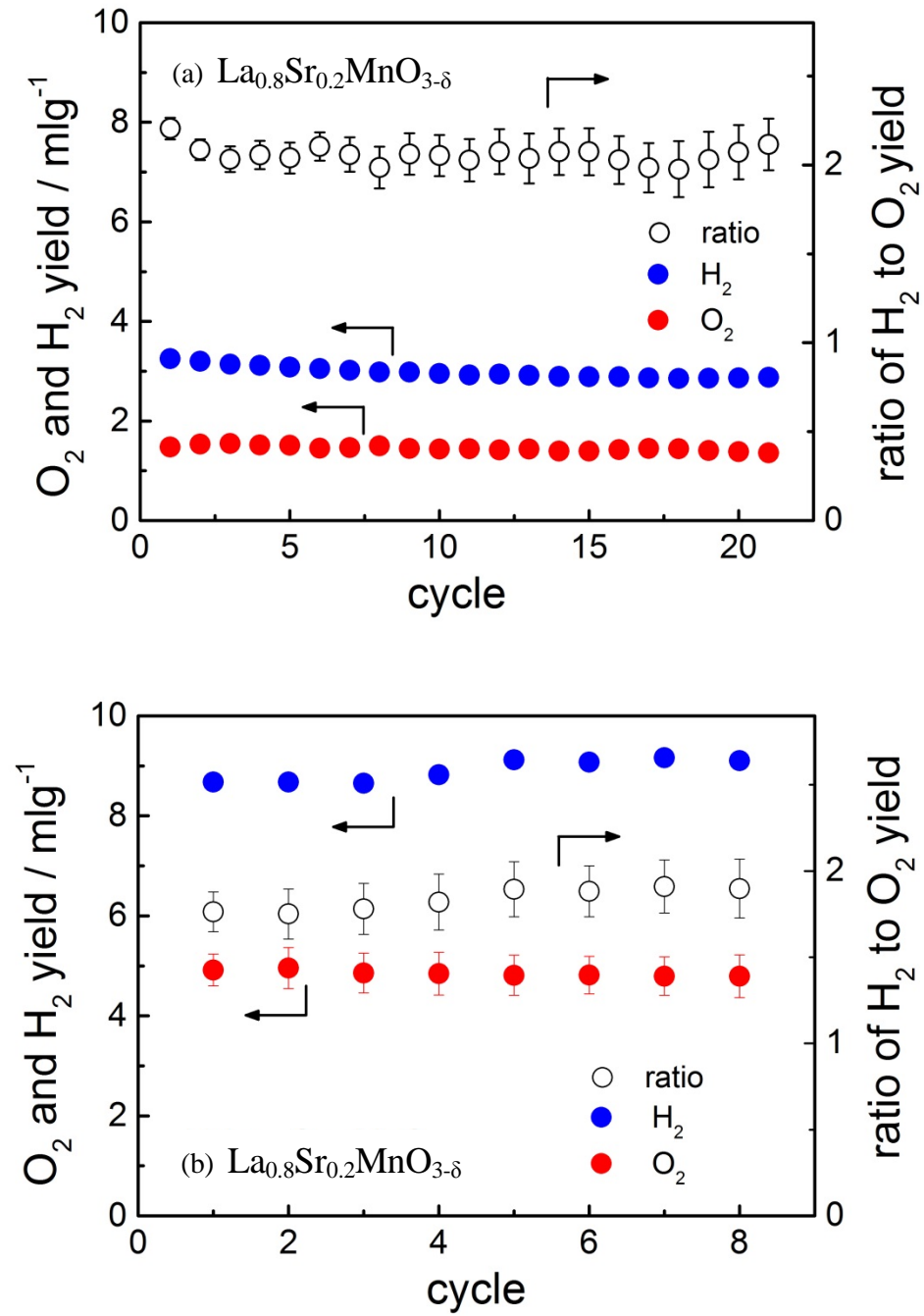


Figure 3-12. Hydrogen and oxygen yield in $\text{La}_{1-x}\text{Sr}_x\text{MnO}_{3-\delta}$: a) $x = 0.2$ and b) $x = 0.4$. Reproducible hydrogen (blue) and oxygen (red) evolution over 21 and 8 cycles was observed in 0.2 and 0.4 Sr pellets, respectively. The reduction and oxidation times for 0.2 Sr were 47 and 16 min, respectively, whereas those for 0.4 Sr were 70 and 65 min, respectively. Uncertainty is estimated from the signal drift as observed during calibration. Where omitted, error bars lie within the data symbol.

Table 3-2 summarizes the fuel production capacity of $\text{La}_{1-x}\text{Sr}_x\text{MnO}_{3-\delta}$ tested in the present study. Reported are the cycle-averaged measured values of oxygen and hydrogen production. The projected quantity of oxygen release corresponding to the amount estimated to result if long reduction times, sufficient to reach equilibrium, had been employed. These projections are computed on the basis of the profile decay behavior and are provided along with estimates of the time required to reach equilibrium, again based on the profile decay behavior. The projected values are useful for comparison against the values estimated from an analysis of the thermogravimetric data, as the latter are also representative of equilibrium behavior. Beyond the monotonic increase in fuel productivity with increasing Sr content already revealed in the raw profiles, it is evident from Table 3-2 that the projected oxygen release (and hence fuel productivity) is in excellent agreement with the thermodynamic predictions. The finite timescale of the measurements implies only a small penalty of about 10% on the fuel productivity. However, accessing that final 10% would require substantial increases in the total cycle time, as much as a factor of three in the case of $\text{La}_{0.6}\text{Sr}_{0.4}\text{MnO}_{3-\delta}$. The experimental hydrogen yields are 0.91, 2.89, 5.68, and 8.91 mL/g, respectively, for the four compositions. The latter two values are favorable in comparison to ceria, which has a hydrogen production capacity of 3.6 mL/g under comparable cycling conditions^[16].

Table 3-2. Cycle-averaged fuel productivity of $\text{La}_{1-x}\text{Sr}_x\text{MnO}_{3-\delta}$. Also reported are the (experimental) measurement time, the measured H_2/O_2 ratio, the projected gas production based on the profile characteristics and a presumed sufficiently long equilibration time, and the estimated time to reach the projected value. In addition, the predicted O_2 release on the basis of the thermodynamic analysis is provided for comparison.

x of $\text{La}_{1-x}\text{Sr}_x\text{MnO}_{3-\delta}$	Measured Gas Production (ml/g)		Measurement time (min)		H_2/O_2 (unitless)
	O_2	H_2	O_2	H_2	
0.1	0.55 ± 0.09	0.91 ± 0.04	12	8	1.64 ± 0.02

0.2	1.45 ± 0.05	2.89 ± 0.07	45	16	2.00 ± 0.04
0.3	3.4 ± 0.30	5.68 ± 0.07	60	31	1.68 ± 0.05
0.4	4.9 ± 0.4	8.91 ± 0.23	70	60	1.84 ± 0.03

x of La _{1-x} Sr _x MnO _{3-δ}	Projected Gas Production (ml/g)		Projection time (min)		Predicted O ₂ Release (ml/g)
	O ₂	H ₂	O ₂	H ₂	
0.1	0.65 ± 0.12	0.91 ± 0.04	46	8	0.5±0.4
0.2	1.53 ± 0.04	2.89 ± 0.07	91	22	0.9±0.3
0.3	3.8 ± 0.3	6.26 ± 0.09	177	92	3.3±0.2
0.4	5.3 ± 0.5	10.3 ± 0.4	192	210	6.1±0.8

3.6 Reaction Kinetics Discussion

Turning from thermodynamic behavior to kinetic characteristics, the ideal reaction substrate for thermochemical cycling will display both rapid bulk diffusion and high surface reaction rates. Diffusion here refers to chemical (or ambipolar) diffusion of neutral oxygen species, a combination of ionic and electronic transport contributions. In the La_{1-x}Sr_xMnO_{3-δ} system, several studies have been carried out using isotope exchange methods to probe oxygen self-diffusion coefficient, D^* , and isotopic surface exchange rate, k^* ^[13-17]. Surprisingly, few have targeted direct measurements of chemical diffusivity, D_{chem} (or D^δ), and chemical surface exchange constant, k_s (or k^δ), under the driving force of a chemical potential gradient^[18-19], the kinetic parameters of relevance to thermochemical cycling. While, it is possible, in principle, to transform between D^* and D_{chem} and analogously between k^* and k_s using the knowledge of the thermodynamic behavior of the material^[21], the discussion here focuses on the direct measurements of D_{chem} and k_s , because of the substantial uncertainty evident in the thermodynamic properties.

Yasuda et al.^[19] determined D_{chem} for compositions in the range of $x = 0.05$ to 0.2 using the conductivity relaxation method, whereas Belzner et al.^[18] determined D_{chem} for compositions with $x = 0.2$ and 0.5 using the potentiostatic step method. Yasuda's studies showed that at the low $p(O_2)$ values that could be probed by conductivity relaxation (10^{-10} - 10^{-17} atm, depending on temperature, over the range 850 to 1000 °C), the chemical diffusivity falls between 10^{-5} and 4×10^{-4} cm²s⁻¹, decreases with increasing $p(O_2)$ (a linear dependence was observed on a double-logarithmic plot) and is insensitive to Sr content. More oxidizing conditions could not be examined because of the insensitivity of conductivity to changes in oxygen partial pressure above $\sim 10^{-9}$ atm. Belzner et al.

measured D_{chem} under somewhat more oxidizing conditions and at slightly lower temperatures. The two sets of results are in general, though not complete, agreement and indicate that the oxygen chemical diffusion at 800 °C during the oxidation half-cycle (water splitting step) of thermochemical fuel production will likely be at least $10^{-8} \text{ cm}^2\text{s}^{-1}$. For a typical diffusion length, l , of $\sim 3 \text{ }\mu\text{m}$ (from the SEM images), this diffusion coefficient implies a characteristic time ($\tau_{\text{diff}} = l^2/4D_{\text{chem}}$) of approximately 2 sec, suggesting that diffusion is unlikely to be rate-limiting for the overall fuel production process.

An important difference between the conclusions of Belzner relative to those of Yasuda concerns the role of Sr content on the chemical diffusivity. As discussed by Belzner, D_{chem} can, under select conditions, have a significant dependence on partial pressure. The dependence is expressed by the equation

$$D_{\text{chem}} = D_{V_o} t_{\text{el}} \left(-\frac{1}{2} \frac{\partial \ln p(O_2)^*}{\partial \ln [V_o^{**}]} \right) = D_{V_o} t_{\text{el}} A \quad (3.1)$$

where D_{V_o} is the diffusivity of oxygen vacancies, t_{el} is the transference number of electronic species, and $[V_o^{**}]$ is the fractional oxygen vacancy concentration. At the relatively low oxygen vacancy concentrations present in $\text{La}_{1-x}\text{Sr}_x\text{MnO}_{3-\delta}$ under moderately oxidizing conditions, both D_{V_o} and t_{el} are largely independent of $[V_o^{**}]$, the latter being close to 1 throughout the experimental conditions, and both are effectively independent of $p(O_2)$. The term in parenthesis in Equation 3.4, named here A , is clearly dependent on $p(O_2)$. This quantity is related, but not identical, to the thermodynamic factor, Γ , defined formally as $d \ln a_o / d \ln c_o$, where a_o and c_o are, respectively, the activity and concentration of oxygen in the solid. Because the specific manner in which oxygen stoichiometry in $\text{La}_{1-x}\text{Sr}_x\text{MnO}_{3-\delta}$ depends on $p(O_2)$ is sensitive to Sr content (Figure 3-5), one can anticipate that D_{chem} will, in turn, also be sensitive to Sr content. Indeed, Belzner directly measured the thermodynamic factor and found that, at close to 1 atm $p(O_2)$, Γ was about an order of magnitude higher for $\text{La}_{0.8}\text{Sr}_{0.2}\text{MnO}_{3-\delta}$ than for $\text{La}_{0.5}\text{Sr}_{0.5}\text{MnO}_{3-\delta}$. The authors concluded that this enhancement was responsible for the observed order of magnitude difference in the diffusion coefficients between the two compositions. In the more limited compositional range examined by

Yasuda, Sr = 5 to 20 at %, no significant dependence on doping level was observed. Although the Belzner result suggests the possibility of a systematic variation of D_{chem} with Sr content, particularly beyond Sr = 20 at %, even an order of magnitude reduction of the diffusivity, resulting in $\tau_{\text{diff}} \sim 20$ sec, is unlikely to render diffusion the rate-limiting step in thermochemical fuel production.

Turning to the experimental results of the present study, figure 3-11 shows that in contrast to oxygen release, fuel production is not only sluggish, but also sensitive to Sr content. Possible explanations for this include a systematic variation in morphological features, a decrease in chemical diffusivity, or a decrease in the surface reaction constant with increasing Sr doping level. From the SEM images (Figure 3-9) the decreasing grain size with increasing Sr content suggests a morphology that favors rapid reaction at large x . However, given the observation of a characteristic time that increases with increasing Sr doping level, the morphological variations can be ruled out as the source of the differing kinetic responses. The chemical diffusivity, as noted, above can be expected to be dependent on Sr content as a result of the differing $\delta(p(O_2), T)$ functional forms for the different compositions. As given in Equation 3.4, D_{chem} is directly proportional to the quantity A , defined as

$$A = -\frac{1}{2} \frac{\partial \ln p(O_2)^*}{\partial \ln [V_O^{**}]} \quad (3.2)$$

The computed values at 800 °C (Figure 3-13) show that A indeed varies with doping level. The value of this parameter at an internal oxygen chemical potential corresponding to a quench from 1400 °C is shown. Although A varies with Sr content, as with the morphological variations, the trend is the opposite of that required to explain the trend in hydrogen production kinetics. Furthermore, as already discussed, the absolute value of D_{chem} reported by both Yasuda et al. and by Belzner et al. implies a characteristic time that is far shorter than the times represented in Figure 3-11. Thus, diffusion (within the bulk) can be ruled out as either the rate-limiting step or the source of the differing fuel production kinetics.

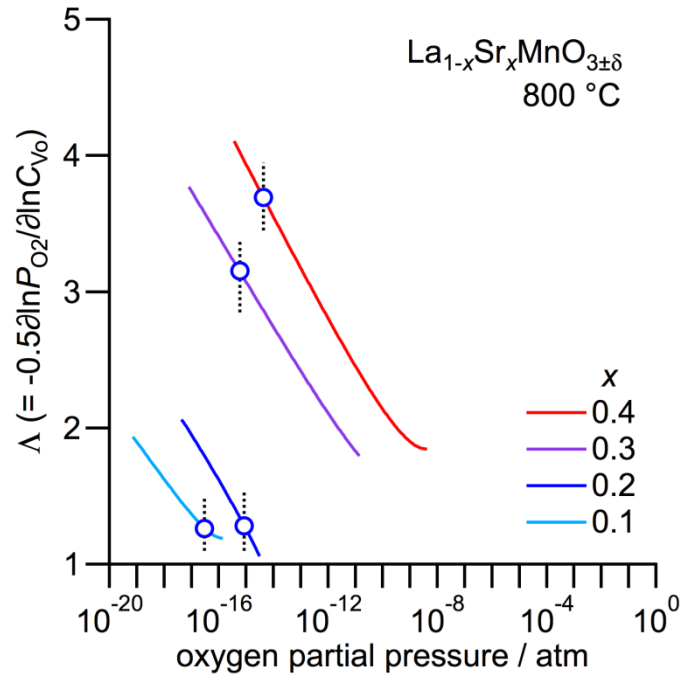


Figure 3-13. Λ plotted as function of oxygen partial pressure and Sr content in $\text{La}_{1-x}\text{Sr}_x\text{MnO}_{3-\delta}$. Open circles indicate the value of Λ after quenching from 1400 °C to 800 °C (under $p(\text{O}_2)=10^{-5}$ atm).

With morphology and bulk diffusivity eliminated as possible explanations for the composition dependent kinetic response, we turn to the surface reaction step. It is common to express the flux, specifically in this case the oxygen flux, J_o , across a surface at which a reaction occurs as

$$J_o = -k_{surf}\Delta C_o \quad (3.3)$$

where k_{surf} is the surface reaction rate constant, ΔC_o is the difference in oxygen concentration across the solid-gas interface, and the reaction is taken to be first order with a rate constant that is independent of concentration. This expression takes the driving force for the reaction to be the difference in concentration, but thermodynamic principles dictate that the driving force is, in fact, the difference in oxygen chemical potential $\Delta\mu_o = \mu_{\text{O},\text{solid}}(\text{interface}) - \mu_{\text{O},\text{gas}}(\text{interface})$. At the initiation of the hydrogen production step, these differences, ΔC_o and $\Delta\mu_o$, can be obtained directly

from the oxygen non-stoichiometry curves, Figure 3-5. The ΔC_o values are essentially given by the $\Delta\delta$ values indicated between oxidizing and reducing conditions (also corresponding to $\Delta\delta_{max}$ described in Figure 3-5).

The thermodynamic driving force (chemical potential difference, $\Delta\mu_o$) of water splitting reaction can, in fact, be derived from the oxygen non-stoichiometry curves, Figure 3-5. The connection is shown schematically in Figure 3-14. The right and left curves represent respectively high and low temperature isothermal measurements; here, for example, the right curve is for 1400 °C and the left curve is for 800 °C. Thermal reduction reaction corresponds to a chemical potential change from point A on the 800 °C curve to point B on the 1400 °C curve. The reduction is performed under the oxygen partial pressure $p(O_2)_B$ and the oxygen nonstoichiometry change is $\Delta\delta = \delta(\text{point } B) - \delta(\text{point } A)$. Upon quenching from 1400 °C to 800 °C, the chemical potential of the working oxide changes from point B on the 1400 °C curve to point C on the 800 °C curve. That is to say that the oxygen content is unchanged (initially) and the internal chemical potential of oxygen in the solid corresponds to that of $p(O_2)_C$. When steam is introduced at 800 °C curve, the oxygen chemical potential in the gas phase is given by $p(O_2)_A$, resulting from the thermolysis of water (for example, for the oxidation at 800 °C under 20% H₂O, $p(O_2)_A$ is around 1.6×10^{-7} atm). The oxide is reoxidized by the steam, following the isothermal curve at 800 °C up to point A.

The working oxide status can be corresponded to the effective oxygen partial pressure via the relation $\mu_o = \mu_o^0 + RT \ln p(O_2)$. For example, after quenching to 800 °C, the initial status represented by the point C corresponds to the effective oxygen partial pressure $p(O_2)_C$. Therefore, length of \overline{CA} corresponds to the initial (maximum) thermodynamic driving force which drives the water splitting reaction, and it can be expressed as the oxide inner chemical difference $\Delta\mu_o = \mu_o(\text{state } C) - \mu_o(\text{state } A) = \frac{1}{2} RT (\ln(p(O_2)_C) - \ln(p(O_2)_A))$. The $\Delta\mu_o$ values correspond to the difference in effective oxygen partial pressures between the quenched state at 800 °C and the oxidized state at the same temperature.

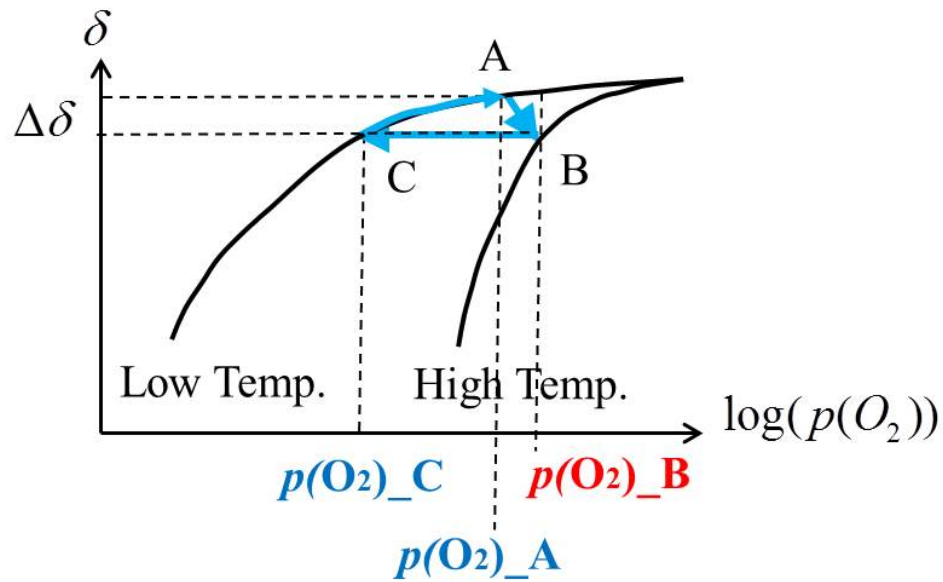


Figure 3-14. Scheme of simplified thermogravimetric measurements. Two curves represent two isothermal thermogravimetric measurements and the measurement temperature decreases from the right curve to left curve. $p(O_2)_B$ is the oxygen partial pressure for thermal reduction reaction and $p(O_2)_C$ is the effective oxygen partial pressure corresponding to the inner chemical potential of the working oxide after quenching to the water splitting temperature.

The correlation between the peak in the hydrogen evolution and two parameters, $\Delta\delta$ (directly proportional to ΔC_o) and $\Delta\mu_o$, is shown in Figure 3-16. In the case of ΔC_o , an anticorrelation is observed, with the peak decreasing in intensity with increasing concentration difference. In contrast, the peak height appears to be positively correlated with the magnitude of $\Delta\mu_o$. This result (in combination with the conclusion that diffusion cannot be rate-limiting) suggests that the hydrogen production half-cycle is surface reaction limited, and that the rate limitation arises from differences in the thermodynamic driving force for the reaction. It is of some value to note that, because the magnitude of $\mu_{O_{gas}}$ (interface) is fixed by the reactor conditions (irrespective of the nature of the reactive oxide), $\Delta\mu_o$ directly scales with $\mu_{O_{solid}}$ (interface). The latter is a measure of the oxygen chemical potential in the material upon quenching and, in turn, directly scales with ΔH_{red} , suggesting that materials with small enthalpies of oxidation will be at a kinetic disadvantage relative to those with large enthalpies. On the other hand, in the absence of direct measurements of the

surface reaction constant, it is premature to rule out a possible dependence of k_{surf} on Sr doping level as the cause of the depression in kinetics with increasing Sr content. Such behavior could arise indirectly from a dependence of k_{surf} on the (initial) bulk oxygen vacancy concentration, which increases monotonically with Sr content for the cycling conditions explored (Figure 3-5). Regardless of these possibilities (reduction of the driving force or inherent variation in k_{surf}), the elimination of diffusion as the rate-limiting step points towards a surface reaction limited process.

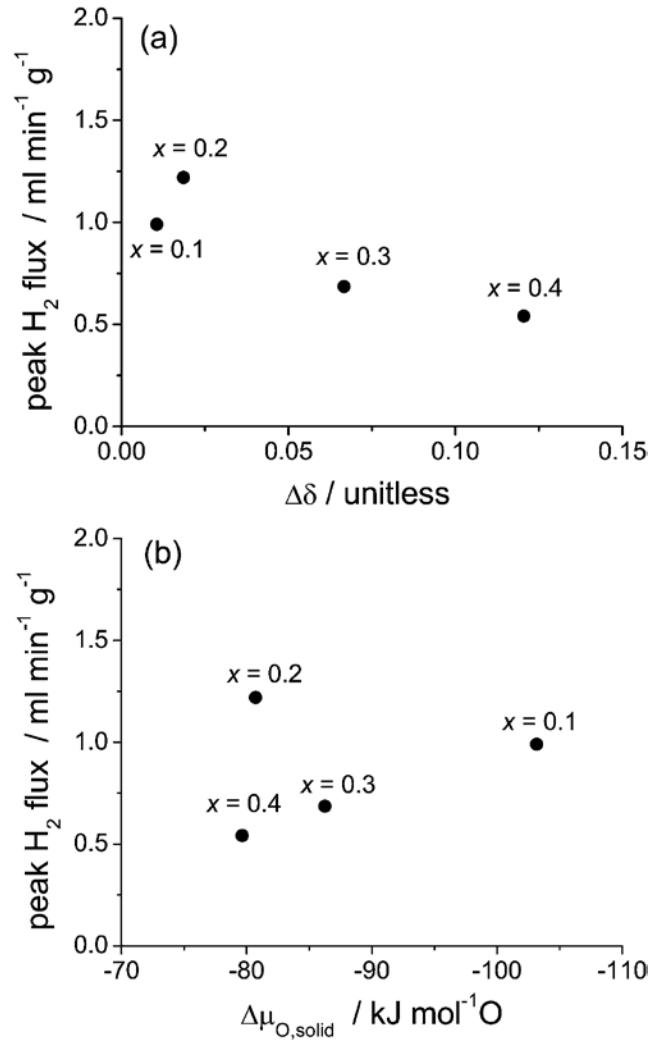


Figure 3-15. Peak flux of hydrogen plotted against (a) change in oxygen content, and (b) change in chemical potential over the course of the oxidation by 0.2 atm steam (balance inert) at 800 °C after quenching from reduction under 10 ppm O₂ (balance inert) at chemical potential of oxide quenched from 1400 °C to 800 °C.

BIBLIOGRAPHY

1. J. Mizusaki, S. Yamauchi, K. Fueki and Akira Ishikawa, *Solid State Ionics*, 1984, 12, 119-124.
2. J. Mizusaki, M. Yoshihiro, S. Yamauchi and K. Fueki, *Journal of Solid State Chemistry*, 1985, 58, 257-266.
3. J. Mizusaki, N. Mori, H. Takai, Y. Yonemura, H. Minamiue, H. Tagawa, M. Dokiya, H. Inaba, K. Naraya, T. Sasamoto and T. Hashimoto, *Solid State Ionics*, 2000, 129, 163-177.
4. S.P Jiang, *Solid State Ionics*, 2002, 146, 1-22.
5. J. Mizusaki, Y. Yonemura, H. Kamata, K. Ohyama, N. Mori, H. Takai, H. Tagawa, M. Dokiya, K. Naraya, T. Sasamoto, H. Inaba and T. Hashimoto, *Solid State Ionics*, 2000, 132, 167-180.
6. J. Mizusaki, H. Tagawa, K. Naraya and T. Sasamoto, *Solid State ionics*, 1991, 49, 111-118.
7. J. R. Scheffe and D. Weibel and A. Steinfeld, *Energy Fuels*, 2013, 27, 4250-4257
8. S. Miyoshi, J. Hong, K. Yashiro, A. Kaimai, Y. Nigara, K. Kawamura, T. Kawada and J. Mizusaki, *Solid State Ionics*, 2003, 161, 209-217.
9. J. F. Mitchell, D. N. Argyriou, C. D. Potter, D. G. Hinks, J. D. Jorgensen and S. D. Bader, *Physical Review B*, 1996, 54, 6172-6183.
10. O. Chmaissem, B. Dabrowski, S. Kolesnik, J. Mais, J. D. Jorgensen and S. Short, *Physical Review B*, 2003, 67, Artn 094431.
11. R. Cortes-Gil, M. Hernando, M. L. Ruiz-Gonzalez, E. Cespedes, C. Prieto, J. M. Alonso, M. Vallet-Regi, A. Hernando and J. M. Gonzalez-Calbet, *Chemistry-a European Journal*, 2008, 14, 9038-9045.
12. T. G. Parsons, H. D'Hondt, J. Hadermann and M. A. Hayward, *Chemistry of Materials*, 2009, 21, 5527-5538.
13. S. Carter, A. Selcuk, R. J. Chater, J. Kajda and J. A. Kilner, B. C. H. Steele, *Solid State Ionics*, 1992, 53-6, 597-605.
14. R. A. De Souza and J. A. Kilner, *Solid State Ionics*, 1998, 106, 175-187.
15. R. A. De Souza and J. A. Kilner and J. F. Walker, *Materials Letters*, 2000, 43, 43-52.
16. S. P. Jiang, *Journal of Materials Science*, 2008, 43, 6799-6833.
17. S. Fearn, J. C. H. Rossiny, J. A. Kilner and J. R. G. Evans, *Solid State Ionics*, 2012, 211, 51-57.
18. A. Belzner, T. M. Gur and R. A. Huggins, *Solid State Ionics*, 1992, 57, 327-337.
19. I. Yasuda and M. Hishinuma, *Journal of Solid State Chemistry*, 1996, 123, 382-390.

20. L. Yan, K. R. Balasubramaniam, S. L. Wang, H. Du and P. A. Salvador, *Solid State Ionics*, 2011, 194, 9-16.
21. J. Maier, *Physical Chemistry of Ionic Materials*, John Wiley & Sons, Ltd, 2005.
22. F. A. Kroger and H. J. Vink, Academic Press, New York, 1956.
23. C. B. Gopal and S. M. Haile, *J Mater Chem A*, 2014, 2, 2405-2417.

Chapter 4

SOLAR TO FUEL PRODUCTIVITY AND EFFICIENCY

4.1 Introduction

Strontium doped lanthanum manganite ($\text{La}_{1-x}\text{Sr}_x\text{MnO}_{3-\delta}$) has been discovered, demonstrated, and investigated for two-step thermochemical water splitting. Its large oxygen nonstoichiometry change during cycling and moderate thermal reduction reaction temperature have attracted significant attention.^[1-3] While equilibrium fuel productivity provides one measure of the suitability of a material for thermochemical cycling, such a metric has the potential to be misleading because it does not account for the steam-to-hydrogen conversion efficiency. The solar to fuel conversion efficiency calculation and the effects of redox properties of active oxides on this efficiency are discussed here.

4.2 Fuel Production Reaction Extent

The oxygen nonstoichiometry change ($\Delta\delta$) within a given thermochemical cycle is a function of $p(\text{O}_2)$ and temperature and is governed by the redox properties, reduction enthalpy and entropy, of the active oxide. Figure 4-1 shows the thermogravimetric curves of $\text{La}_{0.9}\text{Sr}_{0.1}\text{MnO}_{3-\delta}$ and $\text{La}_{0.6}\text{Sr}_{0.4}\text{MnO}_{3-\delta}$ at temperatures for thermal reduction (1400 °C) and water splitting (800 °C). The inset shows schematically the reaction cycle path on the thermogravimetric curves ($A \rightarrow B \rightarrow C \rightarrow A$). \overline{BC} on the inset corresponds to the dot-dash arrow lines connecting the curves of 800 °C and 1400 °C ($\overline{B'C'}$ and $\overline{B''C''}$). As mentioned in Chapter 3, the length of \overline{CA} can be considered the thermodynamic driving force for reoxidization. It is apparent from the plot that $\text{La}_{0.6}\text{Sr}_{0.4}\text{MnO}_{3-\delta}$ has a larger oxygen nonstoichiometry change ($\Delta\delta$) than does $\text{La}_{0.9}\text{Sr}_{0.1}\text{MnO}_{3-\delta}$, and hence higher fuel productivity, but it possesses a smaller thermodynamic driving force (the length of $\overline{C''A''}$ is shorter than it of $\overline{C'A'}$).

Based on the experimental observations reported in Chapter 3, oxides with a smaller thermodynamic driving force generally have a smaller initial hydrogen production flux (lower peak height). Here we further show that a smaller thermodynamic driving force for water splitting results

in a lower steam-to-hydrogen conversion efficacy, meaning a larger amount of steam is required to reach full reoxidation.

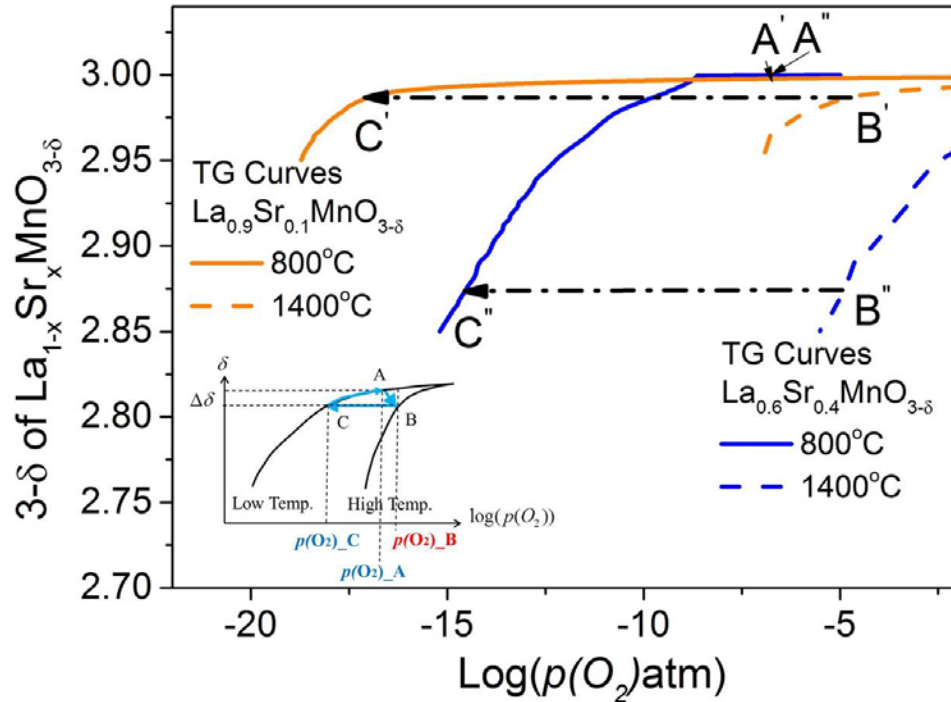


Figure 4-1. Thermogravimetric curves of $\text{La}_{0.9}\text{Sr}_{0.1}\text{MnO}_{3-\delta}$ and $\text{La}_{0.6}\text{Sr}_{0.4}\text{MnO}_{3-\delta}$. The curves of 800 °C are from the TGA data of the ref. [6], and the 1400 °C curves are calculated curves based on the redox properties of oxides.. Figure 3-15 is replotted in the insert plot as an explanation aid. It is worth noting that, in the inserted plot, the $p(\text{O}_2)$ of point B is the reduction reaction oxygen partial pressure and the $p(\text{O}_2)$ of point A is determined by the $p(\text{H}_2\text{O})$ of the steam. For the steam with $p(\text{H}_2\text{O})=0.2\text{atm}$, the $p(\text{O}_2)$ of point A is around 1.6×10^{-7} atm.

The amount of steam required to achieve the water splitting reaction can be determined from the thermodynamic redox properties. Here we apply an equilibrium calculation, implying kinetic factors are irrelevant. Figure 4-2 shows the reactants (steam) entering the reactor at the moment right after quenching from the thermal reduction temperature (T_{TR}) to the water splitting temperature

(T_{WS}). This condition corresponds to the point C in the insert in Figure 4-1. The working oxide located in the reactor exists at this initial point in the reduced state. Its composition is represented as $ABO_{3-\delta_i}$ with an oxygen nonstoichiometry of δ_i . The water splitting reaction is initiated when steam in the amount of $n_{H_2O,i}$ moles, is introduced to the reactor. Upon equilibrium with the oxide, a fraction of the steam is converted to hydrogen, leaving $n_{H_2O,f}$ moles unreacted. We define the reaction extent, ψ , as the extent of steam to hydrogen conversion. The initial and final quantities of steam are thus related according to:

$$n_{H_2O,f} = (1-\psi)n_{H_2O,i} \quad (4.1)$$

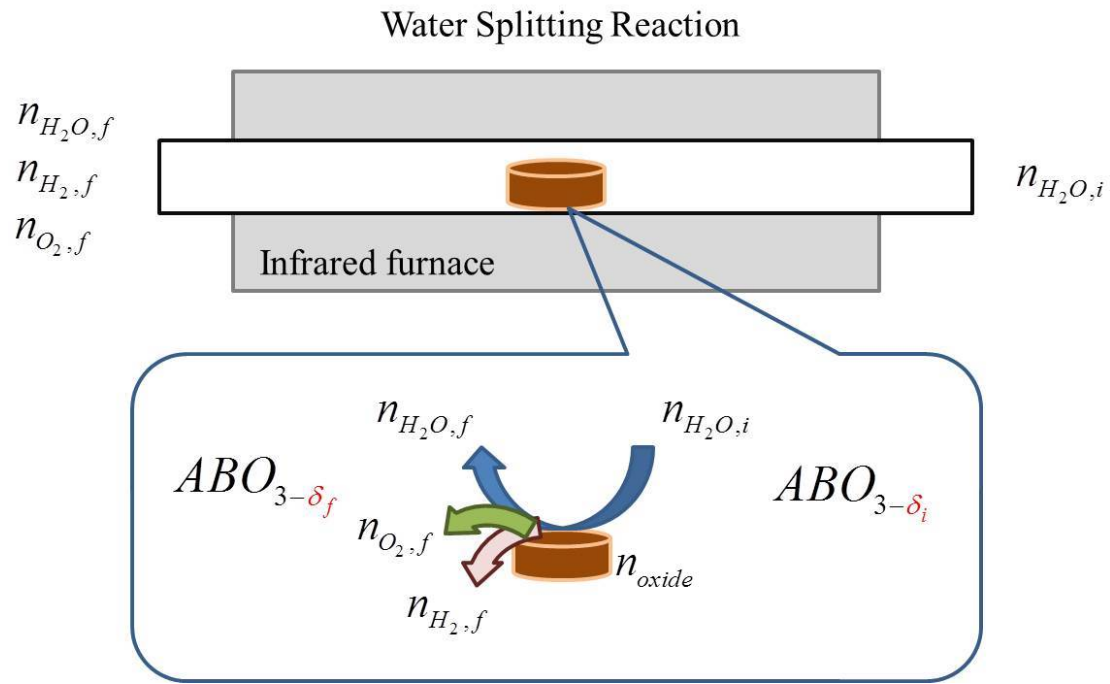


Figure 4-2. Scheme of moles of reactant species involved in water splitting reaction. Within the notation of the reactant species, “i” means the value at the initiation of the reaction (initial state) and “f” describes the value at the completion of the reaction (final state).

Mass conservation of hydrogen implies

$$n_{H_2,f} = \psi n_{H_2O,i} \quad (4.2)$$

Equation 4.2 clearly shows that ψ is precisely the steam to hydrogen conversion ratio. Mass conservation of oxygen implies

$$n_{H_2O,i} = n_{H_2O,f} + (\delta_i - \delta_f)n_{oxide} + 2n_{O_2,f} \quad (4.3)$$

The quantity $(\delta_i - \delta_f)n_{oxide}$ represents the amount of oxygen consumed by the oxide that results in the change of oxygen nonstoichiometry from δ_i to δ_f . The final term $n_{O_2,f}$ is non-zero due to the thermolysis reaction, as described below. Inserting the Equation 4.1 into 4.3, yields:

$$n_{H_2O,i} = (1 - \psi)n_{H_2O,i} + (\delta_i - \delta_f)n_{oxide} + 2n_{O_2,f} \quad (4.4)$$

Then, we get $n_{O_2,f}$ by rearranging Equation 4.4:

$$n_{O_2,f} = \frac{\psi}{2}n_{H_2O,i} - \frac{1}{2}(\delta_i - \delta_f)n_{oxide} \quad (4.5)$$

where $n_{O_2,f}$ can be calculated from the water dissociation (thermolysis) reaction:



with its corresponding equilibrium constant

$$K_{H_2O}(T) = \frac{x_{H_2} x_{O_2}^{1/2}}{x_{H_2O}} \left(\frac{P_{sys}}{P_{ref}} \right)^{1/2} \quad (4.7)$$

for which temperature (T_{WS}) dependent equilibrium constants are tabulated using HSC^[4]. In Equation 4.7, where P_{sys} and P_{ref} are the pressure of the reactor and the reference status, respectively (both set to 1 atm), and x_{gas} is the mole fraction of gas species x defined as:

$$x_{gas} = \frac{n_{gas}}{n_{Total}} \quad (4.8)$$

where n_{Total} is the total reactants mole amount

$$n_{Total} = n_{O_2} + n_{H_2O} + n_{H_2} + n_{Ar} \quad (4.9)$$

n_{Ar} is included in Equation 4.9 because it is used as a carrier gas to bring steam into the reactor. Because argon does not participate in the reaction, $n_{Ar,i} = n_{Ar,f} = n_{Ar}$. As we are interested here in $n_{O_2,f}$, at which point the system has reached equilibrium, we apply Equation 4.7 to the final gas concentrations. The value of the temperature dependent equilibrium constant is obtained from HSC^[4].

Assuming ideal gas behavior, we have

$$x_{O_2,f} = \frac{P_{O_2,f}}{P_{sys}} \quad (4.10)$$

Equation 4.7 can then be expressed as

$$K_{H_2O}(T)^2 = \left(\frac{x_{H_2,f}}{x_{H_2O,f}} \right)^2 P_{O_2,f} = \left(\frac{\psi}{1-\psi} \right)^2 P_{O_2,f} \quad (4.11)$$

implying

$$\left(K_{H_2O}(T) \frac{1-\psi}{\psi} \right)^2 = P_{O_2,f} \quad (4.12)$$

At first glance, the quantities in Equation 4.12 appear independent of the oxide material properties. In fact, however, because the solid and gas are in equilibrium at the conclusion of the reaction, and for the reaction equilibrium, the $\mu_{O_{gas}}$ is equal to $\mu_{O_{solid}}$ ($\mu_{O_2(g)} = \mu_{O_2(g)}^0 + RT \ln(P_{O_2,f})$). Thus, $P_{O_2,f}$ defines the oxygen content of the oxide in the final state. The connection between ψ and material

properties is shown in the following example. Consider ceria that is reduced at $T_{TR}=1400$ °C under 10^{-5} atm $p(O_2)$. The resulting δ_i is then 0.0313 (shown in Figure 4-3). For the water splitting step, the material is quenched to 800 °C and 0.2 atm $p(H_2O)$ is introduced into the reactor. We take the subsequent reaction of the oxide with the supplied steam to occur infinitely quickly and evaluate the oxygen partial pressure of the exhaust gas, defined above as $P_{O_2,f}$. This $P_{O_2,f}$ specifies the δ_f of the oxide and hence the $\Delta\delta$ ($=\delta_i - \delta_f$). It also specifies the steam-to-hydrogen conversion extent, ψ (Equation 4.12). In addition, the fact that the oxygen partial pressure attained a particular value implies a given n_{oxide} was allowed to react with the input $n_{H_2O,i}$. Mass balance shows this amount to be

$$n_{oxide} \approx \frac{1}{\Delta\delta} n_{H_2,f} \approx \frac{\psi}{\Delta\delta} n_{H_2O,i} \quad (4.13)$$

Equation 4.13 is with the assumption that $n_{O_2,f}$ is negligibly small, and this approximation will be adjusted later.

Let $P_{O_2,f}$ in our example be 10^{-19} atm. This corresponds to $\Delta\delta=0.022$ and $\delta_f=0.0095$ (point D on the blue curve in Figure 4-3). At this point, the oxygen chemical potential is -390.34 kJ/(mole- O_2). From Equation 4.12, ψ is around 0.67 (point P on the red curve in Figure 4-3), implying that the molar ratio between the oxide and the input steam must have been $\frac{n_{oxide}}{n_{H_2O,i}} \approx \frac{\psi}{\Delta\delta} = 30.45$. The

maximum possible $P_{O_2,f}$ at 800 °C with $p(H_2O)_i=0.2$ atm is 1.6×10^{-7} atm, which gives a minimum $\delta_f=0.00003$ (maximum $\Delta\delta$ of 0.0313). This condition corresponds to the situation in which an infinite supply of steam is provided and ψ falls to zero.

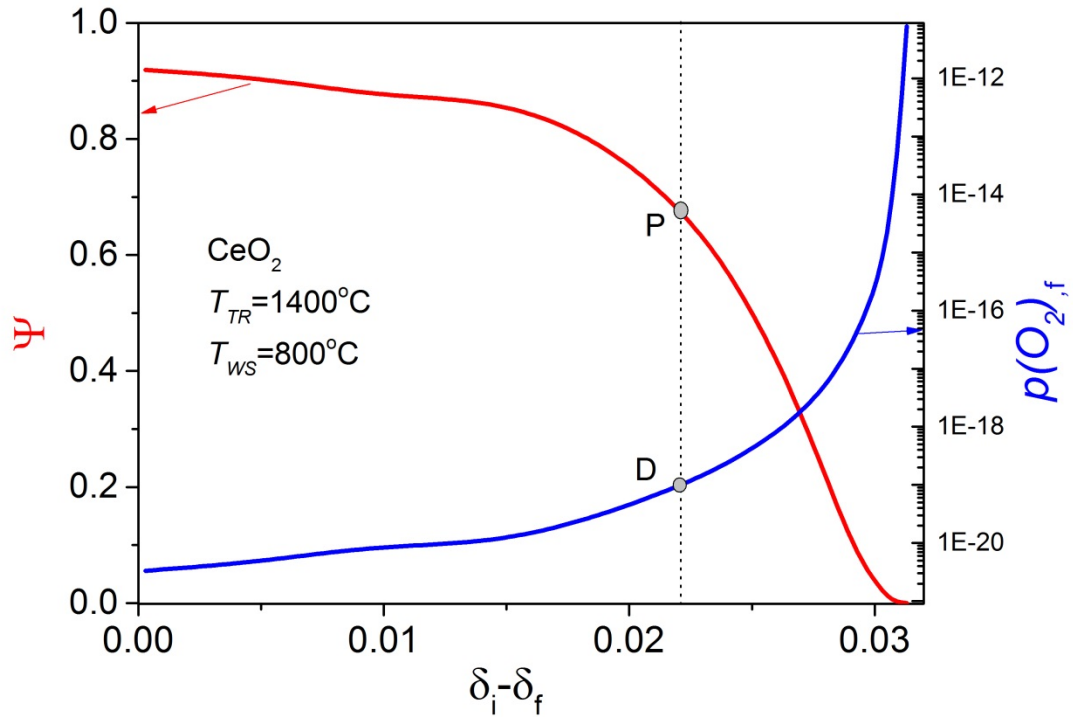


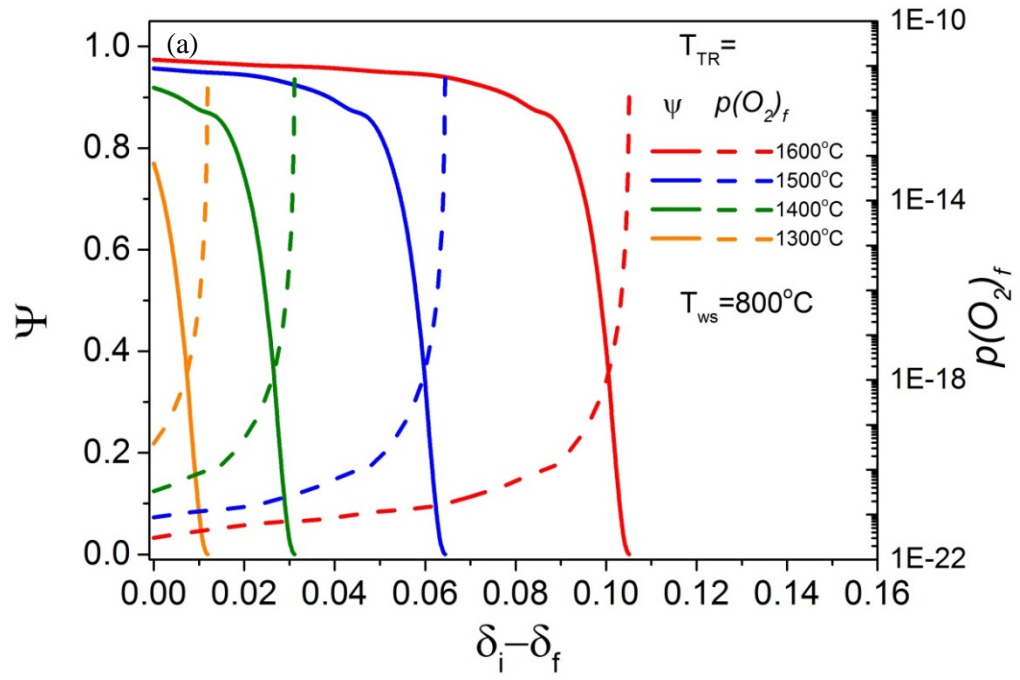
Figure 4-3. Reaction extent of water splitting reaction, ψ , plotted together with the change of the chemical potential corresponding effective oxygen partial pressure among the reaction performed with CeO_2 . The thermochemical cycling conditions are set with 1400°C under $p(\text{O}_2)=10\text{ppm}$ for the thermal reduction step and 800°C with the steam $p(\text{H}_2\text{O}) = 0.2 \text{ atm}$ for the water splitting step.

4.3 Temperature Effect on Reaction Extent

Equation 4.12 shows that the reaction extent, ψ , is a function of temperature. Here, the impact of temperature on reaction extent and the selection of cycling temperatures will be discussed.

Again, CeO_2 is taken as the example for temperature effects. Figure 4-4 (a) shows the reaction extent calculations with fixed water splitting reaction temperature (T_{WS}) and the impact of the thermal reduction temperature (T_{TR}). Thermal reduction temperature determines the maximum oxygen nonstoichiometry change ($\delta_{i,max}$). Therefore, after quenching to T_{WS} , the position of point C in the insert plot of Figure 4-1 is also fixed. In other words, changing T_{TR} will move the point C along the thermogravimetric curve of water splitting temperature and correspondingly vary the

$P_{O_2,f}$ value right before the water splitting reaction begins at $P_{O_2,f,initial}$ (initial value of the $P_{O_2,f}$). Therefore, the reaction with higher T_{TR} , for example, $T_{TR}=1600$ °C, starts with the relatively low $P_{O_2,f,initial}$ and a high ψ due to a higher initial reaction driving force.



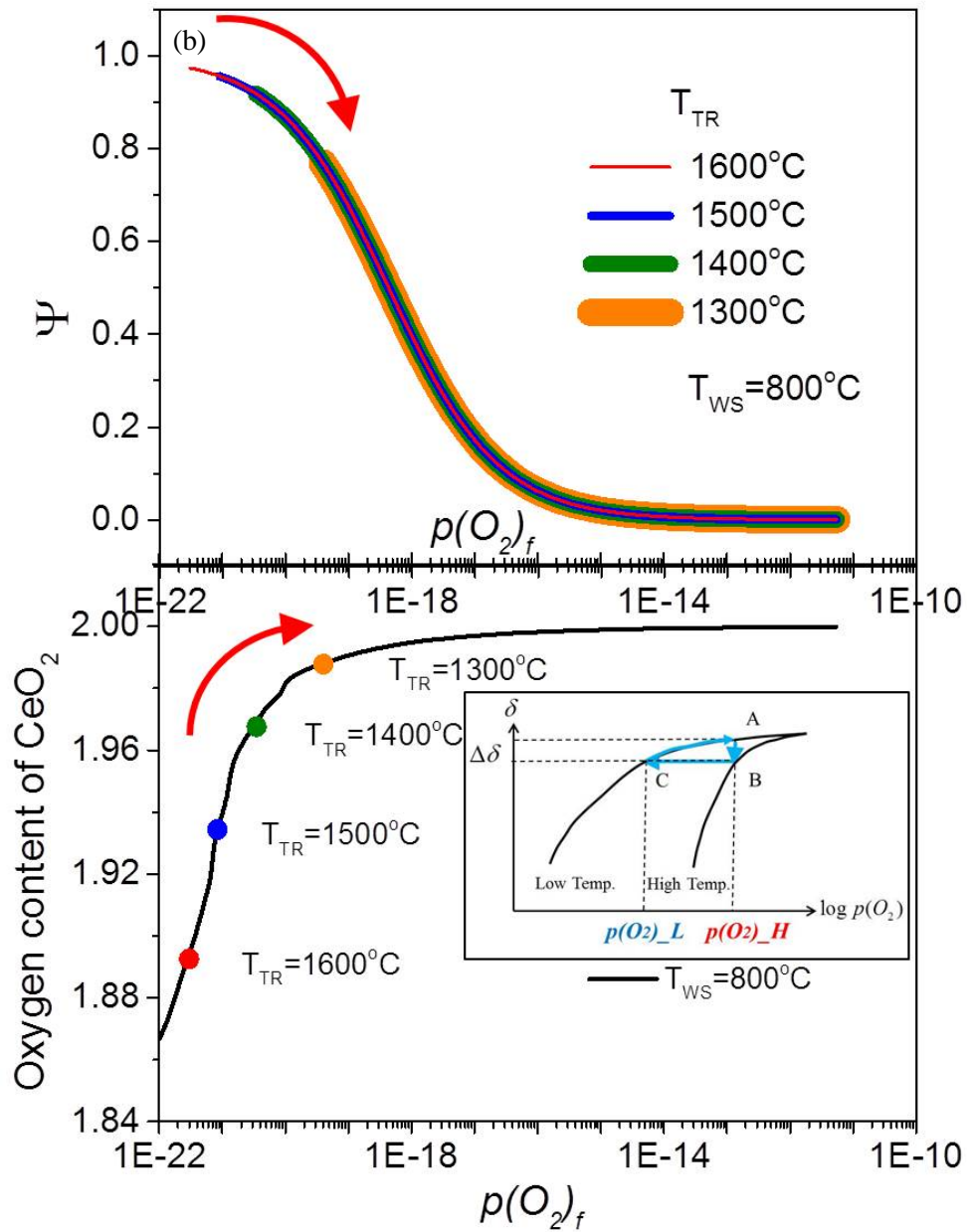
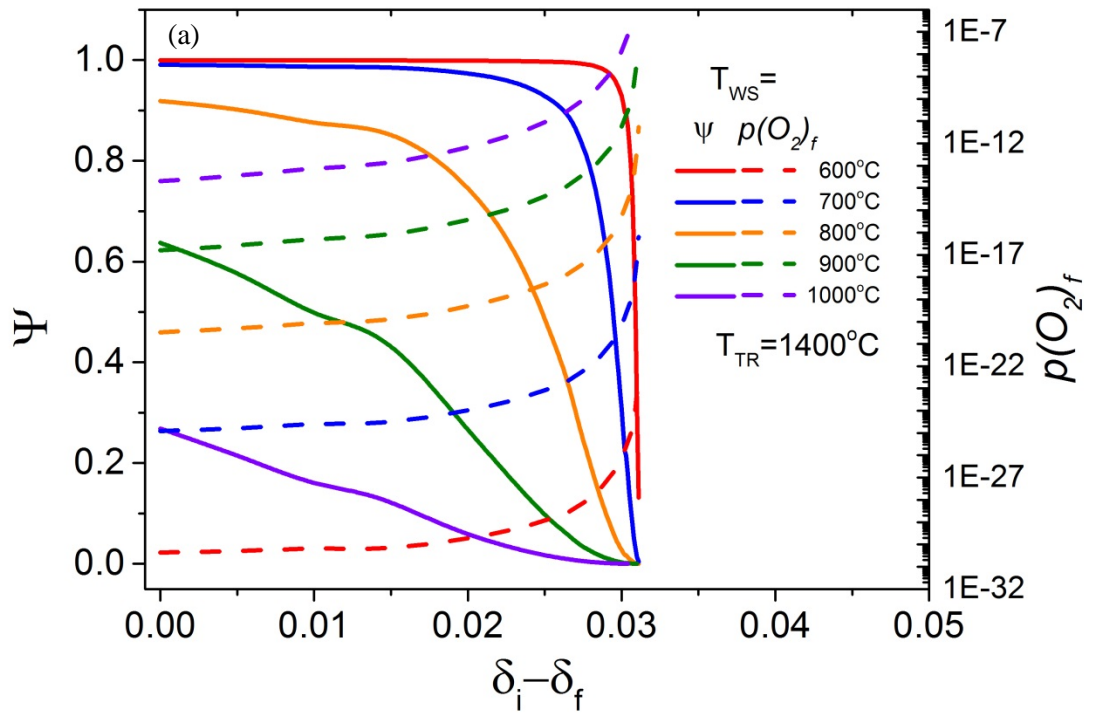


Figure 4-4. Fixed water splitting reaction temperature (T_{WS}) reaction extent computed with the redox properties of CeO_2 . Gas conditions are same as previously mentioned in Figure 4-3. (a) reaction extent and $P_{O_2,f}$ change with $\Delta\delta$, (b-Top) the $P_{O_2,f}$ impact on reaction extent, (b-Bottom) CeO_2 's thermogravimetric curve at 800°C ^[5]. The bold red arrows in (b-Top and Bottom) are the conceptual paths of the reaction.

Figure 4-4 (b) describes the same story in a different way. The relations between ψ and $P_{O_2,f}$ for CeO_2 reduced by different temperatures are shown on the top plot. The water splitting reaction proceeding can be considered as the movement of the point C toward the point A along the thermogravimetric curve of T_{WS} , as shown with the bottom plot. In Figure 4-4, the water splitting temperature is fixed. Hence, the relations between $K_{H_2O}(T_{ws})$, $P_{O_2,f}$, and ψ are also settled. Therefore, as long as the water splitting reaction is conducted at the same temperature, the changes of ψ with $P_{O_2,f}$ should be the same, and the different T_{TR} only changes the initial partial pressure ($P_{O_2,f,initial}$). This explains why the curves with different T_{TR} shown in Figure 4-4 (b-Top) overlap.

We now consider the impact of changing T_{WS} with the case shown in Figure 4-5. In this case, the reduction temperature is fixed at 1400 °C and the water splitting reactions are calculated at five different temperatures. Because T_{TR} is fixed, the initial oxygen nonstoichiometry (δ_i) values are all the same (fixed at $\delta_i=0.0313$). The oxygen nonstoichiometry changes due to reaction with steam ($\Delta\delta = \delta_i - \delta_f$) vary with T_{WS} (δ_f is determined by T_{WS}). The different curves behaviors in the plot show that the water splitting reactor is more favorable at lower temperature, and a lower T_{WS} gives a higher reaction extent. For example, for 1 mole of defective CeO_2 that is fully reduced at 1400 °C under 10ppm $p(O_2)$, the reaction extents during to achieve $\Delta\delta=0.02$ are 0.999, 0.976, 0.744, 0.267, and 0.057, respectively, for the five values of T_{WS} considered. This decrease in reaction extent is because when quenching from T_{TR} to various T_{WS} at the same oxygen nonstoichiometry ($\delta_{i,max}$, determined by T_{TR}), the lower T_{WS} gives the smaller $P_{O_2,f,initial}$ (higher reaction driving force). Figure 4-5(b) links the changes of ψ with $P_{O_2,f}$ and the thermogravimetric curves of CeO_2 based on the reaction equilibrium assumption. This figure explicitly shows that lowering the water splitting temperature can be considered as a shift in the change of oxygen nonstoichiometry to lower $P_{O_2,f}$ range (higher reaction driving force) and this benefits the water to hydrogen conversion ratio (higher ψ).



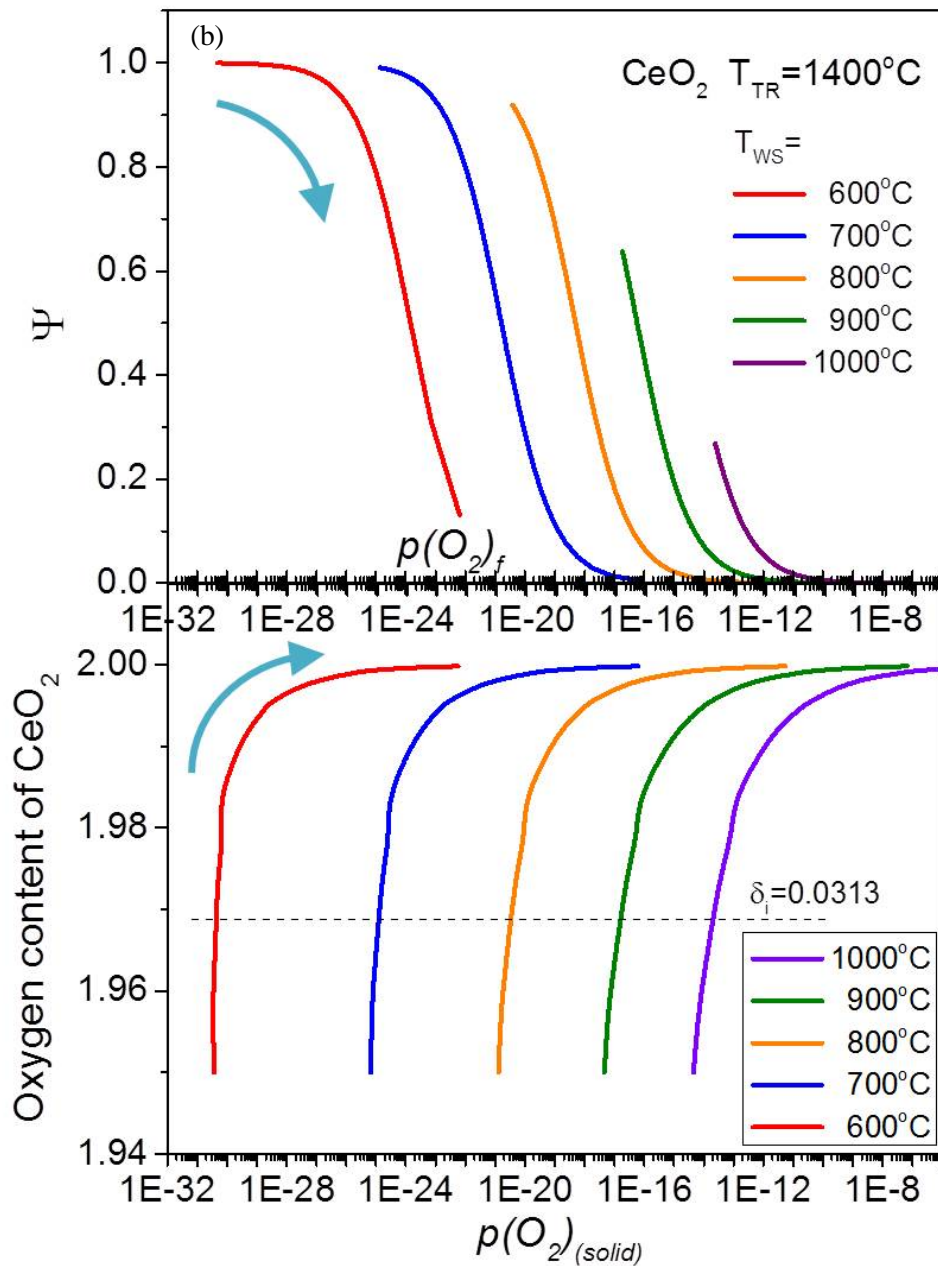


Figure 4-5. Fixed thermal reduction reaction temperature (T_{TR}) reaction extent computed with the redox properties of CeO_2 . Gas conditions are same as those previously mentioned in Figure 4-3. (a) reaction extent and $P_{\text{O}_2,f}$ change with $\Delta\delta$, (b-Top) the $P_{\text{O}_2,f}$ impact on reaction extent, and (b-

Bottom) CeO₂ thermogravimetric curves of the temperatures concerned ^[5]. The bold light blue arrows in (b-Top and Bottom) are the conceptual paths of the reaction.

In summary, increasing T_{TR} and decreasing T_{WS} benefits the water splitting reaction extent. That is, to enlarge the operation temperature window toward both directions boosts the conversion from water to hydrogen. However, within the practical implementations, increasing T_{TR} will bring challenges to the thermostabilities of the oxides. Lowering T_{WS} can improve ψ only when the reaction equilibrium is satisfied. Figure 4-6 shows the water splitting cycling with La_{0.8}Sr_{0.2}MnO_{3- δ} reduced under the same conditions. We can consider the hydrogen production flux as the reaction extent (water to hydrogen conversion ratio) within a unit time interval. Therefore, the high hydrogen production flux implies a large ψ . In Figure 4-6, the hydrogen production flux increases with T_{WS} decreasing from 1000 °C to 800 °C and this can be explained with the mechanism mentioned above. However, the hydrogen evolution peaks show the lower initial peak heights and sluggish decay profiles for the reactions performed at T_{WS} lower than 800 °C, even though the operation temperature windows are broader. The slow surface kinetics (k_s) could be one of the reasons for this discrepancy. The reaction may be limited by the large surface reaction barrier and could not reach equilibrium.

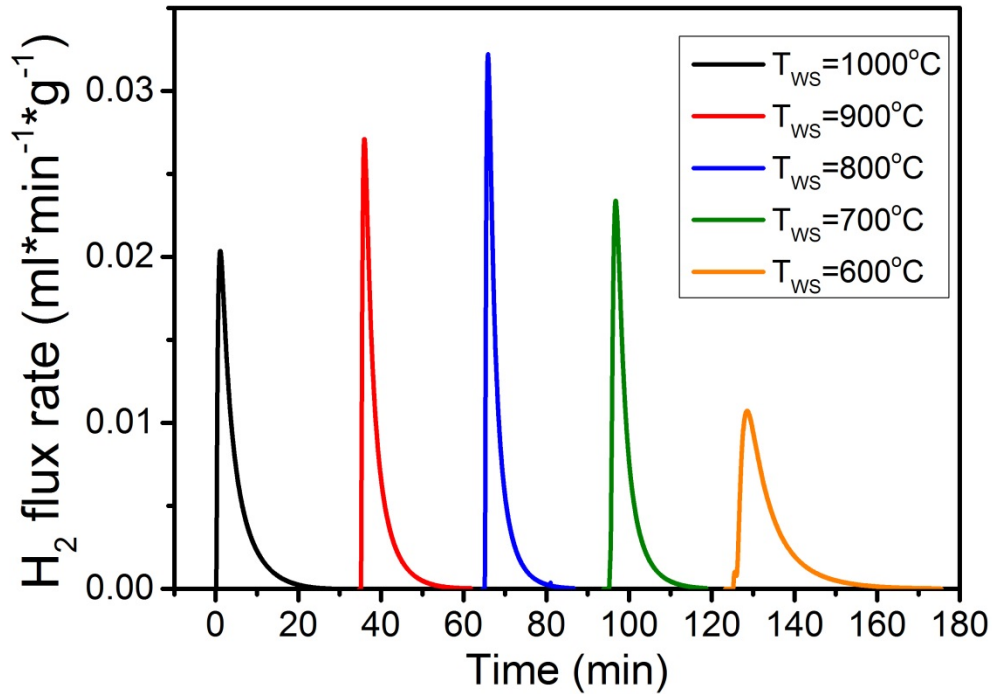


Figure 4-6. Water splitting reactions with $\text{La}_{0.8}\text{Sr}_{0.2}\text{MnO}_{3-\delta}$ conducted at different temperatures. For all cases, $\text{La}_{0.8}\text{Sr}_{0.2}\text{MnO}_{3-\delta}$ was thermally reduced at 1400°C under $p(\text{O}_2)=10\text{ppm}$. For all reoxidization reaction, 20% steam was used.

4.4 Materials-Related Impacts on Reaction Extent

Focusing on Equation 4.12 again, under the assumption of reaction equilibrium, the gas phase oxygen partial pressure, $P_{\text{O}_2,f}$, is synchronized with the chemical potential corresponding oxygen partial pressure of the reactive oxide, $P_{\text{O}_2,solid}$ (the oxygen partial pressure shown on the thermogravimetric curves). Therefore, $P_{\text{O}_2,f}$ in the equation is the only materials-related factor which controls the water splitting reaction extent (ψ). Figure 4-7 shows a comparison of the reaction extent with three different reactive oxides, $\text{CeO}_{2-\delta}$, $\text{La}_{0.7}\text{Sr}_{0.3}\text{MnO}_{3-\delta}$, and $\text{La}_{0.6}\text{Sr}_{0.4}\text{MnO}_{3-\delta}$. As mentioned above, when T_{ws} is fixed, $K_{\text{H}_2\text{O}}(T_{ws})$ is decided and how ψ change with $P_{\text{O}_2,f}$ (as well as

$P_{O_2, \text{solid}}$, when equilibrium) is settled. The top plot shows a very similar impact of T_{TR} as in Figure 4.4. Figure 4.4 shows that, when T_{WS} is fixed, varying T_{TR} means changing $P_{O_2, f, \text{initial}}$ (oxygen chemical potential of the reaction initially). Since the final equilibrium oxygen partial pressure is fixed and determined by $p(H_2O)$ of the steam, changing $P_{O_2, f, \text{initial}}$ places the reoxidation reaction on a different region of the reaction extent curve.

Similar effects can be found in the top plot of Figure 4.7. Three reactive oxides possess distinct redox natures and have different $P_{O_2, f, \text{initial}}$. From the results we can see that for $CeO_{2-\delta}$, most reoxidation reactions proceed with high reaction extent. On the contrary, the ψ values of $La_{0.7}Sr_{0.3}MnO_{3-\delta}$, and $La_{0.6}Sr_{0.4}MnO_{3-\delta}$ are lower than 3% and 2% among the water splitting reactions, respectively. Examining the corresponding thermogravimetric curves shown with the bottom plot, we find that even through both lanthanum strontium manganites give 2 to 3 times fuel productivity (after full reoxidation) as compared to $CeO_{2-\delta}$, their low steam to hydrogen conversion ratio has to be compensated by a larger amount of water in order to complete reoxidation.

The larger reaction extent of $La_{0.7}Sr_{0.3}MnO_{3-\delta}$ as compared to that of $La_{0.6}Sr_{0.4}MnO_{3-\delta}$ suggests $La_{0.7}Sr_{0.3}MnO_{3-\delta}$ has a higher activity for water splitting reaction under such cycling conditions. This also supports the impacts of the Sr content on the hydrogen production kinetics mentioned in Chapter 3: the higher Sr content, the slower hydrogen evolution. To consider the practical experimental settings, the reaction which proceeds under lower ψ will generate less hydrogen within the unit time interval since the steam flow rate is fixed for all measurements. Again, this viewpoint holds only when the reaction equilibrium is reached; otherwise, the impacts from surface reaction energy barrier need to be considered.

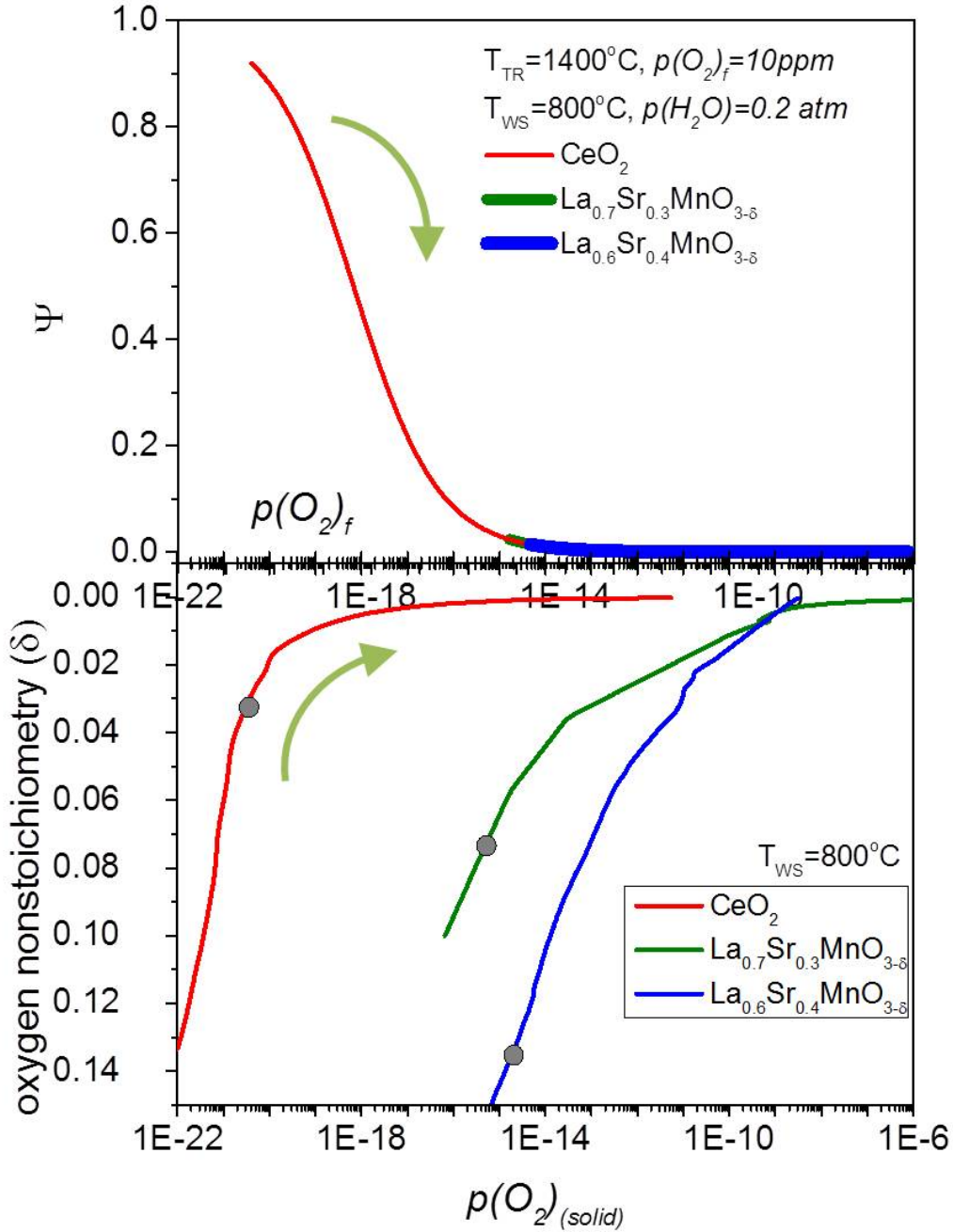


Figure 4-7. (Top) Reaction extent of CeO_2 ^[5], $La_{0.7}Sr_{0.3}Mn_{3-\delta}$, and $La_{0.6}Sr_{0.4}Mn_{3-\delta}$ ^[6] tested under the same cycling conditions shown on the plot. (Bottom) The corresponding thermogravimetric curves of three considered oxides. The grey spots indicate the oxygen nonstoichiometry right after the thermal reduction reaction was completed.

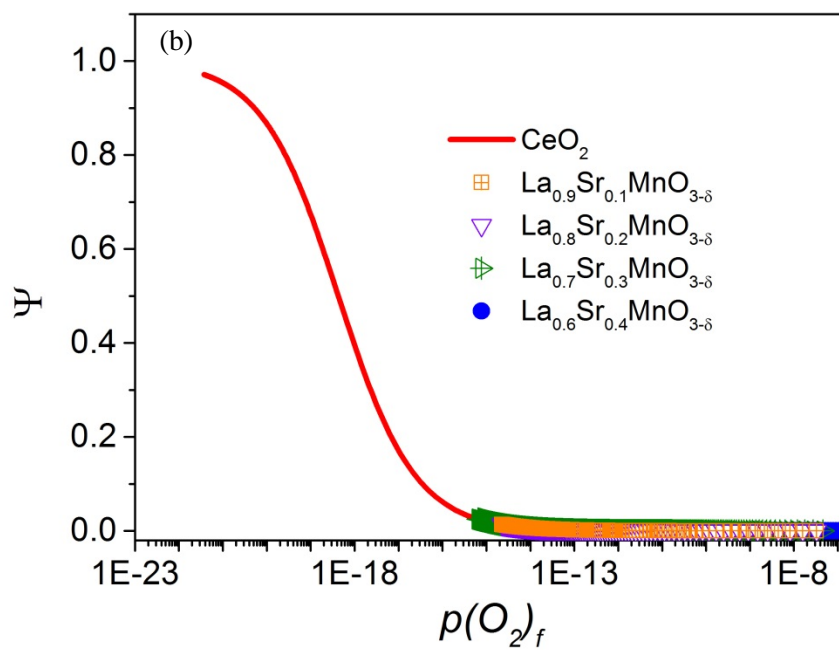
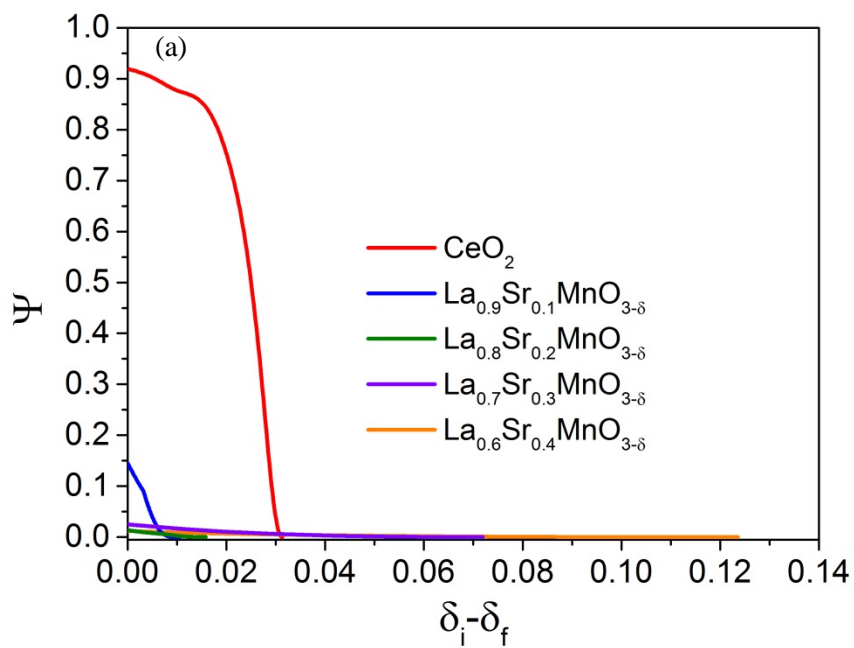


Figure 4-8. Comparisons of (a) reaction extent change with oxygen nonstoichiometry and (b) with

$P_{\text{O}_2, \text{solid}}$ [5-6].

Reaction extent calculation is applied to the strontium-doped lanthanum manganite tested for thermochemical cycling in this study and the results are shown in Figure 4-8. Like Figure 4-4 (a), the ψ values of different locate along the same “path” of the evolution of ψ with $P_{O_2,f}$ since this path is governed by Equation 4.12 and changes with reaction temperature. The $\text{La}_{0.8}\text{Sr}_{0.2}\text{MnO}_{3-\delta}$ curve calculated with Kuo’s TGA data^[7] looks jagged and it is due to the limited resolution for extrapolation within low oxygen nonstoichiometry range (shown in Figure 3-5(c)). As compared to ψ of $\text{CeO}_{2-\delta}$, all $\text{La}_{1-x}\text{Sr}_x\text{MnO}_{3-\delta}$ ($x = 0.1, 0.2, 0.3,$ and 0.4) oxides possess lower ψ among the reoxidization. Also, the Sr content helps the fuel productivity (higher $\Delta\delta$) but lowers the steam-to-hydrogen conversion ratio.

The impacts from the low steam-to-hydrogen conversion ratio are to be discussed. From Equations 4.1, 4.2, 4.5 and 4.9 derived from mass conservation principle; we can arrange it and obtain the relation:

$$n_{Total,f} = n_{O_2,f} + n_{H_2O,f} + n_{H_2,f} = \left(1 + \frac{\psi}{2}\right)n_{H_2O,i} - \frac{1}{2}(\delta_i - \delta_f)n_{oxide} \quad (4.14)$$

The total oxygen release amount for n moles of oxide is $(\delta_i - \delta_f)n_{oxide}$ can be expressed as

$$\begin{aligned} (\delta_i - \delta_f)n_{oxide} &= \psi n_{H_2O,i} - 2n_{O_2,f} = \psi n_{H_2O,i} - 2\left(\frac{P_{O_2,f}}{P_{sys}}\right)n_{Total,f} \\ &= \psi n_{H_2O,i} - 2P_{O_2,f} \left(\left(1 + \frac{\psi}{2}\right)n_{H_2O,i} - \frac{1}{2}(\delta_i - \delta_f)n_{oxide} + n_{Ar,i=f} \right) \end{aligned} \quad (4.15)$$

$$\text{where } x_{O_2,f} = \frac{P_{O_2,f}}{P_{sys}} \text{ and } n_{O_2,f} = x_{O_2,f}n_{Total,f} = \left(\frac{P_{O_2,f}}{P_{sys}}\right)n_{Total,f}$$

Rearranging Equation 4.15, we get

$$(\delta_i - \delta_f)n_{oxide}(1 - P_{O_2,f}) = \psi n_{H_2O,i}(1 - P_{O_2,f}) - 2\left(\frac{P_{O_2,f}}{P_{sys}}\right)(n_{H_2O,i} + n_{Ar,i=f}) \quad (4.16)$$

Finally, the evolution of oxygen nonstoichiometry among the reoxidization can be described as

$$\begin{aligned}
(\delta_i - \delta_f) &= \frac{\psi n_{H_2O,i}}{n_{oxide}} - \frac{2 \left(\frac{P_{O_2,f}}{P_{sys}} \right) (n_{H_2O,i} + n_{Ar,i=f})}{n_{oxide} \left[1 - \left(\frac{P_{O_2,f}}{P_{sys}} \right) \right]} = \frac{\psi \left(\frac{P_{H_2O,i}}{P_{sys}} \right) F}{n_{oxide}} - \frac{2 \left(\frac{P_{O_2,f}}{P_{sys}} \right) F}{n_{oxide} \left[1 - \left(\frac{P_{O_2,f}}{P_{sys}} \right) \right]} \\
&= \frac{F}{n_{oxide}} \left[\psi \left(\frac{P_{H_2O,i}}{P_{sys}} \right) - \frac{2 \left(\frac{P_{O_2,f}}{P_{sys}} \right)}{\left[1 - \left(\frac{P_{O_2,f}}{P_{sys}} \right) \right]} \right]
\end{aligned} \tag{4.17}$$

If the amount of Ar flowed into the water bottle is F (mole), then we have $n_{H_2O,i} = F \left(\frac{P_{H_2O,i}}{P_{sys}} \right)$ and

$n_{Ar,i=f} = F \left[1 - \left(\frac{P_{H_2O,i}}{P_{sys}} \right) \right]$, where $\left(\frac{P_{H_2O,i}}{P_{sys}} \right)$ is the saturated water partial pressure controlled by the

water bottle temperature.

In Equation 4.17, n_{oxide} and δ_i are constants after the thermal reduction reaction is completed, and others variables are linked to each other closely. As shown with Equation 4.12, the reaction extent ψ is a function of $P_{O_2,f}$ and $P_{O_2,f}$ is controlled by the reaction equilibrium of water dissociation with $n_{H_2O,i}$. When part of $n_{H_2O,i}$ is dissociated, the new equilibrium will be created, and $P_{O_2,f}$ will be changed. Simultaneously, ψ will be affected by the new $P_{O_2,f}$, and when ψ varies, the ratio of split $n_{H_2O,i}$ will be different. These interactions among these three parameters will proceed during the reoxidization till the final equilibrium is reached. The conditions of final equilibrium are determined by the water splitting temperature, T_{WS} , and the introduced steam concentration, $p(H_2O)$. For example, with $p(H_2O) = 0.2$ atm at 800 °C, the final equilibrium of water splitting reaction will be attained when $P_{O_2,f} = 1.6 \times 10^{-7}$ atm.

With Equation 4.17, the recursion among $P_{O_2,f}$, ψ , and $n_{H_2O,i}$ from initiation of reoxidization to reaction equilibrium can provide the required water introduced amount for different degree of reoxidization. An estimate of the number of moles of water required to induce a given change in

oxygen content in the oxides studied here is presented in Figure 4-9. The reduction is taken to reach equilibrium under an oxygen partial pressure of 10^{-5} atm and temperature of 1400 °C. This condition fixes the δ_i for each composition. The subsequent oxidation is taken to occur in a closed volume of variable size that allows equilibration between the oxide and the gas phase under an initial condition of 0.2 atm of H₂O partial pressure ($p(O_2) = 1.6 \times 10^{-7}$ atm) and a temperature of 800 °C. The amount of fuel produced corresponds to $\Delta\delta$ and must, on thermodynamic grounds, increase with increasing steam input. The maximum $\Delta\delta$ possible occurs when δ_f reaches the equilibrium non-stoichiometry under $p(O_2) = 1.6 \times 10^{-7}$ atm, a value close to 0, and thus $\Delta\delta_{\max}$ is just less than δ_i .

The results show that the steam requirement for fuel production from strontium-doped lanthanum manganite is rather high. For example, achieving a $\Delta\delta$ of 0.02, which is possible only when x in $\text{La}_{1-x}\text{Sr}_x\text{MnO}_{3-\delta}$ is 0.3 or higher, requires a steam input ranging from about 66 to 93 moles H₂O per mole of oxygen vacancies (per mole of hydrogen production). This steam input requirement in turn implies a steam-to-hydrogen conversion rate of less than 2%. While this calculation corresponds to a worst case scenario and in a real, flowing system the influx of fresh reactant with high oxidizing power will decrease the steam requirement, the results show a clear composition trend. Specifically, the steam requirement increases with Sr content for a given $\Delta\delta$, yet, conversely, as already discussed, the fuel production capacity also increases. The fuel production capacity is alternatively defined with $\Delta\delta_{\max} = \delta_i(T_{\text{TR}}, p(O_2)_{\text{TR}}) - \delta_f(T_{\text{WS}}, p(H_2O)_{\text{WS}})$, where $\delta_i(T_{\text{TR}}, p(O_2)_{\text{TR}})$ represents the oxygen nonstoichiometry change from the thermal reduction performed at T_{TR} under $p(O_2)_{\text{TR}}$; and $\delta_f(T_{\text{WS}}, p(H_2O)_{\text{WS}})$ stands for the oxygen nonstoichiometry change from the reoxidization performed at T_{WS} under $p(H_2O)_{\text{WS}}$. The steam requirement for lanthanum strontium manganite, irrespective of specific composition, is also substantially greater than that when ceria is employed, computed here for comparison. For example, δ_i for ceria is 0.031, and obtaining a $\Delta\delta$ of 0.02 from this material would require introduction of 1.15 moles of H₂O per mole of oxygen vacancies, corresponding to an 86% steam-to-hydrogen conversion ratio.

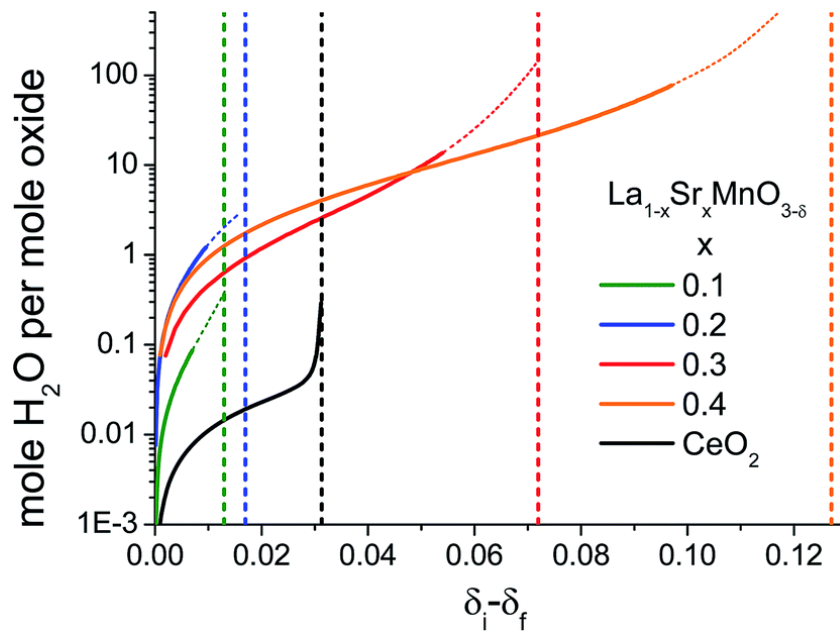


Figure 4-9. Moles of water vapor required to induce the indicated stoichiometry change per mole of oxide at 800 °C using an input gas stream with $p(H_2O) = 0.2$ atm (balance inert), after reduction at 1400 °C under 10 ppm oxygen (balance inert). Results for $La_{1-x}Sr_xMnO_{3-\delta}$ are computed based on the thermogravimetric data reported by Misuzaki *et al.* [6] Behavior is compared to that of $CeO_{2-\delta}$, computed based on the thermodynamic data reported by Panlener *et al.* [5] The computation has large uncertainty due to the absence of data in the raw thermogravimetric plots in the vicinity of $\delta = 0$, therefore, the computed curves within the last 0.5% of $\delta_i - \delta_f$ are calculated with approximation.

In general, the amount of steam required to achieve a target amount of hydrogen production approaches infinity as $\Delta\delta$ approaches $\Delta\delta_{max}$, indicating that efficient fuel production strategies may not be those that attain maximum fuel output per cycle. Instead, cycling that forgoes the final stages of oxidation and hence limits the steam input may be preferable. For example, doubling the fuel output from $La_{0.6}Sr_{0.4}MnO_{3-\delta}$ from a $\Delta\delta$ of 0.05 to 0.1 would require more than an order of magnitude increase in steam input. While it is impossible to achieve such high levels of fuel productivity from ceria (under the specified cycling atmospheres the maximum $\Delta\delta$ is 0.031), one must carefully weigh the tradeoffs between increased fuel production per formula unit of oxide versus the anticipated efficiency penalties of decreased conversion values before concluding which is the superior choice. Scheffe *et al.* recognized the need to operate strontium-doped lanthanum

manganites under high steam input conditions and computed favorable solar-to-fuel conversion efficiencies from these perovskites under the assumption of 100% heat recovery from this large excess of steam ^[7].

From the analysis above, it is evident to see how different redox properties affect the reaction extent and the water amount required for reoxidization. To understand the individual effects from the changes of enthalpy (Δh_o) and entropy (Δs_o) of reduction, we consider hypothetical materials of arbitrary Δh_o and Δs_o , and calculate the resulting ψ and $\Delta\delta$ for a range of cycling conditions. Two examples are shown in Figure 4-10 and 4-11. Impacts from changes in Δh_o are shown in Figure 4-10 taking the Δs_o values of two virtual oxides to be the same as those of $\text{CeO}_{2-\delta}$. Analogously, Figure 4-11 shows the effects due to changes in Δs_o relative to $\text{CeO}_{2-\delta}$. Two things we can learn from this experiment: (1) the oxygen vacancy concentration generated from the thermal reduction reactions can be enhanced by either decreasing Δh_o or increasing Δs_o . (2) Both ways used for improving fuel productivity, however shift the reaction extent toward lower values.

It must be noted that the reaction extent is not the only factor we need to consider within the thermochemical cycling implementation. From the cases discussed above, high conversion ratio gives the less required steam amount but also reduce the fuel production per formula unit of oxide per cycle. Therefore, a figure of merit for determining which oxide is the superior choice for thermochemical cycling by balancing these factors is necessary. The indicator used for weighing the tradeoffs between the fuel productivity and other energy demanding factors is solar to fuel efficiency, $\eta_{\text{solar-fuel}}$.

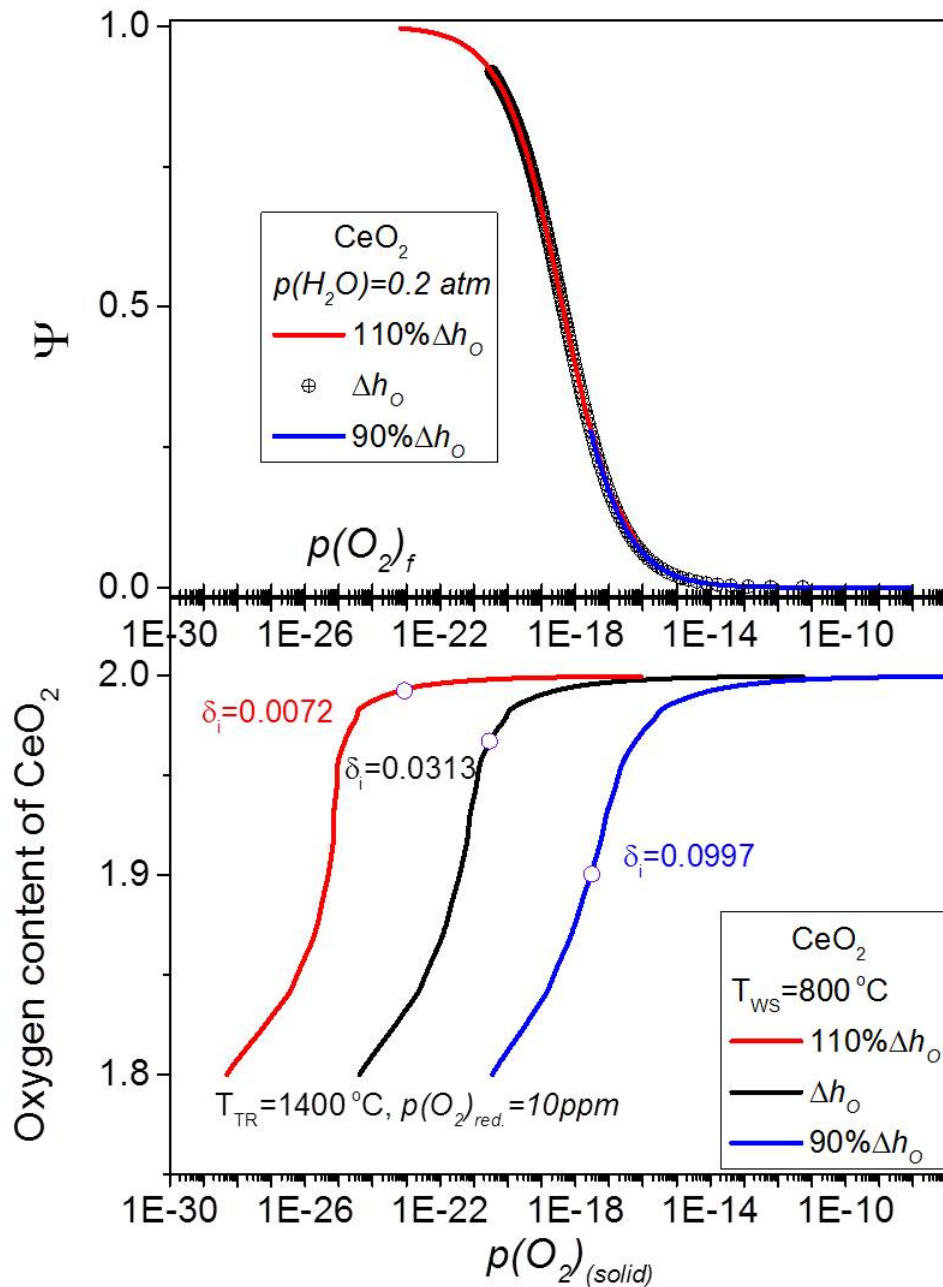


Figure 4-10. Enthalpy of reduction impacts on reaction extent. Two virtual oxides are simulated with 110% and 90% Δh_{O} and same Δs_{O} of $\text{CeO}_{2-\delta}$. δ_i is calculated as the oxygen nonstoichiometry after reduction at 1400°C under 10 ppm oxygen, and the reoxidizations are simulated as the reaction conducted at 800°C using an input gas stream with $p(\text{H}_2\text{O}) = 0.2 \text{ atm}$.

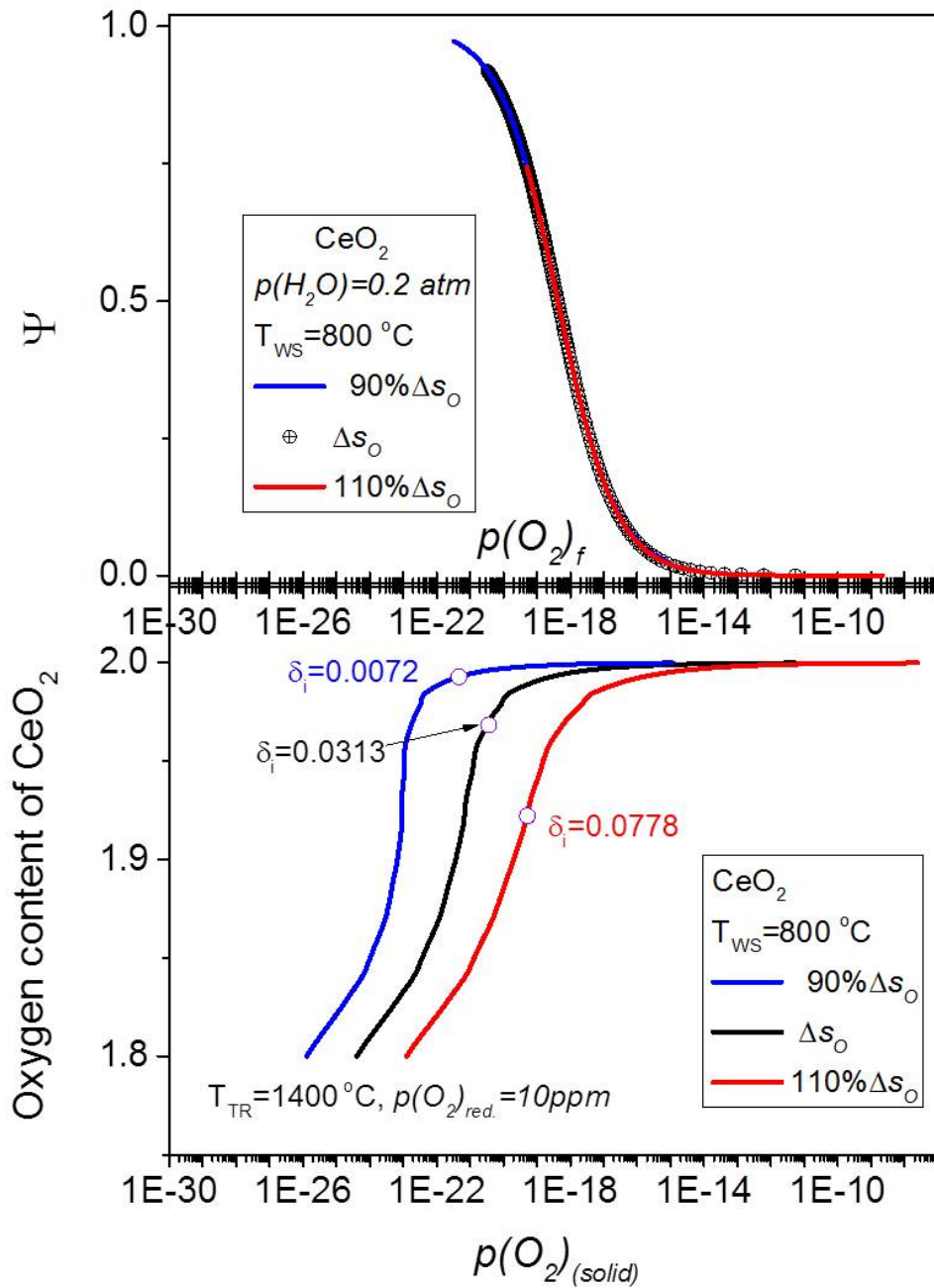


Figure 4-11. Entropy of reduction impacts on reaction extent. Two virtual oxides are simulated with 110% and 90% Δs_O and same Δh_O of $CeO_{2-\delta}$. δ_i is calculated as the oxygen nonstoichiometry after reduction at 1400 °C under 10 ppm oxygen and the reoxidizations are simulated as the reaction conducted at 800 °C using an input gas stream with $p(H_2O) = 0.2 \text{ atm}$.

4.5 Approaches to Designing New Materials from Solar to Fuel Efficiency Aspects

When talking about the figure of merit for materials applied for thermochemical cycling, HHV solar to fuel efficiency ($\eta_{\text{solar-fuel}}$) is often applied^[8]. This methodology of efficiency analysis has been described and applied for $\text{CeO}_{2-\delta}$ in ref. [8]. We first reproduce the $\text{CeO}_{2-\delta}$ results to explain the process then apply the analysis to strontium-doped lanthanum manganite.

The definition of HHV solar to fuel efficiency is

$$\eta_{\text{solar-fuel}} = \frac{HHV_{H_2} n_{H_2}}{Q_{\text{solar}}} \quad (4.18)$$

where HHV_{H_2} is the higher heating value (HHV) of one mole of hydrogen and Q_{solar} represents the sum of required heat inputs. Simply speaking, the term in the numerator stands for energy gain from fuel production and the denominator includes all required energy inputs. Here, the solar to fuel efficiency is mainly defined by materials properties and the factors about reactor design are excluded. Q_{solar} is specifically defined as all heats required to produce one mole of hydrogen and includes three contributions : (1) heat required to heat water from 298 K to T_{WS} , (2) heat required to reduce the reactive oxides from $ABO_{3-\delta_f}$ to $ABO_{3-\delta_i}$ at T_{TR} , and (3) heat required to heat the reactive oxides from T_{WS} to T_{TR} . Together, Q_{solar} can be described as

$$Q_{\text{solar}} = \frac{1}{\eta_{\text{abs}}} \left[nH_2O, i \left(\Delta H_{H_2O(l) \rightarrow (g)}^{298K \rightarrow 373K} + \int_{373K}^{T_{WS}} C_{p, H_2O(g)} dT \right) + \frac{1}{\Delta\delta} \int_{T_{WS}}^{T_{TR}} C_{p, ABO_3} dT + \frac{1}{\Delta\delta} \Delta H_{\text{red}}(T_{TR}) \right] \quad (4.19)$$

where nH_2O, i is the moles of water required for one mole of hydrogen production, $C_{p, j}$ represents the molar heat capacity of species j at constant pressure, and η_{abs} is the absorption efficiency calculated under the blackbody cavity assumption and the cavity is absorbing the radiation flux of $5 \text{ MW}^{-2} \text{ m}$. Equation 4.19 can be alternately described as

$$Q_{\text{solar}} = \frac{1}{\eta_{\text{abs}}} (Q_{\text{water}} + Q_{\text{oxide}}) \quad (4.20)$$

and the heat for the re-radiation loss is defined as

$$Q_{re-radiation} = Q_{solar} - (Q_{water} + Q_{oxide}) = (Q_{water} + Q_{oxide}) \left(\frac{1}{\eta_{abs}} - 1 \right) \quad (4.21)$$

In this calculation, reaction thermodynamic equilibrium is assumed. The first water-related term within the bracket of Q_{solar} is the required heat for water splitting reaction step. The quantities of the other two required heat are closely related to both the thermal reduction and reoxidization steps, since $\Delta\delta$ relies highly on the strategies of cycling operation. The $\Delta\delta$ is noted as the changes of oxygen non-stoichiometry of the reactive oxides, defined as $\delta_i - \delta_f$, and it directly represents the quantity of hydrogen. For the thermal reduction reaction, with the given T_{TR} , the $\delta_{i,max}$ is set. After quenching from T_{TR} to T_{WS} and then introducing steam into the reactor, the oxygen non-stoichiometry value, δ , starts to decrease due to refill of oxygen vacancies generated by thermal reduction. As mentioned above, when reoxidization begins, the reaction extent (ψ) decreases simultaneously. In other words, it is getting more and more difficult to dissociate the introduced steam and it requires more and more water for further reoxidization, as shown in Figure 4-9. Although the full reoxidization ($\Delta\delta = \Delta\delta_{max}$) gives the highest fuel productivity and benefits the efficiency, the high amount of injected steam will decrease the efficiency simultaneously. Furthermore, since $\Delta\delta$ affects $n_{H_2O,i}$ directly, we can say $\Delta\delta$ is greatly related to all three required heat inputs and can be considered as the key role which governs the efficiency. Therefore, utilizing all oxygen vacancies for water splitting might not be advantageous for efficiency optimization and partial reoxidization is necessary for the tradeoff between all required heat inputs.

Here, one new parameter is defined for describing the molar quantity of steam injected into the system at the initiation of the water splitting half-cycle for one mole of hydrogen:

$$r_{H_2O} = \frac{n_{H_2O,i}}{n_{H_2,f}} = \frac{1}{\psi} \approx \frac{n_{H_2O,i}}{n_{oxide} \Delta\delta} \quad (4.22)$$

where the approximation is based on the assumption that $n_{O_2,f}$ is negligibly small. Figure 4-12 takes the $CeO_{2-\delta}$ as the example for demonstrating the impacts from r_{H_2O} on $\eta_{solar-fuel}$. The higher values of r_{H_2O} mean a higher amount of steam is injected. In this case, the δ_f at the highest

efficiency is around 0.002 ($\Delta\delta = 0.0646 - 0.002 = 0.0626$); more water needs to be introduced in order to further utilize the rest of oxygen nonstoichiometry for more fuel production, and accordingly, r_{H_2O} increases. However, this further reoxidization degrades the efficiency. This means that the additional fuel production can't compensate the required energy penalty from the excess injected water. Besides, the r_{H_2O} value which gives the highest efficiency can be considered another indirect indicator of the water to fuel conversion capability of the reactive oxide.

As mentioned, $\eta_{solar-fuel}$ is one of the figures of merit for materials applied for thermochemical cycling and it is related not only to the redox properties of reactive oxides but also to the cycling operation conditions. Therefore, for a given reactive oxide, scanning the operation conditions for targeting the highest efficiency can help to find the optimized operation strategies.

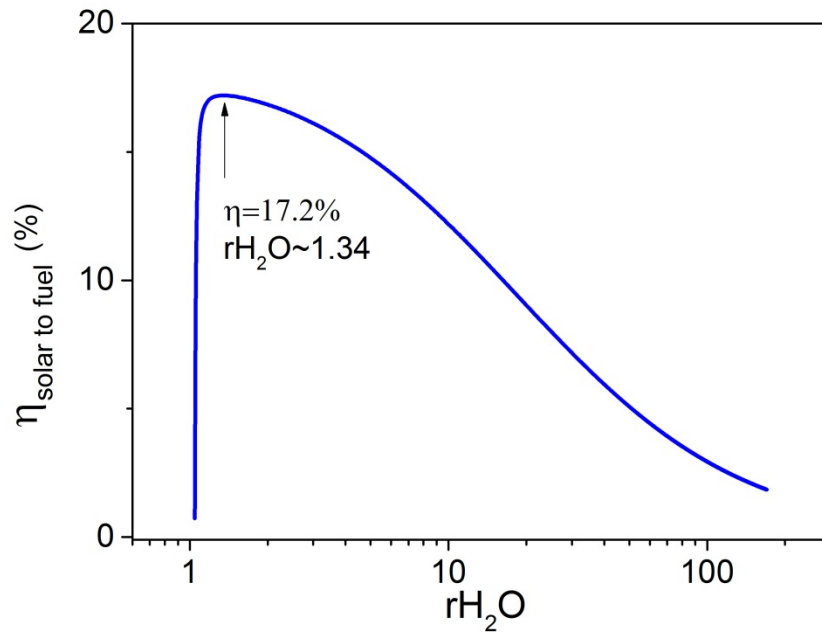


Figure 4-12. Relation between calculated efficiency and r_{H_2O} for $CeO_{2-\delta}$ with the simulated cycling conditions of thermal reduction water splitting reactions performed at $T_{TR}=1500$ °C under $p(O_2)=10$ ppm and $T_{WS}=800$ °C under $p(H_2O)=0.2$ atm, respectively. The maximum available

oxygen nonstoichiometry is $\delta_i=0.0646$. The inputs for calculation are the redox nature of $\text{CeO}_{2-\delta}$ ^[5] and the molar heat capacity of species of water and oxides are from HSC^[4].

The operation conditions screening is performed with three levels optimization. The first level is to look for the optimized $r_{\text{H}_2\text{O}}$ (or δ_i) which shows the highest HHV efficiency with the given T_{TR} and T_{WS} and is demonstrated in Figure 4-12. Then, T_{TR} is fixed in the second level of optimization, and the best reoxidation condition ($r_{\text{H}_2\text{O}}$) is searched for various T_{WS} . Finally, the third level is to repeat the searching loops of previous levels for different T_{TR} .

As example of the second level HHV efficiency optimization is illustrated in Figure 4-13. The same computation shown in Figure 4-12 is repeated for various T_{WS} . The aim is to look for the reoxidation conditions which give the highest efficiency. The peak of the efficiency curve is at 880 °C (± 20 °C) as the water splitting temperature. Therefore, when applying $\text{CeO}_{2-\delta}$ for thermochemical cycling, the cycling temperature windows of $T_{\text{TR}}=1500^\circ\text{C}$ and $T_{\text{WS}}=880^\circ\text{C}$ give the highest efficiency.

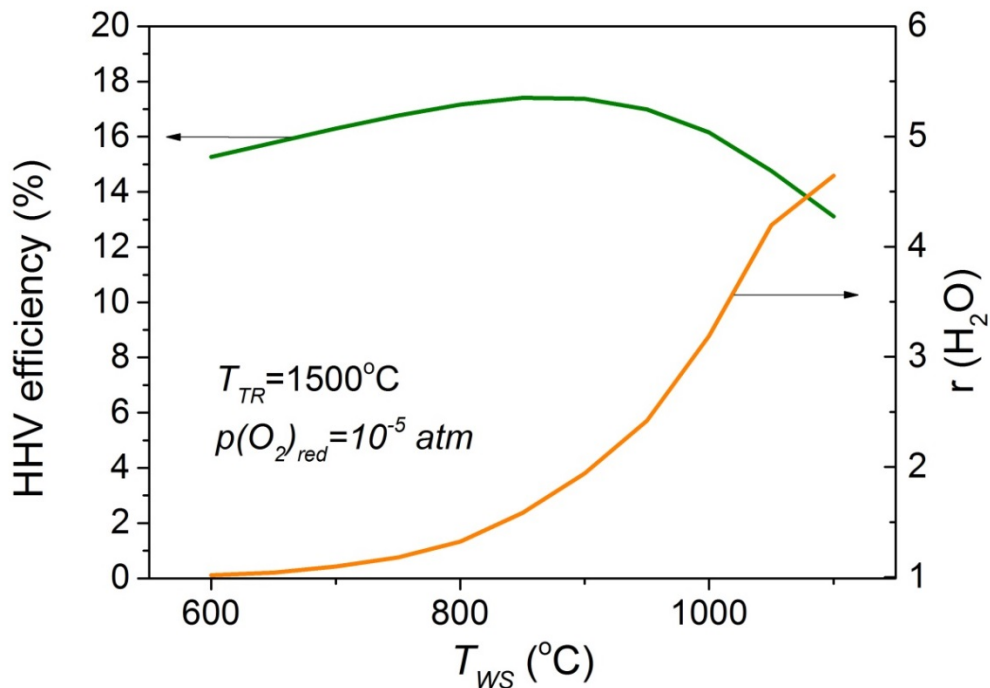


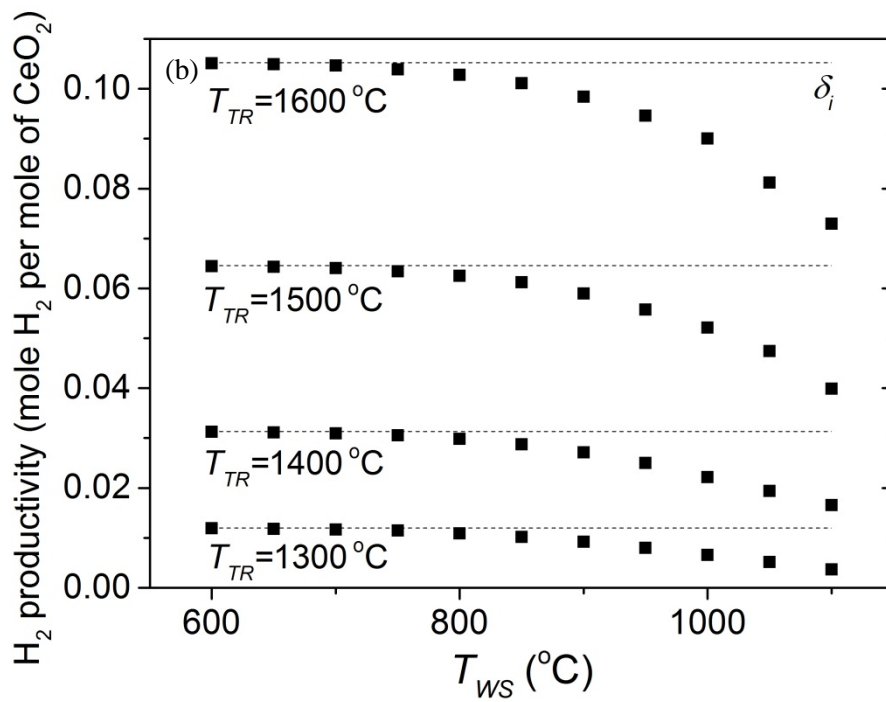
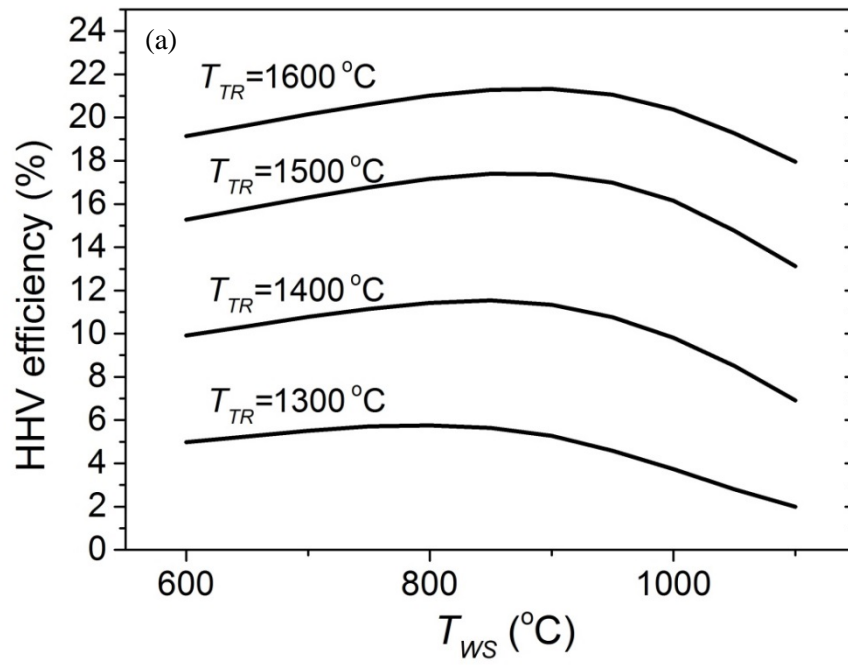
Figure 4-13. Second level HHV efficiency optimization of water splitting cycling with $\text{CeO}_{2-\delta}$. Thermal reduction temperature is fixed (T_{TR}) and the optimized reoxidization conditions which give the highest efficiency are pursued. The calculation temperature step here is 20 °C.

The third level HHV efficiency optimization is to perform the calculations of the earlier levels for various T_{TR} and an example is shown with Figure 4-14. Since all the analysis procedures here follow the method described in ref. [9] and the same TGA data for redox properties extraction are used ^[5], the analyzed results are similar to the results in in ref. [9].

Figure 4-14(a) shows the efficiency as the function of T_{WS} and the higher T_{TR} gives the higher efficiency. With the given T_{WS} , the higher reduction temperature operations contribute to more fuel productivity and less oxide material is needed for producing one mole of fuel. The benefit of lower oxide amount is that less heat is needed for bringing the material to temperature. For every fixed T_{TR} curve, the volcanic shape mainly comes from the energy input for heating oxide ($Q_{oxide_heating} = n_{oxide} \int_{T_{WS}}^{T_{TR}} C_{p,ABO_3} dT$). For the low T_{WS} region, the large temperature window cycling makes the $Q_{oxide_heating}$ large. At the other end when T_{WS} is high, since the optimized $\Delta\delta$ is small and the required oxide amounts (n_{oxide}) are high, the heating oxide required energy inputs are also high.

The square dots in Figure 4-14(b) represent the $\Delta\delta$ ($\delta_i - \delta_f$). The lower T_{WS} gives the higher optimized $\Delta\delta$. This means the utilization of oxygen vacancies for water splitting is more complete. Since the reaction extent (ψ) is low with high water splitting temperature, the complete reoxidization requires huge amounts of energy for heating water. This is because that the injected steam needs to be heated to a higher temperature and the required injected steam amount is very large due to the low ψ .

Figure 4-14(c) and (d) show the best scenario for cycling temperatures in order to get maximum HHV efficiencies. The required heat inputs for the optimized individual processes shown in (d) reveal that thermochemical cycling HHV efficiency is a multi-factors determined target and this analysis gives the optimal tradeoff balance. Further, the efficiency analysis also provides the suggestions for cycling operation and reactor design. For example, the reactor with the improvements of heat recovery can reduce the inputs for heating oxide and water and this will benefit the efficiency, especially for the low reduction temperature case, like $T_{TR} = 1300^\circ\text{C}$ shown in (d).



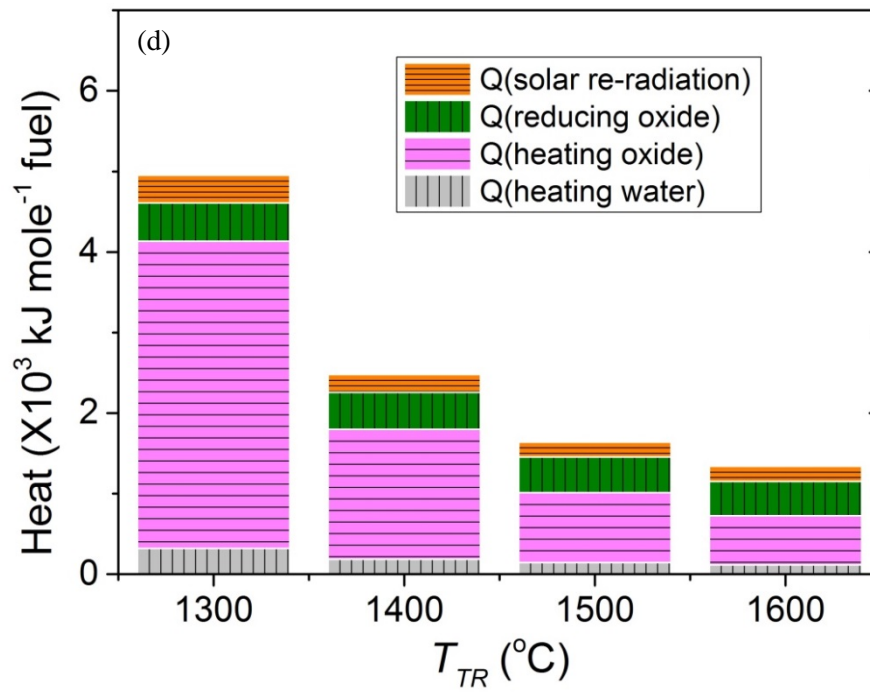
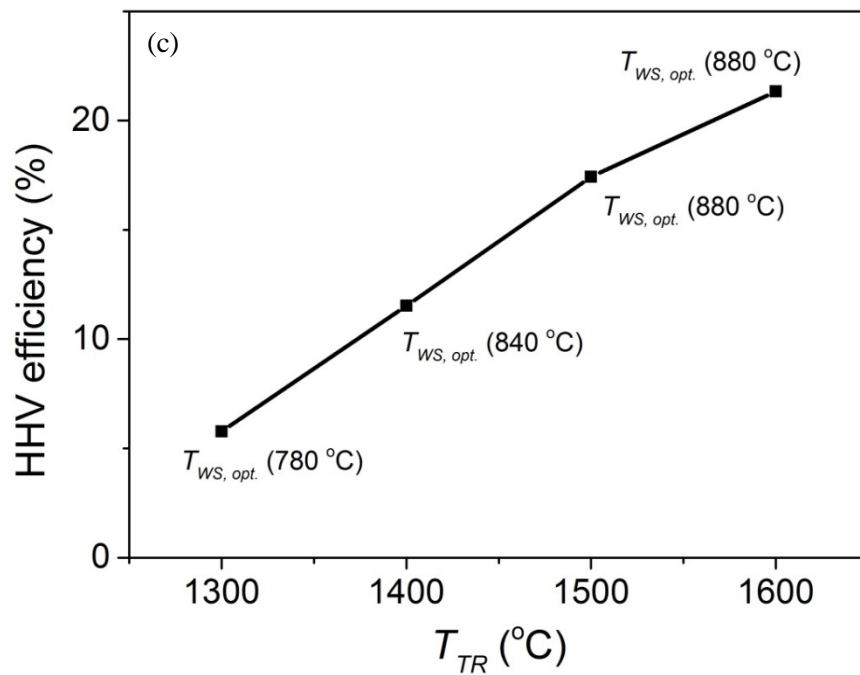


Figure 4-14. Example of third level HHV efficiency optimization for $\text{CeO}_{2-\delta}$. (a) Water splitting temperature optimization for various thermal reduction temperatures. (b) Equilibrium hydrogen productivity expressed as the function of T_{WS} . (c) Maximum HHV efficiency as a function of T_{TR} . (d) Required heat inputs for individual processes of maximum HHV efficiency.

The results of the second level calculation for strontium-doped lanthanum manganite (LSM) are shown in Figure 4-15. The $r_{\text{H}_2\text{O}}$ changes have a similar composition (Sr content) trend as the ψ change shown in Figure 4-8 (b); that is, the higher the ψ is the less injected steam is required. Figure 4-15 (b) shows the optimized oxygen nonstoichiometry change ($\Delta\delta$) of LSM and for all compositions, the utilizations are more complete at low T_{WS} . This is because the reaction extents are higher at lower T_{WS} and the heat penalties from energy for heating water are less. The oxides possess large oxygen nonstoichiometry change within the thermochemical cycling such as $x=0.3$ and 0.4 do not show the highly efficient utilization of $\Delta\delta$ for maximum HHV efficiency due to their low water to fuel conversion ratio (reaction extent, ψ). Even though the ψ of the oxides with $x=0.3$ and 0.4 is low at low T_{WS} regions, the differences in fuel productivities as compared to other higher ψ oxides are increasing. Therefore, the HHV efficiency of $\text{La}_{0.7}\text{Sr}_{0.3}\text{MnO}_{3-\delta}$ and $\text{La}_{0.6}\text{Sr}_{0.4}\text{MnO}_{3-\delta}$ monotonically increases with decreasing of water splitting temperatures because the high fuel productivities are higher. Thus, for the reactive oxides whose redox nature show a low water to fuel conversion ratio, extending the cycling temperature windows to include lower water splitting temperatures is necessary for achieving high HHV efficiency. However, for the practical implementation, the barriers of reaction kinetics when T_{WS} is too low may become a concern (see the case of real measurements shown in Figure 4-6).

Figure 4-16 shows the optimized heat inputs for individual processes of maximum HHV efficiency for all compositions, and the computed settings are applied with the real experimental cycling conditions shown in Chapter 3. For the inputs for heating water, it is mainly governed by their corresponding ψ . Because the $\Delta\delta$ at $T_{WS} = 800^\circ\text{C}$ of $\text{La}_{0.7}\text{Sr}_{0.3}\text{MnO}_{3-\delta}$ and $\text{La}_{0.6}\text{Sr}_{0.4}\text{MnO}_{3-\delta}$ are higher than that of others, their inputs for heating oxides are less due to the lower amount of required moles of oxides to produce the same amount of fuel.

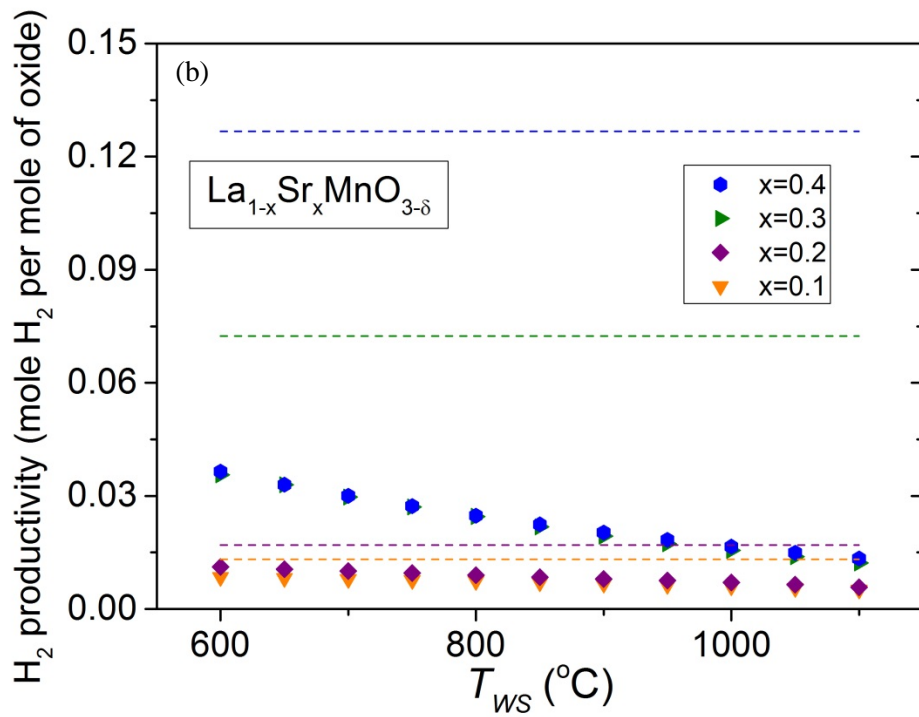
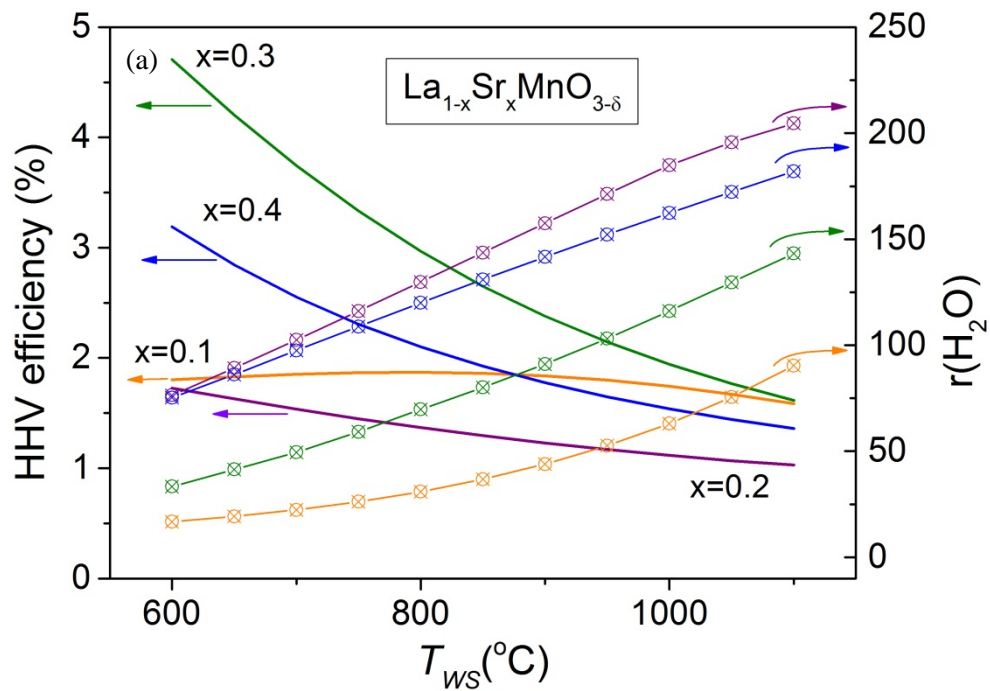


Figure 4-15. (a) Efficiency analysis of $\text{La}_{1-x}\text{Sr}_x\text{MnO}_{3-\delta}$ ($x=0.1, 0.2, 0.3,$ and 0.4) with $1400\text{ }^\circ\text{C}$ as the thermal reduction temperature as the function of water splitting temperature. The atmospheres of thermal reduction and water splitting reactions are $p(\text{O}_2)=10\text{ppm}$ and $p(\text{H}_2\text{O}) = 0.2\text{ atm}$, respectively. The redox natures of oxides are from reference 6 and 7. The solids lines represent the HHV efficiency and the empty cross dots with the corresponding colors represent their $r_{\text{H}_2\text{O}}$. (b) Equilibrium hydrogen productivity expressed as the function of T_{WS} .

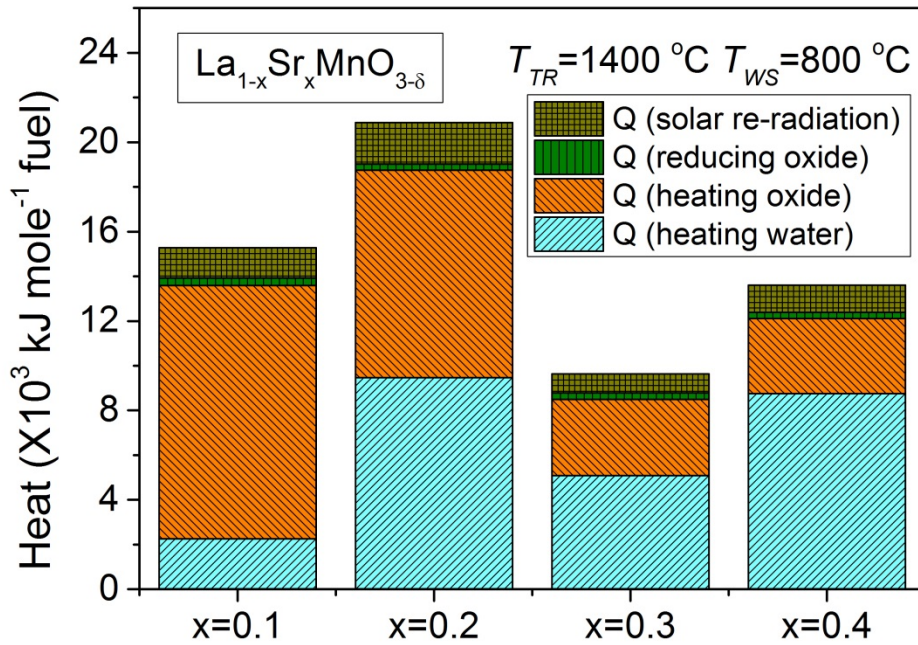


Figure 4-16. Required heat inputs for individual processes of maximum HHV efficiency. Thermochemical cycling conditions are the same as the experimental measurements shown in Chapter 3 ($T_{\text{TR}}=1400\text{ }^\circ\text{C}$, $p(\text{O}_2)_{\text{red}}=10\text{ppm}$, $T_{\text{WS}}=800\text{ }^\circ\text{C}$, and $p(\text{H}_2\text{O})_{\text{WS}}=0.2\text{ atm}$).

For all compositions shown in Figure 4-15, their HHV efficiencies are lower than that of $\text{CeO}_{2-\delta}$ under comparable cycling conditions shown in Figure 4-14. The reason is not only due to the lower ψ of LSM which results in a higher amount of required injected water and lower utilization of the

optimized $\Delta\delta$, but also due to the higher molar specific heat. For example, based on the information from the database HSC 5.2^[4], the C_p of CeO_2 and LaMnO_3 at 1400 °C are 80.132 and 144.375 J/mol/K, respectively. Therefore, when using oxides with high heat capacities, the reactor designs for high solid phase heat recovery are more demanding as compared to using oxide with lower heat capacities.

As described above, HHV efficiency provides a guide for designing a reactor for specific reactive oxides in the thermochemical cycling. For example, the large fuel production potential ($\Delta\delta$) of $\text{La}_{0.6}\text{Sr}_{0.4}\text{MnO}_{3-\delta}$ is eclipsed by the large amount of required heat for the introduced steam, as shown in Figure 4-16. Hence an injected steam heat recovery design is expected to improve the operation efficiency. Two different degrees of injected steam heat recovery are considered and expressed with Figure 4-17. It is expected that the HHV efficiency will increase with the improved heat recovery design because more water can be injected as a result of the energy for heating steam being lowered by the heat recovery. Therefore, the optimal $r_{\text{H}_2\text{O}}$ increases with more efficient heat recovery designs. In the plot (b), we can see the growth of the optimized equilibrium hydrogen productivity and this is because more injected water is beneficial for a higher degree of reoxidization.

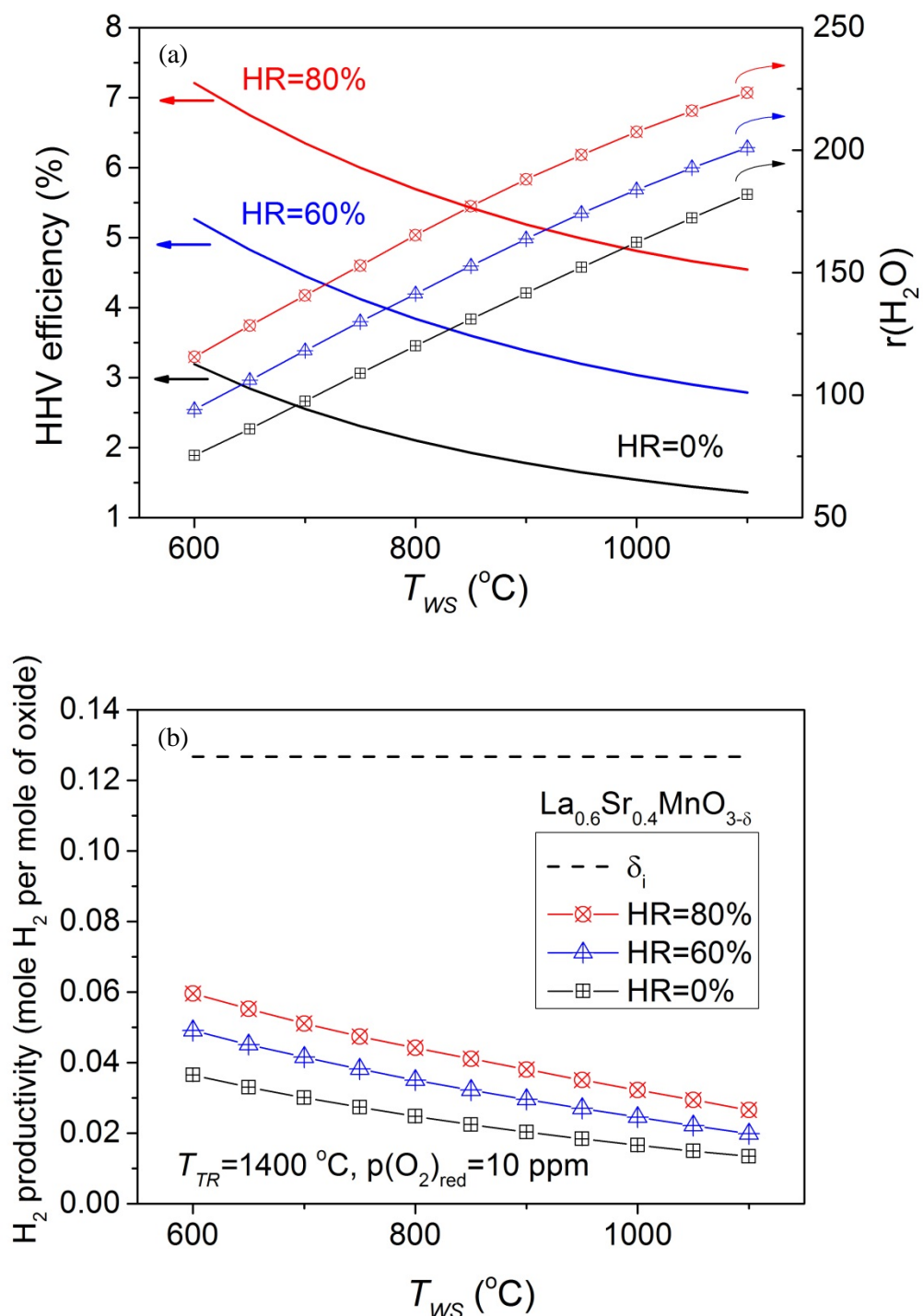


Figure 4-17. HHV efficiency improved by the injected steam heat recovery. (a) Two different degrees of heat recovery (HR) are assumed for the HHV efficiency analysis of $\text{La}_{0.6}\text{Sr}_{0.4}\text{MnO}_{3-\delta}$. (b) The effects of the injected steam heat recovery on the optimized equilibrium hydrogen productivity.

BIBLIOGRAPHY

1. J. R. Scheffe, D. Weibel and A. Steinfeld, *Energy and Fuels*, 2013, 27, 4250-4257.
2. A. H. McDaniel, E. C. Miller, D. Arifin, A. Ambrosini, E. N. Coker, R. O'Hayre, W. C. Chueh and J. H. Tong, *Energy Environ Sci*, 2013, 6, 2424-2428.
3. C. K. Yang, Y. Yamazaki¹, A. Aydin, and S. M. Haile, *Journal of Materials Chemistry A*, 2014, 2, 13612-13623.
4. Antti Roine, O. R. HSC Thermochemistry 5.2.
5. R. J. Panlener, R. N. Blumenthal, J. E. Garnier, *Journal of Physics and Chemistry of Solids*, 1975, 36, 1212-1222.
6. J. Mizusaki, N. Mori, H. Takai, Y. Yonemura, H. Minamiue, H. Tagawa, M. Dokiya, H. Inaba, K. Naraya, T. Sasamoto and T. Hashimoto, *Solid State Ionics*, 2000, 129, 163-177.
7. J. R. Scheffe, D. Weibel and A. Steinfeld, *Energy and Fuels*, 2013, 27, 4250-4257.
8. W. C. Chueh and S. M. Haile, *Philos T R Soc A*, 2010, 368, 3269-3294.

Chapter 5

B SITE DOPING EFFECTS ON THERMOCHEMICAL CYCLING

5.1 Introduction

Strontium (Sr) substituted lanthanum (La) manganese ($\text{La}_{1-x}\text{Sr}_x\text{MnO}_{3-\delta}$, $x=0.1, 0.2, 0.3,$ and 0.4) compounds have been investigated for thermochemical water splitting to determine the effect of A site doping. Strontium (Sr) doping improves fuel productivity, which is consistent with the decrease of reduction reaction enthalpy with increasing Sr contents. Since structure flexibility is one of the beneficial characteristics of perovskites, the impacts from B site cation substitution on the redox natures of reactive oxides attracted our interest.

In the present study, two kinds of cations are substituted for the Manganese (Mn) cation at the perovskites' B site. One is a multi-valence cation and the other is a fixed trivalent cation. When considering the choices, the impacts on thermostability and doping solubility are crucial. For the multi-valent cation, first column transition metals have similar ionic radii to Mn so high doping solubility is expected. Additionally, when considering the thermostability under the harsh reducing operation conditions, Co and Ni are excluded due to their poor thermostability based on the preliminary cycling tests shown in Chapter 3. From the same preliminary measurements, $\text{La}_{0.8}\text{Sr}_{0.2}\text{FeO}_{3-\delta}$ showed the higher fuel productivity from thermochemical cycling than $\text{La}_{0.8}\text{Sr}_{0.2}\text{CrO}_{3-\delta}$, hence, $\text{La}_{0.8}\text{Sr}_{0.2}\text{Mn}_{1-x}\text{Fe}_x\text{O}_{3-\delta}$ will be studied. Regarding the fixed valence selections, Al and Ga are considered because of their close ionic radii. Of these, Al is selected for evaluation due to its high natural abundance, suggesting low cost, and its light atomic mass, suggesting a high mass normalized fuel productivity.

5.2 New Oxides Structure Characterizations

Five different iron concentrations of $\text{La}_{0.8}\text{Sr}_{0.2}\text{Mn}_{1-x}\text{Fe}_x\text{O}_{3-\delta}$ spanning $x=0$ to $x=1$ were studied. Porous samples were made with the solid state reaction method described in Chapter 2, and their crystal structures were identified with X-ray powder diffraction (XRD). The XRD patterns are shown in Figure 5-1, and the analysis results are listed in Table 5-1. All of the as-synthesized

materials are single-phase perovskites of rhombohedral structure ($R\bar{3}c$) indicating complete miscibility between $\text{La}_{0.8}\text{Sr}_{0.2}\text{MnO}_3$ and $\text{La}_{0.8}\text{Sr}_{0.2}\text{FeO}_3$. The unit cell volume increases with Fe doping. However, the ionic radii of Mn and Fe in trivalent state^[1] are very close; this expansion requires more detailed structural studies. (The radii mentioned above are high spin radii. Since the prepared powders are ferromagnetic, the hypothesis of high spin is made. For the low spin radii, Mn is larger than Fe.)

Scanning electron microscopy (SEM) images of $\text{La}_{0.8}\text{Sr}_{0.2}\text{Mn}_{1-x}\text{Fe}_x\text{O}_{3-\delta}$ before and after thermochemical cycling between 800-1400 °C are shown in Figure 5-2. From the low to high Fe content images, it's obvious to see that the grain size increases with increasing Fe content and the grain size is around 2 μm for 0% Fe and 6 μm for 100% Fe. This implies that Fe doping makes $\text{La}_{0.8}\text{Sr}_{0.2}\text{MnO}_{3-\delta}$ less refractory. The porosities of the as-synthesized porous monoliths, Table 5-1, decreased with increasing Fe, but only weakly. After thermochemical cycling between 800-1400 °C, the porosity of all the monoliths decreased slightly.

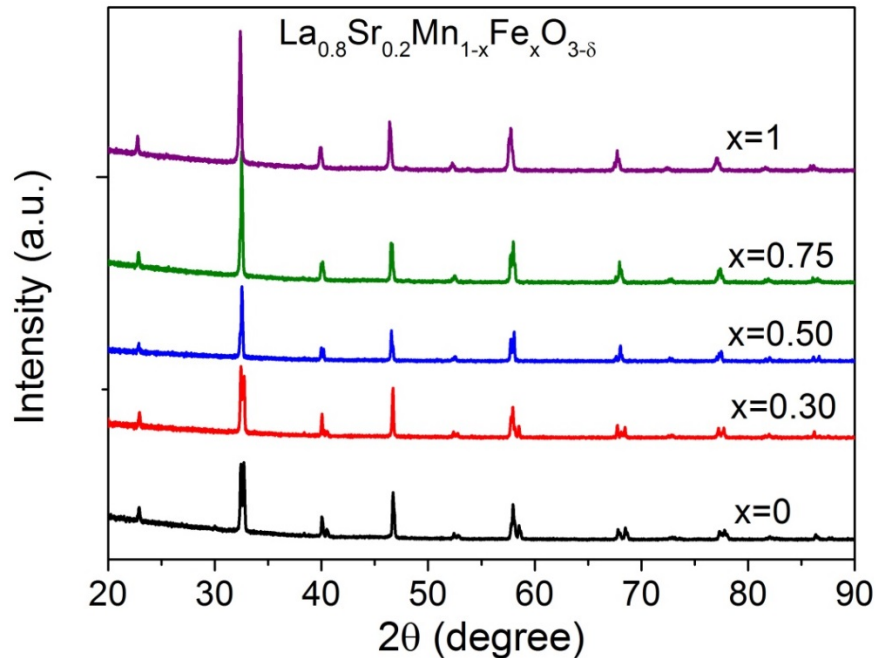


Figure 5-1. X-ray powder diffraction patterns of $\text{La}_{0.8}\text{Sr}_{0.2}\text{Mn}_{1-x}\text{Fe}_x\text{O}_{3-\delta}$ as-synthesized samples. The sintering conditions are 1500°C for 6 hours under air.

Table 5-1. Refined room-temperature structural parameters for $\text{La}_{0.8}\text{Sr}_{0.2}\text{Mn}_{1-x}\text{Fe}_x\text{O}_{3-\delta}$ as-synthesized samples and the porosity of the porous monolith before and after the thermochemical cycle (10 continuous cycles) between 800-1400 °C. The porosities are estimated from a direct measurement of sample dimensions and mass.

[Fe] (x)	a (Å)	b (Å)	c (Å)	Crystal structure (space group)
0	5.5264(1)	5.5264(1)	13.3659(3)	R ($R\bar{3}c$)
0.30	5.5375(1)	5.5375(1)	13.3893(4)	R ($R\bar{3}c$)
0.5	5.5384(2)	5.5384(2)	13.4875(5)	R ($R\bar{3}c$)
0.75	5.5389(2)	5.5389(2)	13.5001(4)	R ($R\bar{3}c$)
1	5.5421(2)	5.5421(2)	13.5269(8)	R ($R\bar{3}c$)

x	Porosity (%) before cycle	Porosity (%) after cycle	Porosity change %
0	58	54	4
0.30	57	45	12
0.5	57	49	8
0.75	48	48	0
1	48	47	1

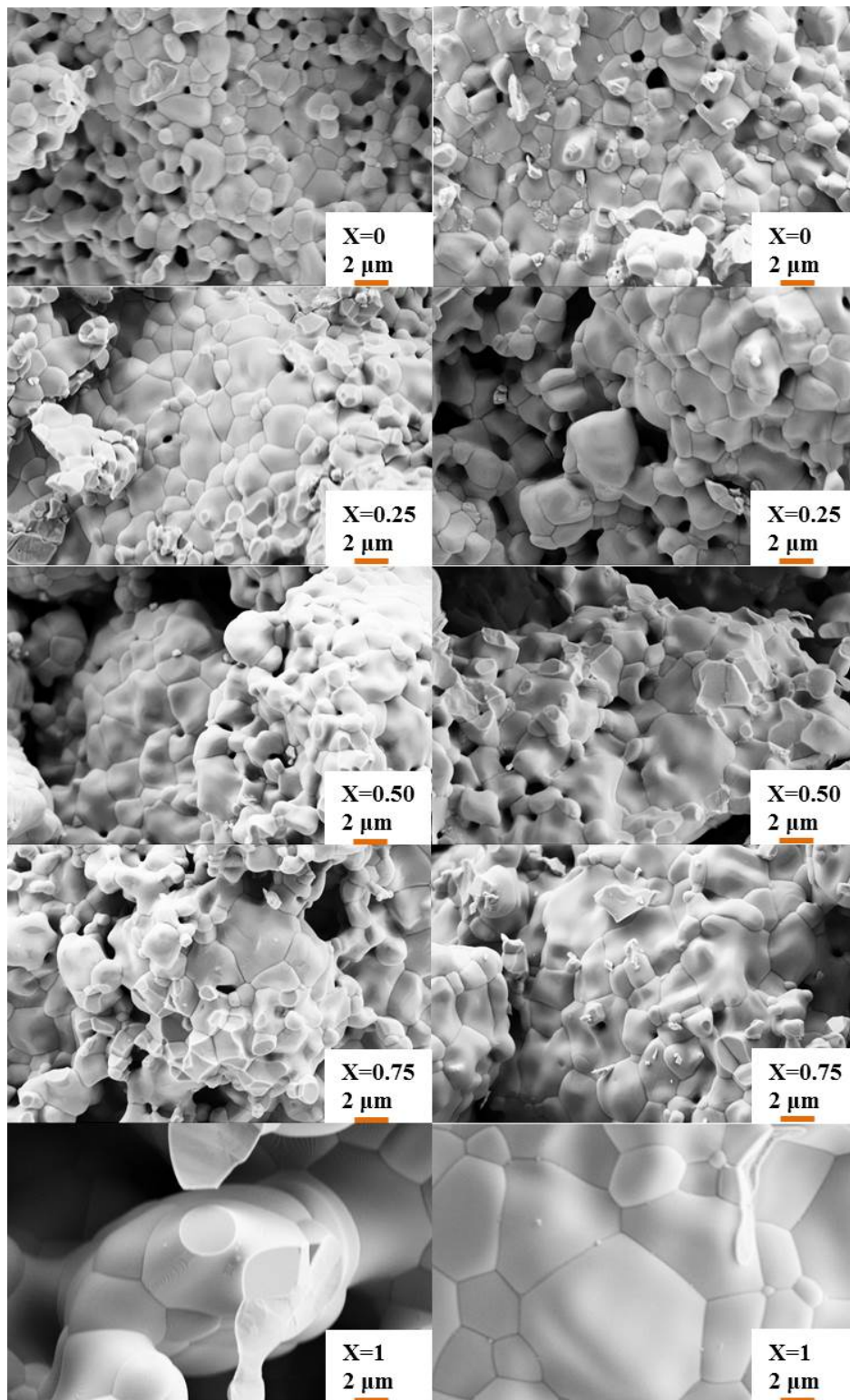


Figure 5-2. Microstructure of $\text{La}_{0.8}\text{Sr}_{0.2}\text{Mn}_{1-x}\text{Fe}_x\text{O}_{3-\delta}$ before (left column) and after (right column) thermochemical cycle (10 continuous cycles) between 800-1400 °C.

The different Al doping concentrations of $\text{La}_{0.8}\text{Sr}_{0.2}\text{Mn}_{1-x}\text{Al}_x\text{O}_{3-\delta}$ porous samples are made with solid state reaction method. The XRD patterns and their analysis results are shown in Figure 5-3 and Table 5-2, respectively. The rhombohedral structure ($R\bar{3}c$) is maintained with the Al doping. Unlike the solid solution of $\text{La}_{0.8}\text{Sr}_{0.2}\text{Mn}_{1-x}\text{Fe}_x\text{O}_{3-\delta}$, Al doping introduces a second phase into $\text{La}_{0.8}\text{Sr}_{0.2}\text{Mn}_{1-x}\text{Al}_x\text{O}_{3-\delta}$ and it is La_2O_3 with hexagonal space group ($P\bar{3}m1$). The sample's second phase content does not show a trend with Al concentration and is less than 3 wt%. The ionic radius of Al (67.5 pm) is much smaller than that of trivalent Mn ions (for high spin, 78.5 pm) and the formation of the additional phase might be due to the octahedra (BO_6) distortion of perovskites from doping. The porosities listed in Table 5-2 were calculated by comparing the theoretical densities and the porous monolith densities. Unlike Fe doping, Al substitution largely increases the porosities and this might be beneficial to the reaction kinetics due to the higher gas flow accessibility.

The microstructure of $\text{La}_{0.8}\text{Sr}_{0.2}\text{Mn}_{1-x}\text{Al}_x\text{O}_{3-\delta}$ as-synthesized porous monoliths was characterized by SEM and is shown in Figure 5-4. The grain size decreases with increasing Al concentration and this reflects that Al doping makes the oxides more refractory. Not only the grain size but also the grain morphology is changed by Al substitution. The shape of the grains evolve from the irregular grain for $x=0\%$ to the rectangular pyramid shape for $x=0.75\%$.

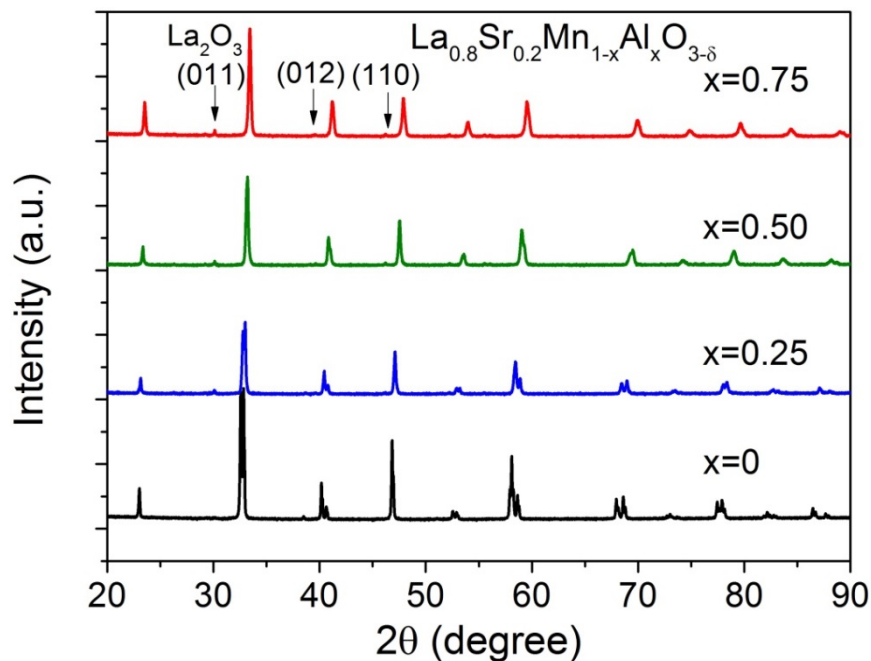


Figure 5-3. X-ray powder diffraction patterns of $\text{La}_{0.8}\text{Sr}_{0.2}\text{Mn}_{1-x}\text{Al}_x\text{O}_{3-\delta}$ as-synthesized samples. The sintering conditions are 1500°C for 6 hours under air.

Table 5-2. Refined room-temperature structural parameters for $\text{La}_{0.8}\text{Sr}_{0.2}\text{Mn}_{1-x}\text{Al}_x\text{O}_{3-\delta}$ as-synthesized samples and the porosity of the porous monolith before and after the thermochemical cycle between 800-1400 °C. The porosities are estimated from a direct measurement of sample dimensions and mass.

x	a (Å)	b (Å)	c (Å)	Crystal structure (space group)	Perovskites (%)	La_2O_3 (%)
0	5.52614(4)	5.52614(4)	13.3698(1)	R ($R\bar{3}c$)	100	0
0.25	5.49014(9)	5.49014(9)	13.3227 (3)	R ($R\bar{3}c$)	97.8(4)	2.2(2)
0.50	5.43590(1)	5.43590(1)	13.2478(4)	R ($R\bar{3}c$)	98.5(3)	1.5(2)
0.75	5.39110(3)	5.39110(3)	13.1930(1)	R ($R\bar{3}c$)	98.7(4)	1.3(1)

x	Porosity (%) before cycle	Porosity (%) after cycle
0	58	54
0.25	71	69
0.50	76	74
0.75	80	79

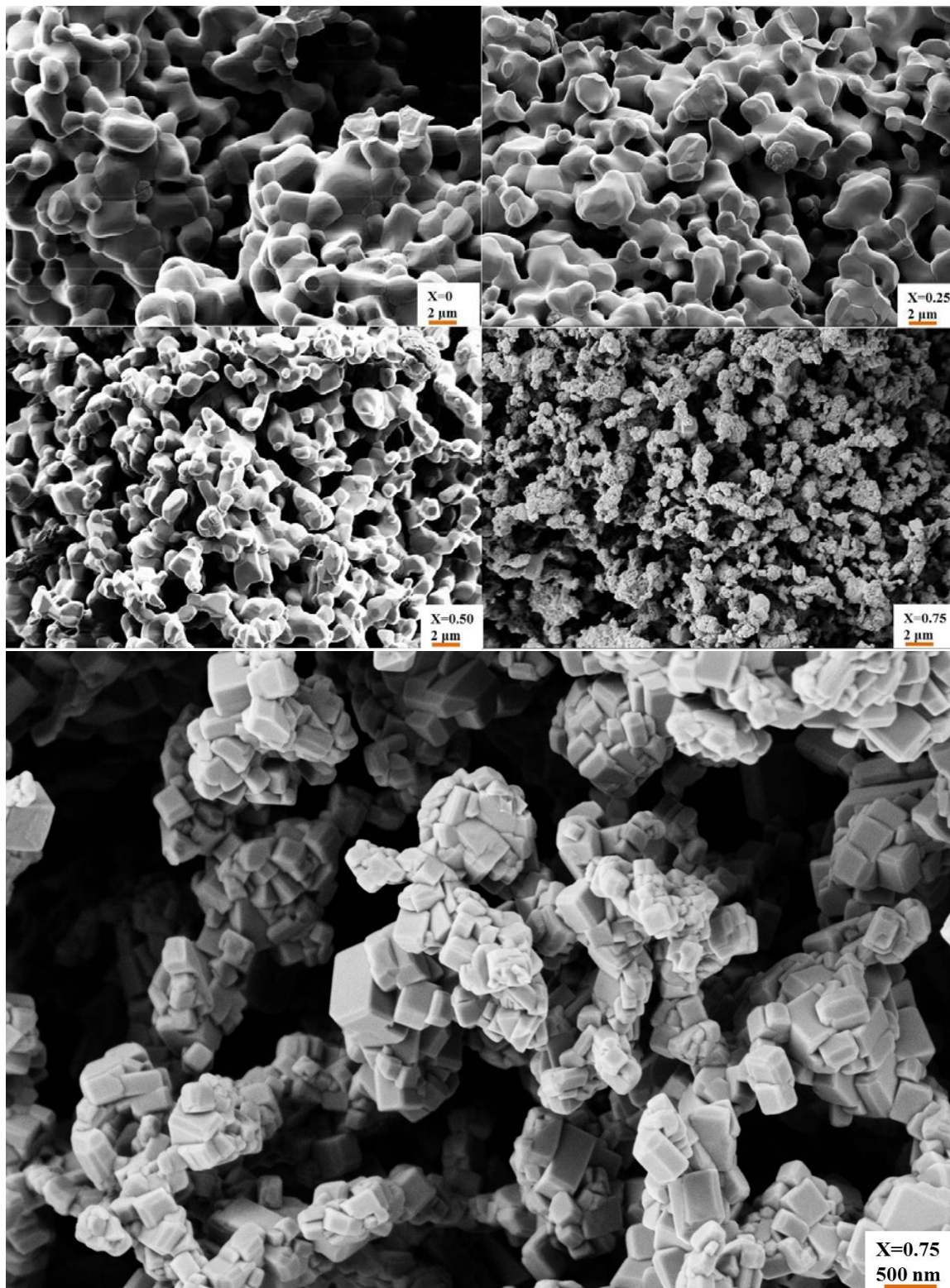


Figure 5-4. Microstructure of $\text{La}_{0.8}\text{Sr}_{0.2}\text{Mn}_{1-x}\text{Al}_x\text{O}_{3-\delta}$ as-synthesized porous monoliths.

5.3 Thermochemical Cycling of $\text{La}_{0.8}\text{Sr}_{0.2}\text{Mn}_{1-x}\text{Fe}_x\text{O}_{3-\delta}$

Thermochemical cycles were carried out with six different iron doping concentrations of $\text{La}_{0.8}\text{Sr}_{0.2}\text{Mn}_{1-x}\text{Fe}_x\text{O}_{3-\delta}$ ($x=0, 0.3, 0.5, 0.75, 0.85, \text{ and } 1$) porous samples. The thermal reduction reactions were conducted at $1400\text{ }^\circ\text{C}$ under flowing 10 ppm oxygen premixed with ultra-high purity (UPH) Ar for 30 minutes. For the subsequent water splitting step, after the oxides were quenched to $800\text{ }^\circ\text{C}$, the UHP Ar gas saturated with purified water at $60\text{ }^\circ\text{C}$ ($p(\text{H}_2\text{O}) = 0.20\text{ atm}$) was injected and the reaction allowed to proceed for 40 minutes. The continuous cycling results for each composition and each step are illustrated in Figure 5-5. Throughout the experiment, the oxygen and hydrogen evolutions are fairly stable. From the cycling results, oxygen release and hydrogen production increase with Fe substitution till $x=0.75$, then decrease with further Fe doping. With 75% Fe substitution, the hydrogen productivity increase from around 3 mlg^{-1} ($x=0$) to 5 mlg^{-1} . After this peak value, the hydrogen productivity decays with increasing Fe content, and the amount of hydrogen produced from $\text{La}_{0.8}\text{Sr}_{0.2}\text{FeO}_{3-\delta}$ is around 0.8 mlg^{-1} .

Figure 5-6 presents the oxygen release and hydrogen production gas evolution profiles of a single cycle of each composition. The initial gas fluxes (peak heights) of both reactions increase with increasing Fe doping till [Fe] equal to 0.75. Recall that we observed a correlation between the initial fuel production fluxes and the initial water splitting driving force (chemical potential) in previous chapters. The different peak profiles reflect the changes in redox natures from Fe substitution. Unlike the case of A site substitutions with Sr ($\text{La}_{1-x}\text{Sr}_x\text{MnO}_{3-\delta}$), the B site substitutions with Fe increase the fuel productivity without introducing a penalty in kinetics. This suggests that Fe doped $\text{La}_{0.8}\text{Sr}_{0.2}\text{MnO}_{3-\delta}$ samples may have high water splitting reaction extents (ψ). Hence, these increases in fuel productivity may not come with a large energy penalty for heating the huge amounts of injected steam. Furthermore, although the microstructure images and porosities show the less gas flow accessibility from the Fe doped samples (larger grain size and lower porosity), the differences of reaction kinetic feature from the microstructures are not obvious (except the sample with $x=1$ which shows large grains, dense microstructure, and lower gas evolution fluxes).

The accessible oxygen non-stoichiometry change ($\Delta\delta$) within the thermochemical cycle can be calculated from the gas generation amounts, and the values for all tested compositions are plotted in Figure 5-7. Ideally, the values computed from the amount of oxygen release and hydrogen production should be same. Therefore, if the blue and the orange dots match together well, this means the measurement errors are small. Good agreement is from the figure, the $\Delta\delta$ calculated

from both kinds of gas generation amounts shows an intermediate maximum at composition with 75% Fe substitution.

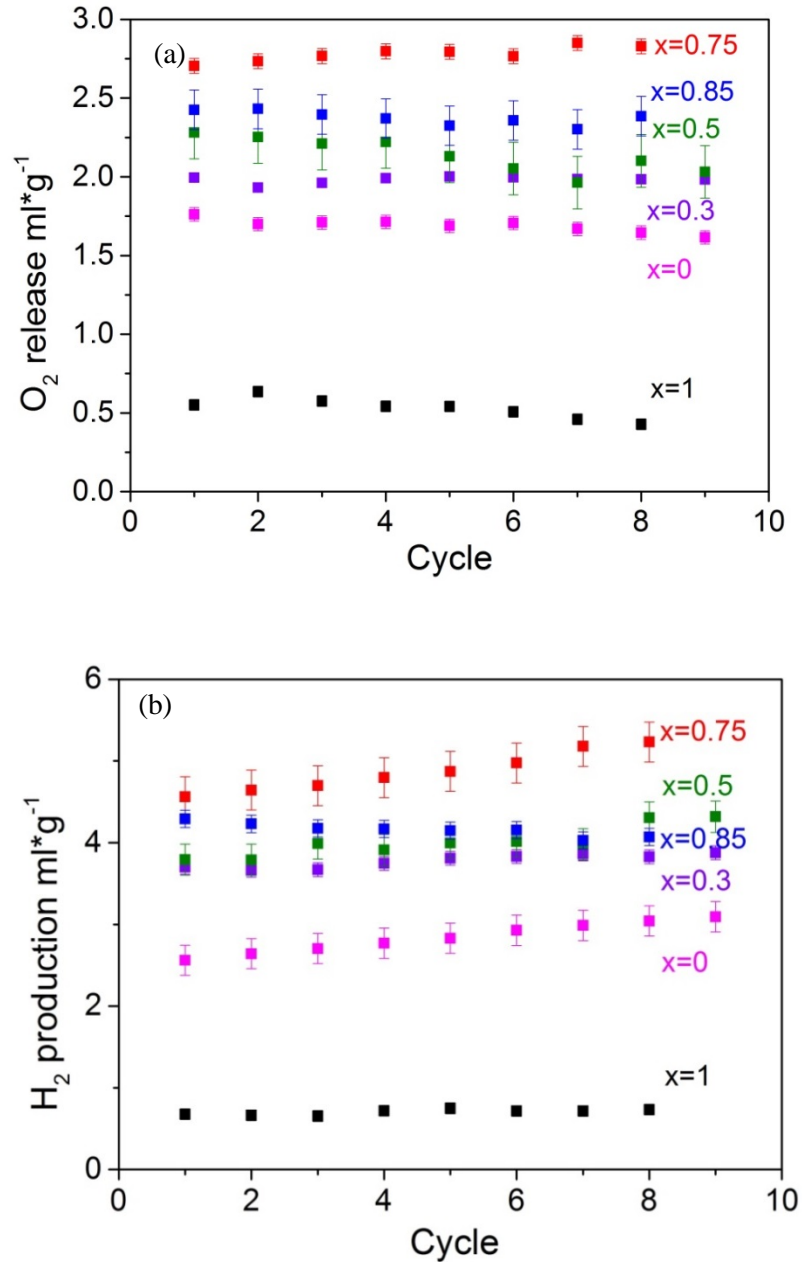


Figure 5-5. Thermochemical cycles between 800-1400 °C performed with $\text{La}_{0.8}\text{Sr}_{0.2}\text{Mn}_{1-x}\text{Fe}_x\text{O}_{3-\delta}$ ($x=0, 0.3, 0.5, 0.75, 0.85,$ and 1) porous samples. (a) Oxygen release amounts per cycle and per

gram of oxide. (b) Hydrogen productivities from water splitting reaction per cycle and per gram of oxide.

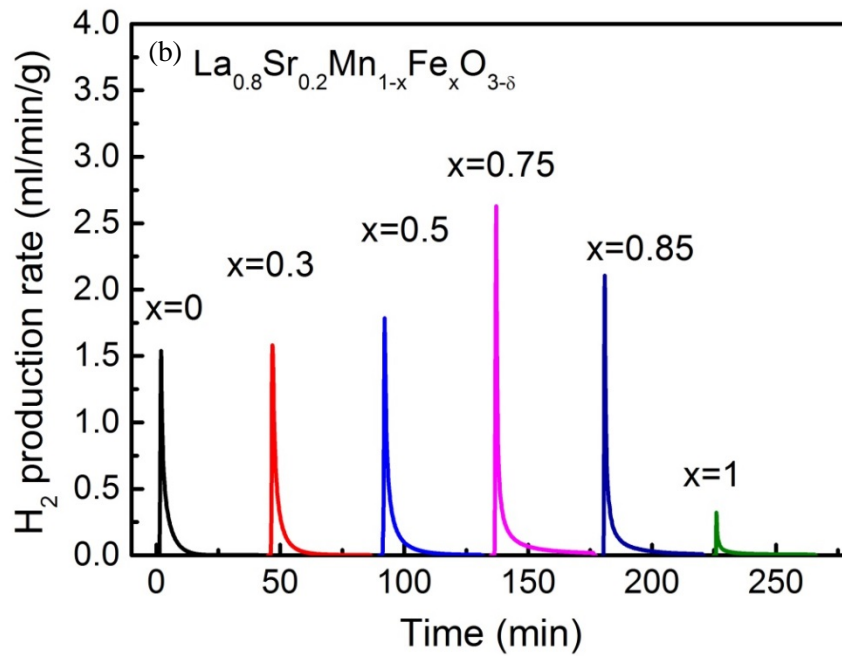
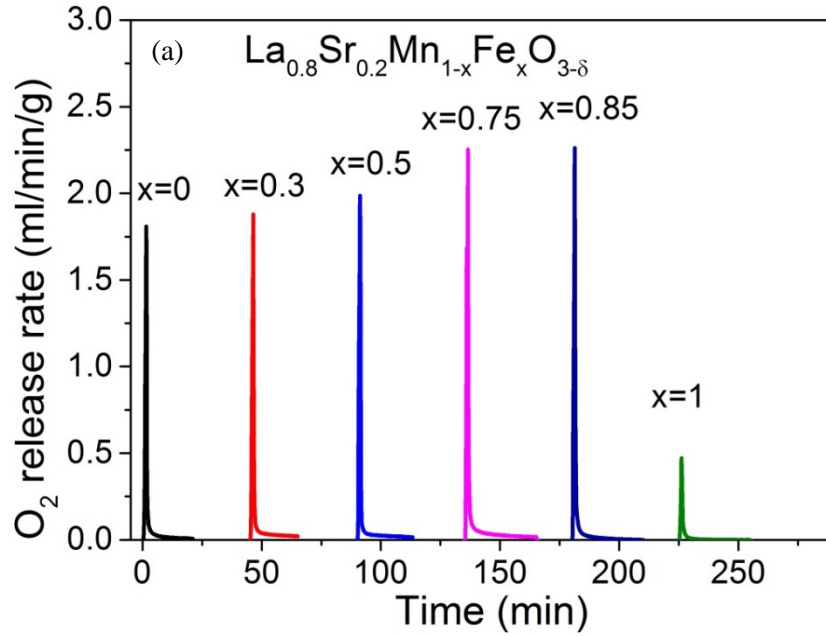


Figure 5-6. 5th thermochemical cycle of $\text{La}_{0.8}\text{Sr}_{0.2}\text{Mn}_{1-x}\text{Fe}_x\text{O}_{3-\delta}$ ($x=0, 0.3, 0.5, 0.75, 0.85,$ and 1) porous samples. (a) Oxygen release ($T_{\text{TR}}=1400$ °C, $p(\text{O}_2)=10^{-5}$ atm) and (b) hydrogen generation profiles ($T_{\text{WS}}=800$ °C, $p(\text{H}_2\text{O})=0.2$ atm) as the function of time.

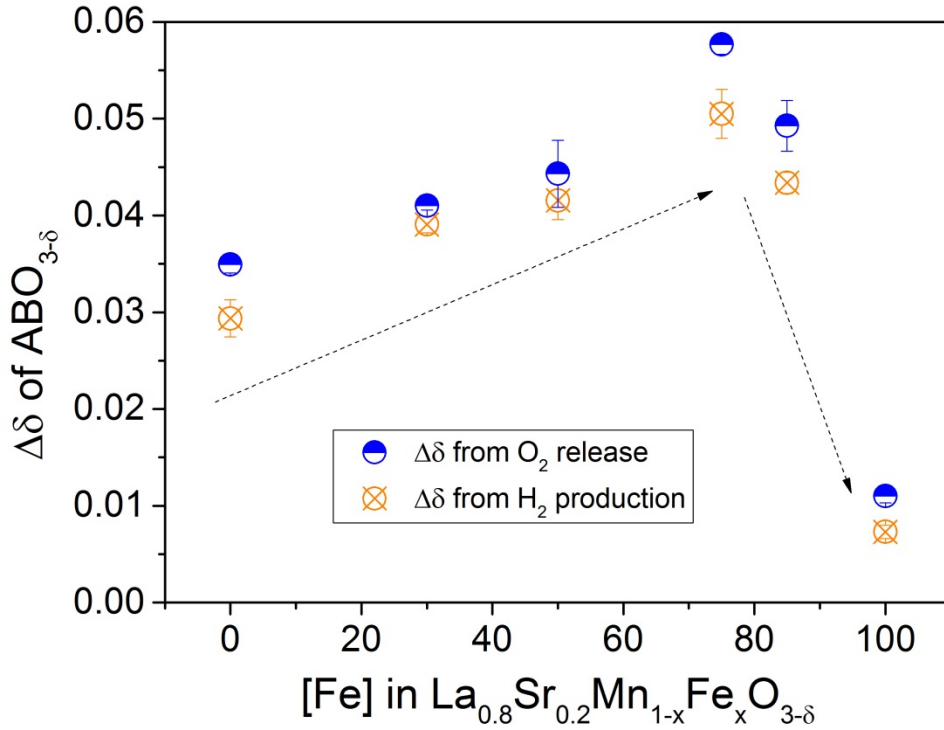


Figure 5-7. Oxygen non-stoichiometry changes within the thermochemical cycle of $\text{La}_{0.8}\text{Sr}_{0.2}\text{Mn}_{1-x}\text{Fe}_x\text{O}_{3-\delta}$ ($x=0, 0.3, 0.5, 0.75, 0.85,$ and 1). The $\Delta\delta$ values are converted from the averages of the oxygen release and hydrogen generation amounts shown in Figure 5-5.

5.4 Fe Substitution Impacts on Redox Natures of $\text{La}_{0.8}\text{Sr}_{0.2}\text{Mn}_{1-x}\text{Fe}_x\text{O}_{3-\delta}$

From the tiny fuel production from $\text{La}_{0.8}\text{Sr}_{0.2}\text{FeO}_{3-\delta}$ shown in Figure 5-5, it seems that it has a lower capacity for water splitting. Unexpectedly, the fuel productivity of $\text{La}_{0.8}\text{Sr}_{0.2}\text{MnO}_{3-\delta}$ is improved by mixing this less capable oxide. Here, we discuss the cause of this improvements introduced by Fe doping from the changes of redox properties resulted from Fe doping. At first, the redox natures of $\text{La}_{0.8}\text{Sr}_{0.2}\text{FeO}_{3-\delta}$ are to be discussed. It's surprising that the high quality redox properties

measurements for $\text{La}_{0.8}\text{Sr}_{0.2}\text{FeO}_{3-\delta}$ can't be found from literature. Fortunately, the careful thermogravimetric measurements of similar compositions, in particular, $\text{La}_{0.75}\text{Sr}_{0.25}\text{FeO}_{3-\delta}$, are available and the results are reprinted in Figure 5-8 (a)^[2]. Like the case of $\text{La}_{1-x}\text{Sr}_x\text{MnO}_{3-\delta}$ shown in Figure 3-2, the oxygen non-stoichiometry of $\text{La}_{1-x}\text{Sr}_x\text{FeO}_{3-\delta}$ as a function of oxygen partial pressure can be divided to three regions. Within the high oxygen partial pressure region, the dominant reduction reaction related defect species is $[\text{Fe}'_{\text{Fe}}]$ (or Fe^{4+}) and it will be reduced to $[\text{Fe}^{\times}_{\text{Fe}}]$ (or Fe^{3+}) when decreasing $p(\text{O}_2)$. As the $p(\text{O}_2)$ is lowered further, a plateau region in which $\frac{\partial\delta}{\partial\log(p(\text{O}_2))}$ is very small is encountered. This occurs when the defect relation $[\text{Fe}'_{\text{Fe}}] = [\text{Fe}^{\times}_{\text{Fe}}]$ (or $[\text{Fe}^{4+}] = [\text{Fe}^{3+}]$) is satisfied. Under very reducing atmospheres, most of the Fe ions are reduced to $[\text{Fe}'_{\text{Fe}}]$ and the $\frac{\partial\delta}{\partial\log(p(\text{O}_2))}$ is very different here as compared to the other two regions^[2].

The reduction enthalpy (Δh_{O}) and entropy (Δs_{O}) of $\text{La}_{0.75}\text{Sr}_{0.25}\text{FeO}_{3-\delta}$ were and shown in Figure 5-8 (b). To consider the same thermochemical cycling conditions applied in the measurements of $\text{La}_{0.8}\text{Sr}_{0.2}\text{Mn}_{1-x}\text{Fe}_x\text{O}_{3-\delta}$ ($T_{\text{TR}}=1400$ °C, $p(\text{O}_2)=10^{-5}$ atm for thermal reduction and $T_{\text{WS}}=800$ °C, $p(\text{H}_2\text{O})=0.2$ atm for water splitting), with the extracted Δh_{O} and Δs_{O} of $\text{La}_{0.75}\text{Sr}_{0.25}\text{FeO}_{3-\delta}$, the $\Delta\delta$ accessible for the thermochemical cycling can be estimated and it is around 0.006. This accessible $\Delta\delta$ is within the third region mentioned above. The changes of oxygen non-stoichiometry, within the first region ($\delta < 0.3$), resulted from the reduction of $[\text{Fe}'_{\text{Fe}}]$ ions, could not be utilized for water splitting due to the small reduction enthalpy (Δh_{O}) and entropy (Δs_{O}) within this δ range (the requirement shown in Equation 1.14).

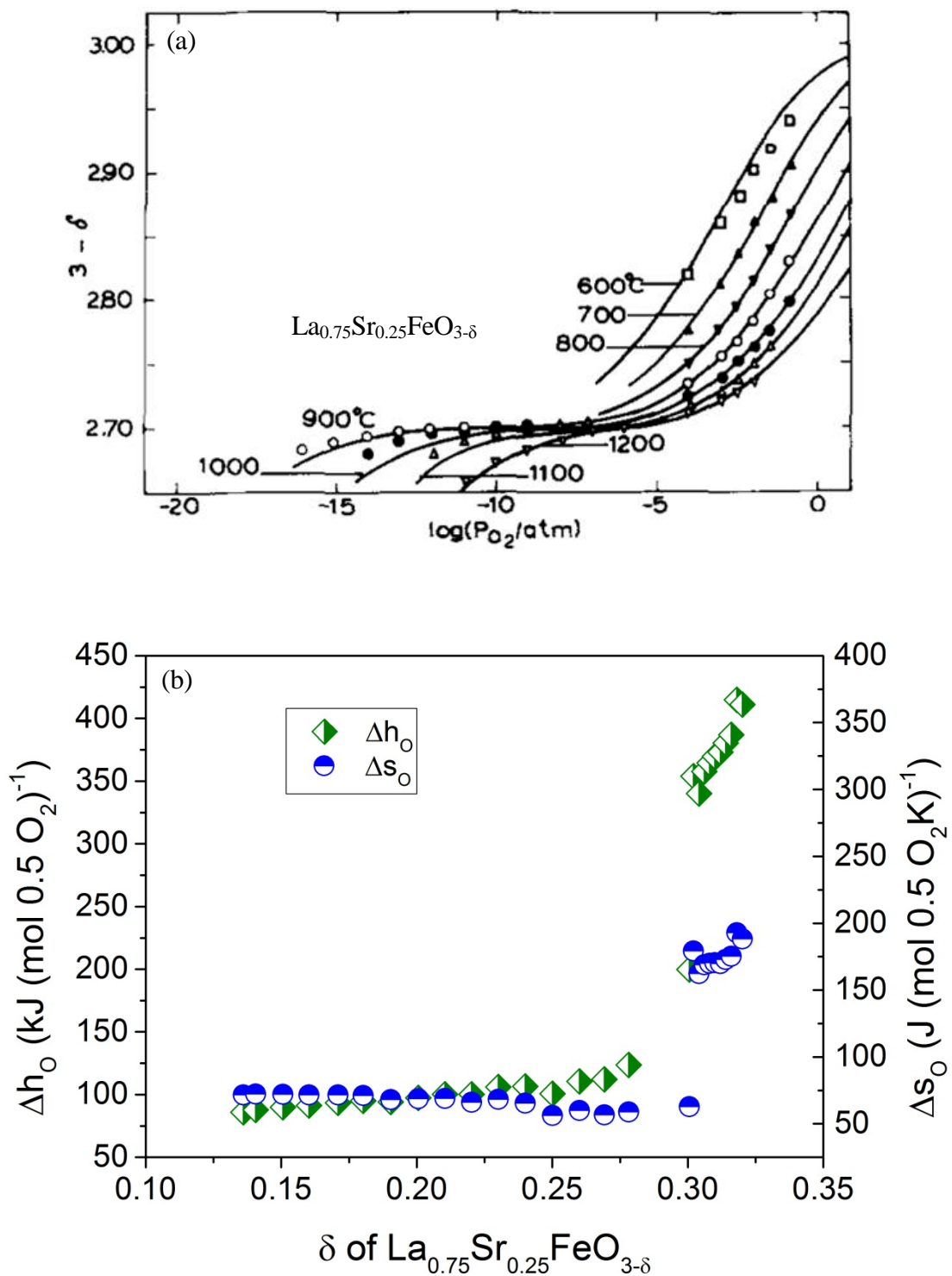


Figure 5-8. (a) Oxygen non-stoichiometry of $\text{La}_{0.75}\text{Sr}_{0.25}\text{FeO}_{3-\delta}$ in $(3-\delta)$ -vs- $\log(p(O_2))$ plots from reference [2] measured by thermogravimetric analyzer. (b) Extracted reduction enthalpy and entropy of $\text{La}_{0.75}\text{Sr}_{0.25}\text{FeO}_{3-\delta}$.

Compared with the redox properties of $\text{La}_{0.8}\text{Sr}_{0.2}\text{MnO}_{3-\delta}$ (shown in Figure 3-6), $\text{La}_{0.75}\text{Sr}_{0.25}\text{FeO}_{3-\delta}$ possesses a higher reduction enthalpy and a lower reduction entropy. Both changes increase the difficulties of reduction; therefore, its $\Delta\delta$ value is much smaller than it of $\text{La}_{0.8}\text{Sr}_{0.2}\text{MnO}_{3-\delta}$. Based on what we learned from the impacts of A site content on the redox nature of $\text{La}_{1-x}\text{Sr}_x\text{MnO}_{3-\delta}$, the $\Delta\delta$ value under the thermochemical cycling condition mentioned above decreases with Sr decrease. Hence, $\text{La}_{0.8}\text{Sr}_{0.2}\text{FeO}_{3-\delta}$ is expected to have less fuel productivity compared with it of $\text{La}_{0.75}\text{Sr}_{0.25}\text{FeO}_{3-\delta}$ and $\text{La}_{0.8}\text{Sr}_{0.2}\text{MnO}_{3-\delta}$.

In order to learn the Fe substitution effects on the redox properties of $\text{La}_{0.8}\text{Sr}_{0.2}\text{Mn}_{1-x}\text{Fe}_x\text{O}_{3-\delta}$, thermogravimetric analysis was performed. Three compositions of this solid solution were synthesized with the solid state reaction method and they are $x=0.25$, $x=0.5$, and $x=0.75$. The test samples are porous and were prepared under the same conditions as the porous pellets used for thermochemical cycling. The most challenging part within this measurement is the determination of the “stoichiometric ($\delta=0$)” or “reference δ ” status of the oxides. In order to determine the absolute δ value of the test oxides, the known status should be set as the reference point when conducting the thermogravimetric measurements. For the oxide systems with more than one kind of nonstoichiometry behavior with changing $p(\text{O}_2)$, such as $\text{La}_{1-x}\text{Ca}_x\text{CrO}_{3-\delta}$ ^[3], $\text{La}_{1-x}\text{Sr}_x\text{MnO}_{3-\delta}$ ^[4], and $\text{La}_{1-x}\text{Sr}_x\text{FeO}_{3-\delta}$ ^[2], the reference states are usually set at the plateau region where $\partial\delta/\partial\log(p(\text{O}_2)) \sim 0$.

Due to the different redox properties of the oxides, the oxygen partial pressure ranges which correspond to the plateau region are different. For example, the saturated plateau ($\delta \sim 0$) of $\text{La}_{0.8}\text{Ca}_{0.2}\text{CrO}_{3-\delta}$ can be identified for within $10^{-5}\text{atm} < p(\text{O}_2) < 1\text{atm}$, but for $\text{La}_{0.8}\text{Sr}_{0.2}\text{MnO}_{3-\delta}$ and the $\text{La}_{0.75}\text{Sr}_{0.25}\text{FeO}_{3-\delta}$, oxygen excess ($3-\delta > 3$) and oxygen deficient ($3-\delta < 3$) are shown in this $p(\text{O}_2)$ range, respectively. Furthermore, the plateau of $\text{La}_{0.8}\text{Sr}_{0.2}\text{MnO}_{3-\delta}$ is assigned as ($\delta \sim 0$) and can be found with the conditions of $800\text{ }^\circ\text{C}$ under $p(\text{O}_2) \sim 10^{-5}\text{atm}$, but the plateau of $\text{La}_{0.75}\text{Sr}_{0.25}\text{FeO}_{3-\delta}$ is assigned as ($\delta = [\text{Sr}]/2$) and is located at a more reducing atmosphere. Therefore, we can expect that the plateau of $\text{La}_{0.8}\text{Sr}_{0.2}\text{MnO}_{3-\delta}$ might be distorted by Fe substitutions, and how the reference status can be set is unclear.

One fair standard is proposed here: first, we set one temporary reference state with assigned temperature and $p(\text{O}_2)$, then this reference state is fixed and applied for every measurement conducted with various gas atmospheres. Therefore, all measurements will have same standard state point. In order to obtain the absolute δ value of the temporary reference state, the additional full reduction measurements are required. After reaching the temporary reference state, the conditions

of high concentration reducing gas and high temperature are applied to the thermogravimetric experiments. When the oxides are decomposed to the corresponding more stable compounds, the absolute oxygen content of the temporary reference state can be calculated from the weight loss of this measurement. For example, $\text{La}_{0.8}\text{Sr}_{0.2}\text{Mn}_{1-x}\text{Fe}_x\text{O}_{3-\delta}$ would be reduced to the compounds of La_2O_3 , SrO , MnO , and Fe . The weight difference between the temporary reference status and the full reduced status is attributed to the oxygen release from the reduction reaction; hence, the absolute δ values of the temporary reference state can be obtained.

The temporary reference state we set within our experiments is the oxygen content of the oxides equilibrated at 800°C under $p(\text{O}_2)=0.02$ atm. So far, only measurements with two kinds of gas atmospheres are completed and the results are illustrated in Figure 5-9. To get better resolution in $\Delta p(\text{O}_2)$ of the measurements, more gas mixtures are required. The results so far can only express the $\Delta\delta$ from one fixed chemical potential difference ($\Delta p(\text{O}_2)$) among oxides with different Fe contents.

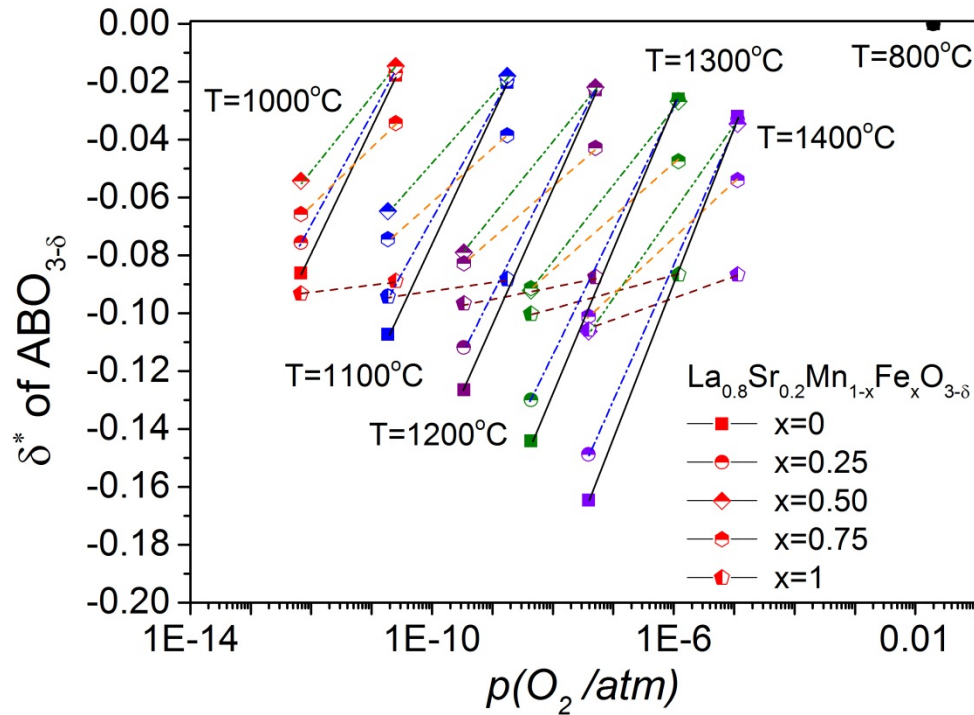


Figure 5-9. Oxygen non-stoichiometry of $\text{La}_{0.8}\text{Sr}_{0.2}\text{Mn}_{1-x}\text{Fe}_x\text{O}_{3-\delta}$ measured by thermogravimetric analyzer. The reference point is set at 800°C under $p(\text{O}_2)=0.02$ atm. Gas mixtures of 1% CO/CO_2

and 0.3% H₂ balanced with Ar are applied for the measurements. Here, δ^* is representing the oxygen non-stoichiometry temporarily set with the temporary reference status.

The lines linking two states under different $p(O_2)$ can approximately show how δ changes with $p(O_2)$. Within the fixed chemical potential difference ($\Delta p(O_2)$), the δ change decreases ($\Delta\delta/\Delta p(O_2)$) with increasing Fe contents. If these lines consider δ as a function of $p(O_2)$ (like the general thermogravimetric measurement curves but with very low resolution in $\Delta p(O_2)$) and the values of corresponding $p(O_2)$ are extracted on the lines with fixed δ^* for each temperature and each composition, the reduction enthalpy and entropy for this δ^* can be computed. Figure 5-10 shows the values of reduction enthalpy and entropy of $\text{La}_{0.8}\text{Sr}_{0.2}\text{Mn}_{1-x}\text{Fe}_x\text{O}_{3-\delta}$ at the fixed δ^* (0.04 for $x \leq 0.75$, and 0.09 for $x=1$) value. It's worth noting that, since the δ^* is temporarily unified for all compositions, the real absolute δ might be shifted. For example, for the TGA results of $\text{La}_{1-y}\text{Sr}_y\text{FeO}_{3-\delta}$ shown in ref. [2], the δ values at 800°C under $p(O_2)=0.02$ atm is much less than zero. Also, since the TG curve resolutions are insufficient, better accuracy for this analysis is required.

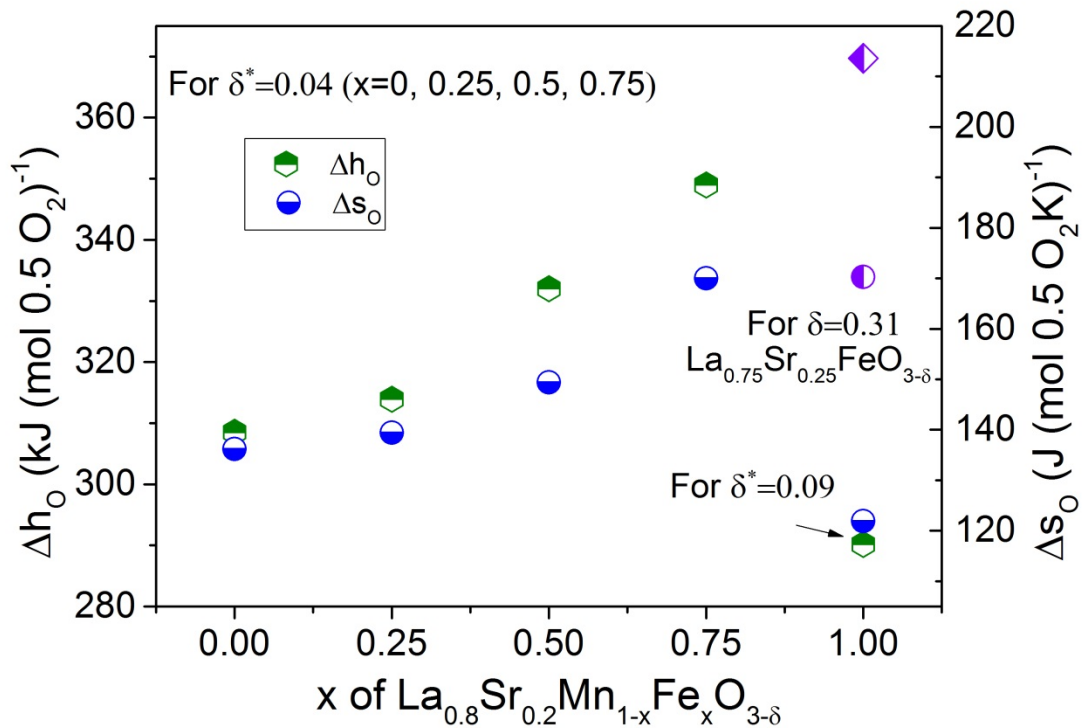


Figure 5-10. Extracted reduction enthalpy (Δh_o) and entropy (Δs_o) of $\text{La}_{0.8}\text{Sr}_{0.2}\text{Mn}_{1-x}\text{Fe}_x\text{O}_{3-\delta}$ and $\text{La}_{0.75}\text{Sr}_{0.25}\text{FeO}_{3-\delta}$ with $\delta=0.31$ (shown in Figure 5-9). δ^* represents the oxygen non-stoichiometry set with the temporary reference state.

The reduction enthalpy and entropy of $\text{La}_{0.8}\text{Sr}_{0.2}\text{MnO}_{3-\delta}$ extracted from the reported TGA results^[4] and Figure 5-9 at δ equal to 0.04 are 285 (Mizusaki) and 308 (this work) $\text{kJ}(\text{mol}^{-1}\text{O}^{-1})$ for Δh_o and 113 (Mizusaki) and 136 (this work) $\text{J}(\text{mol}^{-1}\text{O}^{-1}\text{K}^{-1})$ for Δs_o . The discrepancy in values of Δh_o and Δs_o from our work might be due to the lower δ resolution and the inaccurate assignment of the temporary δ^* for this work. For the $\text{La}_{0.8}\text{Sr}_{0.2}\text{Mn}_{1-x}\text{Fe}_x\text{O}_{3-\delta}$ samples with $x \leq 0.75$, both reduction enthalpy and entropy increase as Fe substitution increases. As mentioned above, the increase of reduction Δh_o will act against the oxygen release due to the stronger bonding with oxygen. On the other hand, the increase of reduction Δs_o favors thermal reduction, especially when the reaction temperature is high. It appears, the higher fuel productivities of Fe substituted samples result from the change of Δs_o . Figure 5-10 furthermore shows that Δh_o and Δs_o drop sharply when the B site cation site is fully occupied by Fe ($\text{La}_{0.8}\text{Sr}_{0.2}\text{FeO}_{3-\delta}$). The distinct behavior of $\text{La}_{0.8}\text{Sr}_{0.2}\text{FeO}_{3-\delta}$ is, in fact, directly evident in the raw TGA results. In contrast to the other compositions, $\text{La}_{0.8}\text{Sr}_{0.2}\text{FeO}_{3-\delta}$ appears to be in the isoelectronic region over the temperature and $p(\text{O}_2)$ measurement range. It is appropriate, therefore, to compare the extracted Δh_o and Δs_o values with those of $\text{La}_{0.75}\text{Sr}_{0.25}\text{FeO}_{3-\delta}$ also in the isoelectronic region known to occur at $\delta \sim 0.3$. As discussed in Chapter 3, Sr doping in $\text{La}_{1-x}\text{Sr}_x\text{MnO}_{3-\delta}$ lowers the reduction enthalpy. It was anticipated, therefore, that $\text{La}_{0.8}\text{Sr}_{0.2}\text{FeO}_{3-\delta}$ (with a smaller Sr content) would have a higher Δh_o than $\text{La}_{0.75}\text{Sr}_{0.25}\text{FeO}_{3-\delta}$. Surprisingly, the Δh_o and Δs_o values determined here for $\text{La}_{0.8}\text{Sr}_{0.2}\text{FeO}_{3-\delta}$ are much smaller than those of $\text{La}_{0.75}\text{Sr}_{0.25}\text{FeO}_{3-\delta}$ (also plotted in Figure 5-10). The unexpected result casts some doubts on our preliminary results. If $\text{La}_{0.8}\text{Sr}_{0.2}\text{FeO}_{3-\delta}$ is instead taken to be similar to be $\text{La}_{0.75}\text{Sr}_{0.25}\text{FeO}_{3-\delta}$, the monotonic increases in reduction Δh_o and Δs_o of $\text{La}_{0.8}\text{Sr}_{0.2}\text{Mn}_{1-x}\text{Fe}_x\text{O}_{3-\delta}$ with Fe content (shown in Figure 5-10) can be plausibly attributed to the solid solution formation.

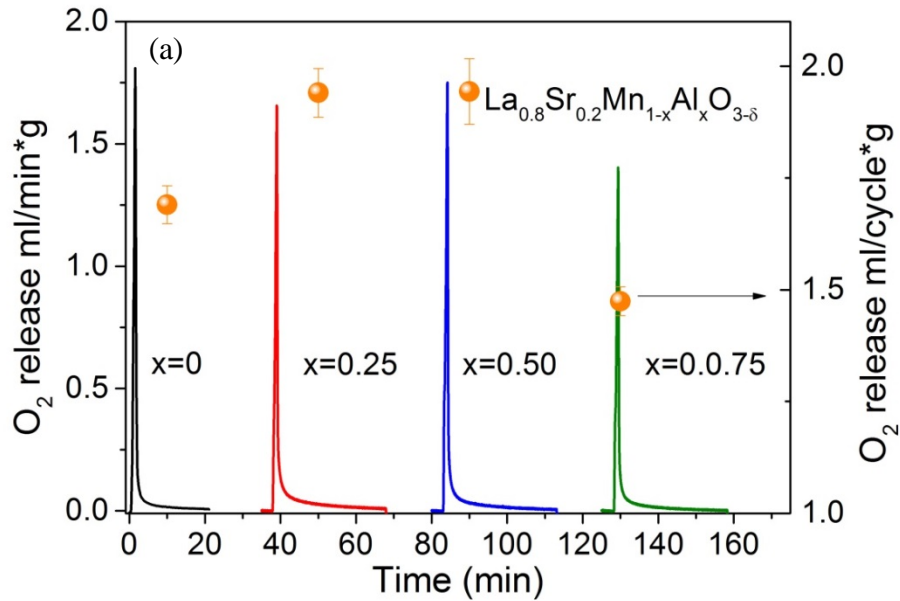
5.5 Thermochemical Cycling of $\text{La}_{0.8}\text{Sr}_{0.2}\text{Mn}_{1-x}\text{Al}_x\text{O}_{3-\delta}$

Another dopant, Al, is substituted into $\text{La}_{0.8}\text{Sr}_{0.2}\text{MnO}_{3-\delta}$. Samples with three different Al contents (25%, 50%, and 75%) were prepared with the same solid state reaction method. $\text{La}_{0.8}\text{Sr}_{0.2}\text{AlO}_{3-\delta}$ is ruled out because it contains no multi-valence element. The thermochemical water splitting cycling

is performed with the same test conditions applied on $\text{La}_{0.8}\text{Sr}_{0.2}\text{Mn}_{1-x}\text{Fe}_x\text{O}_{3-\delta}$ described above. Figure 5-11 shows the cycling results and an intermediate maximum of the fuel productivity at the composition with 50% Al substitution, similar to the Fe substitution.

However, it is worth noting that the profiles are normalized by the test oxide mass, since Al atomic weight is much smaller than that of Mn and Fe, with the same δ change created from one mole of the reactive oxides the gas evolution amount might be amplified if it is normalized by mass. Therefore, to have a fair comparison between samples, the gas evolution amounts should be converted to δ per unit cell of oxide, as is illustrated in Figure 5-12.

There are certain mismatches between the δ values converted from oxygen release and from the hydrogen production. However, from both calculation sources the increases of the δ change due to Al substitutions are clearly evident. Therefore, intermediate Al doping enhances the fuel productivity from thermochemical water splitting.



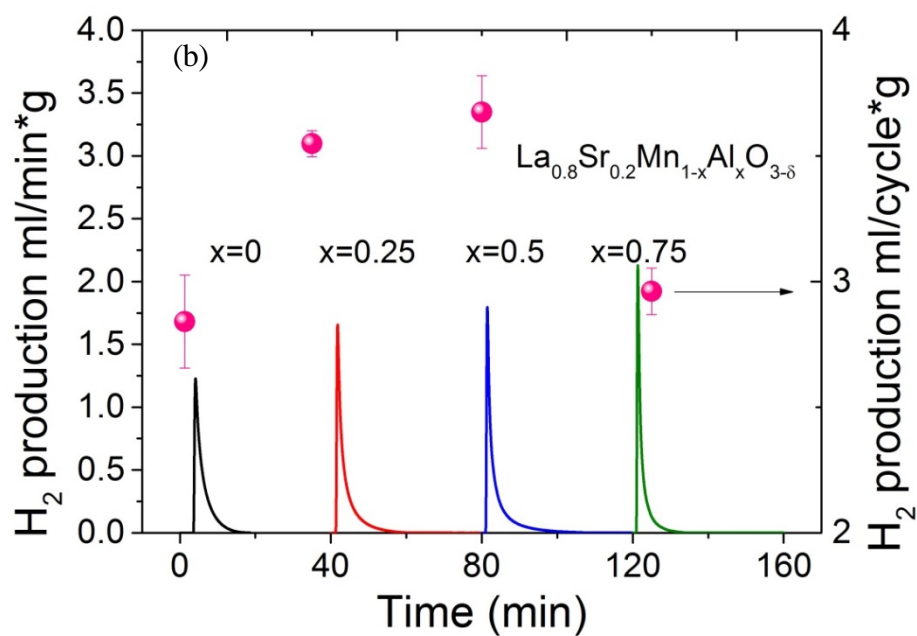


Figure 5-11. 5th thermochemical cycle of $\text{La}_{0.8}\text{Sr}_{0.2}\text{Mn}_{1-x}\text{Al}_x\text{O}_{3-\delta}$ ($x=0, 0.25, 0.5,$ and 0.75) porous samples. (a) Oxygen release and (b) hydrogen generation profiles as the function of time. The corresponding average gas evolution amounts are overlapped on the plots.

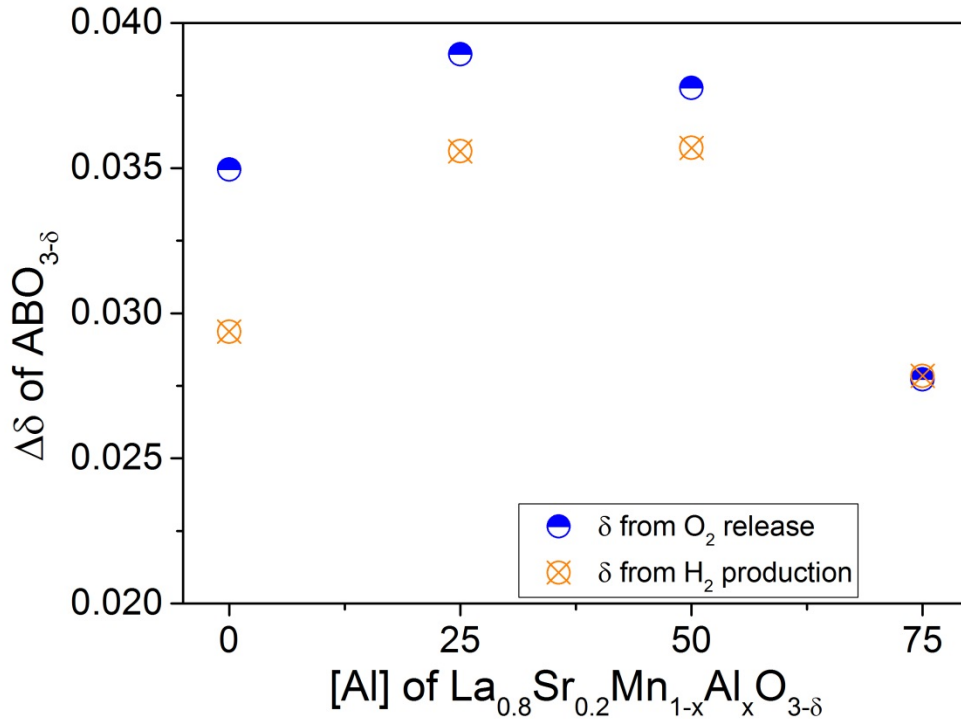


Figure 5-12. Oxygen non-stoichiometry changes within the thermochemical cycle of $\text{La}_{0.8}\text{Sr}_{0.2}\text{Mn}_{1-x}\text{Al}_x\text{O}_{3-\delta}$ ($x=0, 0.25, 0.5,$ and 0.75). The $\Delta\delta$ values are converted from the average oxygen release and hydrogen generation amounts over eight continuous cycles.

Although the Al doping affects the thermochemical cycling performance (see Figure 5-12), the $\Delta\delta$ differences between samples is less than 0.01. Hence, the improvement is not as obvious as Fe substitution. But, since the $\text{La}_{0.8}\text{Sr}_{0.2}\text{Mn}_{1-x}\text{Al}_x\text{O}_{3-\delta}$ sample of $x=0.25$ and $x=0.5$ expresses the higher $\Delta\delta$ within the cycling and they possess less multi-valence element within the oxides, this suggests that when designing the new reactive oxides for thermochemical water splitting cycling, the multi-valence element does not have to comprise the majority of the compound. For example, $\text{Sr}(\text{Ti}_{1-x}\text{Mn}_x)\text{O}_{3-\delta}$ is another new material designed for thermochemical water splitting and it is based on earth-abundant elements. With only 20% Mn content, the $\Delta\delta$ within the cycling between 1400 °C and 800 °C is around 0.06^[6] and this amount of change is double that of $\text{La}_{0.8}\text{Sr}_{0.2}\text{MnO}_{3-\delta}$. This implies that a higher structure flexibility exists than we originally envisioned for the tailoring of oxides.

The mass normalized gas evolution profiles plotted in Figure 5-11 are redrawn with the oxygen non-stoichiometry change fluxes and illustrated in Figure 5-13. There is no systematic trend from the oxygen release peaks shown in Figure 5-11(a). When plotting the δ fluxes, with the exception of the none Al substituted sample, the δ fluxes from oxygen release reaction decrease with increasing Al contents. Regarding the water splitting reaction, the peak profiles, specifically their initial peak heights, show the opposite trend as compared with thermal reduction reaction. In order to learn the surface reaction behaviors among samples, we try to correlate the gas evolution with the sample microstructure. From the SEM images and porosity shown in Figure 5-2 and Table 2, respectively, Al substitution reduces the grain size and increases the sample porosity. Both effects from Al doping imply the increase of reaction surface. The higher reaction surface area might support the higher δ fluxes from water splitting reaction shown in Figure 5-2(b). However, the reverse order of the δ fluxes from thermal reduction reactions displays that the high reaction surface area benefit is not evident with reduction.

Another possibility is that the δ fluxes are affected by the redox nature of the oxides, similar to the correlation we tried to make for the initial hydrogen production flux and the initial oxidization reaction chemical potential of the oxides (Figure 3-16(b)). It could be based on the high reaction extent (ψ) resulting from the large reaction driving force. However, due to the limited knowledge of the redox natures of $\text{La}_{0.8}\text{Sr}_{0.2}\text{Mn}_{1-x}\text{Al}_x\text{O}_{3-\delta}$, the evidence to support this is still insufficient.

Al doped $\text{La}_{1-y}\text{Sr}_y\text{MnO}_{3-\delta}$ for solar thermochemical H_2 production has been also reported by McDaniel et al.^[7] and the reported hydrogen productivities are listed in Table 5-3. The reactive oxides were thermally reduced at 1350°C in He and the water splitting reactions were conducted at 1000°C in steam with $p(\text{H}_2\text{O})=0.4$ atm. Because the oxygen partial pressure of the reduction reaction environment is unclear, it is impossible to estimate the oxygen non-stoichiometry changes ($\Delta\delta$) within the thermochemical cycling by the redox properties of the reactive oxides. For example, if the He gas flow provides the gas atmosphere for the reduction reaction around $p(\text{O}_2)=10\text{ppm}$, the expected $\Delta\delta$ value of $\text{CeO}_{2-\delta}$ should be 0.0194 and it is more than three times higher than the value converted from the reported H_2 productivity (shown in Table 5-3). If this divergence is attributed to the leakage of the reactor, the oxygen partial pressure under this unknown leakage level can be calculated by the $\Delta\delta$ listed in table and it is around $p(\text{O}_2)=0.0032$ atm. If we assume that the thermal reduction reaction is performed under the oxygen partial pressure $p(\text{O}_2)=0.0032$ atm, and apply the same cycling conditions on $\text{La}_{0.6}\text{Sr}_{0.4}\text{MnO}_{3-\delta}$, with its redox properties we reported in Chapter 3, the

$\Delta\delta$ within the thermochemical cycling can be expected around 0.032. As compared to the $\Delta\delta$ values of $\text{La}_{0.6}\text{Sr}_{0.4}\text{Mn}_{0.6}\text{Al}_{0.4}\text{O}_{3-\delta}$ and $\text{La}_{0.6}\text{Sr}_{0.4}\text{Mn}_{0.4}\text{Al}_{0.6}\text{O}_{3-\delta}$ listed in table, we can conclude that Al doping increase the fuel productivity of $\text{La}_{0.6}\text{Sr}_{0.4}\text{MnO}_{3-\delta}$. The fuel productivity improvements from Al substitution have been observed in both our and McDaniel's work. The fuel productivity of $\text{La}_{0.6}\text{Sr}_{0.4}\text{MnO}_{3-\delta}$ is doubled by 40% Al substitution for Mn. This improvement is much great than what we observed from the samples of $\text{La}_{0.8}\text{Sr}_{0.2}\text{Mn}_{1-x}\text{Al}_x\text{O}_{3-\delta}$. In the present study, replacing 50% Mn of $\text{La}_{0.8}\text{Sr}_{0.2}\text{MnO}_{3-\delta}$ by Al increases $\Delta\delta$ by around 15%.

Table 5-3. Fuel productivities of $\text{La}_{1-y}\text{Sr}_y\text{Mn}_{1-x}\text{Al}_x\text{O}_{3-\delta}$ reported by ref. [8]. Thermal reduction and water splitting temperature are 1350°C and 1000°C, respectively. The water splitting reactions were performed under $p(\text{H}_2\text{O})=0.4$ atm (the corresponding $p(\text{O}_2)$ is around 4.77×10^{-6} atm).

Composition	H ₂ productivity (μmole/g)	H ₂ productivity (ml/g)	$\Delta\delta$ within cycling
CeO ₂	32	0.7168	0.0055
$\text{La}_{0.6}\text{Sr}_{0.4}\text{Mn}_{0.6}\text{Al}_{0.4}\text{O}_{3-\delta}$	307	6.8768	0.0645
$\text{La}_{0.4}\text{Sr}_{0.6}\text{Mn}_{0.6}\text{Al}_{0.4}\text{O}_{3-\delta}$	277	6.2048	0.0554
$\text{La}_{0.6}\text{Sr}_{0.4}\text{Mn}_{0.4}\text{Al}_{0.6}\text{O}_{3-\delta}$	220	4.9280	0.0450

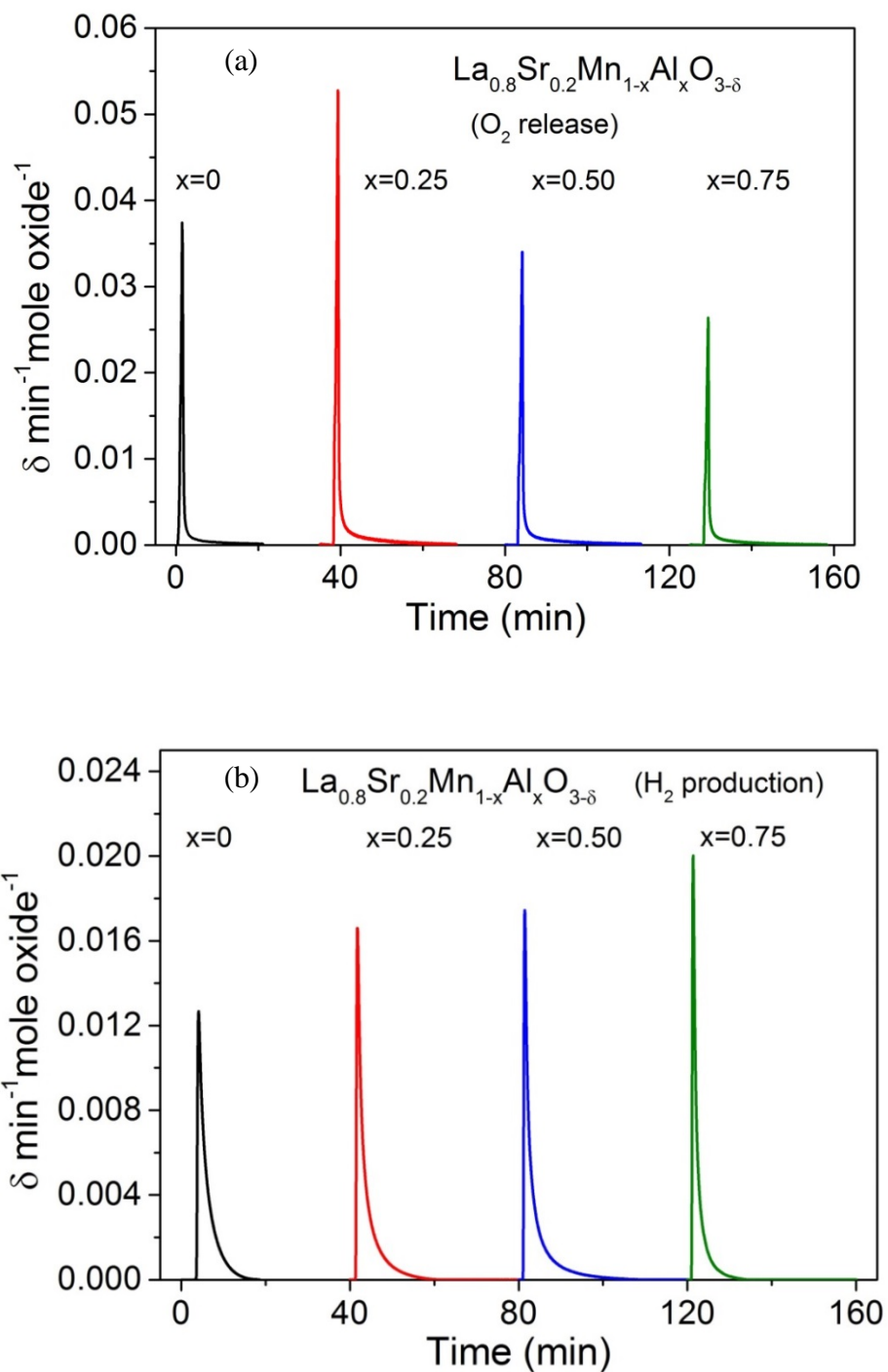


Figure 5-13. Redrawing the thermochemical cycle of $\text{La}_{0.8}\text{Sr}_{0.2}\text{Mn}_{1-x}\text{Al}_x\text{O}_{3-\delta}$ ($x=0, 0.25, 0.5, \text{ and } 0.75$) as the flux of δ . (a) Oxygen release and (b) hydrogen generation profiles as the function of time.

BIBLIOGRAPHY

1. D. Shannon, *Acta Crystallographica*, 1976, A32, 751–767.
2. J. Mizusaki, M. Yoshihiro, S. Yamauchi and K. Fueki, *Journal of Solid State Chemistry*, 1985, 58, 257-266.
3. S. Onuma, K. Yashiro, S. Miyoshi, A. Kaimai, H. Matsumoto, Y. Nigara, T. Kawada, J. Mizusaki, K. Kawamura, N. Sakai and H. Yokokawa, *Solid State Ionics*, 2006, 174, 287-293.
4. J. Mizusaki, Y. Yonemura, H. Kamata, K. Ohyama, N. Mori, H. Takai, H. Tagawa, M. Dokiya, K. Naraya, T. Sasamoto, H. Inaba and T. Hashimoto, *Solid State Ionics*, 2000, 132, 167-180.
5. T. Nakamura, G. Petzow and L. J. Gauckler, *Materials Research Bulletin*, 1979, 14, 649-659
6. C. K. Yang, S. Wilke, Y. Yamazaki, and S. Haile, The 19th International Conference on Solid State Ionics, poster.
7. A. H. McDaniel, E. C. Miller, D. Arifin, A. Ambrosini, E. N. Coker, R. O'Hayre, W. C. Chueh and J. Tong, *Energy and Environmental Science*, 2013, 6, 2424.

Chapter 6

REACTION KINETICIS ASPECTS STUDIES

6.1 Introduction

A preliminary kinetic assessment of strontium-doped lanthanum manganite (LSM) perovskites for two-step thermochemical water splitting has been discussed in Chapter 3. However, due to the limited surface kinetics information from the literature, the only assured conclusion we can draw so far is that the sluggish water splitting reaction kinetics is not because of the bulk diffusion process. Furthermore, the information on kinetics provided by electrical conductivity relaxation (ECR) measurement is from measurements under small chemical potential ($p(O_2)$) perturbations,^[1] whereas the water splitting reaction is performed using a relatively large chemical potential difference. The impact from this large driving force on reaction kinetics needs further study. In the first half of this chapter, we studied the reaction kinetic limitations for both thermal reduction and water splitting steps. Under the assumption of thermodynamic equilibrium, we examine how the thermodynamic driving force (redox nature of the reactive oxide) affects the reaction progress.

In the second half of this chapter, the A site non-stoichiometry of LSM is investigated. When applying LSM for SOFC applications, cation segregation at the surface has been a commonly observed phenomenon and it directly affects the cathode reactivity and stability in oxygen reduction reactions (ORR)^[2-4]. Since SrO segregation has been identified as the reason for activity degradation of the ORR, the idea of A site deficiency in LSM, $(La_{1-x}Sr_x)_{1-y}MnO_{3-\delta}$ ($y>0$), has been investigated for thermochemical water splitting. The purpose is to suppress the SrO segregation, hence, to improve the water splitting reaction kinetics. However, the experimental results reveal the opposite trend with A-site excess materials demonstrating enhance kinetics. The data suggest that the boost in kinetics drive from new hetero-structure composites involving A-site excess phase.

6.2 Thermodynamic Influences on Kinetics

When we perform the thermochemical cycling, the information the mass spectrometer provides is the oxygen release and hydrogen production flux profiles. To put it in another way, the flux profile

can be considered as the oxygen non-stoichiometry (δ) changes within unit time, $\partial\delta/\partial t$. As mentioned in Chapter 4, the $\Delta\delta$ is driven by the chemical potential differences and for the water splitting reaction it can be described with Equation 4.17.

$$(\delta_i - \delta_f) = \frac{F}{n_{oxide}} \left[\psi \left(\frac{P_{H_2O,i}}{P_{sys}} \right) - \frac{2 \left(\frac{P_{O_2,f}}{P_{sys}} \right)}{\left[1 - \left(\frac{P_{O_2,f}}{P_{sys}} \right) \right]} \right] \quad (4.17)$$

Therefore, the flux of oxygen (vacancy) can be expressed as

$$\frac{\partial\delta}{\partial t} = \frac{\partial F}{\partial t} \left[\psi \left(\frac{P_{H_2O,i}}{P_{sys}} \right) - \frac{2 \left(\frac{P_{O_2,f}}{P_{sys}} \right)}{\left[1 - \left(\frac{P_{O_2,f}}{P_{sys}} \right) \right]} \right] = \frac{\dot{F}}{n_{oxide}} \left[\psi \left(\frac{P_{H_2O,i}}{P_{sys}} \right) - \frac{2 \left(\frac{P_{O_2,f}}{P_{sys}} \right)}{\left[1 - \left(\frac{P_{O_2,f}}{P_{sys}} \right) \right]} \right] \quad (6.1)$$

where \dot{F} is the flux of Ar (mole/minute) flowed into the steam generator (water bottle).

Therefore, the equilibrium reaction kinetics is linked by the thermodynamic nature of oxides via the time information embedded in the steam flow rate.

We turn now to the thermal reduction reaction. The derivation is similar to that of water splitting reaction, but it is simpler because the only relevant gas species is oxygen. To unify the notation for the two half-reactions, the initial and final state designations for both reactions follow those for water splitting. Hence, “i” here represents the reduced state and “f” represents the state before thermal reduction. By this convention, thermal reduction reaction of a given oxide is expressed as



Mass conservation of oxygen before and after the reduction, implies

$$n_{O_2,f} + \left[\frac{1}{2}(\delta_i - \delta_f)n_{oxide} \right]_{solid} = n_{O_2,f} + \left[\frac{1}{2}(\delta_i - \delta_f)n_{oxide} \right]_{gas} = n_{O_2,i} \quad (6.3)$$

The index of the bracket stands for the states of the oxygen originally stored within the oxides. The bracket with index of solid represent the oxygen atoms are located within the lattices of the oxide before thermal reduction and bracket with index of gas represents the same amount of oxygen released from the oxide after thermal reduction.

For the practical implementation, we performed the thermal reduction with the carrier gas with an oxygen partial pressure of 10^{-5} atm and balanced with argon. The oxygen partial pressure of the reduction reaction environment should be specified and fixed in order to explicitly analyze the oxygen non-stoichiometry change resulted from the reduction. We index it as $\left(\frac{P_{O_2,inlet}}{P_{sys}} \right)$. Therefore,

for the injected oxygen partial pressure controlled carrier gas, the mass of gases can be expressed as

$$n_{Total,f} = n_{Ar,f=i} + n_{O_2,f} = n_{Total,f} \left[1 - \left(\frac{P_{O_2,inlet}}{P_{sys}} \right) \right] + n_{Total,f} \cdot \left(\frac{P_{O_2,inlet}}{P_{sys}} \right) \quad (6.4)$$

After the reduction, the total moles of gases becomes

$$\begin{aligned} n_{Total,i} &= n_{Ar,f=i} + n_{O_2,i} = n_{Total,f} \left[1 - \left(\frac{P_{O_2,inlet}}{P_{sys}} \right) \right] + n_{Total,f} \cdot \left(\frac{P_{O_2,inlet}}{P_{sys}} \right) + (n_{O_2,i} - n_{O_2,f}) \\ &= n_{Total,f} \left[1 - \left(\frac{P_{O_2,inlet}}{P_{sys}} \right) \right] + n_{Total,f} \cdot \left(\frac{P_{O_2,inlet}}{P_{sys}} \right) + \frac{1}{2}(\delta_i - \delta_f)n_{oxide} \end{aligned} \quad (6.5)$$

Clearly, after the reduction reaction, shown in Equation 6.5, the amount of oxygen in the gas phase increases as a result of the oxygen release from the reactive oxide. Accordingly, the total amount of gas also increases and is given by

$$n_{Total,i} = n_{Total,f} + \frac{1}{2}(\delta_i - \delta_f)n_{oxide} \quad (6.6)$$

Figure 6-1 illustrates the reactor scheme of thermal reduction reaction. The involved reactant gas species are shown in the scheme in term of mole. The total gas evolution in term of mole amount from the reactor inlet (right of the reactor shown in the figure) to the outlet can be expressed as

$$\begin{array}{c}
 \text{Before reduction (reactor inlet)} \quad \quad \quad \text{After reduction (reactor outlet)} \\
 n_{Total,f} \left(\frac{P_{O_2,inlet}}{P_{sys}} \right) + \left[\frac{1}{2} (\delta_i - \delta_f) n_{oxide} \right]_{solid} = n_{Total,f} \left(\frac{P_{O_2,inlet}}{P_{sys}} \right) + \left[\frac{1}{2} (\delta_i - \delta_f) n_{oxide} \right]_{gas} = n_{O_2,i} \quad (6.7)
 \end{array}$$

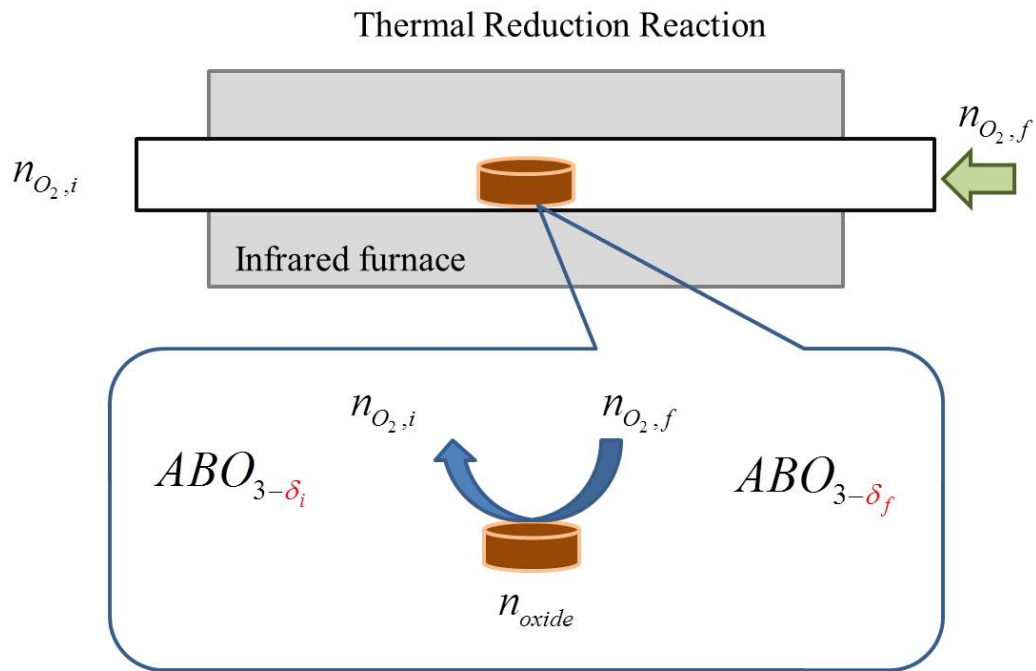


Figure 6-1. Scheme of moles of reactant species involved in thermal reduction reaction. Within the notation of the reactant species, “i” describes the reduced status of the reaction and “f” describes the status before the reaction.

Recall the previous definition of the mole fraction of oxygen mentioned in Chapter 4,

$$x_{O_2,i \text{ or } f} = \frac{P_{O_2,i \text{ or } f}}{P_{sys}} \text{ and } n_{O_2,i \text{ or } f} = x_{O_2,i \text{ or } f} n_{Total,i \text{ or } f} = \left(\frac{P_{O_2,i \text{ or } f}}{P_{sys}} \right) n_{Total,i \text{ or } f} .$$

To prevent confusion about cycling between the reduced and oxidized states of oxides during the two half reactions, we will

always refer the variables with the notations “f” for oxidized state ($n_{O_2,f}$, $P_{O_2,f}$, δ_f , and etc.) and the variables with the notations “i” for reduced state ($n_{O_2,i}$, $P_{O_2,i}$, δ_i , and etc.). With applying the ideal gas and Dalton's law, at the reactor outlet, the total moles of oxygen can be expressed as

$$n_{O_2,i} = x_{O_2,i} n_{Total,i} = \left(\frac{P_{O_2,i}}{P_{sys}} \right) n_{Total,i} \quad (6.8)$$

To insert Equation 6.8 into Equation 6.7,

$$n_{O_2,i} = n_{Total,f} \left(\frac{P_{O_2,inlet}}{P_{sys}} \right) + \frac{1}{2} (\delta_i - \delta_f) n_{oxide} = \left(\frac{P_{O_2,i}}{P_{sys}} \right) n_{Total,i} \quad (6.9)$$

Therefore, we can get

$$\left(\frac{P_{O_2,i}}{P_{sys}} \right) = \frac{n_{Total,f} \left(\frac{P_{O_2,inlet}}{P_{sys}} \right) + \frac{1}{2} (\delta_i - \delta_f) n_{oxide}}{n_{Total,i}} = \frac{n_{Total,f} \left(\frac{P_{O_2,inlet}}{P_{sys}} \right) + \frac{1}{2} (\delta_i - \delta_f) n_{oxide}}{n_{Total,f} + \frac{1}{2} (\delta_i - \delta_f) n_{oxide}} \quad (6.10)$$

To rearrange Equation 6.10,

$$\frac{1}{2} (\delta_i - \delta_f) n_{oxide} \left[1 - \left(\frac{P_{O_2,i}}{P_{sys}} \right) \right] = n_{Total,f} \left[\left(\frac{P_{O_2,i}}{P_{sys}} \right) - \left(\frac{P_{O_2,inlet}}{P_{sys}} \right) \right] \quad (6.11)$$

$$(\delta_i - \delta_f) = \frac{2 n_{Total,f} \left[\left(\frac{P_{O_2,i}}{P_{sys}} \right) - \left(\frac{P_{O_2,inlet}}{P_{sys}} \right) \right]}{n_{oxide} \left[1 - \left(\frac{P_{O_2,i}}{P_{sys}} \right) \right]} \quad (6.12)$$

For thermal reduction reaction, the oxide is in oxidized state at the start of the reaction ($MO_{n-\delta_f}$).

Within Equation 6.12, the variables with notations “F” (δ_f and n_f) are fixed and the variables with

notations “i” (δ_i and $P_{O_2,i}$) evolve with the reaction progress. $P_{O_2,i}$ represents the oxygen partial pressure of the gas atmosphere after passing the reactive oxide. The chemical potential change of the oxide is driven by gas carrier flow. After the oxygen release from the oxide during thermal reduction, the chemical potential of the oxide would be changed due to the change of state (value of δ_i). Since we assume that the reaction kinetic barrier is very small and the new equilibrium will be rebuilt immediately, $P_{O_2,i}$ will be varied by the new chemical potential of the oxide. We can

consider the term on the right hand side of Equation 6.12, $\left(\frac{P_{O_2,i}}{P_{sys}}\right) - \left(\frac{P_{O_2,inlet}}{P_{sys}}\right)$, as the driving force for the thermal reduction reaction, and the oxygen nonstoichiometry evolution will cease when $P_{O_2,i} = P_{O_2,inlet}$.

Similar to our treatment of Equation 6.1 for the water splitting reaction, we apply the flow rate of the carrier gas (\dot{F} (mole/minute)) for the reduction reaction into Equation 6.12. Then, the oxygen nonstoichiometry evolution flux can be illustrated as

$$\frac{\partial \delta}{\partial t} = \frac{2 \dot{F} \left[\left(\frac{P_{O_2,i}}{P_{sys}} \right) - \left(\frac{P_{O_2,inlet}}{P_{sys}} \right) \right]}{n_{oxide} \left[1 - \left(\frac{P_{O_2,i}}{P_{sys}} \right) \right]} \quad (6.13)$$

where \dot{F} is the gas flux for total gas species and it is equal to the flux of $n_{Total,f}$.

Equation 6.13 implies that $\left(\frac{P_{O_2,i}}{P_{sys}}\right)$ is the driving force, which drives the oxygen non-stoichiometry change, and when $\left(\frac{P_{O_2,i}}{P_{sys}}\right)$ is equal to $\left(\frac{P_{O_2,inlet}}{P_{sys}}\right)$, the equilibrium status of the thermal reduction reaction is achieved and the changes of δ cease.

6.3 Concrete Examples: Thermal Reduction Kinetics

In order to learn how the equilibrium reaction kinetics changes with the redox nature of reactive oxides, Equation 6.14 is applied to simulate the reaction evolutions. When applying the equation, the parameters of the real thermochemical cycling are employed. In particular, the system pressure is assumed as 1 atmosphere and $\left(\frac{P_{O_2, inlet}}{P_{sys}}\right)$ is set to 10^{-5} , which is the oxygen partial pressure of the

gas carrier for thermal reduction reaction. Then Equation 6.13 becomes

$$\frac{\partial \delta}{\partial t} = \frac{2 \dot{F} [P_{O_2, i} - 10^{-5}]}{n_{oxide} [1 - P_{O_2, i}]} \quad (6.14)$$

where \dot{F} is the gas carrier (Ar with 10ppm as $p(O_2)$) flux, 1000 cc/min. For every time interval, a fixed amount of Ar will be introduced into the reactor and will flush out the oxygen released from the thermally reduced oxides. Since we are assuming the material is always in equilibrium, any potential kinetic barrier is ignored. Therefore, after every reaction with the pulse of steam, the chemical potential of oxides change ($P_{O_2, i}$) and this change triggers the new equilibrium immediately. This kind of reaction equilibrium loop will continue until $P_{O_2, i}$ equals 10ppm.

The simulation is executed with a homemade Matlab[®] code, and the Runge–Kutta numerical method is employed^[5]. The inputs for this calculation are the redox properties (reduction enthalpy (Δh_o) and entropy (Δs_o)) of the relevant oxides. Thus, the quality of the extraction of Δh_o and Δs_o affects the accuracy of the computed results. In particular, within the thermogravimetric experiments, it is very challenging to obtain highly accurate weight loss for tiny oxygen release. Therefore, the extractions of Δh_o and Δs_o with small δ values have more uncertainty (at which δ_i is very close to δ_f). Hence, this decreased accuracy would happen on the initial section of thermal reduction reaction calculation and the final section of water splitting reaction calculation, respectively.

Figure 6-2 shows a typical δ evolution during thermal reduction as simulated with Equation 6.13. At first glance, the very long reaction time appears incompatible with practical implementation. Nevertheless, the long reaction time is a thermodynamic reality, and results from the large chemical

potential difference between the solid oxide phase and the carrier gas ($p(O_2)=10\text{ppm}$). From the figure, within the first 64 of the total 1170 minute half-cycle, 96% reduction reaction is completed; only approximates 0.005 of 0.125 of δ can be obtained from the remaining 18.4 hours of reaction. This implies that fully completed thermal reduction is not the practical scenario because the time required is long and the process is inefficient. Also, the long evolution tail and small δ value change (tiny oxygen release) would mislead us into thinking that the reaction is complete because the detection of such low oxygen concentration change might not be possible due to the detection limit of the gas phase mass spectrometer. The values of the completed reaction times of $\text{La}_{1-x}\text{Sr}_x\text{MnO}_{3-\delta}$ are 204 ($x=0.1$), 289 ($x=0.2$), 829 ($x=0.3$), and 1170 ($x=0.4$) minutes, respectively.

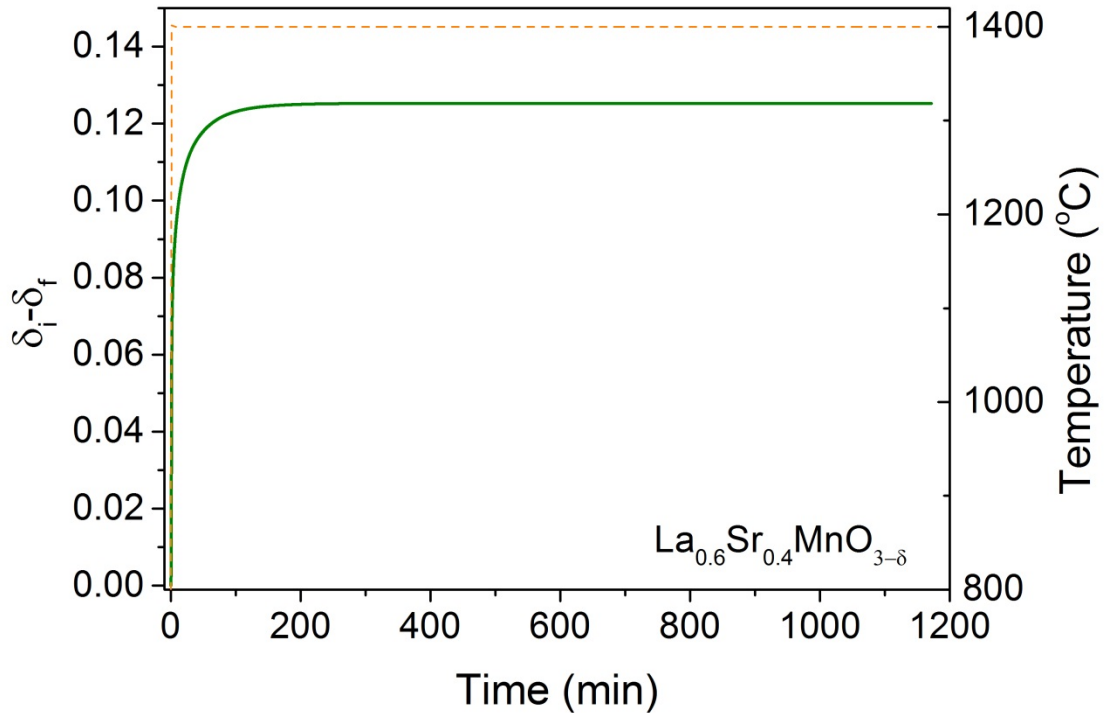


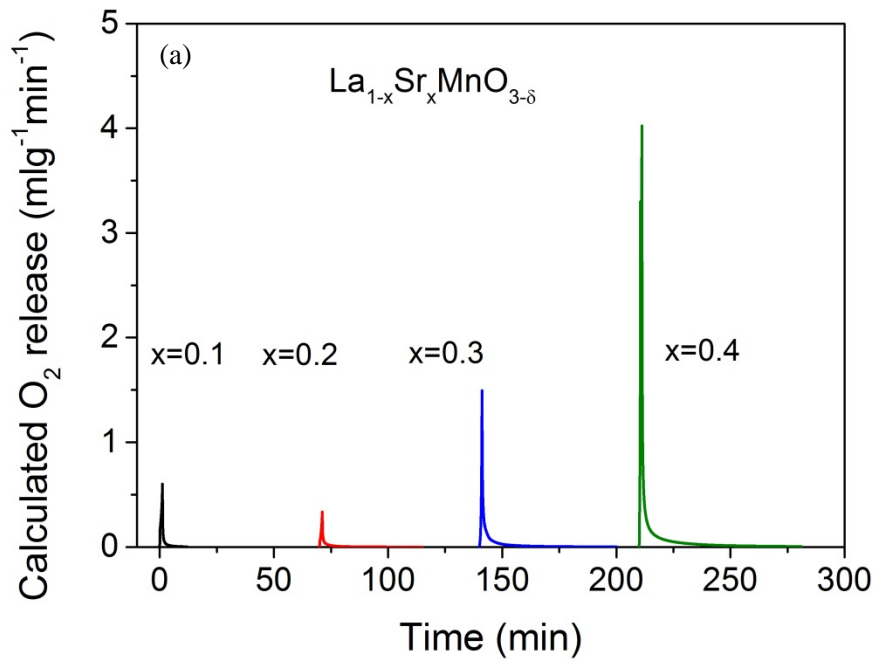
Figure 6-2. Simulation of oxygen non-stoichiometry (δ) evolution of $\text{La}_{0.6}\text{Sr}_{0.4}\text{MnO}_{3-\delta}$ during thermal reduction reaction at $1400\text{ }^\circ\text{C}$ under a $p(O_2)$ of 10 ppm . The initial state is $800\text{ }^\circ\text{C}$ and the temperature ramping rate is $500\text{ }^\circ\text{C}/\text{min}$. The redox natures from reference [6] are applied for this calculation. Simulated conditions are set with gas carrier flux at 1000 sccm Ar and the sample mass is 0.514 gram , which is the same as the real experiment environments.

To link this simulation to the real thermochemical cycling, the flux of δ evolution is converted to the flux of oxygen release ($\text{mlg}^{-1}\text{min}^{-1}$). The simulated oxygen release fluxes are illustrated in Figure 6-3 and the real experiment results shown in Chapter 3 have been overlaid for comparisons. From the simulated oxygen release fluxes, the gas evolution behaviors are very distinguishable between samples and these differences result from the different redox natures of oxides. Unlike the water splitting reaction, thermal reduction is activated during the temperature ramping and is not an isothermal reaction. From the calculation results, the peak height occurs during the temperature ramping. The thermogravimetric analysis results^[6] can help to explain the order of the peak heights shown in Figure 6-3. With the fixed $p(O_2)$, the oxides with higher Sr content possess higher $(\Delta\delta/\Delta T)$ (can be checked by drawing a vertical line across different isothermal TGA curves). Since we are neglecting the reaction kinetics barriers for current discussions, new equilibrium will be obtained when new temperature (thermodynamic status) is reached. Since the ramping rate of the thermal reduction steps is the same for all samples, within the same time interval, the oxides with more Sr will release more oxygen (same ΔT , but higher $\Delta\delta$). Therefore, high Sr content samples show high oxygen release flux.

When comparing the simulations with the real thermal reduction gas evolutions, it is surprising to see the very similar trends of the gas evolutions with samples compositions shown in two plots. However, the absolute values of simulation results are different and higher (except $x=0.2$ of $\text{La}_{1-x}\text{Sr}_x\text{MnO}_{3-\delta}$) as compared to the values from experiments. The differences are larger for the high Sr content oxides, and the values are very close for the $\text{La}_{1-x}\text{Sr}_x\text{MnO}_{3-\delta}$ with $x=0.1$ and 0.3 . Since the gas evolution flux can be described as $J = k\Delta\mu$ and only the chemical potential changes within reaction ($\Delta\mu$) are considered for current simulations, the differences between simulation and experimental fluxes can be attributed to the effects of k , surface reaction coefficient. Therefore, we can conclude that the reduction reactions are limited by surface reaction kinetics barriers. For the sample which shows agreement between calculated and measurement profiles, such as $\text{La}_{0.9}\text{Sr}_{0.1}\text{MnO}_{3-\delta}$, there is also the possibility that the reaction kinetics are limited by the gas carrier flow rate since the ratio of the gas carrier flux to mass (\dot{F}/n_{oxide}) also affects the δ evolution as shown in Equation 6.13. The impacts of the gas carrier flow rate on the δ evolution can be observed

with the example shown in Figure 6-4. The example reveals that higher gas carrier flow rate accelerates the δ evolution and this trend is expected from the description of Equation 6.13.

Also, the differences between calculated and measurement profiles can be also due to approximation of the simulation. Most significantly, $\delta_{\text{solid}}(x)$ is assumed constant along length of gas flow direction. The quality of the TGA measurements also affects the simulated profiles.



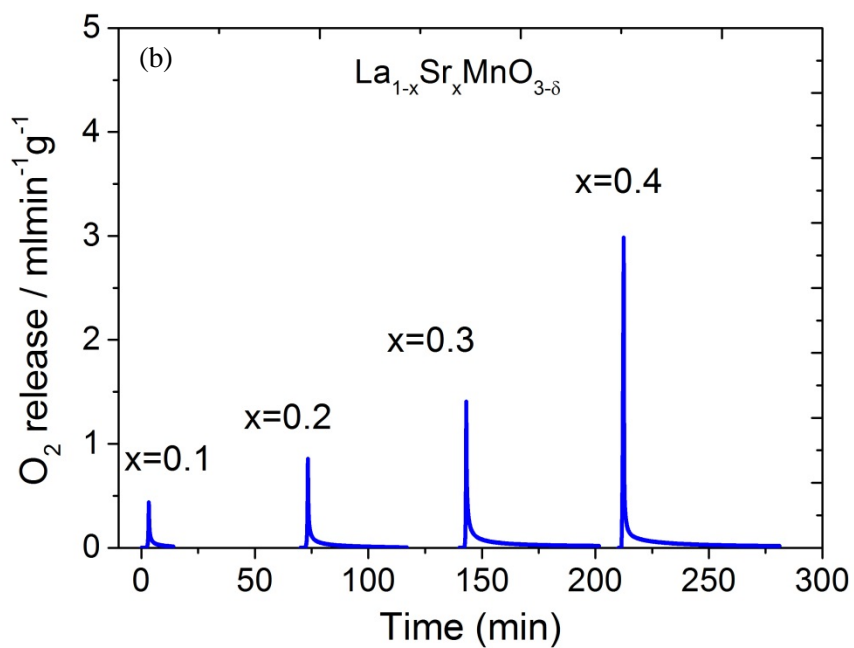


Figure 6-3. (a) Simulation of oxygen release fluxes of $\text{La}_{1-x}\text{Sr}_x\text{MnO}_{3-\delta}$ ($x=0.1, 0.2, 0.3,$ and 0.4) during thermal reduction reaction at $1400\text{ }^\circ\text{C}$ under $p(\text{O}_2)$ as 10 ppm. The inputs of materials redox natures are from reference [6] and [7]. The curves are cut and plotted with the experimental thermochemical cycling time frames. (b) Reprint of Figure 3-11(a) for comparison.

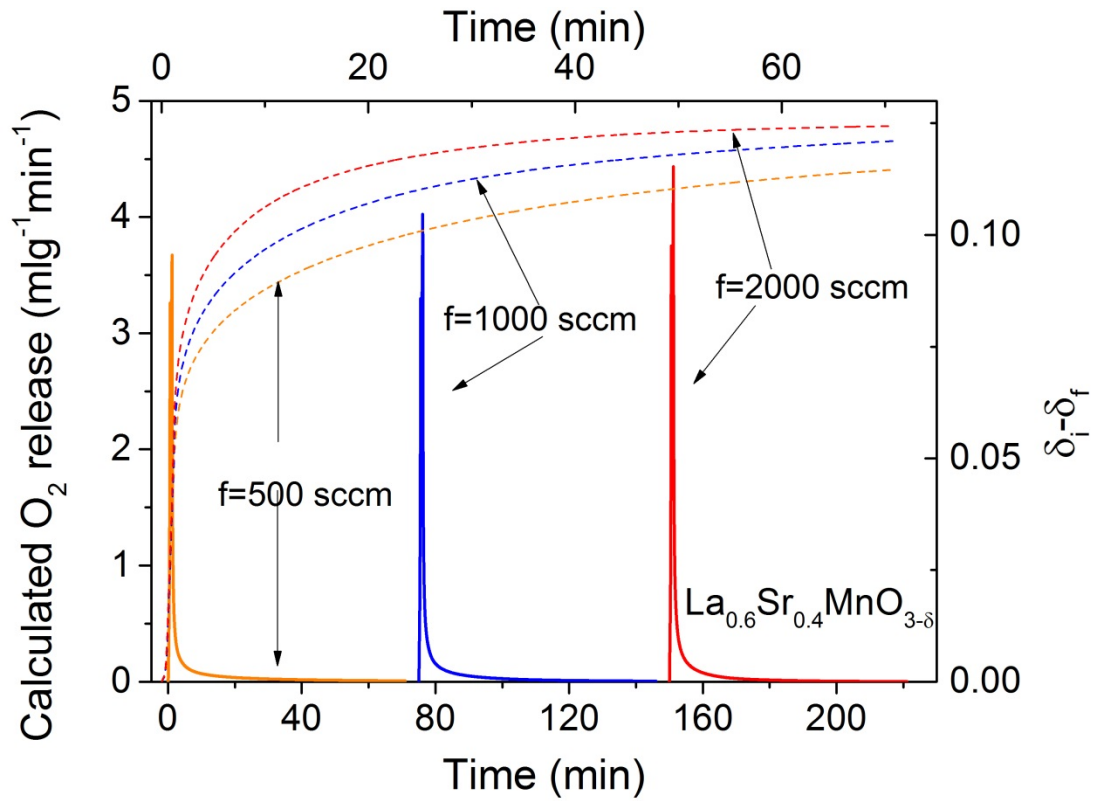


Figure 6-4. Gas carrier flow rate impact on reduction reaction equilibrium kinetics. The redox properties of $\text{La}_{0.6}\text{Sr}_{0.4}\text{MnO}_{3-\delta}$ from reference [6] are applied to this calculation. Solid lines are the simulated oxygen release fluxes with different gas carrier flow rates and the dash lines stand for the corresponding computed δ evolutions.

6.4 Concrete Examples: on Water Splitting Kinetics

For the equilibrium reaction kinetics of water splitting reactions, Equation 6.1 is applied to simulate the reaction evolutions. The system pressure is assumed as 1 atmosphere, and the equation can be simplified as following:

$$\frac{\partial \delta}{\partial t} = \frac{\dot{F}}{n_{oxide}} \left[\psi P_{H_2O,i} - \frac{2P_{O_2,f}}{[1 - P_{O_2,f}]} \right] \quad (6.15)$$

where \dot{F} can be the injected steam flux and is set with the same flow rate applied in experiments, 200 ml/min. For every time interval, a fixed amount of steam will be introduced into the reactor where it interacts with the reduced oxide. Without considering kinetic limitations from the pulse of steam, the chemical potential of oxides change ($P_{O_2,f}$) and this change triggers both the new reaction extent (ψ) and reaction equilibrium immediately.

The typical oxygen non-stoichiometry (δ) evolution for water splitting looks like it does for thermal reduction, in Figure 6-2, except that it is shown with the “opposite” variable on the y axis ($\delta_f - \delta_i$) as it describes the reverse process. However, the calculated reaction equilibrium time in this case is likely to be overestimated (simulated time for complete reaction is too long) because, at the final equilibrium state, the oxide has a very small δ and this region the uncertainty in the relationship between $p(O_2)$ and δ is large. Again, this depends on the quality of thermogravimetric experiments. For example, among the available thermogravimetric experiments for $CeO_{2-\delta}$, the redox properties extracted for $\delta=0.001$ are still reliable. But for the case of $La_{1-x}Sr_xMnO_{3-\delta}$, because the location of the plateau region varies with temperature and because of the scarcity of accurate measurements in the literature, the dependence of δ on $p(O_2)$ is unclear even up to $\delta=0.01$.

Figure 6-5 shows simulations of the water splitting reaction for $La_{1-x}Sr_xMnO_{3-\delta}$ ($x=0.1, 0.2, 0.3,$ and 0.4) in comparison with experimental results. Similar to the correlation of hydrogen production flux peak heights and the oxygen chemical potential difference between the oxide and the injected steam discussed in Chapter 3 and shown in Figure 3-15 (b), the peak higher hydrogen production flux increases with increasing chemical potential difference between the gas and the oxide. The behavior can be understood as follows. A higher driving force leads to a higher steam-to-hydrogen conversion ratio (ψ), Figure 4-8 (b), and, as shown in Equation 6.1, a larger ψ leads to a larger $\partial\delta/\partial t$. Comparing the simulations for two half reactions, Figure 6-3 and 6-5, the opposite trends of the gas evolution fluxes over compositions can be found. High Sr content sample shows high flux for oxygen release but low flux for hydrogen production. It is almost inevitable that a material with high driving force for reduction and have a high O_2 evolution flux, will have a small driving force for oxidization and have a low H_2 generation flux, and vice versa.

Comparing the simulations with the experimental results, it is evident the simulations give higher hydrogen production fluxes. As mentioned, the hydrogen production flux is proportional to $k\Delta\mu$ and the simulations only consider the effects from $\Delta\mu$. Therefore, the flux differences between

simulation and experimental results can likely be attributed to the surface reaction barriers (k) (or the assumption of constant $\delta_{\text{solid}}(x)$). Furthermore, we can observe an important trend with composition. For thermal reduction, the difference between the simulations and measurements is roughly constant with Sr content. In contrast, for hydrogen production, the difference is most severe at low Sr content. Thus, even though low Sr content oxides have a larger oxygen chemical potential difference and hence promise high steam-to-fuel conversion effectiveness, the surface reaction barriers limit the water splitting progress.

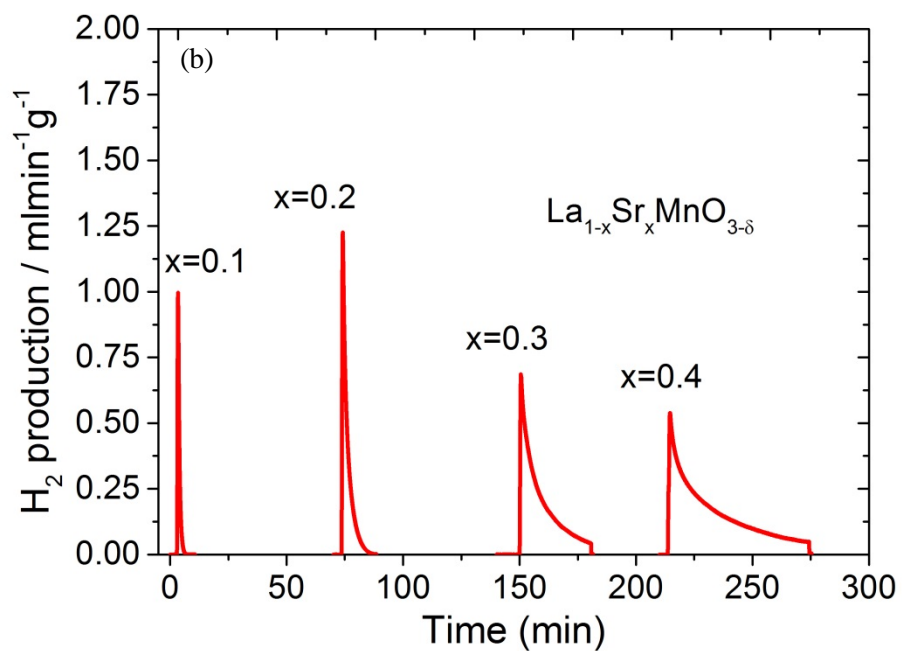
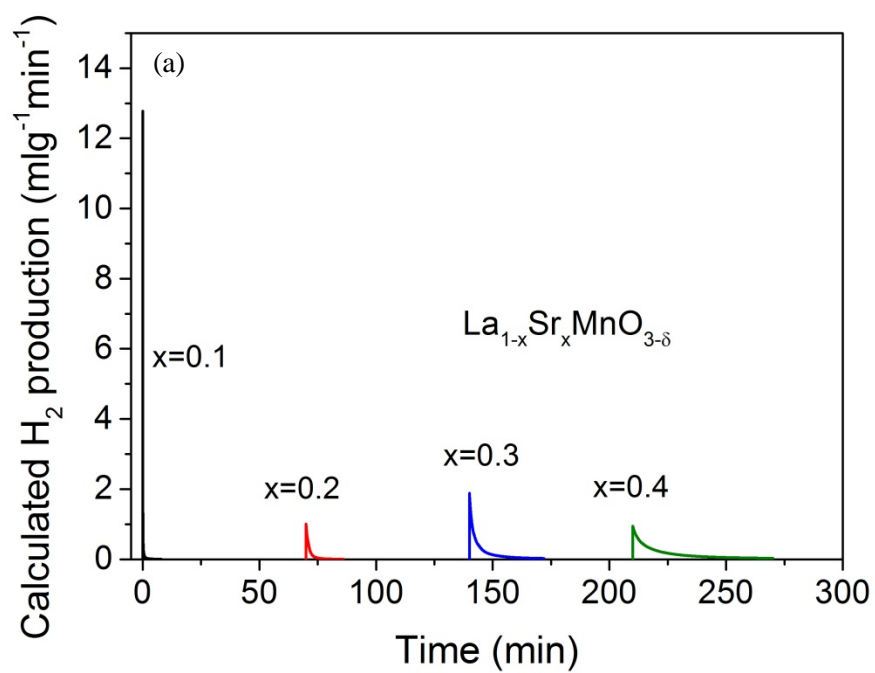


Figure 6-5. (a) Simulation of hydrogen release fluxes of $\text{La}_{1-x}\text{Sr}_x\text{MnO}_{3-\delta}$ ($x=0.1, 0.2, 0.3,$ and 0.4) during water splitting reaction at $800\text{ }^\circ\text{C}$ under $p(\text{H}_2\text{O})$ as 0.2 atm . The inputs of materials redox properties are from reference [6]. The curves are cut and plotted with the experimental thermochemical cycling time frames. (b) Reprint of Figure 3-11(b) for comparisons.

Predicting the impacts from different thermochemical cycling conditions on reaction kinetics can help us to optimize thermochemical cycling operations and improve reactor designs. Based on Equation 6-1, for the water splitting reaction, varying the injected steam flux (\dot{F}) will affect the hydrogen evolution. Figure 6-6 expresses an example of how steam flux affects the water splitting reaction (under fixed $p(\text{H}_2\text{O})$). The higher steam flux means the higher amount of steam is introduced within unit time and this can also be achieved by varying the $p(\text{H}_2\text{O})$. Therefore, the impacts of varying steam flux and varying $p(\text{H}_2\text{O})$ are similar (since the value of $(P_{\text{O}_2,f})$ shown in Equation 6-15 is relatively small as compared to $p(\text{H}_2\text{O})$, the first term in the equation mainly governs the $\partial\delta/\partial t$).

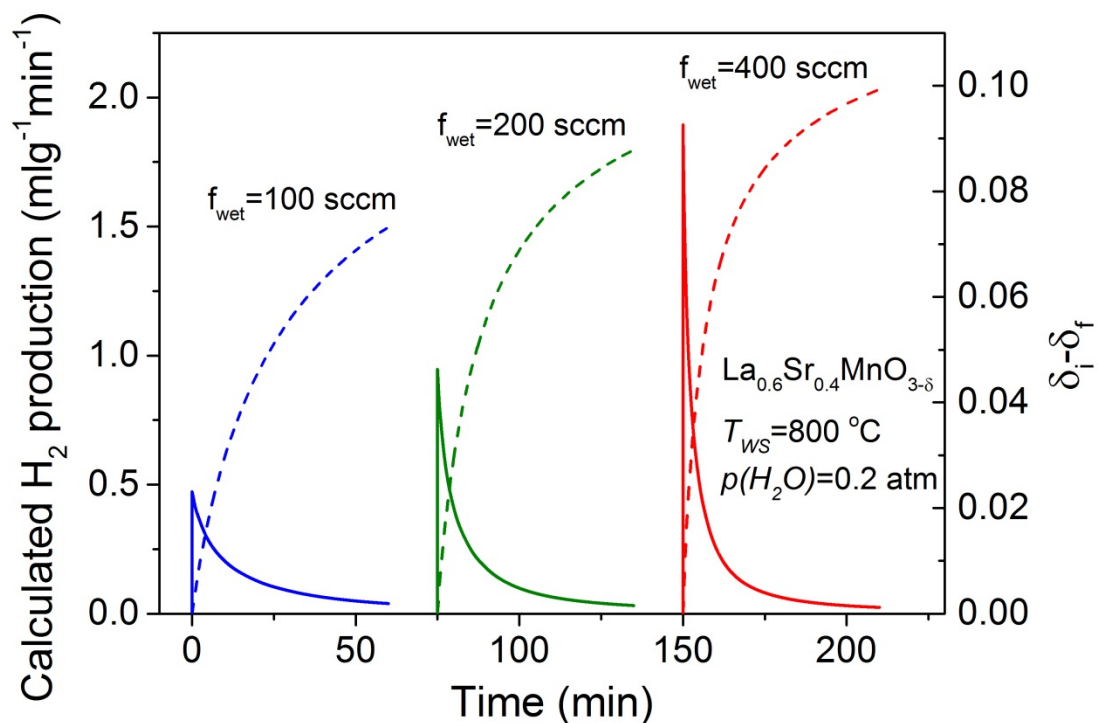


Figure 6-6. Inject steam flow rate impacts on water splitting reaction. The redox natures of $\text{La}_{0.6}\text{Sr}_{0.4}\text{MnO}_{3-\delta}$ from reference [6] are applied to this calculation. Solid lines are the simulated hydrogen production fluxes under different steam flow rate and the dash lines stand for the corresponding computed δ evolutions. All calculations are cut off at the computed reaction time of 60 minutes for saving the calculating resources since the main feature of the impacts have been shown.

6.5 Enhancing Reaction Kinetics through Materials Modification

The experimental and analytical results suggest that, when applying $\text{La}_{1-x}\text{Sr}_x\text{MnO}_{3-\delta}$ to thermochemical cycling, the reaction kinetics are limited by the surface reaction rate. Sluggish reactions carry an energy penalty not captured in the efficiency analysis presented in Chapter 4. These additional energy costs include the consumption of inert gas, the electricity for reactor

operation, pumping work for improving the chemical reaction, etc. The sum of these extra energy costs can be presented as E_{system} and combined into the efficiency calculation

$$\eta_{solar-fuel-r.o.} = \frac{HHV_{H_2} n_{H_2}}{Q_{solar} + E_{system}} \quad (6.16)$$

where “r.o.” stands for real operation.

Clearly, E_{system} increases with reaction time. Therefore, improving the reaction kinetics to lower E_{system} is critical for high solar-to-fuel conversion efficiency.

As mentioned in the introduction, for the system of $La_{1-x}Sr_xMnO_{3-\delta}$, SrO segregation is often suggested to be the source of sluggish surface reaction rates. Therefore, the approach for promoting the thermochemical process is to reduce the possibility of SrO segregation. Introduction A site deficiency to LSM, $(La_{1-x}Sr_x)_{1-y}MnO_{3-\delta}$ ($y > 0$), is hence pursued to achieve this target. For this study, we choose $La_{0.5}Sr_{0.5}MnO_{3-\delta}$ as the reactive oxide. Since this composition has a high potential for SrO segregation due to its high Sr content, the changes resulting from A site deficiency can be expected to be obvious. Six different compositions were prepared by solid state reaction methods with 1500 °C as the sintering temperature. The composition of the samples in this study are denoted by the ratio and they are A/B=0.9 ($La_{0.45}Sr_{0.45}MnO_{3-\delta}$), A/B=0.94 ($La_{0.47}Sr_{0.47}MnO_{3-\delta}$), A/B=1 ($La_{0.50}Sr_{0.50}MnO_{3-\delta}$), A/B=1.04 ($La_{0.52}Sr_{0.52}MnO_{3-\delta}$), A/B=1.08 ($La_{0.54}Sr_{0.54}MnO_{3-\delta}$), and A/B=1.16 ($La_{0.58}Sr_{0.58}MnO_{3-\delta}$). From what we learned from both the Sr doping effects on fuel productivity and kinetics simulations, for such high Sr content oxides, completion of the thermal reduction and reoxidation steps is an impractical strategy because the reaction times become excessive. In this study, the thermochemical cycling is carried out with the fixed reaction times; of 40 minutes for each half-cycle. This consistent approach reveals whether the modified compositions display the higher fuel productivity within the same and fixed reaction time framework.

The results of the thermochemical cycling of each sample are illustrated in Figure 6-7 and the corresponding oxygen release and fuel productivity results are plotted in Figure 6-8 as the function of A/B ratio.

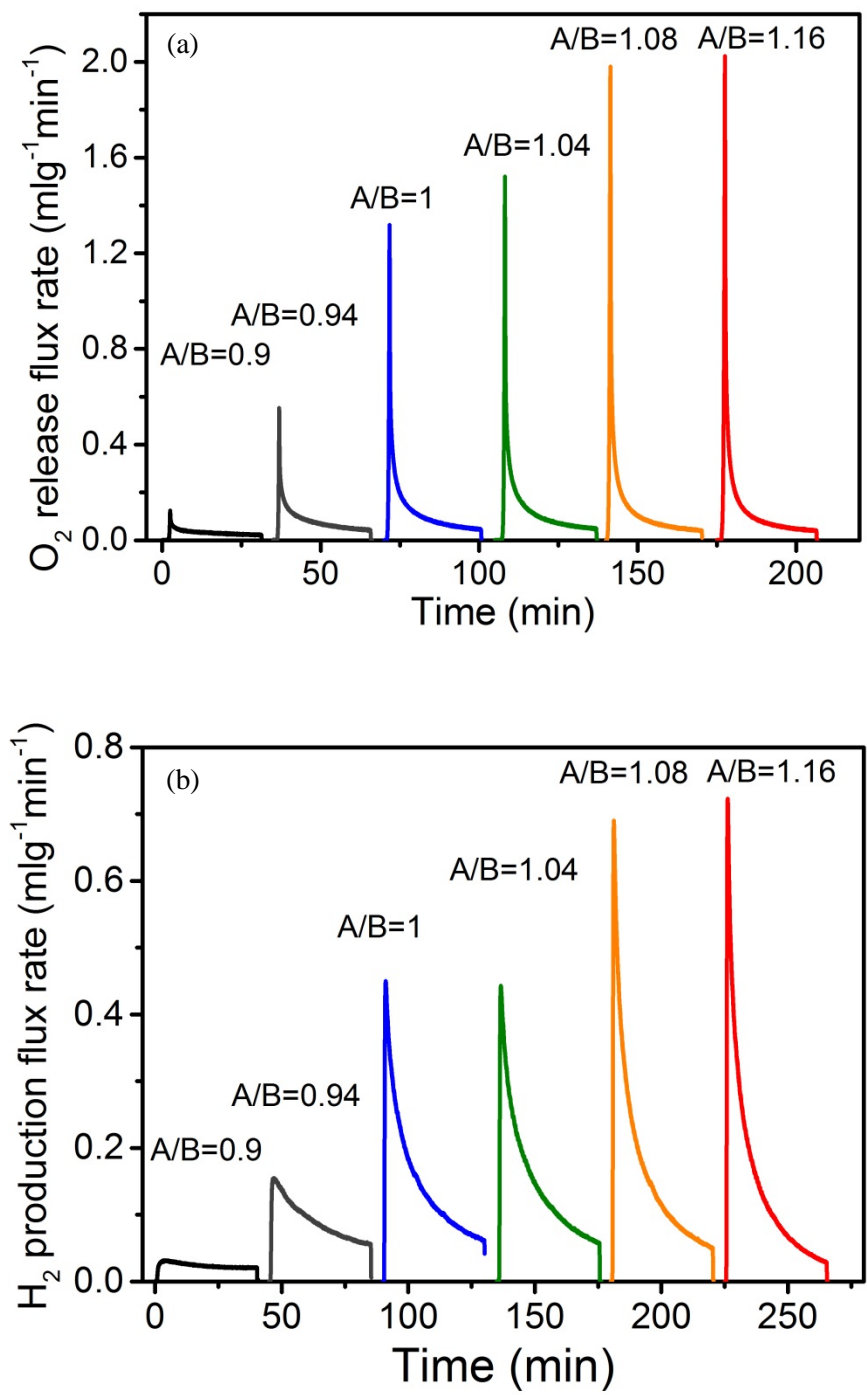


Figure 6-7. Thermochemical cycle of 1400 – 800 °C of $(\text{La}_{0.50}\text{Sr}_{0.50})_x\text{MnO}_{3-\delta}$ ($x=0.9, 0.94, 1, 1.04, 1.08, \text{ and } 1.16$). (a) Oxygen evolution fluxes of the thermal reduction reactions performed at 1400 °C under $p(\text{O}_2)=10^{-5}$ atm with gas flow rate of 1000 sccm (b) Hydrogen production fluxes of the

water splitting performed at 800 °C under $p(H_2O)=0.2$ atm with gas flow rate of 200 sccm. The tested samples are with similar mass for the measurements (0.33 to 0.37 gram).

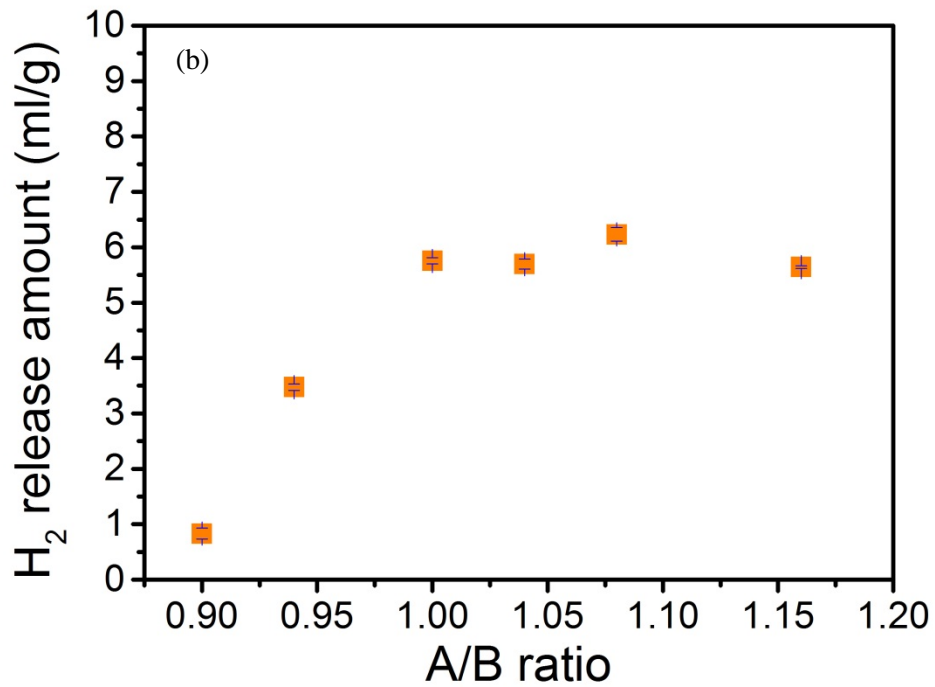
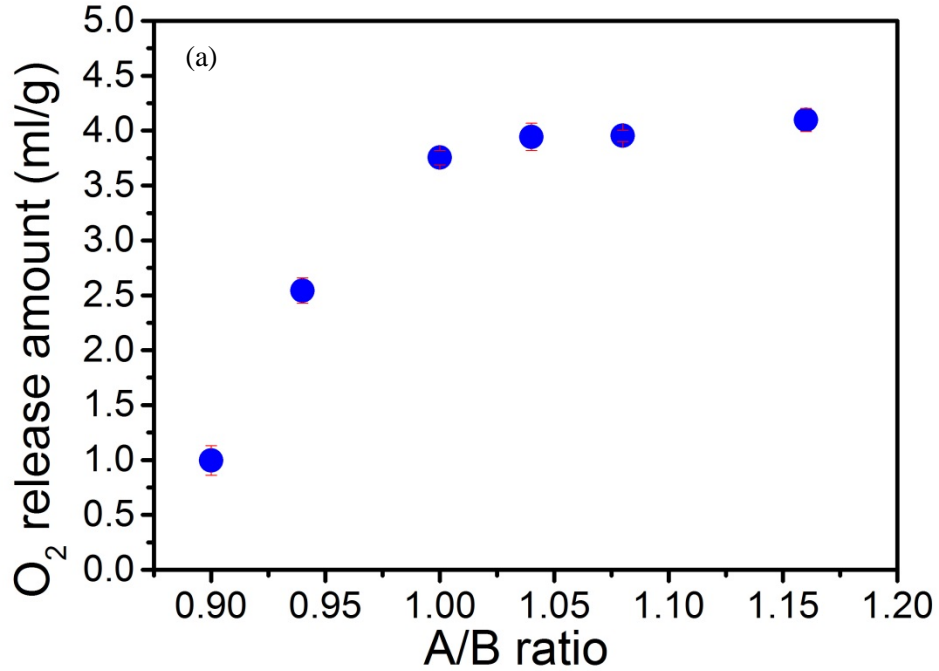


Figure 6-8. Gas evolution amounts of $(\text{La}_{0.50}\text{Sr}_{0.50})_x\text{MnO}_{3-\delta}$ generated from the thermochemical cycle of 1400 – 800 °C. (a) Oxygen releases and (b) hydrogen productions plotted as the function of A/B ratio.

Surprisingly, the samples with A site deficiency exhibit worse gas evolution kinetics and productivities in both thermal reduction and water splitting than the stoichiometric sample, $(\text{La}_{0.50}\text{Sr}_{0.50})_x\text{MnO}_{3-\delta}$. Another unanticipated finding is that the A site cations excess samples provide better performance from both steps. Due to the potential segregation on the surface, the microstructures of the reactive oxides are sensitive to oxide compositions and would affect the reaction kinetic. Secondary electron microscopy was applied to examine the oxide morphologies. Figure 6-9 shows the different microstructures between A site cation deficient ($A/B < 1$) samples and other compositions. Apparently, A site cation deficiency promotes grain growth during the sintering process. This A-site-cation-deficiency-enhanced grain growth is also found in $\text{Sr}_{1-x}\text{FeO}_{3-\delta}$ ^[7] and it is explained by the enhanced diffusion of Sr cations resulting from A site vacancies. Also, the densification of $\text{Sr}_{1-x}\text{FeO}_{3-\delta}$ caused by Sr deficiency is also found in the $(\text{La}_{0.50}\text{Sr}_{0.50})_x\text{MnO}_{3-\delta}$ samples with $x < 1$ and the lower porosity shown on their SEM images also shows evidence of higher densification. Therefore, from a microstructural standpoint, A site cation deficient samples possess morphologies which might be harmful to the reaction kinetics. Regarding the A site cation excess samples ($x > 1$ of $(\text{La}_{0.50}\text{Sr}_{0.50})_x\text{MnO}_{3-\delta}$), there is no obvious, systematic microstructural trend with the composition stoichiometry.

To summarize the information given above, results of present study suggest that A-site deficiency alters the thermodynamic redox properties in a detrimental way. This is convoluted with an obvious lose in surface area which has a negative influence on kinetics and due to the fixed cycling time, may also contribute to decreased fuel productivity. The results also indicate that A-site excess leaves thermodynamic properties unchanged, but a positive influence on surface reaction kinetics.

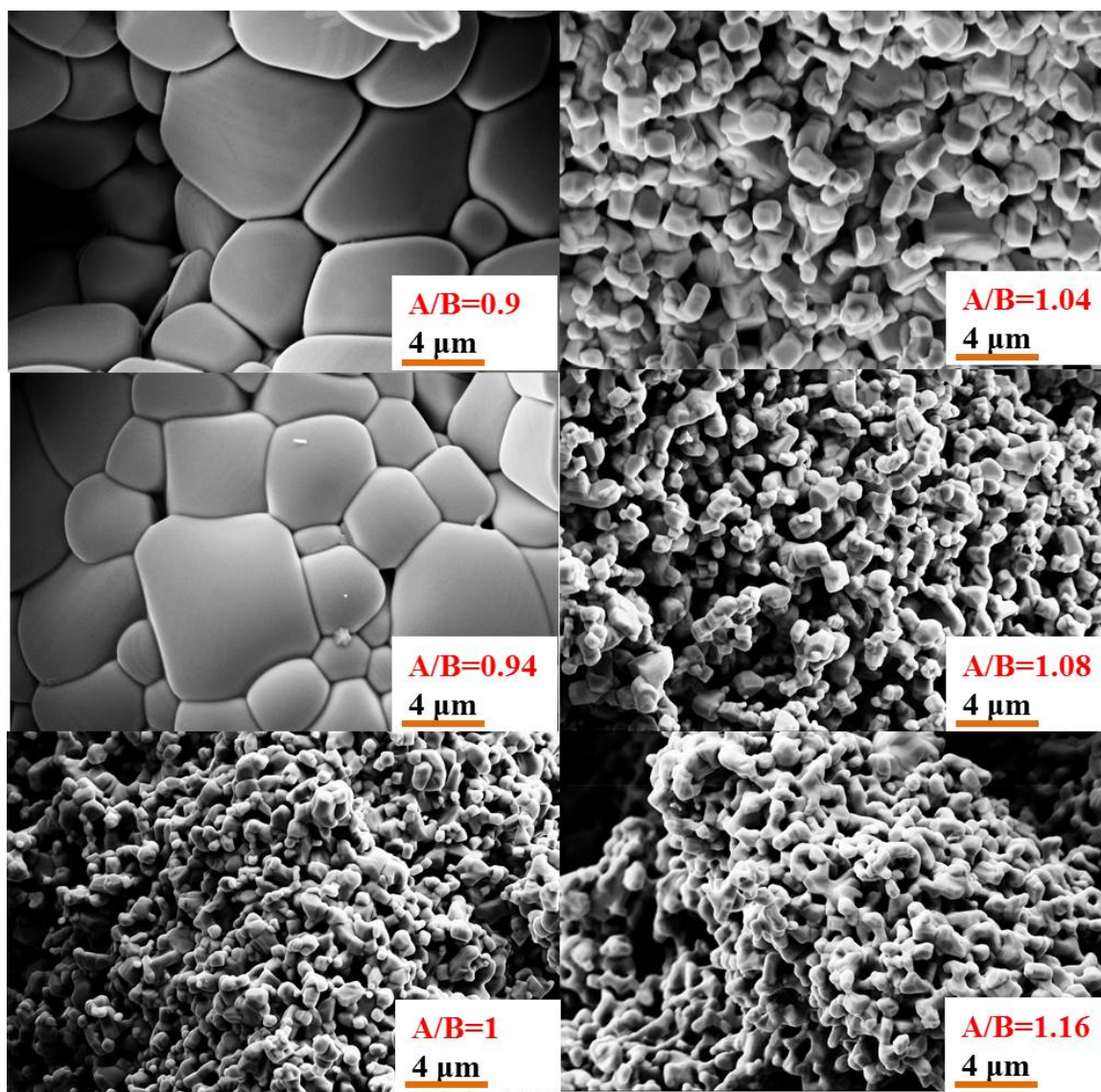


Figure 6-9. Microstructure of as-synthesized porous $(\text{La}_{0.50}\text{Sr}_{0.50})_x\text{MnO}_{3-\delta}$ ($x=0.9, 0.94, 1, 1.04, 1.08,$ and 1.16) pellets.

Since A site cation excess compositions do not show obvious microstructure change, more information is necessary for discussing the improvements from $(\text{La}_{0.50}\text{Sr}_{0.50})_x\text{MnO}_{3-\delta}$ ($x>1$) shown in thermochemical cycles. The surface segregation is expected, due to the additional cations, and X-ray powder diffraction is performed for the structural investigations. Five A/B ratios of porous $(\text{La}_{0.50}\text{Sr}_{0.50})_x\text{MnO}_{3-\delta}$ ($x=0.9, 0.94, 1, 1.16,$ and 1.24) pellets were prepared by solid state reaction with same sintering conditions ($1500\text{ }^\circ\text{C}$ under laboratory air for 6 hours), and their XRD patterns

are illustrated in Figure 6-10. Additional diffraction peaks with the strongest appearing at 32° in 2θ are clearly evident in the A-site excess compositions. The structural parameters are summarized in Table 6-1. As expected based on prior literature, the stoichiometric sample, $(\text{La}_{0.50}\text{Sr}_{0.50})\text{MnO}_{3-\delta}$, has a tetragonal structure which differs from the rhombohedral phase of oxides with less Sr content $(\text{La}_{1-x}\text{Sr}_x\text{MnO}_{3-\delta}$, $x=0.1$ to 0.4). Phase behavior of lanthanum strontium manganites with ratio A/B has been studied^[8] and it has been reported that $(\text{La}_{0.50}\text{Sr}_{0.50})_x\text{MnO}_{3-\delta}$ remains in the tetragonal structure for a non-stoichiometric ratio from 0.9 to 1.1. However, from our results, the $(\text{La}_{0.45}\text{Sr}_{0.45})\text{MnO}_{3-\delta}$ sample has the rhombohedral phase with the space group of R ($R\bar{3}c$). Compared to the sample prepared in literature, our sample was prepared with 50°C higher (1500°C vs 1450°C) and four hours (2 vs 6 hours) longer for sintering temperature and time, respectively. To learn whether this different preparation conditions cause the different phase for $(\text{La}_{0.45}\text{Sr}_{0.45})\text{MnO}_{3-\delta}$, more investigations are necessary.

The additional peaks in the A-site excess compositions are attributed to the existence of a secondary phase is identified as $(\text{La}_{1-y}\text{Sr}_y)_3\text{Mn}_2\text{O}_{7-\delta}$ which is also called Ruddlesden-Popper phase. This phase belongs to a class of materials of general stoichiometry $\text{A}_{n+1}\text{B}_n\text{O}_{3n+1}$ shown in Figure 6-11 known as Ruddlesden-Popper phase. Ruddlesden-Popper phase have structures in which rock-salt AO (here is LaO) layers alternate with single ($n=1$), double ($n=2$), or triple ($n=3$) perovskite $(\text{ABO}_3)_n$ layers along the c -axis. When n goes to infinite, the structure becomes perovskite. The candidate applied for the structure analysis is $(\text{La}_{0.5}\text{Sr}_{0.5})_3\text{Mn}_2\text{O}_{7-\delta}$, however, the precise La:Sr ratio is unknown, and the secondary phase is more correctly described as $(\text{La}_{1-y}\text{Sr}_y)_3\text{Mn}_2\text{O}_{7-\delta}$.

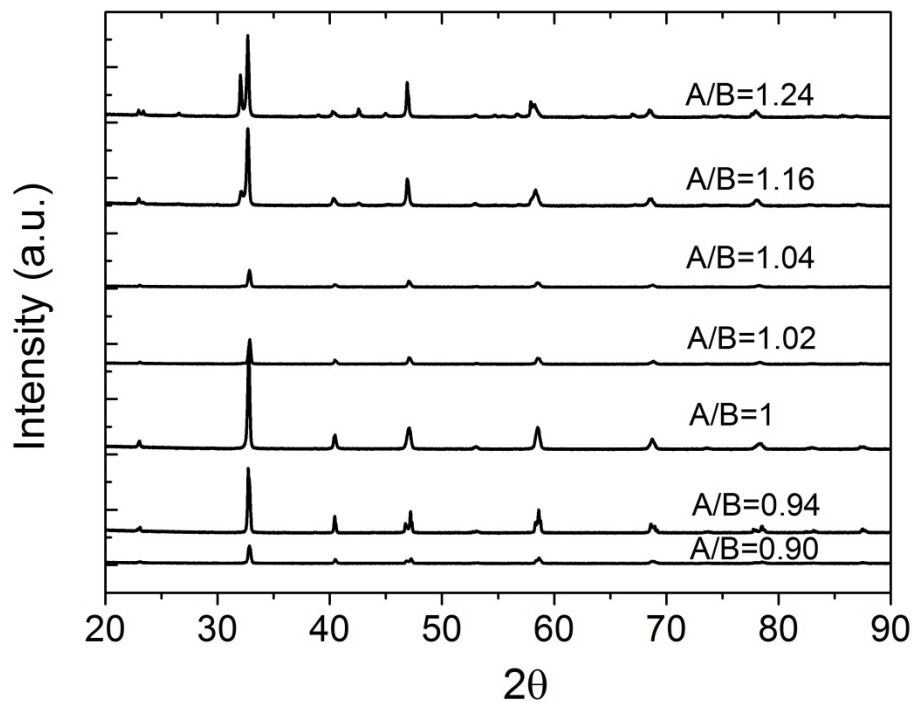


Figure 6-10. X-ray powder diffraction patterns of as-synthesized porous $(\text{La}_{0.50}\text{Sr}_{0.50})_x\text{MnO}_{3-\delta}$ ($x=0.9, 0.94, 1, 1.04, 1.08, 1.16,$ and 1.24) pellets. Final processing step was sintering at $1500\text{ }^\circ\text{C}$ under laboratory air for 6 hours.

Table 6-1. Room-temperature structural parameters for as-synthesized $(\text{La}_{0.50}\text{Sr}_{0.50})_x\text{MnO}_{3-\delta}$ ($x=0.9, 0.94, 1, 1.04, 1.08, 1.16,$ and 1.24) samples. The additional phase is temporarily assigned with the compositions of $(\text{La}_{0.5}\text{Sr}_{0.5})_3\text{Mn}_2\text{O}_{7-\delta}$ and the evidence for supporting this assumption is still missing. The input structure file for 2nd phase was created by modifying the crystal structure data of $(\text{La}_{1.4}\text{Sr}_{1.6})\text{Mn}_2\text{O}_7$ reported in Inorganic Crystal Structure Database with collection code 89382.

A/B	a (Å)	b (Å)	c (Å)	Crystal structure (space group)
0.90	5.4567(3)	5.4567(3)	13.291(2)	R ($R\bar{3}c$) (167)
0.94	5.44129(8)	5.44129(8)	7.7620(1)	I4/mcm (140)
1.00	5.4523(1)	5.4523(1)	7.7404(3)	I4/mcm (140)
1.04	5.4689(3)	5.4689(3)	7.7059(6)	I4/mcm (140)

1.08	5.4684(6)	5.4684(6)	7.729(2)	I4/mcm (140)
1.16	5.4721(4)	5.4721(4)	7.739(1)	I4/mcm (140)
2 nd phase	3.8694(2)	3.8694(2)	20.005(2)	I4/mcm (139)
1.24	5.4762(2)	5.4762(2)	7.7779(7)	I4/mcm (140)
2 nd phase	3.87292(8)	3.87292(8)	20.1579(7)	I4/mcm (139)

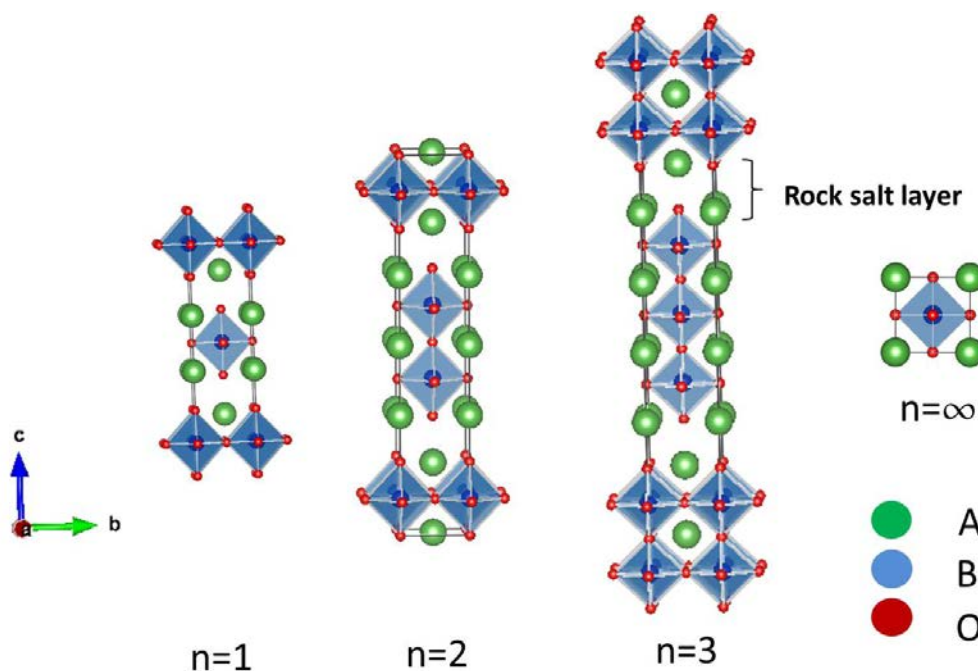


Figure 6-11. Crystal structures of Ruddlesden-Popper phase ($A_{n+1}B_nO_{3n+1}$) materials of general stoichiometry. Crystals were drawn via VESTA^[14] and the corresponding crystal structure data are from Inorganic Crystal Structure Database with collection code 157402 (Sr_2TiO_4 , $n=1$), 63704 ($Sr_3Ti_2O_7$, $n=2$), 34630 ($Sr_4Ti_3O_{10}$, $n=3$), and 80874 ($SrTiO_3$, $n=\square$).

Therefore, the samples that possess A site cations excess can be considered to be composites of $(La_{0.50}Sr_{0.50})MnO_{3-\delta}$ and $(La_{1-y}Sr_y)_3Mn_2O_{7-\delta}$. The system with the combinations of perovskites and Ruddlesden-Popper phases have been studied for SOFC cathode materials such as $(La,Sr)CoO_{3-\delta}$ - $(La,Sr)_2CoO_{4+\delta}$ ^[11, 12] and $La_{n+1}Ni_nO_{3n+1}$ ($n=1, 2, \text{ and } 3$)-YSZ^[13], and the presence of Ruddlesden-Popper phase has been found to enhance the oxygen reduction reaction (ORR) kinetics at 600 to 800 °C. It has been proposed that the Ruddlesden-Popper phase is electronically activated through

an interface coupling with the perovskite, facilitates the charge transfer from the oxide surface to the oxygen near the interface. It is unclear whether a similar mechanism is operative here. First, $(\text{La,Sr})_2\text{CoO}_{4-\delta}$ and $\text{La}_{n+1}\text{Ni}_n\text{O}_{3n+1}$ have different electronic structures than that of $(\text{La}_{1-y}\text{Sr}_y)_3\text{Mn}_2\text{O}_{7-\delta}$. Second, this active interface only explains the enhanced ORR kinetics which is an explicit electrochemical reaction, but thermal reduction and oxidization by steam are nominally only chemical reactions. Furthermore, the thermochemical cycling temperature and oxygen partial pressure conditions are different from the operation conditions usually applied for cathode materials, therefore, whether the high activity exists under the environments of thermochemical cycling needs to be confirmed. To answer the questions above, careful interface properties studies are necessary. In summary, the introduction of excess A site cations into $(\text{La}_{0.50}\text{Sr}_{0.50})\text{MnO}_{3-\delta}$ enhances both thermal reduction and water splitting, an apparent result of the presence of additional Ruddlesden-Popper phase. This finding indicates that $(\text{La}_{0.50}\text{Sr}_{0.50})\text{MnO}_{3-\delta}$ can produce more hydrogen by thermochemical cycling for a fixed cycling time. It is mentioned above that $J = k\Delta\mu$ can be used to describe the gas evolution flux and samples with A-site excess, in present study, be considered to be composites of $\text{La}_{0.50}\text{Sr}_{0.50}\text{MnO}_{3-\delta}$ and $(\text{La}_{1-y}\text{Sr}_y)_3\text{Mn}_2\text{O}_{7-\delta}$. Since the A-site excess is so small, the chemical potential ($\Delta\mu$) of samples for both half-reaction can be viewed as the same ($\Delta\mu$ of $\text{La}_{0.50}\text{Sr}_{0.50}\text{MnO}_{3-\delta}$). The enhancements shown in present study, therefore, can be attributed to the enhanced surface reaction coefficient (k).

BIBLIOGRAPHY

1. J. Yoo, A. Verma, S. Wang and A. J. Jacobson, *Journal of The Electrochemical Society*, 2005, 152, A497-A505.
2. S.P. Simner, M.D. Anderson and M.H. Engelhard, J.W. Stevenson, *Electrochemical and Solid-State Letters*, 9 (2006) A478.
3. Z. Cai, M. Kubicek, J. Fleig and B. Yildiz, *Chemistry of Materials*, 2012, 24, 1116–1127
4. A. K. Huber, M. Falk, M. Rohnke, B. Luerssen, M. Amati, L. Gregoratti, D. Hesse and J. Janek, *Journal of Catalysis*, 2012, 294,79–88
5. http://en.wikipedia.org/wiki/Runge%E2%80%93Kutta_methods
6. J. Mizusaki, Y. Yonemura, H. Kamata, K. Ohyama, N. Mori, H. Takai, H. Tagawa, M. Dokiya, K. Naraya, T. Sasamoto, H. Inaba and T. Hashimoto, *Solid State Ionics*, 2000, 132, 167-180.
7. K. Kleveland, M.-A. Einarsrud and T. Grande, *Journal of the American Ceramic Society*, 2000, 83, 3158-3164.
8. P. M. Woodward, T. Vogt, D. E. Cox, A. Arulraj, C. N. R. Rao, P. Karen and A. K. Cheetham, *Chemistry of Materials*, 1998, 10, p3652-3665.
9. F. Zheng and L. R. Pederson. *Journal of The Electrochemical Society* , 1999, 146, 2810-2816.
10. A. Manthiram, J.-H. Kim, Y. N. Kim and K.-T. Lee, *Journal of Electroceramics*, 2011, 27, 93-107.
11. Y. Chen, Z. Cai, Y. Kuru, W. Ma , H. L. Tuller and B. Yildiz, *Advance Energy Materials*, 2013, 3, 1221–1229.
12. M. Eva, J. C. Ethan, D. B. Michael, M. C. Hans and S.-H. Yang, *Energy & Environmental Science*, 2011, 4, 3689-3696.
13. S. Choi, S. Yoo, a J.-Y. Shin and G. Kima, *Journal of The Electrochemical Society*, 2011, 158, B995-B999.
14. K. Momma and F. Izumi, *Journal of Applied Crystallography*, 2011, 44, 1272-1276.

CONCLUSIONS AND FUTURE OUTLOOK

7.1 Conclusions

Strontium-doped lanthanum manganite perovskites, $\text{La}_{1-x}\text{Sr}_x\text{MnO}_{3-\delta}$ ($x=0.1, 0.2, 0.3, \text{ and } 0.4$), were assessed for two-step thermochemical water splitting. Oxides with different Sr contents exhibit distinct redox and thermochemical cycling behavior. Increasing Sr substitution for the A site cation mainly reduces the oxidization reaction enthalpy, which enhances the reducibility and increases the fuel productivity. However, particularly for high Sr content oxides, in order to produce such large quantities of fuel, large amounts of reactant steam are required. This is reflected in the fact that the steam to hydrogen conversion or reaction extent (ψ) is small.

In order to predict how changes in material redox properties affect the water splitting reaction extent, ψ was calculated using hypothetical values for the reduction enthalpy and entropy values of oxygen in the oxide phase. The results reveal that *increasing* of the reduction enthalpy and *decreasing* of the reduction entropy relative to the values in ceria each results in higher reaction extents (ψ). This occurs because such changes favor the oxidization reaction. On the other hand, thermal reduction, which largely fixes the fuel productivity by setting δ_i , is favored when the magnitude of Δh_o decrease and that of Δs_o increase (*i.e.* reduction is favored). Thus, the thermodynamic considerations that favor reaction extent are exactly opposite those that favor fuel productivity.

In order to balance the goals of high fuel productivity and high reaction extent, solar to fuel efficiency ($\eta_{\text{solar-fuel}}$) has been established as the figure of merit for assessing candidate oxides for two-step thermochemical cycling.

Besides the thermodynamic considerations for material characteristics in selecting the optimal material, models for equilibrium reaction kinetics simulations have been developed. The simulations reflect the impacts from redox properties on the optimized reaction kinetics. Since the possibility of bulk diffusion limited has been ruled out, the comparisons of the simulations and experimental results for $\text{La}_{1-x}\text{Sr}_x\text{MnO}_{3-\delta}$ up to $x=0.4$ reveal that the surface reactions are the rate determining steps of the thermochemical cycling.

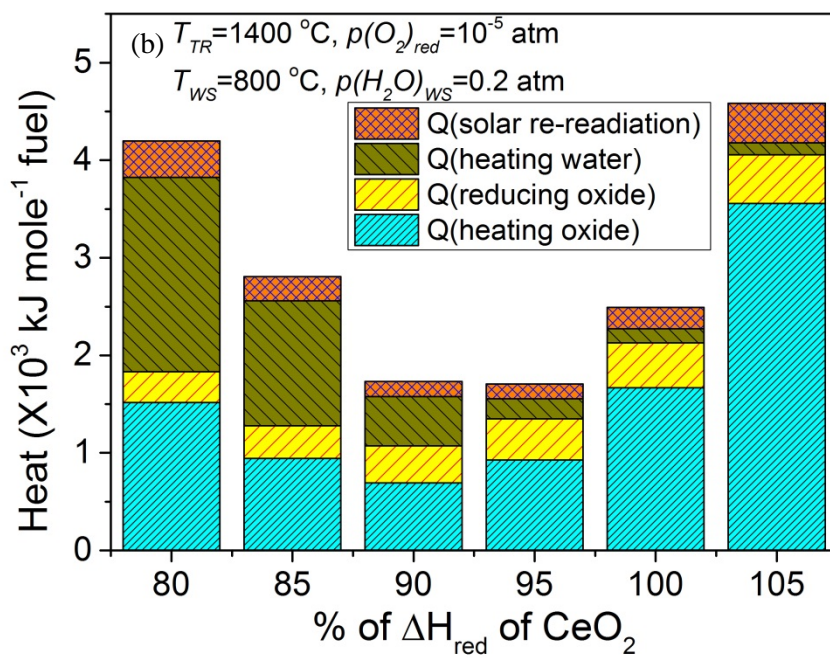
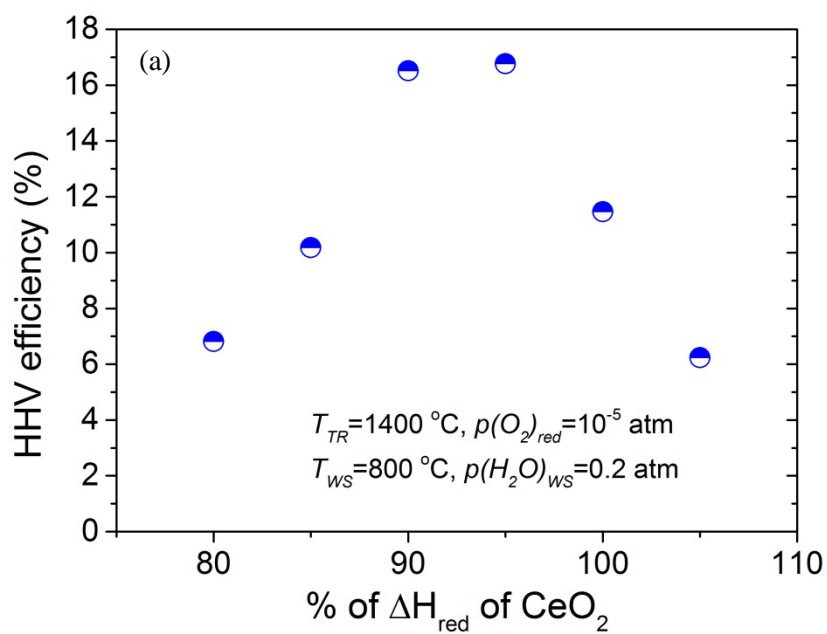
For actual thermochemical cycle implementations, when considering the lengthy reaction time due to the sluggish surface reaction, how to obtain the most fuel productivity with the unit time interval is crucial for obtaining the high actual solar to fuel efficiency. Within the study of A site cation stoichiometry modifications for $\text{La}_{0.5}\text{Sr}_{0.5}\text{MnO}_{3-\delta}$, excess A site cation doping promotes the reaction kinetics on both thermochemical cycle steps. It is believed that this enhancement is related to the presence of the additional Ruddlesden-Popper phase that resulted from the excess A site cation doping. The actual mechanism for explaining this kinetics improvement is still unclear and future work for understanding is necessary.

7.2 Future Work

Efficiency analysis helps us to look for the subtle trade-off between material characteristics in selecting the optimal material for solar-driven thermochemical fuel production. Like the ψ simulations of hypothetical materials we did for learning the individual effects from varying reduction enthalpy and entropy, we can also apply the efficiency analysis on the hypothetical materials for efficiency optimization. Since the reduction enthalpy can be viewed as the bonding strength between oxygen ions and cations, prediction of the optimal reduction enthalpy values can guide efforts on how to best use doping strategies to tune the bonding.

We again take $\text{CeO}_{2-\delta}$ as a base and evaluate the influence of modifying the properties of the oxide. In particular, we consider the impact of changing the reduction enthalpy of $\text{CeO}_{2-\delta}$, while taking the reduction entropy to be fixed. The HHV efficiency analysis results of these hypothetical materials under fixed thermochemical cycling conditions are shown in Figure 7-1. From Figure 7-1(a), we can see that if we can lower the reduction enthalpy of $\text{CeO}_{2-\delta}$ by 5-10% without alternating (significantly) the reduction entropy the HHV efficiency would improve from 11.5% to 16.7% (95% of Δh_{O}). Figure 7-1(b) shows that the energy input required for heating steam increases as the reduction enthalpy decreases, consistent with the concomitant decrease in ψ discussed previously (Figure 4-10). However, as expected, the fuel productivity increases with decreasing reduction enthalpy, Figure 7-1(c), and generally leads to a lowering of the energy input required for heating the oxide. For the hypothetical materials with 90-95% reduction enthalpy of $\text{CeO}_{2-\delta}$, the benefits from their increased $\Delta\delta$ ($\delta_i - \delta_f$) outweigh the penalties the decrease of ψ , and such materials provide maximum efficiency. Significantly, even at optimal $\Delta\delta$ (the value that maximizes efficiency rather than fuel productivity) also shown in Figure 7-1(c), a hypothetical materials with 90% reduction

enthalpy of $\text{CeO}_{2-\delta}$ will possess high fuel productivity as compared to others. Based on these results, we can try to design the new oxide for thermochemical water splitting by lowering the reduction enthalpy of $\text{CeO}_{2-\delta}$ for 10% via doping. Therefore, with the given operation conditions of thermochemical cycling, HHV efficiency analysis can help us to look for the optimal redox properties of the reactive oxide and this guides us how to screen or modify the material characteristics.



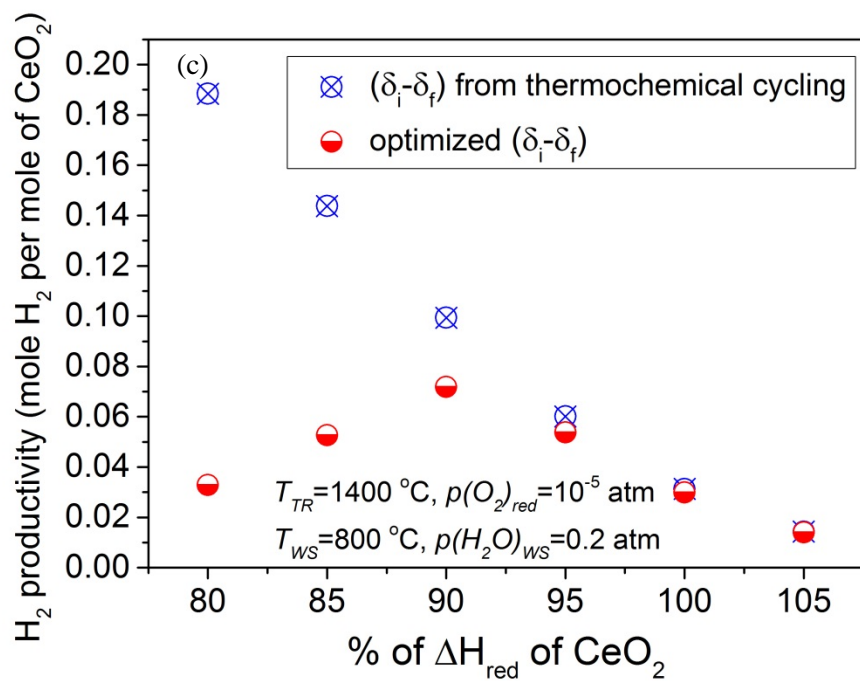


Figure 7-1. HHV efficiency optimization for hypothetical materials. (a) HHV efficiency. (b) Required heat inputs for individual processes of maximum HHV efficiency. (c) Oxygen non-stoichiometry change from thermal reduction and the optimized $\Delta\delta$ ($\delta_i - \delta_f$) of maximum HHV efficiency.